COMPUTATIONAL AND EXPERIMENTAL INVESTIGATION OF LOW FREQUENCY NOISE IN PASSENGER VEHICLES

by

Akın Oktav

B.S., in Metallurgical Engineering, İstanbul Technical University, 2003

M.S., in Automotive Engineering, Boğaziçi University, 2005

Submitted to the Institute for Graduate Studies in
Science and Engineering in partial fulfillment of
the requirements for the degree of
Doctor of Philosophy

Graduate Program in Mechanical Engineering

Boğaziçi University

2016

COMPUTATIONAL AND EXPERIMENTAL INVESTIGATION OF LOW FREQUENCY NOISE IN PASSENGER VEHICLES

APPROVED BY:

Prof. Günay Anlaş ..... (Thesis Supervisor)

Assoc. Prof. Çetin Yılmaz ..... (Thesis Co-supervisor)

Assoc. Prof. Hasan Bedir .....

Prof. Hilmi Luş .....

Assist. Prof. Alpay Oral .....

Prof. Bülent Yardımoğlu .....

DATE OF APPROVAL: April 29, 2016

dedicated to Ayşenur Demirtel

ACKNOWLEDGEMENTS

This work is supported by the Ministry of Science, Industry and Technology. SAN-TEZ Project: 00641.STZ.2010-II

ABSTRACT

COMPUTATIONAL AND EXPERIMENTAL INVESTIGATION OF LOW FREQUENCY NOISE IN PASSENGER VEHICLES

In this study, low frequency noise characteristics of passenger vehicles are addressed. Vehicle noise variability and dominant paths that cause low frequency booms are investigated. To diagnose the cause of variability, a systematic approach is proposed, where all steps are explained briefly. Current practice of experimental transfer path analysis is discussed in the context of trade-offs between accuracy and time cost. An overview of methods, which propose solutions for structure borne noise, is given, where assumptions, drawbacks and advantages of methods are stated theoretically. Applicability of methods is also investigated, where the engine induced structure borne noise of the sedan studied is taken as a reference problem. Sources of measurement errors, processing operations that affect results and physical obstacles faced in the application are analyzed. Effects of damping, reasons and methods to analyze them are discussed in detail. In this regard, a new procedure, which increases the accuracy of results, is also proposed. Coupled vibro-acoustic response of the sedan is analyzed, and the effect of folding rear seat aperture is studied. An analytical solution is proposed to calculate acoustic eigenfrequencies. Then, uncoupled acoustic eigenfrequencies of the actual cavity, where trunk and cabin cavities are connected through the aperture are computed. It is shown that planar acoustic eigenfrequencies of the sedan can approximately be calculated using the analytical solution proposed. To further clarify the impact of folding rear seat aperture, coupled vibro-acoustic response of the sedan is analyzed through different case studies. Experimental modal analysis studies are carried out to update the computational model. The updated model is then used in modification prediction studies.

ÖZET

BİNEK ARAÇLARDAKİ DÜŞÜK FREKANSLI GÜRÜLTÜNÜN HESAPLAMALI VE DENEYSEL YÖNTEMLERLE ARAŞTIRILMASI

Bu çalışmada binek araçların gürültü karakteristikleri üzerinde durulmuştur. Araç gürültüsündeki değişkenlik ve düşük frekanslı uğultu problemlerine yol açan baskın iletim yolları araştırılmıştır. Değişkenliğin nedenlerini teşhis etmek için sistematik bir prosedür önerilmiştir. Deneysel iletim yolu analizinin güncel pratiği, hesapların doğruluğu ve zaman maliyeti arasındaki ödünleşim kapsamında tartışılmıştır. Yapısal iletimli gürültü problemine ilişkin metotlar ele alınmış, avantajları ve sakıncaları teorik olarak ifade edilmiştir. Çalışmalarda kullanılan sedanın motor kaynaklı yapısal gürültü problemi referans alınmak suretiyle bahsi geçen metotların uygulanabilirliği de araştırılmıştır. Ölçüm hatalarının nedenleri, veri işleme prosedürlerinin olumsuz tesirleri ve uygulamada karşılaşılan fiziksel engeller incelenmiştir. Yapısal ve viskoz sönümlemenin etkileri, bu etkilerin neden araştırıldığı ve çözümleme metotları kapsamlı bir şekilde tartışılmıştır. Bu bağlamda, sonuçların doğruluğunu arttıran yeni bir prosedür de teklif edilmiştir. Çalışılan sedanın, birleştirilmiş vibro-akustik tepkisi çözümlenmiş ve tepkide katlanan arka koltuk açıklığının etkisi çalışılmıştır. Akustik öz frekansların hesaplanmasında kullanılmak üzere analitik bir çözüm önerilmiştir. Sonrasında aracın akustik öz frekansları, kabin ve bagaj hacminin bahse konu açıklıkta birleştiği göz önüne alınarak hesaplanmıştır. Aracın düzlemsel akustik öz frekanslarının bu çalışmada önerilen analitik çözüm yoluyla yaklaşık olarak hesaplanabileceği gösterilmiştir. Katlanan arka koltuk açıklığının etkisini net bir şekilde ortaya koymak için aracın birleştirilmiş vibro-akustik tepkileri farklı durum çalışmalarıyla irdelenmiştir. Nümerik modelin güncellenmesi için deneysel modal analiz çalışmaları gerçekleştirilmiştir. Sonrasında, güncellenen model modifikasyon tahmin çalışmalarında kullanılmıştır.

TABLE OF CONTENTS

ACKNOWLEDGEMENTS iv
ABSTRACT v
ÖZET vi
LIST OF FIGURES x
LIST OF TABLES xxiv
LIST OF ACRONYMS/ABBREVIATIONS xxvi
1. INTRODUCTION 1
1.1. Motivation 1
1.2. Literature Survey 3
1.3. Objective 11
1.4. Methods Employed 12
1.5. Original Contributions 13
1.6. Outline 14
2. EXPERIMENTAL ANALYSIS 16
2.1. Sound and Human Perception 16
2.2. Acquisition and Processing of Data 19
2.3. Test Configurations and Environments 25
2.4. Experimental Setup and Test Vehicles 28
2.5. Road Tests and Variability 30
2.5.1. Road Test Results 33
2.6. Laboratory Mock up Tests 49
2.6.1. Road - Laboratory Test Comparison 50
2.7. Diagnosis and Problem Definition 60
2.8. Transfer Path Analysis 61
2.8.1. Force Methods 65
2.8.2. Transmissibility Methods 70
2.8.3. Applicability of Methods 72
2.8.4. The Results of Transfer Path Analysis 74
2.8.4.1. Overview 75

2.8.4.2. Detailed Results for the Vehicle L84 77
2.8.4.3. Detailed Results for the Vehicle L38 85
2.9. An Approach to the Assessment of Inter Variability 108
2.10. Panel Contribution Analysis 111
2.11. Hybrid Transfer Path Analysis 134
2.11.1. Identification of structural and viscous damping 135
2.11.2. Proposed procedure 138
2.12. Remarks 141
3. COMPUTATIONAL ANALYSIS 145
3.1. Construction of the Finite Element Model 145
3.2. Computation of Acoustic Modes 153
3.2.1. Analytical Box Model 158
3.2.2. Coupling of Adjacent Cavities 163
3.3. Computation of Structural Modes 177
3.3.1. Normal Modes Analysis 177
3.3.2. Preparation for EMA 179
3.4. Remarks 181
4. SYNTHESIS 182
4.1. Experimental Modal Analysis 182
4.1.1. Modal Data Acquisition 182
4.1.1.1. Benchmark for BIW Excitation 185
4.1.2. Modal Parameter Estimation 190
4.1.3. Modal Data Validation 196
4.2. Correlation Analysis 198
4.3. Coupled Vibro-Acoustic Analysis 199
4.4. Modification Prediction Analysis 210
5. DISCUSSION AND FUTURE WORK 214
6. CONCLUSION 215
REFERENCES 217
APPENDIX A: Coherence Function 239
APPENDIX B: Vibration of Thin Plates 242
APPENDIX C: Derivation of Finite Element Equation: Structural Domain . . 246

APPENDIX D: Derivation of Finite Element Equation: Acoustic Fluid Domain 248
APPENDIX E: Eulerian Displacement-Pressure Formulation 254

LIST OF FIGURES

Figure 1.1. Sound pressure level measurements in the mid 60's 4

Figure 1.2. Vibration flow through engine mounts 8

Figure 2.1. Equal loudness contours 17

Figure 2.2. Frequency weights due to ANSI S1.4 standard 18

Figure 2.3. Aliasing problem 25

Figure 2.4. Windowed signal 25

Figure 2.5. Vehicle L38 28

Figure 2.6. Vehicle L84 29

Figure 2.7. The experimental setup 29

Figure 2.8. Vehicle L38 in road test 31

Figure 2.9. Microphone locations 31

Figure 2.10. Engine mounts 34

Figure 2.11. Exhaust mounts 35

Figure 2.12. Waterfall plot of Vehicle L84, BT: D, in Hz, rpm and Pa . 36

Figure 2.13. Sound pressure levels at Vehicle L84 targets, dB vs. rpm . 36

Figure 2.14. Orders plot 37

Figure 2.15. Sound pressure level curves of five L38 vehicles, dB vs. rpm 38

Figure 2.16. Engine block accelerations of L38 test vehicles 39

Figure 2.17. Engine mount (SM01)-active side acceleration curves . . . 39

Figure 2.18. Engine mount (SM02)-active side acceleration curves . . . 40

Figure 2.19. Engine mount (SM03)-active side acceleration curves . . . 40

Figure 2.20. Engine mount (RH01)-passive side acceleration curves . . . 41

Figure 2.21. Engine mount (RH02)-passive side acceleration curves . . . 41

Figure 2.22. Engine mount (RH03)-passive side acceleration curves . . . 42

Figure 2.23. Exhaust mount (FE22)-active side acceleration curves . . . 42

Figure 2.24. Exhaust mount (FE31)-active side acceleration curves . . . 43

Figure 2.25. Exhaust mount (FE41)-active side acceleration curves . . . 43

Figure 2.26. Exhaust mount (EC22)-passive side acceleration curves . . 44

Figure 2.27. Exhaust mount (EC31)-passive side acceleration curves . . 44

Figure 2.28. Exhaust mount (EC41)-passive side acceleration curves . . 45

Figure 2.29. Booms observed at the targets of test vehicle # 170 46

Figure 2.30. Exhaust mount (FE22)-active side acceleration curves . . . 46

Figure 2.31. Exhaust mount (FE31)-active side acceleration curves . . . 47

Figure 2.32. Exhaust mount (FE41)-active side acceleration curves . . . 47

Figure 2.33. Exhaust mount (EC22)-passive side acceleration curves . . 48

Figure 2.34. Exhaust mount (EC31)-passive side acceleration curves . . 48

Figure 2.35. Exhaust mount (E41)-passive side acceleration curves . . . 49

Figure 2.36. Road - laboratory test comparison, L84 50

Figure 2.37. Locations of engine and exhaust mounts, Vehicle L38 . . . 52

Figure 2.38. Road - laboratory test comparison, L38, #170 52

Figure 2.39. Booming regions, L38, #170 53

Figure 2.40. Engine block acceleration, L38 53

Figure 2.41. Engine mount (SM01)-active side acceleration curves . . . 54

Figure 2.42. Engine mount (SM02)-active side acceleration curves . . . 54

Figure 2.43. Engine mount (SM03)-active side acceleration 55

Figure 2.44. Engine mount (RH01)-passive side acceleration 55

Figure 2.45. Engine mount (RH02)-passive side acceleration 56

Figure 2.46. Engine mount (RH03)-passive side acceleration 56

Figure 2.47. Exhaust mount (FE22)-active side acceleration 57

Figure 2.48. Exhaust mount (FE31)-active side acceleration 57

Figure 2.49. Exhaust mount (FE41)-active side acceleration 58

Figure 2.50. Exhaust mount (EC22)-passive side acceleration 58

Figure 2.51. Exhaust mount (EC31)-passive side acceleration 59

Figure 2.52. Exhaust mount (EC41)-passive side acceleration 59

Figure 2.53. An assembled structure 65

Figure 2.54. Removal of the engine, Vehicle L38 75

Figure 2.55. Comparison of SPL curves using mount stiffness 76

Figure 2.56. Comparison of SPL curves using matrix inversion 77

Figure 2.57. Comparison of SPL curves using diagonal matrix inversion 77

Figure 2.58. Accelerance FRFs 79

Figure 2.59. Coherence plots of the driving points 79

Figure 2.60. Measured and calculated SPLs at target BT:D 80

Figure 2.61. Measured TPA result, SPLs at target BT:D 80

Figure 2.62. Calculated TPA result, SPLs at target BT:D 81

Figure 2.63. Improvement in the condition number 83

Figure 2.64. Contributions of all paths (1000-4600 rpm), BT:D 84

Figure 2.65. Contributions of all paths (1200-4400 rpm), BT:D 84

Figure 2.66. Contributions of all paths (3000-4200 rpm), BT:D 85

Figure 2.67. Main contributors of the booming 86

Figure 2.68. RH03:Z and RH03:X path SPLs 87

Figure 2.69. Measured and calculated SPLs at BT:K 88

Figure 2.70. Contributions of all paths (1500-4500 rpm), BT:K 88

Figure 2.71. Contributions of all paths (2250-4250 rpm), BT:K 89

Figure 2.72. TPA test vehicles 90

Figure 2.73. Measured and calculated SPLs at BT:D, 6 scenarios 91

Figure 2.74. Measured and calculated SPLs at BT:D 91

Figure 2.75. Measured and calculated SPLs at BT:D1 92

Figure 2.76. Measured and calculated SPLs at BT:K 92

Figure 2.77. Coherence plots of driving points 93

Figure 2.78. Exhaust hanger mount 93

Figure 2.79. The contributions of all paths (1000-5500 rpm), BT:D . . . 94

Figure 2.80. The contributions of all paths (1000-5500 rpm), BT:D1 . . 95

Figure 2.81. The contributions of all paths (1000-5500 rpm), BT:K . . . 95

Figure 2.82. The contributions of all paths (1500-4500 rpm), BT:D . . . 96

Figure 2.83. The contributions of all paths (1500-4500 rpm), BT:D1 . . 96

Figure 2.84. The contributions of all paths (1500-4500 rpm), BT:K . . . 97

Figure 2.85. Contributions of all paths (3000-4500 rpm), BT:D 97

Figure 2.86. Contributions of all paths (3000-4500 rpm), BT:D1 98

Figure 2.87. Contributions of all paths (3000-4500 rpm), BT:K 98

Figure 2.88. Contributions of all paths (1500-2250 rpm), BT:K 99

Figure 2.89. Measured and calculated SPLs at BT:D 99

Figure 2.90. Measured and calculated SPLs at BT:D1 100

Figure 2.91. Measured and calculated SPLs at BT:K 100

Figure 2.92. Contributions of all paths (3000-4500 rpm), BT:D 101

Figure 2.93. Contributions of all paths (3000-4500 rpm), BT:D1 101

Figure 2.94. Contributions of all paths (3000-4500 rpm), BT:K 102

Figure 2.95. Contributions of all paths (1500-2250 rpm), BT:K 102

Figure 2.96. Road test results for the vehicles #170 and #250, BT:D . . 103

Figure 2.97. Road test results for the vehicle #170 and #250, RH:03:Y 103

Figure 2.98. Overall and harmonics of second order, BT:D, L38 #170 . 104

Figure 2.99. Measured and calculated 4^{th} order SPLs at BT:D 105

Figure 2.100. Measured and calculated 4^{th} order SPLs at BT:D1 105

Figure 2.101. Measured and calculated 4^{th} order SPLs at BT:K 106

Figure 2.102. Measured TPA result, 4^{th} order SPLs at BT:D 106

Figure 2.103. Contributions of all paths, BT:D, 4^{th} order, Vehicle# 170 . 107

Figure 2.104. Contributions of all paths, BT:D1, 4^{th} order, Vehicle# 170 107

Figure 2.105. Contributions of all paths, BT:K, 4^{th} order, Vehicle# 170 . 108

Figure 2.106. Comparison of sound pressure levels measured at BT: D . . 109

Figure 2.107. Contributions of the predominant path RH:03:Y 109

Figure 2.108. Comparison of sound pressure levels measured at BT: K . . 110

Figure 2.109. Contributions of dominant paths predicted at BT: K 110

Figure 2.110. Wireframe used for sensor locations 112

Figure 2.111. BIW test configuration 113

Figure 2.112. Full vehicle test configuration 114

Figure 2.113. Acceleration of body panels: all of the panels 115

Figure 2.114. Acceleration of body panels: back floor 116

Figure 2.115. Acceleration of body panels: front floor 116

Figure 2.116. Acceleration of body panels: parcel shelf 117

Figure 2.117. Acceleration of body panels: back screen 117

Figure 2.118. Acceleration of body panels: front left door 118

Figure 2.119. Acceleration of body panels: front right door 118

Figure 2.120. Acceleration of body panels: rear left door 119

Figure 2.121. Acceleration of body panels: rear right door 119

Figure 2.122. Acceleration of body panels: roof 120

Figure 2.123. Acceleration of body panels: windscreen 120

Figure 2.124. Acceleration of body panels: all of the panels 121

Figure 2.125. Shaker driven test, acceleration of body panels: back floor . 121

Figure 2.126. Shaker driven test, acceleration of body panels: front floor 122

Figure 2.127. Shaker driven test, acceleration of body panels: parcel shelf 122

Figure 2.128. Shaker driven test, acceleration of body panels: back screen 123

Figure 2.129. Shaker driven test, acceleration of body panels: FLD . . . 123

Figure 2.130. Shaker driven test, acceleration of body panels: FRD . . . 124

Figure 2.131. Shaker driven test, acceleration of body panels: RLD . . . 124

Figure 2.132. Shaker driven test, acceleration of body panels: RRD . . . 125

Figure 2.133. Shaker driven test, acceleration of body panels: roof 125

Figure 2.134. Shaker driven test, acceleration of body panels: windscreen 126

Figure 2.135. Coherence, back floor 126

Figure 2.136. Coherence, front floor 126

Figure 2.137. Coherence, parcel shelf 127

Figure 2.138. Coherence, back screen 127

Figure 2.139. Coherence, front left door 127

Figure 2.140. Coherence, front right door 127

Figure 2.141. Coherence, rear left door 128

Figure 2.142. Coherence, rear right door 128

Figure 2.143. Coherence, roof 128

Figure 2.144. Coherence, windscreen 128

Figure 2.145. BIW test, acceleration of body panels: back floor 129

Figure 2.146. BIW test, acceleration of body panels: front floor 129

Figure 2.147. BIW test, acceleration of body panels: parcel shelf 130

Figure 2.148. BIW test, acceleration of body panels: back screen 130

Figure 2.149. BIW test, acceleration of body panels: roof 131

Figure 2.150. BIW test, acceleration of body panels: windscreen 131

Figure 2.151. BIW test, acceleration of body panels: firewall 132

Figure 2.152. Coherence, back floor 132

Figure 2.153. Coherence, front floor 132

Figure 2.154. Coherence, parcel shelf 133

Figure 2.155. Coherence, back screen 133

Figure 2.156. Coherence, roof 133

Figure 2.157. Coherence, windscreen 133

Figure 2.158. Coherence, firewall 134

Figure 2.159. Plots of elements of viscous damping matrix 138

Figure 2.160. Viscous damping matrix 138

Figure 2.161. SPL curves predicted using diagonal NFRF matrix method 141

Figure 2.162. SPL curves predicted using the described procedure 141

Figure 3.1. L84 BIW CAD in Catia V5 146

Figure 3.2. L38 BIW CAD received, 2201 components 147

Figure 3.3. L38 BIW CAD reduced, 249 components 147

Figure 3.4. Right mudguard geometry, edge view 148

Figure 3.5. L38 BIW, confirmed weight 150

Figure 3.6. FE model of L84 BIW 152

Figure 3.7. FE model of L38 BIW 152

Figure 3.8. Connector locations for assembling of L38 BIW 153

Figure 3.9. Domains Ω, Ω_c and boundary Γ 153

Figure 3.10. Box cavity 158

Figure 3.11. Vehicle L84 cavity and the box depicted 160

Figure 3.12. 1st eigenfrequencies of the box and Vehicle L84 cavity . . . 160

Figure 3.13. 2nd eigenfrequencies of the box and Vehicle L84 cavity . . 161

Figure 3.14. 3rd eigenfrequencies of the box and Vehicle L84 cavity . . . 161

Figure 3.15. 4th eigenfrequencies of the box and Vehicle L84 cavity . . . 161

Figure 3.16. 5th eigenfrequencies of the box and Vehicle L84 cavity . . . 162

Figure 3.17. A simplified model of trunk and passenger cavities 166

Figure 3.18. First three values of k_x 171

Figure 3.19. First three longitudinal acoustic mode shapes of the box . . 173

Figure 3.20. First planar mode shapes of the box 173

Figure 3.21. Two cavities in Vehicle L38 are connected by an aperture . 174

Figure 3.22. First longitudinal acoustic mode shape of the sedan 174

Figure 3.23. Second longitudinal acoustic mode shape of the sedan . . . 175

Figure 3.24. First planar acoustic mode shape of the sedan 175

Figure 3.25. FEM of assembled Vehicle L38, # of DOF 3,620,607 . . . 179

Figure 4.1. The physical mesh 183

Figure 4.2. Nodes tagged on the computational model 184

Figure 4.3. The wireframe constructed using 380 output locations . . . 184

Figure 4.4. Excitation flowchart and Parameter sets I and II 185

Figure 4.5. Input signals 187

Figure 4.6. Ordinary coherence plots of FRFs, hammer test 188

Figure 4.7. Ordinary coherence plots of FRFs, SIMO 188

Figure 4.8. Multiple coherence plots of FRFs, MIMO 189

Figure 4.9. FRFs estimated through the reference accelerometer 189

Figure 4.10. Stabilization plot 195

Figure 4.11. Complex mode indicator function 195

Figure 4.12. Bode diagram of identified damped natural frequencies . . 196

Figure 4.13. Euler axes are attached on every node of the wireframe . . 199

Figure 4.14. MAC plot of test and computational eigenvectors 200

Figure 4.15. Identified operational force vectors, Vehicle L38. 201

Figure 4.16. Measured vs predicted SPLs at BT:D, Cases 1, 2 and 3. . . 202

Figure 4.17. Measured vs predicted SPLs at BT:K, Cases 1, 2 and 3. . . 202

Figure 4.18. Coupled vibro-acoustic response of the system at 62 Hz . . 205

Figure 4.19. Coupled vibro-acoustic response of the system at 83 Hz . . 206

Figure 4.20. Coupled vibro-acoustic response of the system at 155 Hz . 207

Figure 4.21. Coupled vibro-acoustic response of the system at 127 Hz . 208

Figure 4.22. Coupled vibro-acoustic response of the system at 175 Hz . 209

Figure 4.23. An additional 2.5 kg mass is added on the node 211

Figure 4.24. Additional 3 and 5 kg masses are added on the nodes . . . 212

Figure 4.25. Original and modified SPL predictions at BT:D 212

Figure 4.26. Original and modified SPL predictions at BT:K 213

Figure B.1. An arbitrary plate and boundary conditions 242

Figure B.2. Forces and moments acting on the deformed plate element 243

LIST OF TABLES

Table 2.1. Frequency response functions 21

Table 2.2. Excitation functions 26

Table 2.3. Accelerometer locations 35

Table 2.4. Summary of TPA methods 74

Table 2.5. Measurement locations in engine driven full vehicle test . . . 115

Table 2.6. Measurement locations in shaker driven BIW test 127

Table 2.7. Summary of first three contributor paths 142

Table 2.8. Resonance frequencies of the body panels 143

Table 2.9. Assessment of TPA results 144

Table 3.1. Material properties used in computational analysis 150

Table 3.2. Element types and quantities 151

Table 3.3. Criterions used in mesh refinement 151

Table 3.4. Comparison of the first five eigenfrequencies 162

Table 3.5. Dimensions of the simplified model given in Figure 3.17. . . 165

Table 3.6. Comparison of first three eigenfrequencies 170

Table 3.7. Uncoupled acoustic eigenfrequencies of the actual cavity . . 172

Table 3.8. Uncoupled acoustic eigenfrequencies of the sedan 176

Table 4.1. Parameters determined for experimental modal analysis . . . 187

Table 4.2. Experimental modal analysis results 194

Table 4.3. L_2 norm of differences between SPLs 202

Table 4.4. Refinement achieved on the booms diagnosed. 211

LIST OF ACRONYMS/ABBREVIATIONS

AMLS	Automated multi-level substructuring
ARMA	Auto regression and moving average
BC	Boundary condition
BEM	Boundary element model
BF	Blocked force
BIW	Body in white
BR	Balanced realization
BT:D	Driver's left ear
BT:D1	Driver's right ear
BT:K	Rear seat middle
CMIF	Complex mode indicator function
CPU	Central processing unit
CVA	Canonical variate analysis
DFT	Discrete fourier transform
DMI	Diagonal matrix inversion
DOF	Degree of freedom
DOFs	Degrees of freedom
DPRs	Driving point residues
DSP	Digital signal processing
EBEM	Energy boundary element method
EC	Body (passive) side of the exhaust mount
ECD	Eddy current dampers
EFA	Energy flow analysis
EFEM	Energy finite element method
EM	Engine mount
EMA	Experimental modal analysis
EOM	Equation of motion
ERA	Eigensystem realization algorithm
ExM	Exhaust mount

FE	Finite element
FE	Exhaust (active) side of the exhaust mount
FEA	Finite element analysis
FEM	Finite element method
FFT	Fast fourier transform
FIM	Fisher information matrix
FRAC	Frequency response assurance criterion
FRF	Frequency response function
GUI	Graphical user interface
HCM	Hybrid computational method
IRF	Impulse response function
KEOT	Kinetic energy optimization technique
L84	Renault Mégane™
L38	Renault Fluence™
LHS	Left hand side
LSCE	Least squares complex exponential
LTI	Linear time invariant
MDOF	Multi degree of freedom
MI	Matrix inversion
MIMO	Multi-input multi-output
MPFs	Modal participation factors
NExT	Natural excitation technique
NFRF	Normal frequency response function
NVH	Noise, vibration and harshness
ODS	Operational deflection shape
OEM	Original equipment manufacturer
OMA	Operational modal analysis
PCA	Principal component analysis
RH	Body (passive) side of the engine mount
RHS	Right hand side
RMA	Running modes analysis

SDOF	Single degree of freedom
SEA	Statistical energy analysis
SM	Engine (active) side of the engine mount
SPL	Sound pressure level
SVD	Singular value decomposition
SWL	Sound power level
TAM	Test-analysis model
TMD	Tuned mass damper
TPA	Transfer path analysis
WBS	Wave based substructuring
WOT	Wide open throttle

1. INTRODUCTION

In the context of vehicle acoustics, noise and vibration studies are commonly classified in different frequency regimes, such as low-(20-200 Hz), mid-(200-600 Hz) and high-frequency (600 Hz and beyond) bands and handled using different methods like experimental, computational and hybrid considerations. This dissertation investigates noise and vibration characteristics of passenger vehicles in the low frequency regime, using experimental and computational methods.

The introduction part gives the motivation and a literature survey in an historical perspective. Objectives of the dissertation and employed methods, which are currently used in prediction and reduction of interior noise of production vehicles, are also stated. The aim is to give an overview on the use of solution methods and their applications in automotive vibro-acoustics problem rather than to describe approaches and solution techniques itself in detail. Nevertheless, in next chapters, methods used in this dissertation are described in a more detailed and systematic manner to give a clear understanding on the studies performed. Major contributions of this study are rendered in Section 1.5. Finally, the introduction part includes a brief outline of the dissertation.

1.1. Motivation

The European Automotive Research Partners Association (EARPA) carried out a project called "FURORE - Future Road Vehicle Research Thematic Network" looking at research needs for vehicles in the year 2020 and beyond [1]. In this report the following research targets have been identified:

(i) Fuels and energy supply
(ii) Emissions and greenhouse gases
(iii) Safety
(iv) Traffic and congestion
(v) Noise (Interior and Exterior)
(vi) Recycling

Interior and exterior noise is one of the important research topics through 2020 and beyond. Although, the sources and potential solutions are very similar for interior and exterior noise in road vehicles, the main driving forces are different. Exterior noise problems, such as pass-by-noise and traffic noise are regulated due to legislation. On the other hand, interior noise quality and comfort strongly come into question mainly due to customer expectation, competition among original equipment manufacturers (OEM) and brand image. Interior noise and vibration problems and solution techniques are addressed in this thesis.

For a large section of automotive customers, interior noise quality may be not an important decision parameter as much as styling, power, fuel consumption and budget, while choosing an automobile to buy. But in long term, noise, vibration and harshness (NVH) quality significantly influences the customer satisfaction, which in turn shapes the brand image of vehicle manufacturer. Moreover, it is a well known fact that, noise problems take up an important part of warranty and customer satisfaction departments of OEMs.

In the development of a new vehicle, major design criterions are defined due to fuel economy, vehicle safety, crashworthiness, durability, ride comfort, handling behaviors and NVH concepts. The competitive nature of vehicle industry forces OEMs to make critical decisions among design parameters, which seem to be in conflict with each other. The trend to build lighter and more fuel efficient vehicles generally results in poor noise and vibration quality. Reducing the thickness of structure could increase the amplitudes of vibrations, which in turn cause higher noise levels. To deal with this problem, there is a need for advanced materials with low weight and high damping properties. Another solution is to employ multi-disciplinary optimization methods to change the vibration response of vehicle panels.

Since nearly all systems and components affect vehicle interior noise levels, from the very beginning of the virtual prototyping stage, a systematic approach is needed to deal with noise and vibration problems. For instance, novel vehicle power systems such as electric and hydrogen could cause new challenges on the level of subjective

perception, transient states, secondary noises, etc. More fuel efficient engines can cause different combustion induced noise problems.

Since 1975, the booming noise measured at the driver's ear at wide open throttle (WOT) tests, has been decreased averagely 3 dB/decade in the 3000-4000 rpm range [1]. This improvement is achieved through advances made in experimental methods, prototype based design modification predictions, diagnosis analysis and computational tools. On the contrary, the NVH design development itself is under pressure to be more efficient and to date there is no unique methodology that proposes a solution for a wide frequency range, and/or guarantees the desirable NVH characteristics before, or after vehicle launch.

The structure-borne aspect of the problem spans both the low- and mid-frequency regimes. The assembly procedures also must be carefully taken into account due to the fact that present manufacturing procedures introduce variability into the vehicle structure. The virtual prototype modeling process should be parameterized to count for the design uncertainties and variability. There is a need for research on advanced vibro-acoustic simulation methods to assess the NVH performance of vehicles at the earliest possible design step to render possible optimization and modification studies.

1.2. Literature Survey

The research in vehicle interior noise development has a nearly 45 year history. In the 60's and early 70's the preferred method is the binaural sound recording technique [2]. As seen in Figure 1.1., to acquire data, the test vehicle has to be accompanied by a chase vehicle equipped with a heavy two channel audio recorder and 110 Volts AC power unit.

In the 70's unibody vehicles showed up in the market are 15-20 dB much louder in the sense of low frequency noise than the ones built with separate chassis. The advantage of separate chassis vehicles is the high vibration transmission loss from the chassis into the body. Moreover, non-homogeneous materials used in body manufac-

turing provide high damping ratios. This situation gives a rise to the interior noise investigations in early 70's. In 1972, Jha [3] pointed out that, the basic mechanism of vehicle interior noise is due to *vibrating cabin walls*. The first numerical analysis on the investigation of structural-acoustic characteristics of an automobile was reported in 1975 [4]. Nastran ^{TM} (NASA Structural Analysis) is the software to perform the finite element analysis. Due to the structural-acoustic interaction, panels are reactive to the cavity pressure and the structural motion couples with the acoustic field through the pressure loadings on the panel.

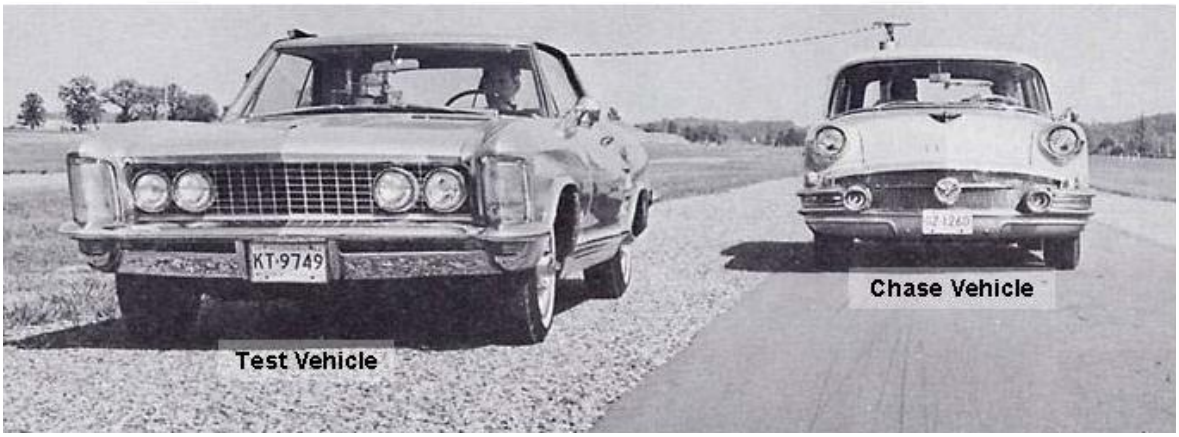


Figure 1.1. Sound pressure level measurements in the mid 60's[1]

Vehicle interior noise is made up of both random background noise, which originates mainly from road inputs and discrete engine frequency components superimposed on the background noise. In the sense of the human perception, [5] the background noise is the determining parameter for the *loudness* of the internal noise, while the discrete frequency components is the main cause for the *annoying* sense. The trimmed body is the most complex vibratory system of a vehicle due to its huge number of degree of freedom and it is the main part of the noise assessment analysis, since it is the structure, which finally radiates the sound energy perceived by occupants. Preide et al. [6] brings into the open that the highest level of the dynamic response of a trimmed body lies over the 70-200 Hz band for a typical passenger car. Although the excitation level of different harmonics varies with engine speed, most important resonances within the mentioned band are typically excited by only first few harmonics of the engine. In 1977, Dowell et al. reported a comprehensive theoretical and experimental study

[1] "Reprinted with permission from SAE Paper No. 2003-01-1518 ©2003 SAE International"

on the low frequency structural-acoustic interactions [7]. The calculation of acoustic modes of a complicated geometry is the point of interest. On this subject, many authors report experimental studies for regular and irregular geometries [8, 9]. In one of them, an experimental and theoretical study of acoustic modes of a rectangular cavity containing a rigid, incomplete wall is presented. Theoretical results are obtained by using finite element techniques. In another experiment, acoustic pressure distribution inside a pressurized tank is simulated in laboratory conditions using small loudspeakers [9]. Nieter and Singh make significant contributions on determining the acoustic characteristics of 3-D cavities [10]. They propose an experimental modal technique for acoustic ducts, mufflers and resonators. To show correlation between the theory and experiment, they apply the technique on closed-closed and closed-open tubes and symmetrical and unsymmetrical lumped systems. In another paper, identification of modal parameters including damping of a 3-D cavity is proposed [11]. Experiments are based on the excitation of cavity using a convertible acoustic driver, whose volume velocity is monitored.

In 1982, Nefske et al. published an article on the structural-acoustic finite element analysis of the passenger vehicles [12]. In this article, the structural-acoustic coupling relationship is formulated as follows:

$$\begin{bmatrix} M_s & 0 \\ \rho_0 c_o^2 H_{sf}^T & M_f \end{bmatrix} \begin{Bmatrix} \ddot{u}_s \\ \ddot{p}_f \end{Bmatrix} + \begin{bmatrix} C_s & 0 \\ 0 & C_f \end{bmatrix} \begin{Bmatrix} \dot{u}_s \\ \dot{p}_f \end{Bmatrix} + \begin{bmatrix} K_s & -H_{sf} \\ 0 & K_f \end{bmatrix} \begin{Bmatrix} u_s \\ p_f \end{Bmatrix} = \begin{Bmatrix} F_s \\ F_f \end{Bmatrix} \quad (1.1)$$

where

u nodal displacement vector of the structure at the boundary,

p sound pressure vector of the interior sound field,

M, C, K mass, damping and stiffness matrices,

F structural or acoustical load vector,

H spatial coupling matrix,

s structure,

f fluid.

Acoustic modes of a sedan are calculated using rigid and flexible boundary conditions by means of finite element analysis in 2-D [12]. To illustrate the calculation capability in 3-D, a simplified finite element model of a truck cab is used. Uncoupled and coupled frequency response calculations are also presented in this study. It is pointed out that the prediction of structure-borne noise in passenger vehicles requires the knowledge of exciting forces, acoustic modal characteristics of the cavity and the structural modal characteristics of the vehicle. Remarks of Ref. [12] are as follows:

(i) At the design stage, finite element analysis (FEA) can be used to compute cavity resonances.
(ii) Structural vibration data determined from tests and/or FE model can be used in the diagnosis of critical panels.
(iii) For the prototype, or production vehicles, FEA can be used to investigate whether a cavity resonance is excited, or not.
(iv) FEA can be also used in the same manner to inquire effects of proposed modifications on the structure.

Actually, the objective is to predict the vehicle interior noise at the conceptual design stage and to solve noise and vibration problems before the prototype development. Nevertheless, this aim cannot be achieved to date. As mentioned in the introduction part, finite element method (FEM) is an effective prediction tool for structural characteristics only at the low frequency region. Moreover, results tend to deviate from experimental ones above 125 Hz, well below the low frequency limit.

By the way, a very important problem that affects vehicle interior noise development studies was noticed and reported in 1984: the variability. Wood and Joachim [13] examine the variability in the interior noise levels of 12 nominally identical passenger vehicles. They observe that variability significantly changes the measured SPL at predefined critical measurement points, above 50 Hz. As the frequency value is increased from 50 to 200 Hz, variations up to 10 dB are observed. It is shown that mainly spot welds and bolts cause variations in damping values, which in turn change dynamic characteristics of the vehicle structure. Variations in damping do not only change reso-

nant amplitudes, but also alter the phase. Later on, a study on the variability concept, which verifies the former and extends the measurement frequencies, is reported [14].

In mid 80's, statistical energy analysis (SEA) method is implemented in vehicle interior noise development targeting high frequencies [15]. Some authors report their attempts on the use of SEA at low frequencies [16], but till mid 90's the use of SEA is very limited in automotive applications.

The application of boundary element method (BEM) for complex geometries is considered by Suzuki et al. [17]. A new formulation for complicated boundary conditions is proposed and applied to a vehicle cavity. Same authors explain the use of BEM in vehicle interior acoustics and report an application study [18]. To compute the sound power of machines, Koopman and Benner [19] use Helmholtz integral equation method with planar elements. Multi-domain BEM formulations were introduced to calculate acoustic fields [20] and applied to vehicle cavity by Soenarko, in 1991 [21]. A new BEM formulation that computes the effect of seats is presented and used in the cavity noise analysis by Banerjee et al. [22].

To improve computational efficiency for FEM solutions, a symmetrical formulation for coupled structure-acoustic problem is proposed [23]. The derivation of this formulation is based on the Galerkin method and on the weak solution of conservation of mass and linear momentum.

Experimental modal analysis and spectral methods are unique options before deterministic elementary based approaches are introduced. As the studies that improve the accuracy and reduce the computational cost in numerical methods are proceed, in the early 90's development studies at modal methods used in vibro-acoustics come into question again. The theory is well outlined [24, 25], but applications in complex structures such as an automobile should have been studied in a more comprehensive manner. In 1992, Verheij put into print a study on the quantification of sound paths for interior noise of road vehicles [26]. In this paper, he proposes methodologies to quantify the structure borne sound that occurs through transmitted vibration flow

through engine mounts and airborne sound of engine that reaches to the cavity. He states that the calculation of SPL in the cavity can be illustrated for a single DOF as

$$\text{mount} \begin{cases} F_s = Z_{ss}V_s + Z_{sr}V_r \\ F_r = Z_{rs}V_s + Z_{rr}V_r \end{cases} \qquad \text{reciever} \begin{cases} -V_r = Y_r F_r \\ P_i = H_{r,i}F_r \end{cases} \tag{1.2}$$

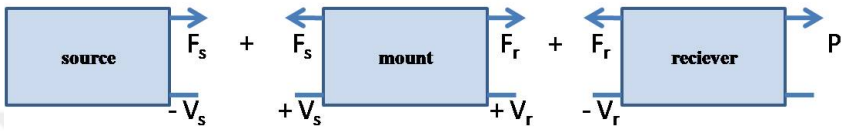


Figure 1.2. Vibration flow through engine mounts

$$p_i = H_{r,i}F_r = H_{r,i}\frac{Z_{rs}V_s}{1 + Z_{rr}V_r} = H_{r,i}Z_{rs}V_s \qquad \text{if} \quad Z_{rr} << Y_r^{-1} \tag{1.3}$$

where

F and V are the force and velocity vectors,
H is the transfer function and $Z(= Y^{-1})$ is the impedance.

This approach requires that the receiver point impedance should be significantly larger than the mount impedance, which means that $V_r << V_s$. In general, the superposition principle is used, i.e. the sound pressure level at any point inside the vehicle cavity can be expressed by the summation of p_i results of Equation (1.3) [26].

Sources of structure borne sound governed by mount properties and vehicle structure dynamics are engine and road inputs. Different wheel inputs transmitted to the body through suspension system are non-coherent and can be assessed using partial coherence and principal component analysis (PCA) techniques. On the other hand, all driveline to body connections transmit coherent powertrain forces. Vis et al. [27] state that contribution to the total interior noise of all individual connections can be identified by Transfer Path Analysis (TPA), which is based on the linear superposition of p_i's.

In vibro-acoustics analysis, force identification is a troublesome task. Direct methods require precise complex dynamic stiffness matrix data, which are difficult to populate in application due to nonlinear characteristics of mounts. While measuring complex dynamic stiffness of mounts, it is crucial to pre-load them as close as possible to actual operational conditions. The temperature of the environment also should be taken into account. On the other hand, the indirect method requires the inversion of an ill-conditioned frequency response function (FRF) matrix that has to be obtained after the vibration source is removed. In many applications, it has been observed that, indirect force estimation method does not always give reliable results. Problems associated with this method are discussed by Mas et al. in detail [28]. Importance of the condition number of an FRF matrix in the error propagation is shown through simulations and it is concluded that over determination can improve the condition number. Another significant contribution that develops the experimental procedure is reciprocity methods in modal analysis. It is shown [29] that the non-symmetrical nature of the coupled vibro-acoustic formulation is not contradictory to the vibro-acoustic reciprocity principle. The theory is proven by experiments using structural and acoustic exciters. For road noise analysis, multiple-reference TPA that relates modal analysis results and vibrational flow energy on suspensions is proposed by Wyckaert et al [30]. The source-path-receiver model, modal analysis experiments and FRF based substructuring techniques are assessed in Ref [31]. Indirect dynamic force estimation technique and transfer path analysis are well documented in Refs. [32, 33].

In Ref. [34], derivations of energy finite element method (EFEM) and energy boundary element method (EBEM) are given for the coupled structural-acoustic problem. Subsystems are modeled as point driven flat plates that radiate sound into the cavity. The formulation is derived such that two subsystems are modeled separately and the coupling has been included through the structural acoustic joint matrix. Wang and Bernhard develop a generalized joint process to handle the joints between subsystems in a hybrid EFEM-SEA solution of a heavy equipment cab [35]. Gür et al. [36] state that EFEM is appropriate for analyzing vibrations in automotive structures in the frequency range of 80-250 Hz, only for plates that have a characteristic length greater than 90 cm. EFEM requires that the plate length should be greater than 2.4

times the bending wavelength of the lowest frequency of interest [37]. An EFEM based interior noise prediction model that considers direct acoustic coupling besides the indirect coupling is also developed. The coupling relationship is based on the conservation of energy flow and the energy superposition principle. EBEM is used to model the acoustic cavity and to relate the pressure variables to structural response modeled by EFEM [38].

In the wave based substructuring (WBS) method, which is based on the indirect Trefftz approach, field variables in the domain are expressed in terms of wave functions. Instead of approximate shape functions of FEM, wave functions are used in this approach and each wave function stands for a degree of freedom (DOF) of the wave model. A detailed discussion of the theory is given in [39]. In [40], the application of the WBS for 3D uncoupled, acoustic problems is discussed and results compared with FEM results. WBS results are relatively more useful, especially in the mid-frequency range. Since the method needs convex domains to guarantee the convergence, the complexity of the geometry is a measure of the applicability of the method.

In 2000, the automated multi level substructuring (AMLS) method, that significantly reduces the computational time, was introduced by Bennighof for frequency response analysis of large FE models [41]. Due to the algorithm, a large FE (DOF number $\geqslant$ one million) model is automatically divided into many substructures, and the model is transformed such that response is represented in terms of substructure eigenvectors. In [42], for a typical vehicle NVH problem, direct, modal and AMLS methods are used to compare the accuracy and CPU time. It is reported that while Lanczos type algorithms are best for low frequency regimes, AMLS is the most efficient one for mid frequencies. AMLS can be used with Nastran® solvers, such as SOL 103 (normal modes), SOL 111 (modal frequency response) and SOL 200 (structural optimization).

To span low-mid and/or mid-high frequency bands, hybrid computational methods (HCM) are introduced. FE-SEA [43], FEM-EFEM [44], EFEM-EBEM [45], FEM-WBS [46] and FEM-BEM [47] are examples of this class and they are widely used in

automotive applications to overcome mid-frequency modeling troubles. These hybrid approaches are based on the use of above stated methods, in the frequency bands, where they are thought to be efficient.

1.3. Objective

Modal analysis [25] techniques are suitable at low frequencies due to relatively low values of structural and acoustical modal densities. Deterministic element based techniques, such as finite element and boundary element methods are also extensively used at low-frequency problems, but the computational cost is an obstacle to extend the usage of these methods to mid-frequency bands.

At high frequencies, the number of modes is significantly increased and modal overlapping obstructs to distinguish the modes. The system becomes highly sensitive to boundary conditions, material properties and geometry, which requires very precise descriptions at node locations. For the very reason, probabilistic techniques such as Statistical Energy Analysis (SEA) are developed. Statistical methods are suitable only for the high frequency band [48].

There is still a gap in the 100 - 300 Hz band, where the booming and low-medium frequency noise occurs. Remarkably, there is a transition zone in between 50 and 200 Hz, where the basic mechanism of sound radiation is changing [3]. In this regard, objectives of this dissertation are:

(i) to evaluate advantages and drawbacks of the current practice,
(ii) to apply the methods itemized in Section 1.4 on real passenger vehicles,
(iii) to get a verified modal model to study on, and
(iv) to construct a robust procedure in the low frequency band.

1.4. Methods Employed

Finite element method (FEM) is a numerical prediction tool for solving engineering problems by approximating exact solutions of the governing differential equations at only discrete points. FE model is a representation and has many assumptions. Throughout the text, we will use the linear assumption and in computational studies, it will be assumed that known parameters are valid for the entire domain of the structure. In computations of structural and acoustic modes, HyperMesh® is used for preprocessing and the solvers are Nastran®, Radioss® and Sysnoise®. VirtualLab® is used for post processing, coupled analysis and modification prediction studies.

Experimental modal analysis (EMA) is the process of determining dynamic characteristics, such as natural frequencies, mode shapes and damping ratios from the transfer functions of a linear system, by using experimental procedures. Experimental procedures involve the assessment of the model in laboratory conditions and data acquisition to identify operating loads. Acquired data render possible to investigate the influence of system characteristics on the response. This is done by evaluating FRFs, or by extracting the model parameters of the transfer system, which constitutes the basis of EMA. Alternatively, acquired data can be used to assess particular contributions, which is the starting point of the Transfer Path Analysis (TPA). Eventually, experimental modeling techniques such as black-box FRF, EMA and TPA have become standard practices in NVH engineering.

Transfer path analysis (TPA) describes the total interior noise as a vector sum of individual contributions from a defined set of force inputs entering the body over a known set of connections, i.e. engine, exhaust and suspension mounts [33]. The method requires two data sets: knowledge of the operating forces at the body side of the mount, and measurements of vibro-acoustic transfer functions between that point and the target receiver. Ranking of the transfer paths becomes possible using this method.

Running modes analysis (RMA) or operational deflection shape (ODS) is the output measurement process of a system, while it is in service. If one is interested in a particular phenomenon at a certain frequency, it will give an insight to see what the output levels are at this frequency for each measurement DOF.

1.5. Original Contributions

The foremost original contributions of this dissertation are as follows:

(i) Current practice of experimental transfer path analysis is discussed in the context of trade-offs between accuracy and time cost. An overview of methods, which propose solutions for structure borne noise is given, where assumptions, drawbacks and advantages of methods are stated theoretically. Applicability of methods is also investigated, where an engine induced structure borne noise of a vehicle is taken as a reference problem. It is observed that although many aspects of the problem are investigated in the literature, damping and its effects are not considered. Damping effect is embedded in the measured complex frequency response functions and it is needed to be analyzed in the post processing step. Effects of damping, reasons and methods to analyze them are discussed in detail. In this regard, a new procedure, which increases the accuracy of results, is also proposed.

(ii) Vehicle noise variability and dominant paths that cause low frequency booms are investigated. The inter variability observed among the sound pressure levels of five identically produced vehicles is studied by means of a commonly used experimental tool: structural transfer path analysis. To diagnose the cause of variability, a systematic approach is proposed, where all steps consist of experimental studies only. It is deduced that predominant paths, which are found to be main contributors of diagnosed booms, are also the root causes of inter variability observed.

(iii) In computational vehicle acoustics, sound pressure level predictions and measurements do not perfectly match. Reasons for the mismatch are generally thought to be nonlinearities in the vehicle structure, assumptions of the source-path-receiver approach and inadequate modeling of damping. Coupled vibro-acoustic response

of a sedan is analyzed, and the effect of folding rear seat aperture is studied. First, a simplified model of acoustic cavity that consists of two adjacent boxes connected by an aperture is modeled. An analytical solution is proposed to calculate acoustic eigenfrequencies of the simplified model. Then, uncoupled acoustic eigenfrequencies of the actual cavity, where trunk and cabin cavities are connected through an aperture are computed. It is shown that planar acoustic eigenfrequencies of the sedan can approximately be calculated using the analytical solution proposed. To further clarify the impact of folding rear seat aperture, coupled vibro-acoustic response of the sedan is analyzed through different case studies. It is observed that booms are highly correlated with the calculated uncoupled planar acoustic eigenfrequencies. It is concluded that proposed analytical solution can be effectively used in calculation of acoustic eigenfrequencies and identification of booms, rather performing a detailed computational work.

1.6. Outline

This dissertation is organized as follows. In Chapter 2, experimental procedures in vibro-acoustics, their derivations, the need for them and the use of them are explained. Experimental studies consist of (i) road tests, (ii) laboratory mock up tests, (iii) transfer path analysis, and (iv) panel contribution analysis. All laboratory experiments are performed in the Vibration and Acoustics Laboratory of Boğaziçi University, while road tests are followed out on appropriate tracks.

The computational framework is outlined in Chapter 3. Computational studies applied on the FE models of two different sedans are presented, where the construction of models is explained in detail. Acoustic eigenfrequencies are calculated using analytical approaches, such as room acoustics, coupling of adjacent cavities and a new procedure proposed. Structural and acoustic modes of models are computed. Different solvers are employed to verify computational results.

In Chapter 4, results of experiments and computations are used together to synthesize modal models. Experimental modal analysis and correlation studies are pre-

sented. It is shown that results of experimental studies are not only critical for verification, but they also complement the computational model. Simulations are performed in a coupled scheme to expose effects of solid-fluid interaction. Damping behavior of model is examined through structural and viscous damping approaches. Experimentally identified operational forces are also applied to simulate displacements occurred on the shell and sound pressure levels generated in the cabin. Next to the derivation of a robust modal model, modification prediction practices are also performed.

2. EXPERIMENTAL ANALYSIS

2.1. Sound and Human Perception

Sound is a periodic process and involves energy transport due to oscillations of particles of medium, rather than the transfer of matter [49]. In order to those particles may oscillate about their usual position of rest, the medium through which sound propagates must have both elasticity (so that a restoring force is imposed on a displaced particle) and inertia (so that a returning particle overshoots its usual position of rest and oscillates back and forth). This acoustic oscillatory disturbance is in fact fluctuations of three variables, namely; pressure, density and temperature. It is not easy to measure fluctuating density or temperature accurately. Thus, sound is detected by the fluctuating pressure using a microphone which converts data into an electric signal. Sound levels are usually described in terms of the sound power (W) output of noise sources or the sound pressure (Pa) amplitude at a given location. However, logarithmic scales (dB) are useful due to the wide range of sound powers and sound pressure amplitudes [50]. The sound pressure level (SPL) and sound power level (SWL) are expressed by

$$\text{SPL} = 20\log_{10}\left(\frac{p}{p_{ref}}\right)\text{dB} \quad \text{and} \quad \text{SWL} = 10\log_{10}\left(\frac{w}{w_{ref}}\right)\text{dBW} \tag{2.1}$$

where $p_{ref} = 20 \times 10^{-6}\text{Pa}$ and $w_{ref} = 10^{-12}\text{W}$.

In NVH engineering terms,
1dB change the level of noise as 21% reduction in sound power,
3dB change the level of noise as 50% reduction in sound power,
20dB change the level of noise as 99% reduction in sound power.

Actually human ear is a nonlinear transducer. Our ears do not perceive all sounds equally at various frequencies, or sound intensities. Equal loudness contours are shown

in Figure 2.1. [51]. The sound pressure levels for a particular sound as defined by the level at 1000 Hz will be the identical for any given frequency along that curve. For example a 20 dB sound at 1000 Hz would be perceived as the same sound pressure level of 50 dB at 100 Hz. This points out that our ears are more sensitive to low frequency sounds than mid to high frequencies.

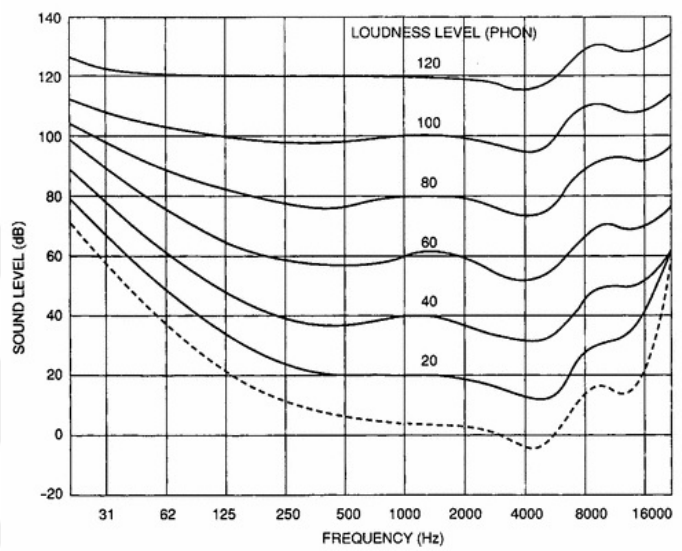


Figure 2.1. "Equal loudness contours. Every point on a single curve describes a sine tone with the same loudness. The dashes line corresponds to absolute threshold, the weakest sound the average human can hear."

Fletcher, following Helmholtz, suggested that the peripheral auditory system behaves as if it contains a bank of bandpass filters. When trying to detect a signal in a broadband noise background, the listener is assumed to make use of a filter with a center frequency close to that of the signal. This filter passes the signal and removes a great deal of the noise. Only components in the noise, which pass through the filter, have effect in masking the signal. These are the components, which have sound frequencies close to, or the same as, those of the signal. Note that, this property of the peripheral auditory system is definitely important to the acoustic environment of a car as the dominant noise in the audible range lies within the 50-250 Hz band.

Most of the sound meters are equipped with an A-weighting setting in addition to linear (un-weighted) setting. The A-weighting is a standard filter for noise measurements in automotive industry. This frequency weight reduces the sensitivity of the

measuring instrument to both low and very high frequency sounds. It approximately follows the inverted shape of the equal loudness contour passing through 40 dB at 1000 Hz. The shape of B-weighting is same with the inverted shape of the contour passing through 70 dB at 1000 Hz. There is also C-weighting which is defined with the same approach [49].

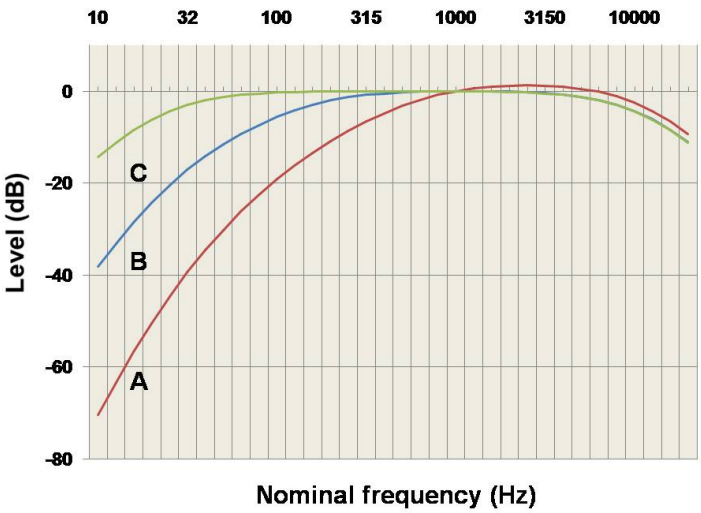


Figure 2.2. Frequency weights due to ANSI S1.4 standard

Although useful in a large range of applications, the estimation of *loudness* based on the frequency weighting of SPL levels has some limitations. These weights based on curves that are obtained in experiments, using pure tones. These results cannot be used to estimate the loudness of a broadband noise, or of sound consisting of both tonal and broad-band noise components. Moreover, they do not take into account the effects of spectral masking. 1/3 octave is a constant percentage bandwidth type filter used in automotive industry. In this type, the noise bandwidth B_n is a constant percentage of f_c throughout the frequency range. B_n is defined as the bandwidth of the ideal filter that would pass the same signal power as the real filter, when each is driven by stationary random noise. B_n is given as

$$B_n = f_1 - f_2 = \int_0^\infty |H(f)|^2 \, df \tag{2.2}$$

In the ideal filter, the modulus of the amplitude transfer function $H(f)$ is zero outside the pass band (given by $f_1 - f_2$) and unity within the pass band. The center, lower and upper frequencies of the 1/3 octave filter can be calculated using band numbers (n) as

$$f_c = 10^{(n/10)} \quad f_2 = 10^{((n-0.5)/10)} \quad f_1 = 10^{((n+0.5)/10)} \tag{2.3}$$

For the audio range, the 1/3 octave filter is given by all integer values of n between 12 and 43.

2.2. Acquisition and Processing of Data

Structural dynamics modeling can be described as relating force inputs to displacement-velocity-acceleration outputs. Modal analysis is the study of structural dynamics modeling, using modal parameters, such as natural frequencies, damping and mode shape vectors. Natural frequencies can be calculated using analytical or computational methods at the design stage, or can also be measured after a prototype has been built. Actually, each natural frequency of a system has a corresponding damping ratio that must be obtained by measurements. Frequency response function (FRF) is the structural response of a system to an input. To perform an experimental modal analysis for any structure, the following four basic assumptions have to be validated; the structure

(i) is assumed to be linear,
(ii) is time invariant,
(iii) obeys Maxwell's reciprocity, and
(iv) is observable.

These basic assumptions are approximately true up to some extent in experimental studies, but each assumption can be evaluated by measurements [52]. Therefore, it is possible to quantify the validation of the assumptions. Considering MDOF systems, equations for the impulse response function, the frequency response function and the

transfer function are defined as follows:

$$[h(t)] = \sum_{r=1}^{N} [A_r]\, e^{\lambda_r t} + [A_r^*]\, e^{\lambda_r^* t} \qquad \text{(Impulse Response Function)} \tag{2.4}$$

$$[H(\omega)] = \sum_{r=1}^{N} \frac{[A_r]}{j\omega - \lambda_r} + \frac{[A_r^*]}{j\omega - \lambda_r^*} \qquad \text{(Frequency Response Function)} \tag{2.5}$$

and

$$[H(s)] = \sum_{r=1}^{N} \frac{[A_r]}{s - \lambda_r} + \frac{[A_r^*]}{s - \lambda_r^*} \qquad \text{(Transfer Function)} \tag{2.6}$$

where

N number of modal frequencies,
A coefficient,
r modal vector number,
λ system pole.

Here, the coefficient A and λ is considered as complex conjugates due to under-damped ($\zeta < 1$) system assumption. This is suitable, since for most real structures the damping ratio is rarely greater than ten percent.

The transfer function is equal to the frequency response function only along the imaginary axis. From an experimental point of view, the transfer function is not estimated from measured input-output data. Instead, the FRF is estimated by the discrete Fourier transform (DFT). Coherence function is used to evaluate the FRFs. It is given as

$$\gamma_{xy}^2(f) = \frac{|S_{xy}(f)|^2}{S_{xx}(f) S_{yy}(f)} \qquad 0 \le \gamma_{xy}^2(f) \le 1 \tag{2.7}$$

where

S_{xx}, S_{yy} Power Spectral Density or Auto-powers
S_{xy} Cross Spectral Density or Cross-powers,

and if $\gamma_{xy}^2(f)$ is less than unity, one or more of the following conditions exist:

(i) extraneous noise is present in the measurements
(ii) resolution bias errors are present in the spectral estimates
(iii) the system relating $y(t)$ to $x(t)$ is not linear
(iv) the output $y(t)$ is due to other inputs besides $x(t)$

Derivation of coherence function and definitions of related terms are given in Appendix A. Different frequency response functions formulations are tabulated in Table 2.1.. Estimation procedures of frequency response functions are related to the transformation of measured data from time to frequency domain. Integral Fourier transform requires time histogram from $-\infty$ to $+\infty$ by definition. Since this is experimentally impossible, the computation of transformation is performed digitally, using fast Fourier algorithms, which is based upon a limited time history. In Ref [53], errors caused by limited time record are discussed.

Table 2.1. Frequency response functions

receptance	dynamic stiffness	impedance	mobility	accelerance	apparent mass
disp./force	force/disp.	force/vel.	vel./force	acc./force	force/acc.

There are three algorithms that commonly available for the estimations of frequency response functions, namely, H_1, H_2 and H_v [54]. The H_1 algorithm

(i) assumes that there is no noise on the input and all the X measurements are accurate,
(ii) minimizes the noise on the output in a least squares sense,

(iii) tends to give an underestimate of the FRF if there is noise on the input, and
(iv) estimates the anti-resonances better than the resonances.

$$H_1(\omega) = \frac{\frac{1}{N}\sum_{i=1}^{N} Y_i(\omega)X_i^*(\omega)}{\frac{1}{N}\sum_{i=1}^{N} X_i(\omega)X_i^*(\omega)} = \frac{G_{YX}(\omega)}{G_{XX}(\omega)} \tag{2.8}$$

The H_2 algorithm

(i) assumes that there is no noise on the output and all the Y measurements are accurate,
(ii) minimizes the noise on the input in a least squares sense,
(iii) tends to give an overestimate of the FRF if there is noise on the output, and
(iv) estimates the resonances better than the anti-resonances.

$$H_2(\omega) = \frac{\frac{1}{N}\sum_{i=1}^{N} Y_i(\omega)Y_i^*(\omega)}{\frac{1}{N}\sum_{i=1}^{N} Y_i(\omega)X_i^*(\omega)} = \frac{G_{YY}(\omega)}{G_{YX}(\omega)} \tag{2.9}$$

The H_v algorithm

(i) minimizes the global noise contribution in a *total* least squares sense,
(ii) provides the best overall estimate of the frequency function, and
(iii) approximates to the H_2 estimator at the resonances and the H_1 estimator at the anti-resonances.

The H_v estimator calculates $H(\omega)$ from the eigenvector corresponding to the smallest eigenvalue of the matrix $[G_{xxy}]$, i.e.

$$[G_{xxy}] = \begin{pmatrix} G_{xx} & G_{xy} \\ G_{yx} & G_{yy} \end{pmatrix} \tag{2.10}$$

therefore

$$\gamma^2(\omega) = \frac{|H_1(\omega)|}{|H_2(\omega)|} \Rightarrow |H_1(\omega)| \leq |H_2(\omega)| \tag{2.11}$$

and

$$|H_1(\omega)| \leq |H_{true}(\omega)| \leq |H_2(\omega)| \tag{2.12}$$

The measured input and response data must be processed and put into a form, which is compatible with test and modal parameter estimation algorithms. At this point, the use of digital signal processing (DSP) techniques is a critical step in experiments. Acquired data, which are in a digital form, can be transferred from the time domain to the frequency domain, using discrete Fourier transform (DFT) technique. The ever present noise come with measurements can be classified as non-coherent noise (due to the unmeasured sources and/or transducer signals), signal processing noise (aliasing, or leakage) and nonlinear noise.

Errors in the estimation of FRF measurements can be classified as *variance* and *bias* errors. The variance is due to random deviations of each sample function from the mean, whereas bias is due to a system characteristic, or measurement procedure. Aliasing (amplitude error) and leakage (nonlinear error due to finite sampling time)

are the most known bias errors.

Depending on the dynamic performance of the analyzer, the analog-digital conversion introduces two concepts that affect magnitude and phase accuracy. One of them, *sampling*, is the part of the process related to the timing between individual digital pieces of the time history. The other one, *quantization*, is the part of the process related to describing an analog amplitude as a digital value. Shannon's sampling theorem states that the sampling frequency (f_s) must be greater than twice the maximum frequency (f_{max}) of interest, i.e.

$$f_s = \frac{1}{\delta t} = 2 \times f_N \quad \text{and} \quad f_N \geq f_{max} \tag{2.13}$$

The Nyquist frequency (F_N) is the theoretical limit for the maximum frequency. This means that there must be at least two samples per period for any frequency below the Nyquist frequency. Violating this rule introduces amplitude and frequency errors, which is known as *aliasing*. This problem can be illustrated graphically from a time domain point of view as shown in Figure 2.3.

Today, any modern data acquisition system uses the discrete Fourier transform algorithm. This algorithm is based upon two important assumptions concerning the discrete sequence of values. The first one is that the signal must be a completely observed transient with respect to the time period of observation. Alternatively, the second is that the signal must be composed only of harmonics of the time period of observation. If one of these two assumptions is not fulfilled by any discrete history processed by DFT, or FFT algorithms, then the resulting spectrum will contain *leakage* errors. If both, input and output are completely observable, or they are harmonic functions of the time period of observation, there will be no leakage error due to the truncation of time data. Since this is not the case in testing real systems, it is not possible to completely eliminate the effects of leakage. Leakage error can be reduced using some methods, such as cyclic averaging, increasing frequency resolution and using window functions. Window functions (a.k.a. weighting functions) are common tools

in compensation of leakage errors [53]. As an example, the Hanning type window is illustrated in Figure 2.4. [52]

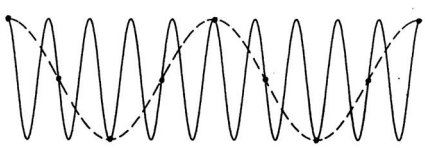


Figure 2.3. Aliasing problem



Figure 2.4. Original signal – the Hanning type window function – windowed signal

2.3. Test Configurations and Environments

The configuration of a basic setup required for FRF measurements includes a controller (software), an analyzer, sensors and an exciter. Environmental conditions, such as anechoic chambers and fixtures for supporting the structure are also critical. The type of the structure and the frequency bandwidth of interest dictate specifications and choices for a setup and environmental conditions.

The controller and the analyzer provide data acquisition, signal conditioning and digital signal processing tools. The raw time data acquired through sensors are processed, using functions like windowing, averaging and FRF estimations. Today analyzers are versatile and channel numbers can be increased by accommodating many channels in a single frame, as well as using multi analyzers in master-slave configurations. Input channels receive measurement signals from strain gages, accelerometers, microphones and impact hammers. Shakers can be driven over output channels, using a variety of periodic and transient signals. Characteristics of some of the excitation

functions that are occasionally used in shaker applications are compared and contrasted in Table 2.2.

Table 2.2. Excitation functions

feature	steady sine	random	periodic chirp	burst random	impact
minimize leakage	no	yes	yes	yes	yes
S/N ratio	high	fair	high	fair	low
RMS/Peak ratio	high	fair	high	fair	low
measurement time	long	fair	fair	short	short
controlled frequency	yes	yes*	yes*	yes*	no
controlled amplitude	yes	no	yes*	no	no
removes distortion	no	yes	no	yes	no
render nonlinearity	yes	no	no	no	no

* requires additional equipment

Excitation systems are described in four categories: step relaxation, self-operating, shakers and impact hammers [55]. Step relaxation method is usually preferred for very large structures that have to be tested in the field. This method basically requires an initial known pre-loading and measurements acquired, when the load is suddenly removed. Self-operating excitation is indispensable in some cases, where it is difficult, or impossible to excite the structure by external forces. Basic drawback of this method is the lack of information about applied forces.

Electrodynamic shakers used in modal tests can produce 2-1000 lbf up to 20 kHz. Hydraulic types are used for higher force levels. The maximum frequency range is getting smaller with increasing force capabilities. Since they have to be physically mounted to the structure to be tested, shakers may alter the dynamics of the structure. FRFs are single input functions, i.e. only one component of the applied force has to be transmitted to the test structure. To deal with these drawbacks, 'stingers' are improved in such a way that their stiffness characteristics are strong in axial direction, but weak for bending and shear.

Impact hammer testing is widely used in EMA to obtain FRFs. The relation between the impulse response and frequency functions is as follows [56]. For $h(\tau)$:IRF, $H(\omega)$:FRF, and $x(t) : \delta(t)$ (impulsive input),

$$X(\omega) = \frac{1}{2\pi} \int_{-\infty}^{\infty} \delta(t) e^{-i\omega t} dt = \frac{1}{2\pi} \tag{2.14}$$

and

$$Y(\omega) = \frac{1}{2\pi} \int_{-\infty}^{\infty} h(t) e^{-i\omega t} dt \tag{2.15}$$

Since

$$Y(\omega) = H(\omega) X(\omega) \quad \Rightarrow H(\omega) = \int_{-\infty}^{\infty} h(t) e^{-i\omega t} dt \tag{2.16}$$

the FRF, $H(\omega)$, is the Fourier transform of the IRF.

The frequency content is managed by changing the tip of the hammer. Using softer tips will increase the pulse duration, which in turn lower the frequency content. Potential problems associated with impact testing are noise and leakage. Since the impact time is very short relative to the measurement record time, the force signal after the impact is noise, and must be eliminated using a force-exponential type window. The response may not be fully decayed in the record time, thus has to be forced to decay to compensate for the leakage. Nevertheless, the windowing functions actually come up with new problems in the sense that they destroy the originality of the signals.

Many times vibro-acoustics experiments may require special types of environmental laboratory conditions, such as anechoic chambers. Basically, anechoic chambers are reflectiveness rooms that have walls coated with sound absorber materials. As in the real conditions, semi-anechoic types that are used in automotive applications have normal rigid floors that reflect the sound waves.

Note that the type of supporting the test structure is also critical in vibro-acoustics studies. Theoretically, to solve the governing differential equations, we use perfect defined boundary conditions, such free, clamped, or pinned. In reality, for many structures it is impossible to provide these conditions perfectly, since all of them exhibit different levels of flexibility, when grounded. To provide free boundary condition, the structure can be hanged up, using soft cords, or may be supported by air springs. Anyway, once it is constrained, rigid body mode frequencies will no longer take zero value. Even so, if rigid body modes could be well separated from the flexible ones, one can assume that the free boundary condition is achieved.

2.4. Experimental Setup and Test Vehicles

All laboratory experiments are performed in the Vibration and Acoustics Laboratory of Boğaziçi University, while road tests are followed out on appropriate tracks. Experiments are performed on Renault passenger vehicles equipped with four-cylinder diesel and gasoline engines, hereinafter referred to as Vehicle L84 and Vehicle L38, respectively, throughout the text.

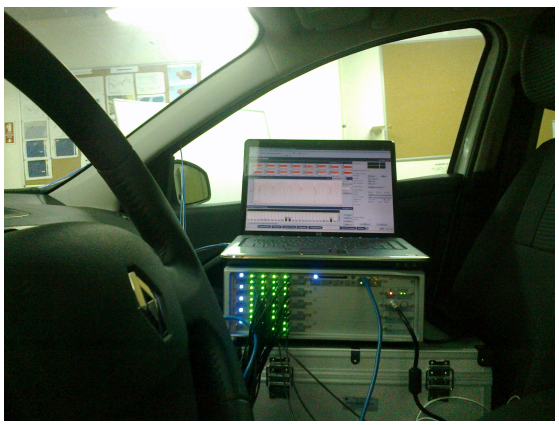


Figure 2.5. Vehicle L38, where the photograph is taken in the Vibration and Acoustics Laboratory of Boğaziçi University. "Photo courtesy of OYAK Renault Co."

LMS™ Scadas SCM-05 and SCM-09, i.e. mobile type analyzers are used for signal conditioning and data acquisition. Modal Shop™ 2100E11 type, 100 lbf shakers and a PCB™ 086C03 type, modally tuned impulse hammer are put into use as artificial exciters, when measuring FRFs. All signals are measured using various types of PCB accelerometers and microphones. For modal tests, free boundary condition is provided by engaging Modal Shop 8032S type air springs.



Figure 2.6. Vehicle L84, where the photograph is taken in the Vibration and Acoustics Laboratory of Boğaziçi University. "Photo courtesy of OYAK Renault Co."



(a) Mobile type analyzer



(b) Vehicle L38 in test

Figure 2.7. The experimental setup

2.5. Road Tests and Variability

As revealed in past studies [13, 14, 57], up to 20 dB magnitude differences are observed in measured sound pressure levels of identical vehicles, which further obstruct to diagnose root causes of noise problems. Evans [58] states that the transmitted vibrational energy may vary significantly due to apparently small changes in the source, or receiver structures, or characteristics of the connections. The term *variability* includes measurement, inter and intra variability. Note that, measurement variability implies measurement procedure, which is different from repeatability of a test. Lionnet et al. [59] describe inter variability as variances at responses of identical systems in the same environmental conditions and intra variability as variances at the response of a system under different environmental conditions. Intra variability occurs due to different operating conditions and environmental parameters, such as different ambient temperatures. Related studies and complementary information can be found in references [57, 59, 60]. Inter variability mainly occurs due to manufacturing errors, assembly procedure and assumptions in the modeling. The terms variability and uncertainty are often used together. Details about uncertainty terminology and related issues can be found in references [61, 62]. Note that, in this work, variability is relevant to aleatory uncertainty rather than epistemic uncertainty. Uncertainties in material properties, geometrical and physical parameters also cause inter variability.

All road tests are performed, while engines of vehicles are operating in the third gear at the wide open throttle (WOT) position. This is a well-known engine run up test that gives an access to spectra, which spans the whole range from the idle to the maximum crankshaft rotation speed [63]. Actually, this test is performed to record sound signals in the time domain at predefined locations to quantify the acoustical comfort of the vehicle. Two microphone locations, namely BT: D and BT: K, are chosen as shown in Figures 2.9(a) and 2.9(b), respectively. Front microphone (BT: D) is used to record sound signals at the driver's left ear level. Likewise, using the rear microphone (BT: K), sound signals perceived at rear seat are acquired. Additionally, more microphone locations can be chosen, such as driver's right ear level position (BT:D1) and front passenger's ear level positions to acquire more data about the

interior acoustics of the test vehicle.



(a) A view from the path (b) The test vehicle

Figure 2.8. Vehicle L38 in road test. "Photo courtesy of OYAK Renault Co."

The vehicle L38 is equipped with a four-cylindered gasoline engine and a manual transmission. Vehicles L38 and L84 have same type of engine installation, such that the engine is hanged to the body through two engine mounts. These mounts support the engine statically and dynamically. A third mount located at the bottom is used to compensate the y-axis moment and serves only for dynamic loads. Nowadays this type of engine installation is very common, especially for front wheel drive vehicles. The exhaust is connected to the body with two mounts in L84, whereas the number of exhaust mounts is three in L38.



(a) Driver's ear level position (BT:D & BT:D1) (b) Passengers' ear level position (BT:K)

Figure 2.9. Microphone locations

Road tests are carried out for the serial production Vehicle L84. Results are compared with previous test results of serially produced identical vehicles to ensure that the mentioned test vehicle represents the general acoustic characteristics of L84. This is important, because present manufacturing techniques introduce variability into the vehicle structure. It is shown that [12], mainly spot welds and bolts cause variations in damping values, which in turn change dynamic characteristics of the vehicle structure. Results of sound records are processed using digital signal processing tools. Since the engine is a four-cylindered one, the second harmonic of crankshaft rotational frequency is critical. The pulse frequency can be computed using the engine rpm as

$$F_0 = \frac{rpm}{60}\frac{p}{2} \tag{2.17}$$

where p is the number of cylinders. To inspect inter variability and to acquire data, road tests are also performed for randomly selected five identically produced L38 vehicles that have the same equipment packages. Three digits of their production numbers are used to differentiate the vehicles, which are 170, 216, 244, 250 and 251. The aim is to determine capabilities of the test vehicles in representing general acoustic characteristics of the vehicle studied and to reveal inter variability, if any. In Vehicle L38 tests, the sound pressure level (SPL) records are acquired from BT:D, BT:D1 and BT:K targets and acceleration measurements are acquired from engine and exhaust mounts in three directions. During tests, data are acquired from three microphones, one reference uniaxial accelerometer and twelve triaxial accelerometers that correspond to 40 channels, in total. Overall variability is mainly composed of inter and intra variability. Since inter variability is focused in this work, measures are taken to prevent intra variability. To minimize intra variability, following conditions are inspected. Road tests are performed on an appropriate track. Before tests, inside and outside temperatures, pressure values of tires, torque values of mount studs are recorded. Fuel and water tanks are topped up to ensure identical total weight value for all test vehicles. Temperature inside the vehicles are recorded in between 21-25 °C, while the outside temperature is recorded in between 27-32 °C. Tire pressure values are monitored as 32 and 30 psi for front and rear wheels, respectively. Since air inside vehicle cavity is assumed to be stationary, all windows and air conditioning system are closed. As indicated in the related ISO

standard [63], road test should not be performed in rainy weather. The asphalt path must be dry and smooth with no inclines. Two alternative paths are examined and one of them is chosen which seems appropriate for road tests. The smooth track with no curves is passed in two directions to inspect if there is an inclination that affects results. All tests are repeated at least 3 times, where measurements are performed up to 1280 Hz.

According to source-path-receiver approach, the system is assumed to be a combination of active and passive subsystems. We refer to the monocoque body as passive subsystem and engine and exhaust as active subsystems, where interfaces are mounts. Considering the operational acceleration force vector, which will be used in force identification step, acceleration measurement locations are determined. By the definition of TPA, these locations are chosen at the passive (body) and active (source) side of engine and exhaust mounts. Acceleration data are acquired in three translational directions on the body and source side of engine and exhaust mounts, employing 100 mV/g and 10 mV/g accelerometers, respectively. During the test, a reference signal is also measured from a point on the engine block. It is assumed that engine is a rigid body and a single coherent excitation source. Consequently, force inputs through all engine mounts are correlated with each other. The locations of accelerometers attached to engine and exhaust mounts are shown in Figures 2.10. and 2.11., respectively. For clarity, the locations are also described in Table 2.3.

2.5.1. Road Test Results

After processing the acquired data, an order analysis is followed out. As expected, results show that second order contributions dominate the instant sound pressure rises. Waterfall plot of sound pressure level measured at BT:D of Vehicle L84 is given in Figure 2.12. Second order sound pressure (SPL) values calculated for BT: D and BT: K locations are given in Figures 2.13(a) and 2.13(b). Around 3800 rpm, clear and annoying booming effects are observed at the BT:D and BT:K levels during the test. As observed in Figures 2.12. and 2.13., the booming is present on a wide band, namely between 3400 - 4200 rpm, at the firing frequency of the engine.

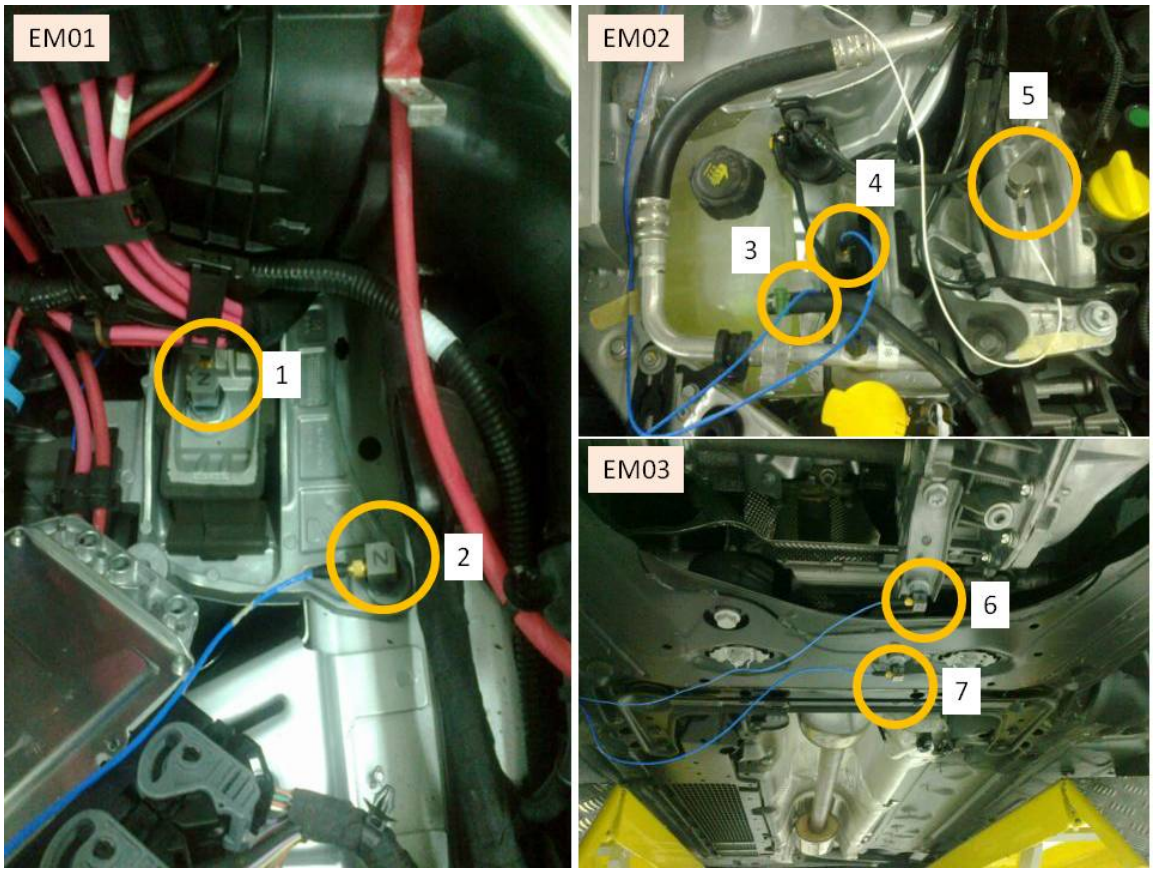


Figure 2.10. Engine mounts

Order analysis results are quite similar for all test vehicles and the results for BT: D and BT: K targets of test vehicle # 170 are shown in Figures 2.14(a) and 2.14(b), respectively. Second order sound pressure (SPL) values at BT: D and BT: K locations are calculated for five test vehicles. Results for the targets are given in Figures 2.15(a) to 2.15(c). Measured data of five vehicles are also compared with the database of previous tests performed by the vehicle manufacturer. SPL variations are inspected in the guideline of this database. Two of L38 test vehicles, namely # 170 and # 250, are selected for further assessments and TPA studies. Acceleration signals recorded during tests are not only useful for dynamic force identification, but they also give an insight into the evaluation of variability in a systematic manner. Test results can be interpreted step by step in the following context: (i) signals acquired from reference accelerometer represent the engine, the single coherent vibration source, in full spectra, (ii) signals acquired from engine and exhaust mounts represent the filtration characteristics, and (iii) microphone measurements show the resulting response of the system in the frequency domain.

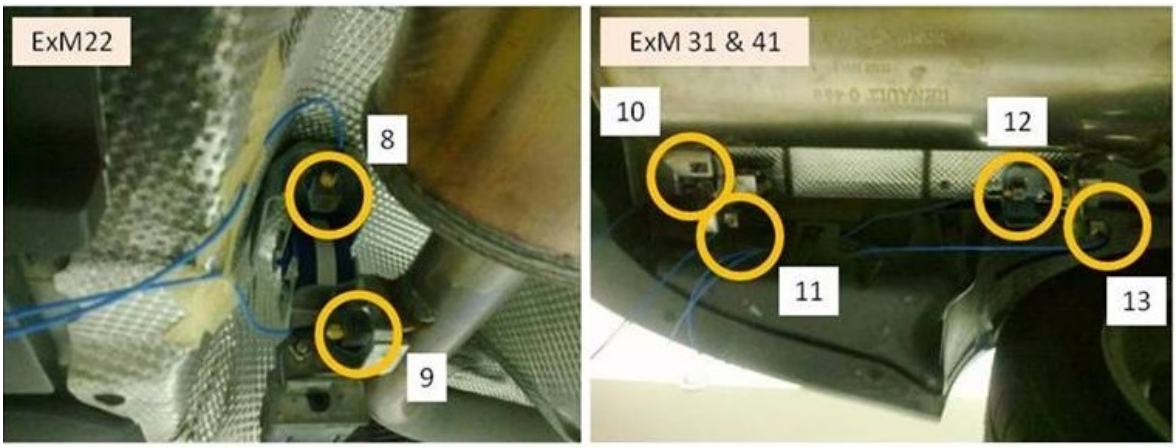


Figure 2.11. Exhaust mounts

Table 2.3. Accelerometer locations

#	location	active/passive	specification
1	SM01	active	10 mV/g
2	RH01	passive	100 mV/g
3	RH02	passive	100 mV/g
4	SM02	active	10 mV/g
5	Block	active	10 mV/g
6	SM03	active	10 mV/g
7	RH03	passive	100 mV/g
8	EC22	passive	100 mV/g
9	FE22	active	10 mV/g
10	EC31	passive	100 mV/g
11	FE31	active	10 mV/g
12	EC41	passive	100 mV/g
13	FE41	active	10 mV/g

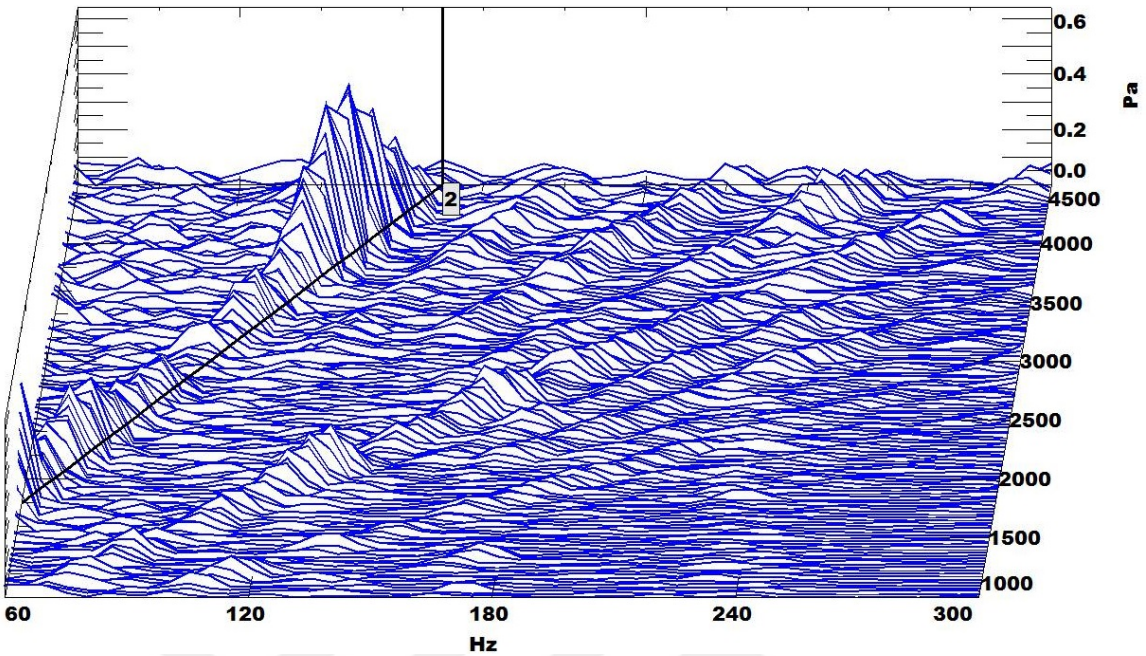
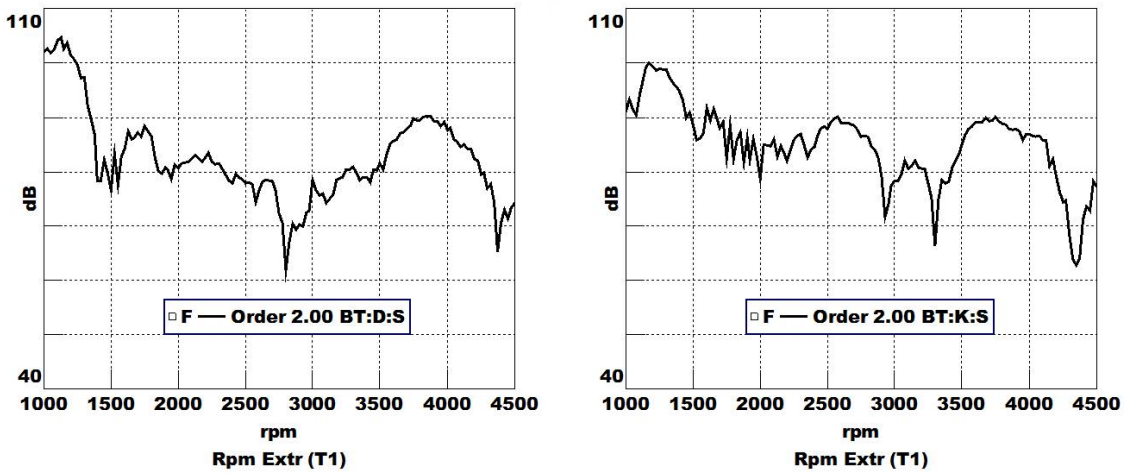


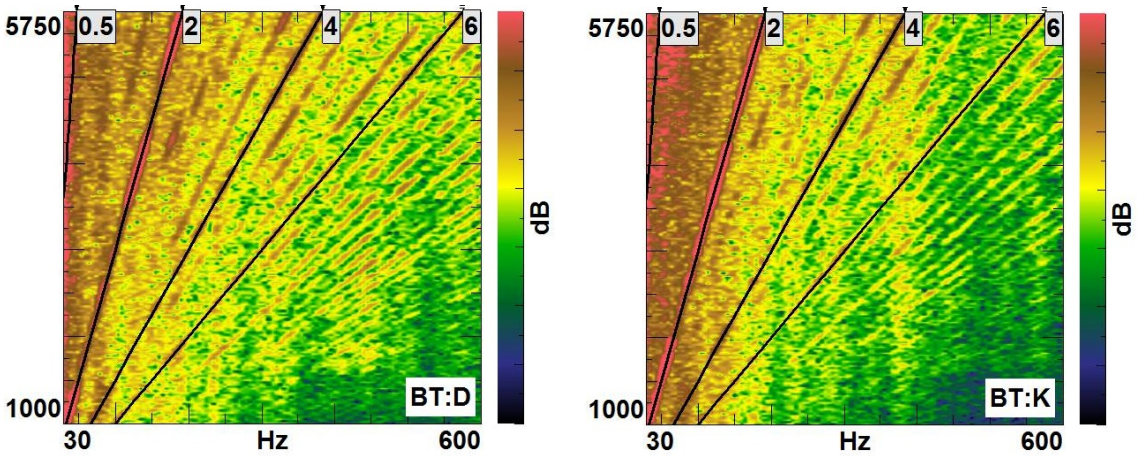
Figure 2.12. Waterfall plot of Vehicle L84, BT: D, in Hz, rpm and Pa



(a) Second order SPL at BT: D, Vehicle L84 (b) Second order SPL at BT: K, Vehicle L84

Figure 2.13. Sound pressure levels at Vehicle L84 targets, dB vs. rpm

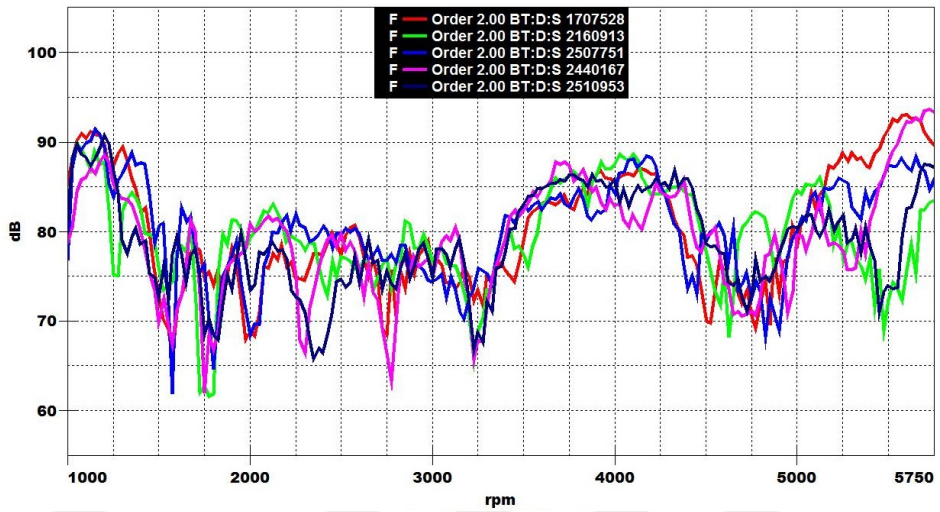
In Figure 2.16., acceleration curves that belong to five identical engines are given. Although one of the curves has lower amplitude values, it seems that all of them have same characteristics. It is reasonable to assess that the vibrational inputs are the same, for all of the test vehicles.



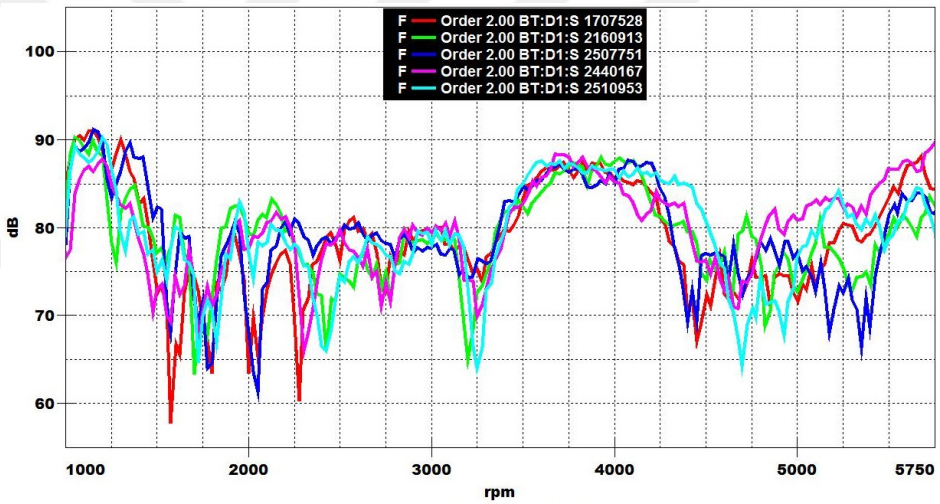
(a) Orders plot of Vehicle L38 #170, BT: D (b) Orders plot of Vehicle L38 #170, BT: K

Figure 2.14. Orders plot

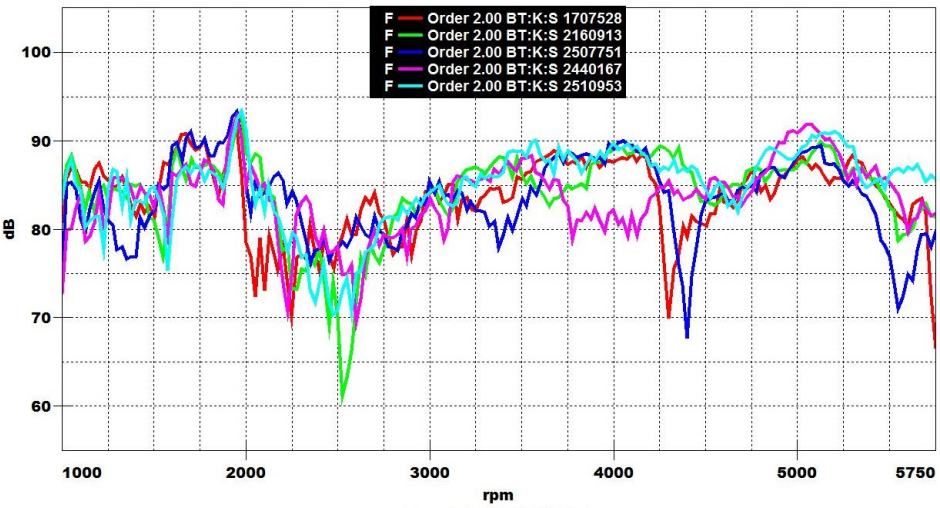
One can analyze test measurements in a source (input) - path (system) - receiver (output) context. After the source, the vibrational energy passes through mounts and is filtered, before it is transmitted to the vehicle structure. Acceleration measurement results acquired from active and passive sides of engine mounts are given in Figures 2.17. to 2.22. As seen in Figures 2.17. to 2.19., the active side acceleration curves are similar up to 5000 rpm. After 5000 rpm, deviations are observed at amplitude values. Nevertheless, one can say that the resulting inputs from engines and engine side of mounts are similar for five vehicles. On the other hand, the passive side curves tend to deviate after 4000 rpm, as observed in Figures 2.20. to 2.22. Moreover, there are some small amplitude differences before 4000 rpm at some small intervals of the spectra. Considering the results, one can come to a conclusion that filtration characteristics of the mounts are different. By the way, it should not be forgotten that the passive sides of the engine mounts are not only subjected to vibrations transmitted from the active side, but they also experience the response of the vehicle structure. Depending on the available data, it is impossible to separate these influences at this stage. More data about the vehicle structure are needed to come to a certain conclusion, where available in next sections.



(a) Second order SPL at BT: D, Vehicle L38



(b) Second order SPL at BT: D1, Vehicle L38



(c) Second order SPL at BT: K, Vehicle L38

Figure 2.15. Sound pressure level curves of five L38 vehicles, dB vs. rpm

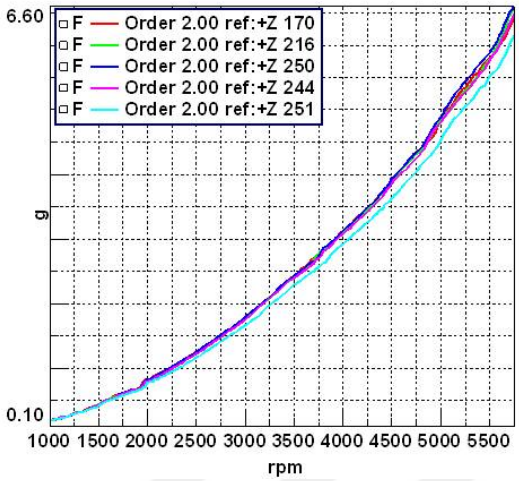
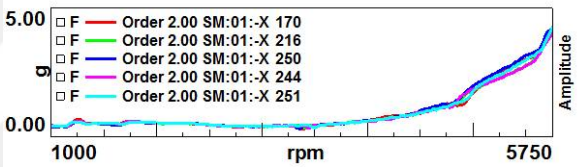
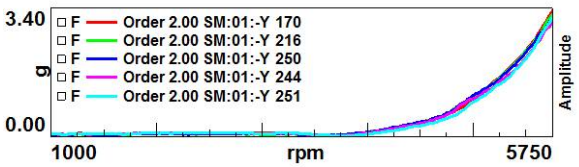


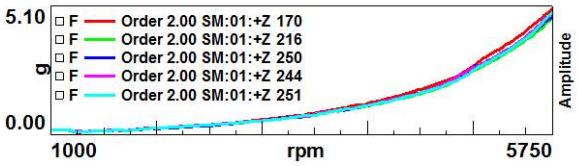
Figure 2.16. Engine block accelerations of L38 test vehicles, (2^{nd} order)



(a) x-direction

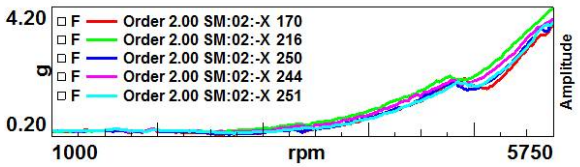


(b) y-direction

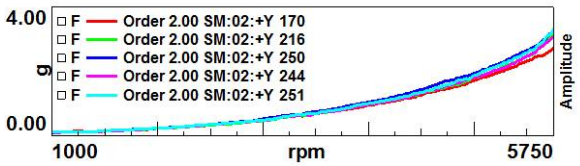


(c) z-direction

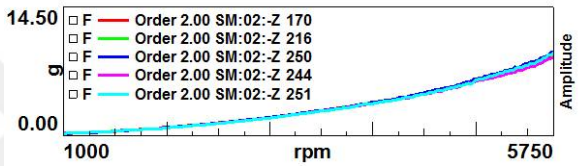
Figure 2.17. Engine mount (SM01)-active side acceleration curves, (2^{nd} order)



(a) x-direction

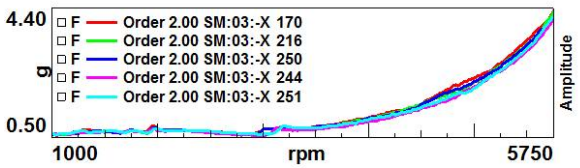


(b) y-direction

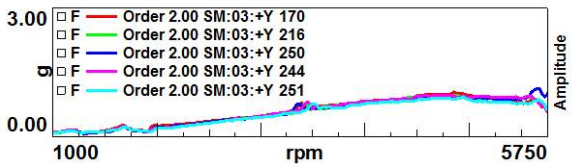


(c) z-direction

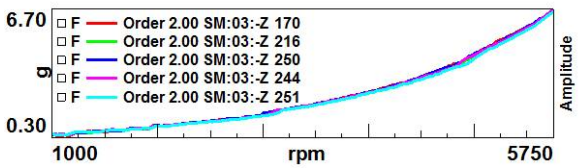
Figure 2.18. Engine mount (SM02)-active side acceleration curves, (2^{nd} order)



(a) x-direction

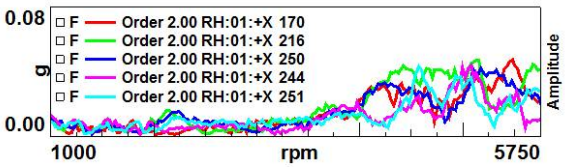


(b) y-direction

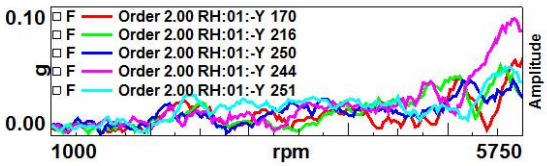


(c) z-direction

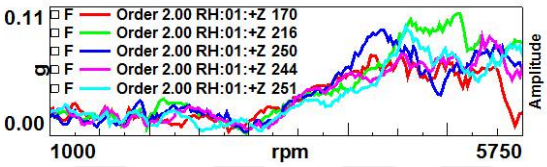
Figure 2.19. Engine mount (SM03)-active side acceleration curves, (2^{nd} order)



(a) x-direction

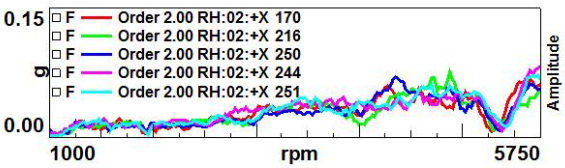


(b) y-direction

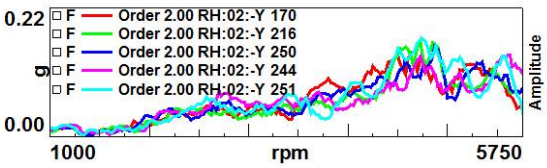


(c) z-direction

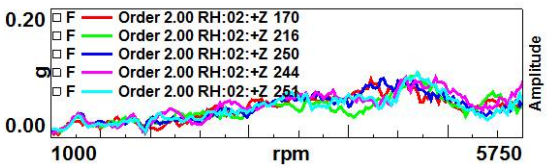
Figure 2.20. Engine mount (RH01)-passive side acceleration curves, (2^{nd} order)



(a) x-direction

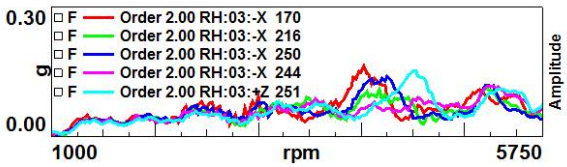


(b) y-direction

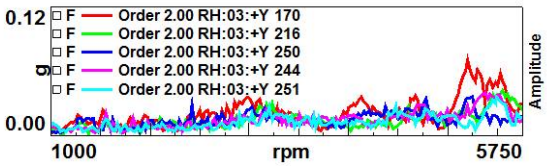


(c) z-direction

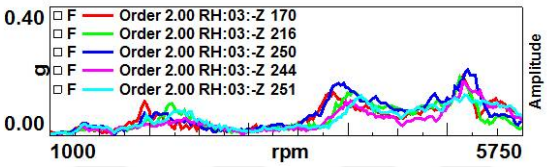
Figure 2.21. Engine mount (RH02)-passive side acceleration curves, (2^{nd} order)



(a) x-direction

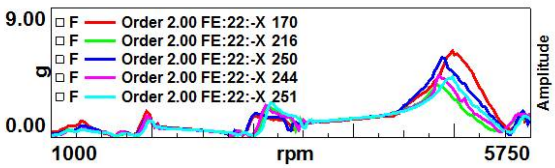


(b) y-direction

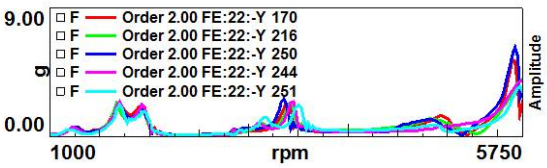


(c) z-direction

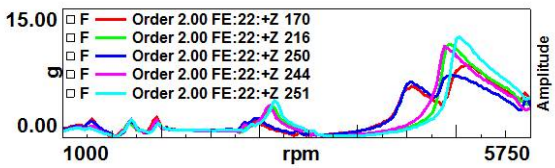
Figure 2.22. Engine mount (RH03)-passive side acceleration curves, (2^{nd} order)



(a) x-direction

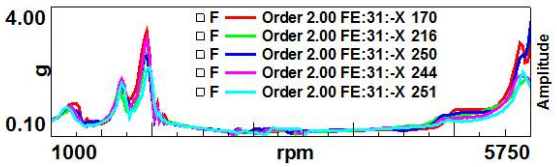


(b) y-direction

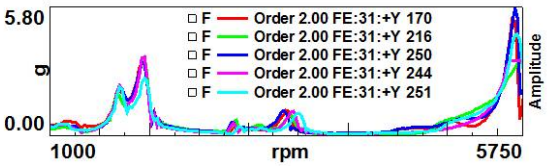


(c) z-direction

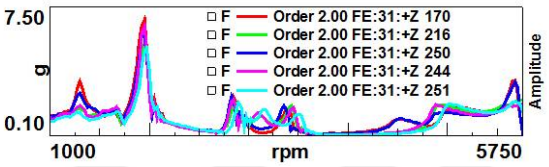
Figure 2.23. Exhaust mount (FE22)-active side acceleration curves, (2^{nd} order)



(a) x-direction

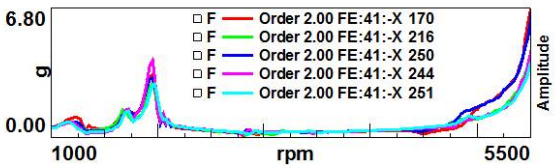


(b) y-direction

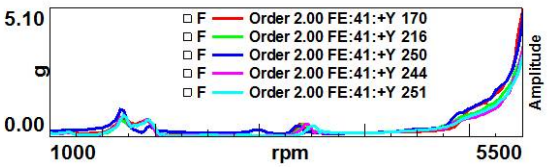


(c) z-direction

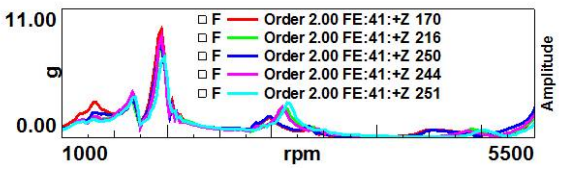
Figure 2.24. Exhaust mount (FE31)-active side acceleration curves, (2^{nd} order)



(a) x-direction

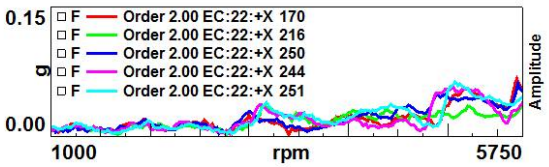


(b) y-direction

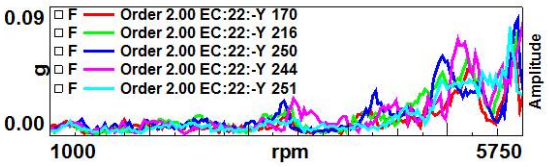


(c) z-direction

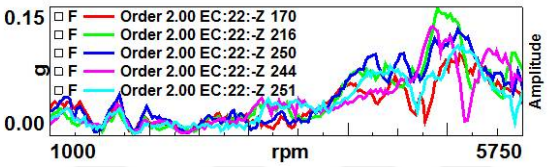
Figure 2.25. Exhaust mount (FE41)-active side acceleration curves, (2^{nd} order)



(a) x-direction

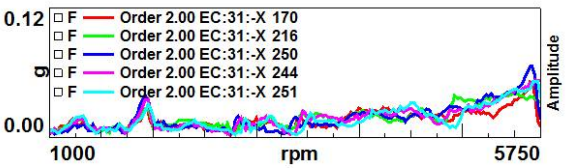


(b) y-direction

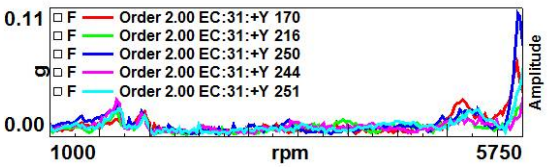


(c) z-direction

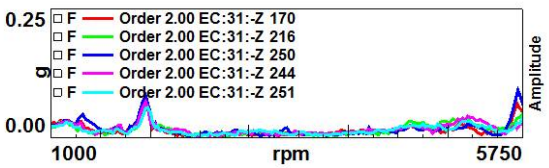
Figure 2.26. Exhaust mount (EC22)-passive side acceleration curves, (2^{nd} order)



(a) x-direction

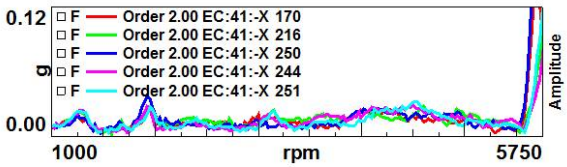


(b) y-direction

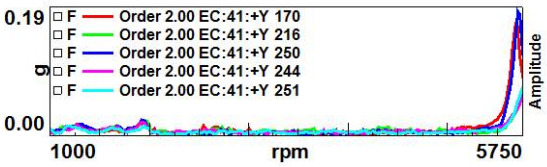


(c) z-direction

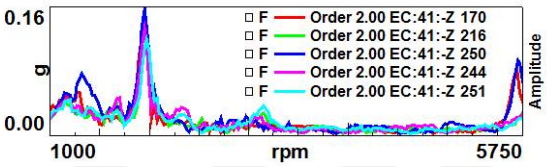
Figure 2.27. Exhaust mount (EC31)-passive side acceleration curves, (2^{nd} order)



(a) x-direction



(b) y-direction

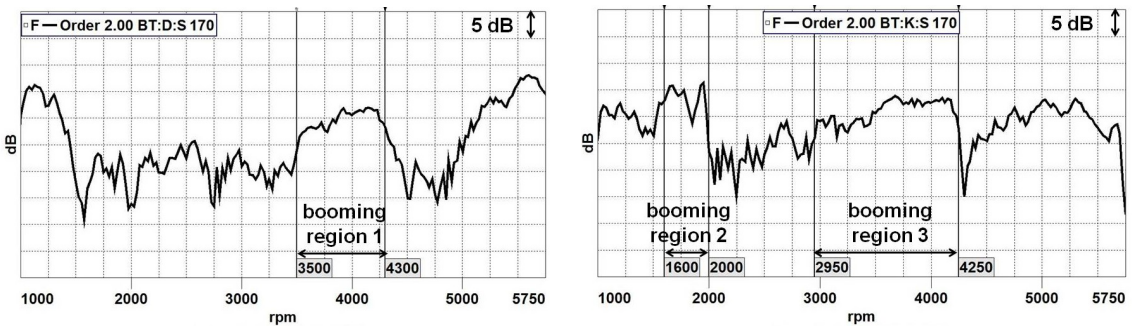


(c) z-direction

Figure 2.28. Exhaust mount (EC41)-passive side acceleration curves, (2^{nd} order)

Exhaust active side acceleration values are high enough to make significant contributions to the system response, as can be observed in Figures 2.23. to 2.25. Peaks around 2000 rpm observed in Figures 2.24. and 2.25. are remarkably important, and they are in accordance with the peaks observed in the SPL curve of BT:K target(see Figure 2.15(c)). Considering all of the exhaust mount acceleration curves, important variations are observed mostly in the active and passive sides of ExM22 (see Figure 2.26.)

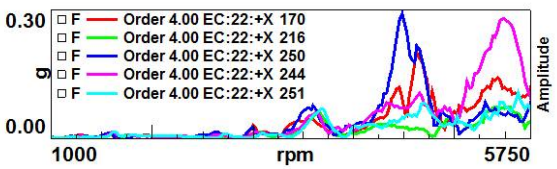
Inter variability observed in the SPL curves of five test vehicles (see Figure 2.15.) and the deviations observed in acceleration curves of passive sides of mounts (see Figures 2.26. to 2.28.) are in accordance. Among test vehicles, # 170, which represents the general vibro-acoustic behavior of serially produced L38 vehicles, is chosen for further experiments. Note that amplitude variations in SPL curves can be accepted up to some extent, namely $\pm$ 5 dB. However, it is expected that the locations of resonances and anti-resonances in the dB vs. rpm (or derived frequency) plots should match for identical test structures. If this is not the case, one can conclude that a fault is present in the structure studied.



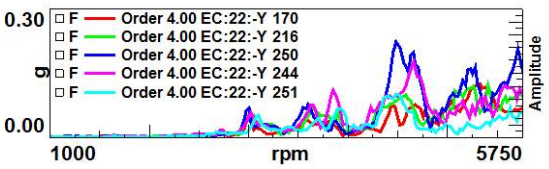
(a) Booming observed at BT: D (b) Booms observed at BT: K

Figure 2.29. Booms observed at the targets of test vehicle # 170

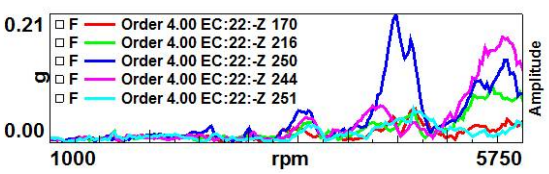
Vehicle manufacturers often define interior NVH targets depending upon their expectations, inspired mostly by competition. Booms of the vehicle are determined using these targets, rather than legislation, which is the case in exterior noise. In Figure 2.29(a), the first booming region at target BT: D is shown, whereas other two booms identified at target BT: K are shown in Figure 2.29(b). Instant pressure rises over 5000 rpm are not so important, since drivers seldom run the engine at these speeds. Conversely, the booms observed in 3500-4300 rpm and 2950-4250 rpm intervals are critical, because they are ever present in the cruise speed.



(a) x-direction

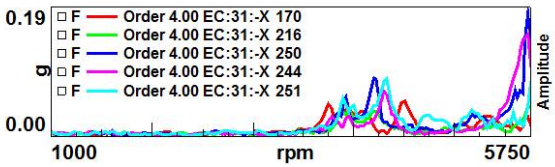


(b) y-direction

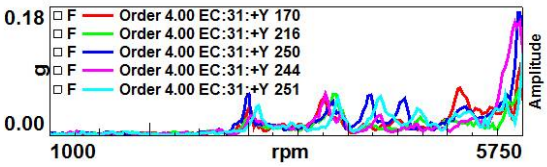


(c) z-direction

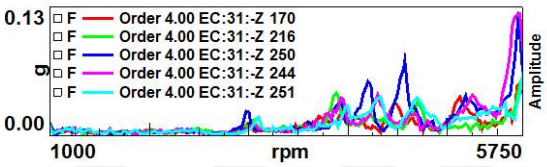
Figure 2.30. Exhaust mount (FE22)-active side acceleration curves, (4^{th} order)



(a) x-direction

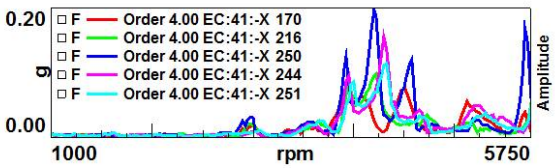


(b) y-direction

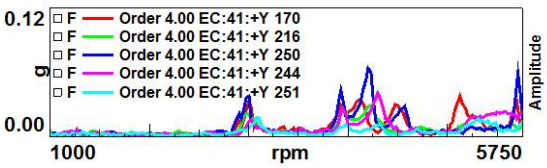


(c) z-direction

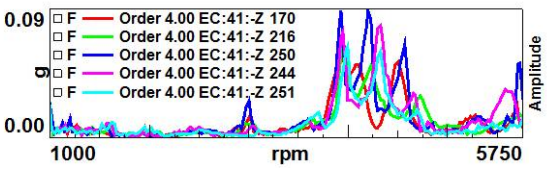
Figure 2.31. Exhaust mount (FE31)-active side acceleration curves, (4^{th} order)



(a) x-direction

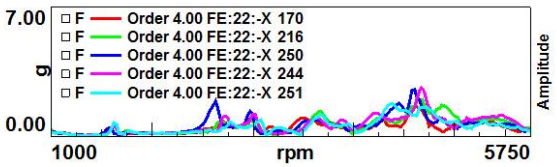


(b) y-direction

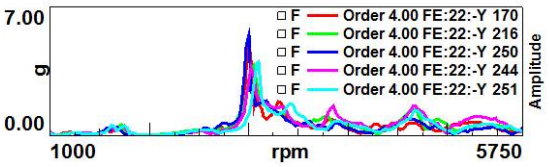


(c) z-direction

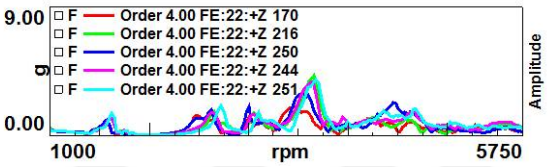
Figure 2.32. Exhaust mount (FE41)-active side acceleration curves, (4^{th} order)



(a) x-direction

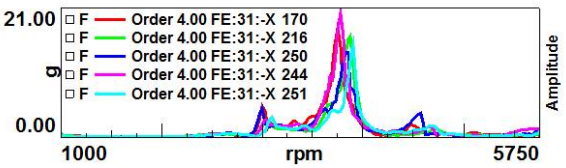


(b) y-direction

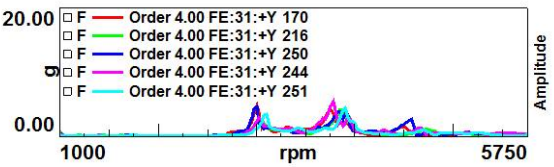


(c) z-direction

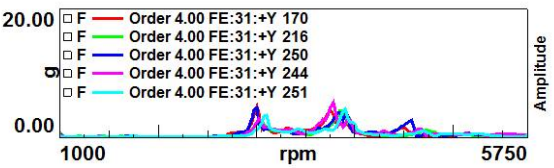
Figure 2.33. Exhaust mount (EC22)-passive side acceleration curves, (4^{th} order)



(a) x-direction

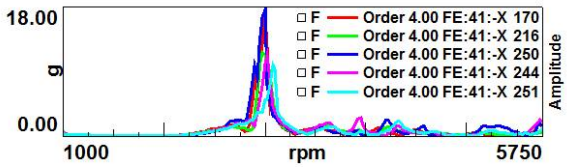


(b) y-direction

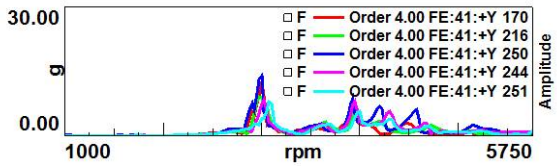


(c) z-direction

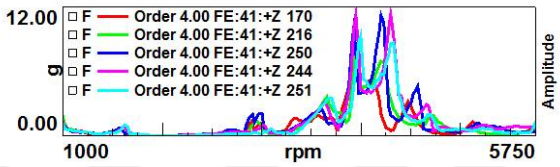
Figure 2.34. Exhaust mount (EC31)-passive side acceleration curves, (4^{th} order)



(a) x-direction



(b) y-direction



(c) z-direction

Figure 2.35. Exhaust mount (E41)-passive side acceleration curves, (4^{th} order)

Raw measurements are processed in all orders to compare the contributions of them to the SPLs at predefined locations. As expected, exhaust mount inputs are also important for the fourth order SPLs. The fourth order active and passive side accelerations measured at exhaust mounts are given in Figures 2.30. to 2.35. As in the second order curves, important variations are observed in ExM22 plots for active, as well as passive sides (see Figures 2.30. and 2.33.).

2.6. Laboratory Mock up Tests

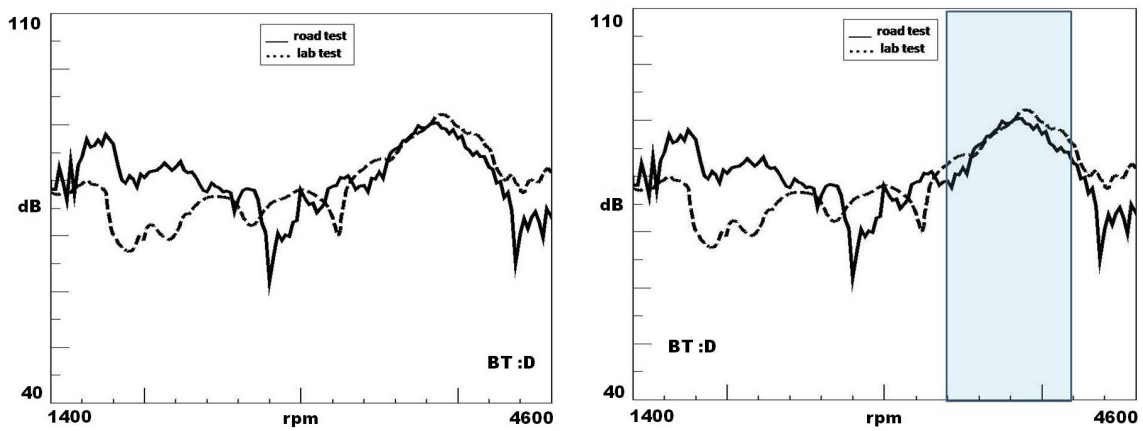
A laboratory test is developed, which mocks up the aforementioned standard road test, such that the crankshaft experiences the same acceleration at the same time interval, but the engine is not loaded, and there is no road input. Since the maximum rpm experienced by the crankshaft is about 6000 and the dominant order is 2; the frequency interval of interest can be computed as 200 Hz, according to Equation (2.17). Below 200 Hz, structure borne noise is strictly dominant, whereas airborne noise is dominant above 600 Hz [64]. The 200 - 600 Hz interval can be taken as a transition

zone, such that the structure borne noise begins to lose its significant contribution on the NVH characteristics of the structure.

Since the engine is loaded during road tests, a time period is required to sweep all engine frequencies. This period is measured as 42.5 and 24 seconds for L84 and L38, respectively. In laboratory mock up tests, the throttle has to be opened slowly to sweep all engine frequencies at the same period. Since the engine is not loaded and there is no road input, it is not surprising to see some differences in between SPL curves, derived from the road and laboratory mock up tests.

2.6.1. Road - Laboratory Test Comparison

The second order SPL curves of L84 measured at BT:D target, during road and laboratory tests are given in Figure 2.36(a). The curves have the same characteristics in general, such that resonances and anti-resonances seem to appear at same frequencies. There are moderate differences at amplitude values, especially in low frequency region. The marked area in Figure 2.36(b), namely 3400 - 4200 rpm interval, is the booming region, where the SPL curve has a peak at around 3850 rpm. Since the road and laboratory test results are very similar in the marked area, it is reasonable to come to a conclusion, such that for this case road inputs and transmission have negligible contributions to the stated booming problems.



(a) BT:D level, L84 (b) Booming region at BT:D level, L84

Figure 2.36. Road - laboratory test comparison, L84 (2^{nd} order)

To get insight into the dynamics of the structure, it is determined to acquire more data for Vehicle L38, in laboratory mock up test. Data from 40 channels have been acquired from targets and selected locations (see Figures 2.10. and 2.11.), as in the road test. Using identical sensor locations (see Figure 2.37.) and acquisition parameters the aforementioned laboratory test is performed on L38. SPL results at BT:D and BT:K targets for road, as well as laboratory test are given in Figure 2.38. For this case, acceleration measurements taken during both the road and laboratory tests are also evaluated. First of all, SPL results are analyzed to observe booming regions of Vehicle L38. As shown in Figure 2.39., there are two booming regions. One of them, namely the region between 2950 and 4300 rpm, is valid for both of the targets. The second one 1600 - 2000 rpm band is valid only for BT:K target.

As seen in Figure 2.39., there is an acceptable consistency in between SPL results at the booming region appeared in 2950 - 4250 rpm, whereas results do not match well in the 1600 - 2000 rpm booming region. Beside amplitude variations, resonance and anti-resonance frequencies are not compatible in this region.

Considering the engine mounts in road-laboratory test comparison, active side inputs match well, except the deviations after 5000, rpm as can be observed in Figures 2.41. to 2.43.. On the other hand, some of the body side inputs, namely RH01-X,-Y and RH03-X,-Z, exhibit some deviations, especially in booming regions (see Figure 2.44.).

Exhaust mount inputs are compared in Figures 2.47. to 2.52. There are important deviations in the active and passive side inputs of the carrier mount (see Figure 2.50.). Deviations observed in the exhaust mount acceleration and SPL measurements in the 1600-2000 rpm region match well. Peaks around 1900 rpm, which can be observed in Figures 2.27(c) and 2.28(c) plots are important. The peak around 1900 rpm indicates a resonance behavior. Although this resonance frequency is the same for both of the road and laboratory measurements, amplitude values are significantly different.

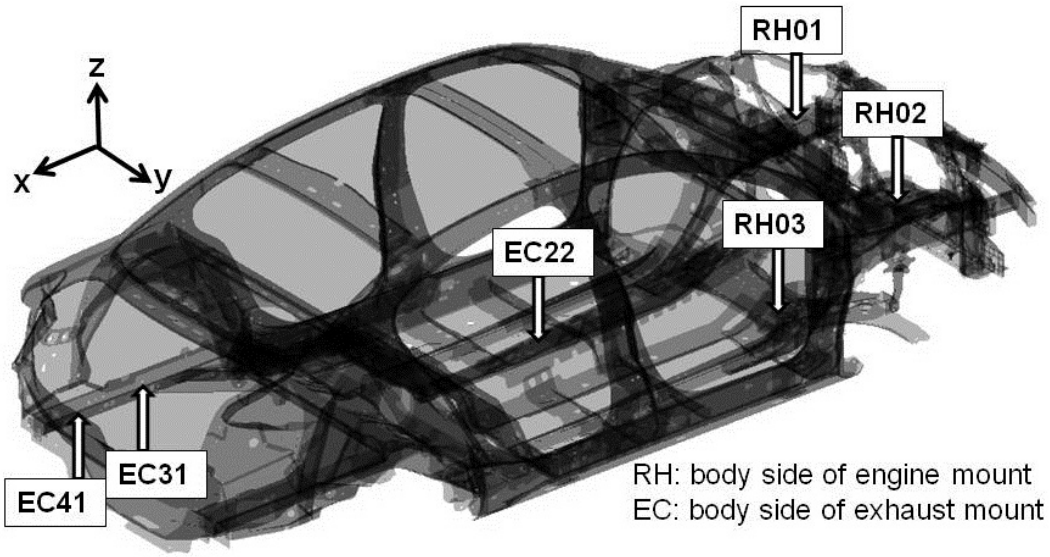
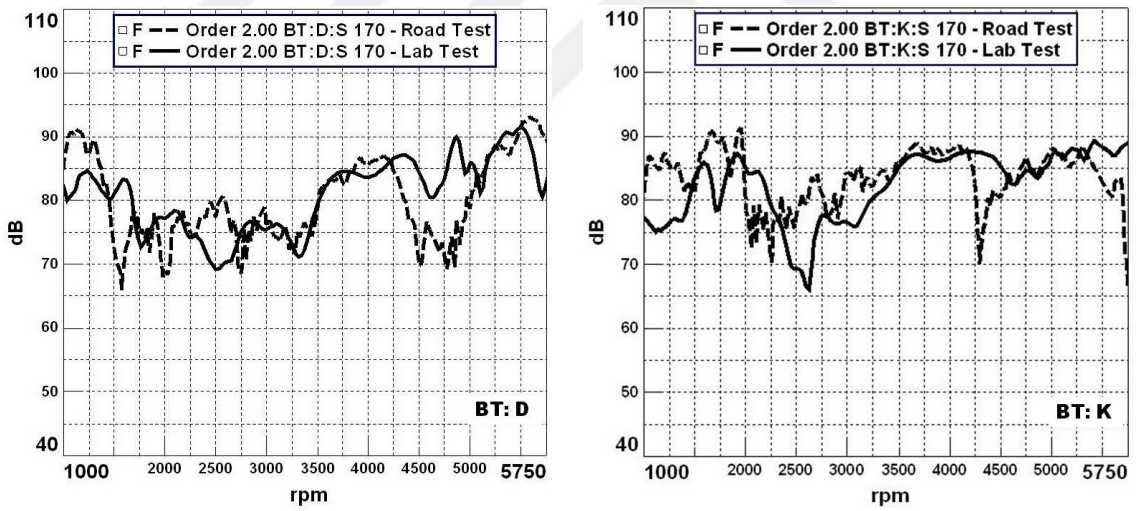


Figure 2.37. Locations of engine and exhaust mounts, Vehicle L38



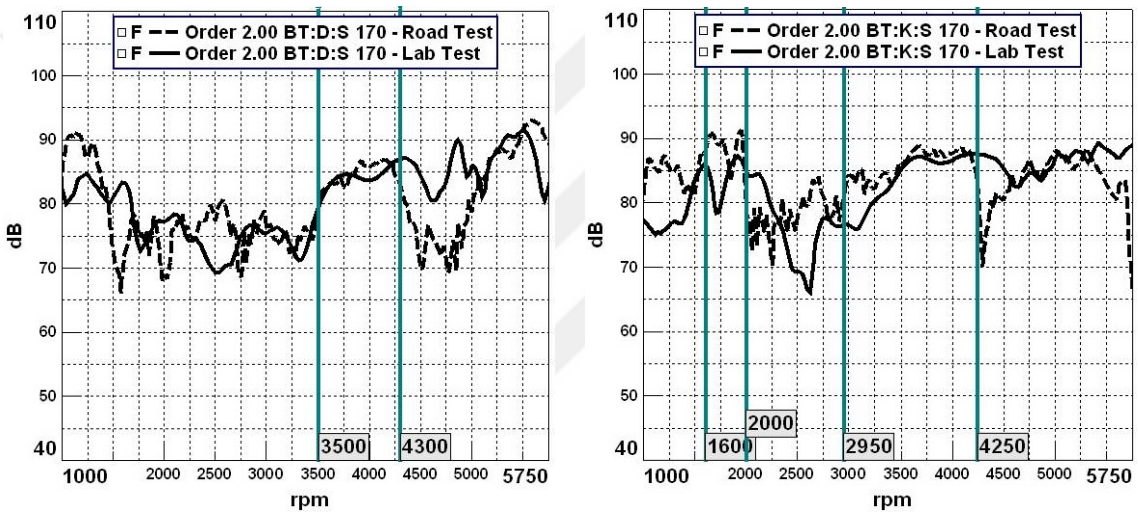
(a) BT:D target

(b) BT:K target

Figure 2.38. Road - laboratory test comparison, L38, #170, (2^{nd} order)

A remarkable difference stands out at the SPL curves measured at the target BT:D, in between 4250 and 5000 rpm. This difference is thought to be caused by body side inputs of ExM22, which have high acceleration values at the mentioned band (see Figure 2.26.). Acceleration curves of active and passive side exhaust mounts have similar characteristics. Exhaust mount acceleration curves of road and laboratory tests tend to deviate after 4200 rpm for the mount ExM22 (see Figures 2.47. and 2.50.).

In between 1600 and 2000 rpm, drastic differences are observed in acceleration values of mounts ExM31-Z and ExM41-Z (see Figures 2.48(c), 2.49(c), 2.51(c) and 2.52(c)). Above mentioned observations are important in the sense of gaining an insight into the differences of system response observed in laboratory and road tests. Measurements performed so far are not enough to come to certain conclusions about NVH characteristics of the structure. Nevertheless, analyzed data are adequately enough to make diagnosis and to determine a road map for further studies.



(a) Booming region at BT:D target (b) Booming regions at BT:K target

Figure 2.39. Booming regions, L38, #170, (2^{nd} order)

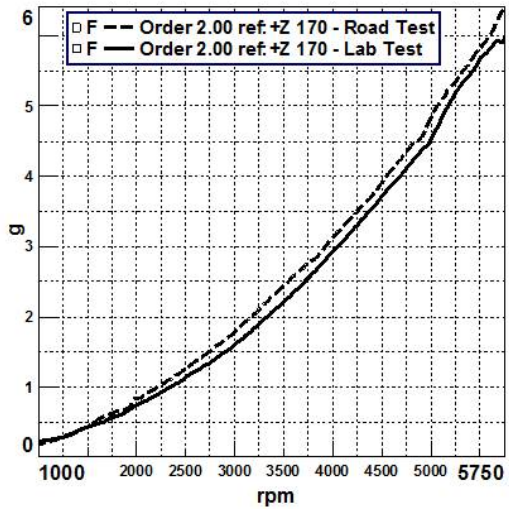
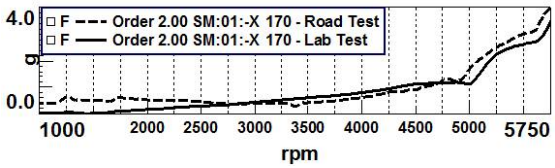
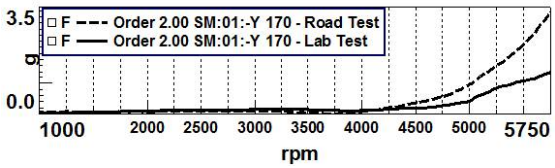


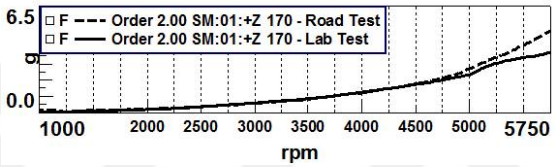
Figure 2.40. Road - laboratory test comparison, engine block acceleration, L38 (2^{nd} order)



(a) x-direction

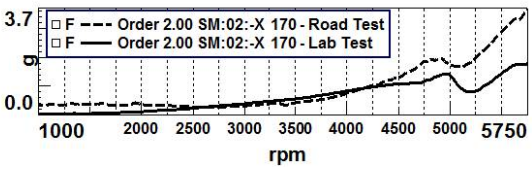


(b) y-direction

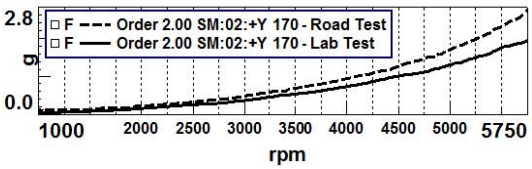


(c) z-direction

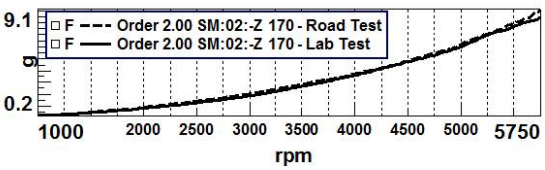
Figure 2.41. Road - laboratory test comparison, engine mount (SM01)-active side acceleration curves (2^{nd} order), L38



(a) x-direction

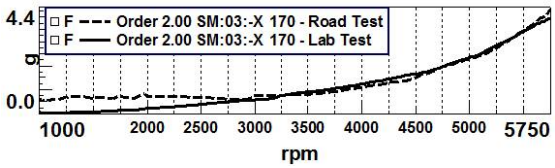


(b) y-direction

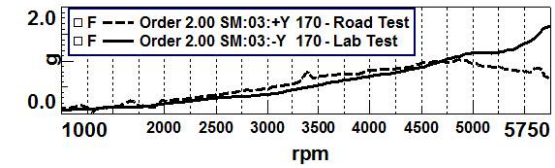


(c) z-direction

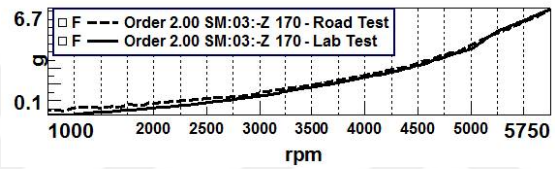
Figure 2.42. Road - laboratory test comparison, engine mount (SM02)-active side acceleration curves (2^{nd} order), L38



(a) x-direction

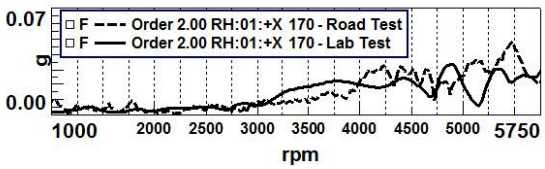


(b) y-direction

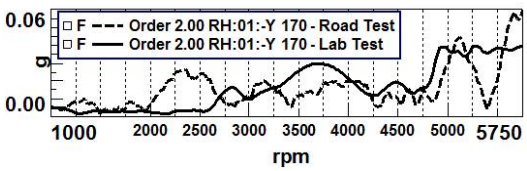


(c) z-direction

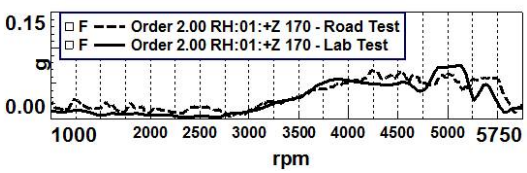
Figure 2.43. Road - laboratory test comparison, engine mount (SM03)-active side acceleration curves (2^{nd} order), L38



(a) x-direction

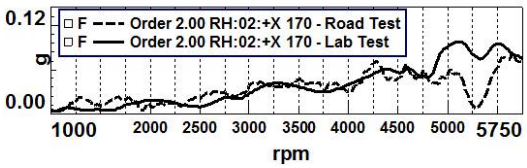


(b) y-direction

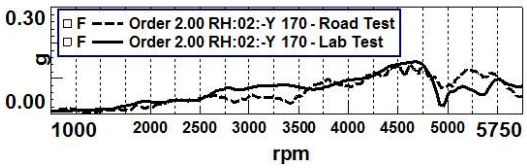


(c) z-direction

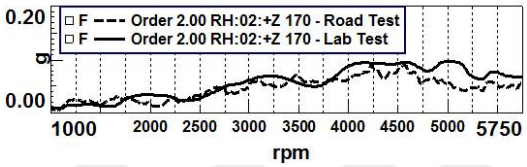
Figure 2.44. Road - laboratory test comparison, engine mount (RH01)-passive side acceleration curves (2^{nd} order), L38



(a) x-direction

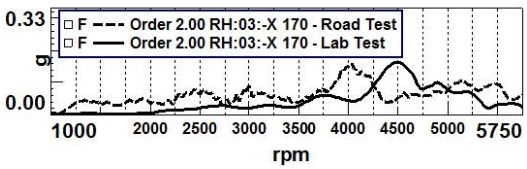


(b) y-direction

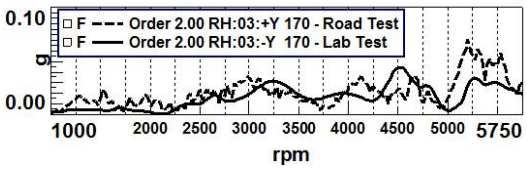


(c) z-direction

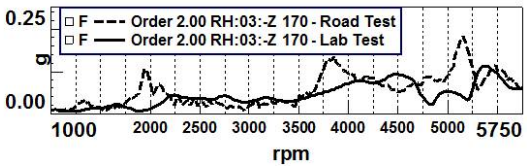
Figure 2.45. Road - laboratory test comparison, engine mount (RH02)-passive side acceleration curves (2^{nd} order), L38



(a) x-direction

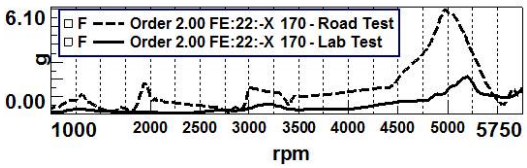


(b) y-direction

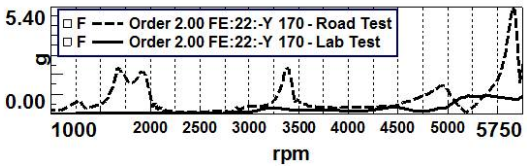


(c) z-direction

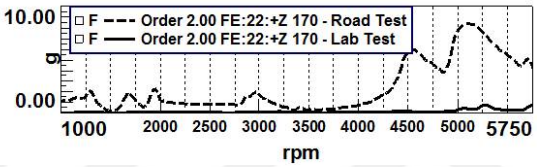
Figure 2.46. Road - laboratory test comparison, engine mount (RH03)-passive side acceleration curves (2^{nd} order), L38



(a) x-direction

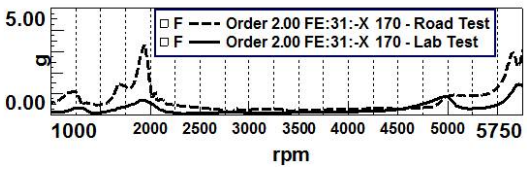


(b) y-direction

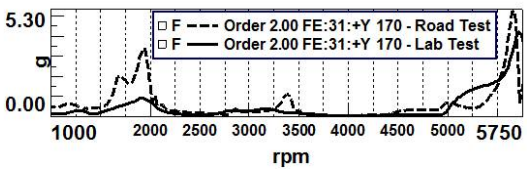


(c) z-direction

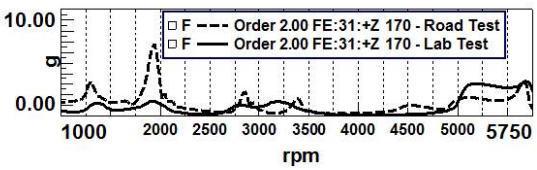
Figure 2.47. Road - laboratory test comparison, exhaust mount (FE22)-active side acceleration curves (2^{nd} order), L38



(a) x-direction

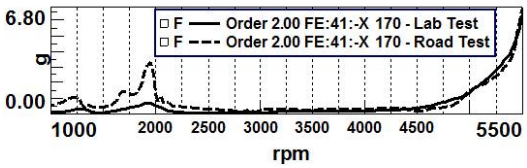


(b) y-direction

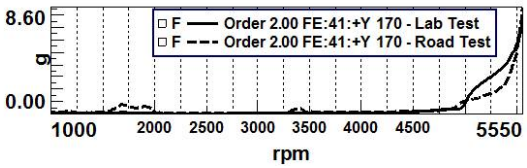


(c) z-direction

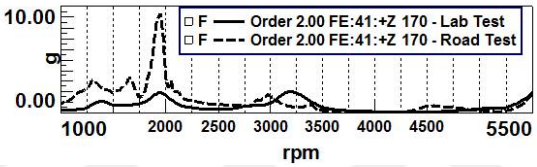
Figure 2.48. Road - laboratory test comparison, exhaust mount (FE31)-active side acceleration curves (2^{nd} order), L38



(a) x-direction

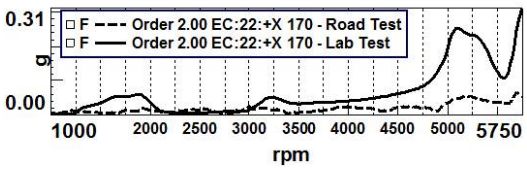


(b) y-direction

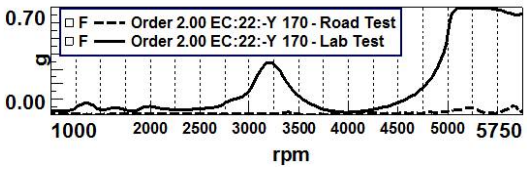


(c) z-direction

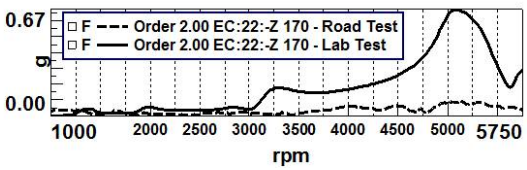
Figure 2.49. Road - laboratory test comparison, exhaust mount (FE41)-active side acceleration curves (2^{nd} order), L38



(a) x-direction

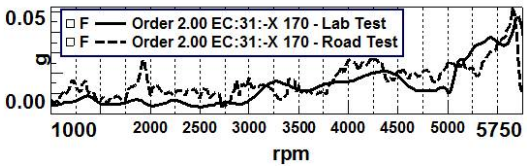


(b) y-direction

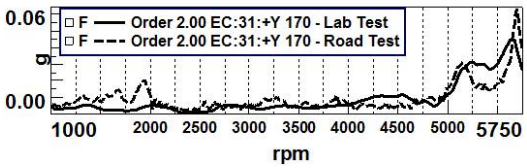


(c) z-direction

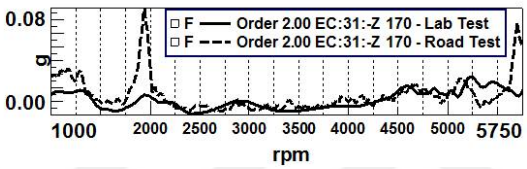
Figure 2.50. Road - laboratory test comparison, exhaust mount (EC22)-passive side acceleration curves (2^{nd} order), L38



(a) x-direction

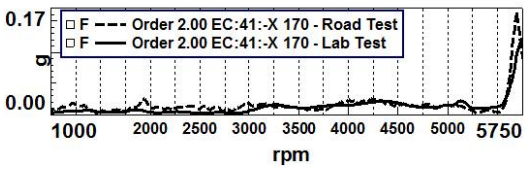


(b) y-direction

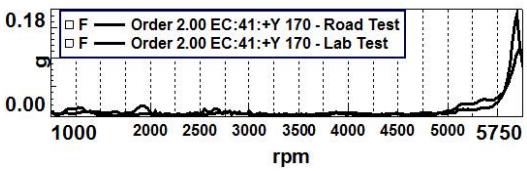


(c) z-direction

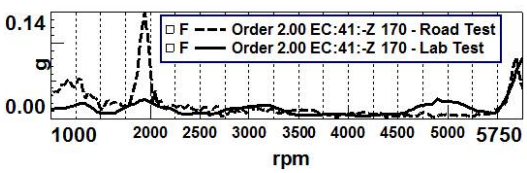
Figure 2.51. Road - laboratory test comparison, exhaust mount (EC31)-passive side acceleration curves (2^{nd} order), L38



(a) x-direction



(b) y-direction



(c) z-direction

Figure 2.52. Road - laboratory test comparison, exhaust mount (EC41)-passive side acceleration curves (2^{nd} order), L38

2.7. Diagnosis and Problem Definition

According to the road and laboratory tests (see Sections 2.5 and 2.6), the problem and probable solutions can be outlined as follows. The problem is *low frequency booming noise* and the problem frequency is in the structure-borne region. In this region, as shown in this particular application again, the dominant contributor is the second order of the engine [65]. Here, second order implies the second harmonic of crankshaft rotational frequency. At the booming region, sound pressure levels are nearly same (see Figures 2.36. and 2.38.), either for road, or laboratory test, which means that further experimental studies considering the stated booming problems may be performed in laboratory conditions.

It is a known fact [3, 5, 6] that booming noise is primarily designated by acoustic modes of the cavity and structural vibrations of body panels, which behave like loudspeakers. In this regard, it is indispensable to compute acoustic modes, and to perform panel measurements to understand, whether or not a cavity resonance problem is present. Alternatively, the problem may be caused by forced vibration response of the engine, rather than the cavity resonance.

For a general vibro-acoustics modeling, structural and acoustic modes of the structure should be known. These modes can be calculated using experimental and/or computational procedures. To assess contributions of engine mounts, frequency response functions have to be measured and evaluated e.g., using transfer path analysis (TPA) method. To evaluate disturbances of panels, surface normal velocities, namely mobility type frequency response functions should be known.

In Section 2.8, TPA results that identify critical paths and force terms are given. These results are important, since they orient the subsequent experimental and computational studies presented in forthcoming chapters.

2.8. Transfer Path Analysis

Transfer path analysis (TPA) describes a noise, or vibration response at a selected target, as a superposition of vectorial contributions from a defined set of force inputs that excite the structure through a chosen set of connections [66, 67]. To express the problem in this way gives an insight and a capability in the attenuation of response at the source and/or on the structure, using various techniques of active, or passive vibration control [35]. In the widespread practice, TPA is a two-step experimental procedure: first step is the identification of forces and the second one is to relate identified forces to target receivers through assumed paths. The first step, identification of forces, is mostly the main problem that affects results and developed solutions, accordingly. Operational forces that excite a structure are generated by a single coherent source, or multiple partially-correlated sources [68–70]. In the context of vehicle acoustics, typical examples for single and multiple coherent sources are engine and road inputs, respectively, where the former is addressed in this dissertation.

The method chosen to identify operational forces shapes the procedure of transfer path analysis. To measure operational forces directly is generally hard, since force transducers are required to be located between the structure and source, where vibration isolators or mounts are present. These non-linear isolators respond differently in the presence of transducers, since local stiffness changes significantly [71]. Direct force measurement often gives unreliable results [72]; instead, indirect force estimation techniques are widely used. Mount stiffness and matrix inversion methods are the tools in identifying operational forces [67, 72]. These indirect methods have their own advantages and drawbacks. Mount stiffness method requires precise mount data, which are seldom available, while matrix inversion method requires accelerance matrix data, which can be obtained by a troublesome and time consuming experimental campaign. Even mount data are available, non-linear characteristic of the material is an important drawback that causes variability [14], both in repeated measurements and between sound pressure levels of identical vehicles [73]. The matter in question with the matrix inversion method is the decoupling of source during frequency response function measurements. Removal of the source changes the dynamic behavior of the

passive part, which is expected to be different, while the system is operating [74]. Additionally, the system may not be linearized at chosen locations for artificial excitation, or linearity assumption may be held more reasonably at another location, other than the chosen one. Brandl et al. performed a sensitivity analysis to quantify measurement errors caused by deviations at excitation locations and directions [75]. Frequency response functions, which are used to populate the accelerance matrix, differ substantially according to the chosen location and the direction of applied force. Inversion of accelerance matrix further increases deviations, which results in poor outcomes. Even these problems are resolved; measurement of frequency response functions is prone to some other deficiencies in representing actual system characteristics. Ozgen et al. investigated variance and bias type errors in measured data of an aluminum beam [76]. They reveal that leakage in frequency response function measurements is responsible for unexpected results. Leakage in measurements is mainly the result of short time record and can be reduced using window functions [53]. All common data acquisition systems offer exponential windows to compensate for leakage. Unfortunately, once included in raw data, total elimination of leakage is not possible; moreover, windowing functions introduce artificial damping effects to processed data [77]. Schoukens et al. offered a Taylor series based method to reduce leakage in SISO systems [78]; in follow-up studies, leakage phenomenon is further discussed and extension of the method to MIMO systems is given [79, 80].

Above stated experimental difficulties and potential measurement errors of indirect force estimation techniques induce researchers to come up with more accurate and feasible methods. Operational transfer path analysis (OTPA), a one-step method, is presented as one of the promising alternatives. The method, based on transmissibility concept [81–83], does not require the removal of active part, e.g. engine. Since the method requires only operational data, it stands out rapidly for ease of use. Due to the direct and indirect application of transmissibility, two classes of OTPA are proposed. The former uses a transmissibility matrix instead of an accelerance matrix [84, 85], whereas the latter indirectly estimates an accelerance matrix by using measured transmissibilities [74]. Gajdatsy et al. assessed the applicability of OTPA methods in the sense of their limitations and associated errors. Effects of neglected

paths, cross-coupling in between passive side accelerations and orthogonality problems in estimated transmissibilities are pointed out [86]. OTPA methods are further studied to increase the accuracy of results [87]. Based on a parametric load modeling technique, a new TPA procedure [88] is also proposed, which needs extra measurements for the identification of operational forces. This method offers to combine the widely accepted accuracy of traditional TPA approaches with time efficiency of operational TPA methods.

Trade-offs between accuracy and time cost motivate researchers to develop several approaches. In pseudo force method [89,90], estimation of operational forces are based on transfer function measurements in combination with operational response measurements. However, the characterization of source is not completely independent of the passive part of an assembled structure and besides, to compare sets of pseudo forces, which are determined at different locations of the same source, or on another source, may lead into errors, although they might be equivalent. Power based methods are also proposed to characterize the structure borne noise [91,92]. Dynamic coupling between active and passive parts of the structure prevents source characterization based upon the transmitted power. Although it is possible to assume the passive part to be dynamically stable in certain cases, to generalize this assumption is not reasonable [93]. A blocking force approach, which isolates forces from the environment, is presented [94,95]. The need of specified test rigs for measurements is the main disadvantage of this approach. Global transfer direct transfer (GTDT) is one of the two-step path analysis methods, which does not require the knowledge of operational forces [96]. In the first step, direct transfer functions (DTFs) are calculated from measured GTDT functions, whereas in the second step, operational signal reconstruction is made by means of calculated DTFs. In an analytical study, the path blocking GTDT method and traditional TPA procedure are discussed and their prediction capabilities are assessed [97]. Recently, an experimental work on a simple mechanical setup is first time presented [98], where GTDT method is adopted. Although, in conclusion it is said that the method can be applied to a more complex structure like a vehicle, a generic application will not be so straightforward. First, to model engine mounts as linear springs is not realistic; second, without removing the active part, it is often impossible

to access excitation locations.

Advances in testing and measurement technologies provide new solution approaches for TPA. Using PU (pressure-velocity) probes, both sound pressure and particle velocity can be simultaneously acquired [99]. Particle velocity based methods are efficiently used for airborne TPA studies [100, 101]. Since the lower limit for measurements is around 200 Hz, it is not possible to use the method for structure borne TPA, at least for now. Unlike for airborne sources, there are no widely applicable methods yet available for independent characterization of structure borne sound sources. As mentioned, blocked force method that characterizes the source independently is not practical, since it requires a tailored test rig. An in situ measurement method that identifies the blocked force, without decouple the source, is proposed by Moorhouse et al [102]. Blocked forces, or independent characterization of a source are vital in prediction of the vibration transmission on a different receiver. In the case of inverse force estimation techniques that are used as the first step of traditional TPA, identified forces can only be used for a specific source-receiver assembly. In situ measurement of blocked force technique is tested to characterize structure borne road noise of a vehicle. The results of proposed technique are compared to ones achieved from traditional TPA. Elliott et al. [103] reported that, compared results are acceptably similar; moreover, their method has an important advantage in terms of reduced test time. However, in situ measurement technique gives no information about mounts, which are obviously important in any source-path-receiver type problem. Mounts play a substantial role in the refinement of structure borne noise problems in vehicles and other machinery. Yet another possible problem for an engine TPA type application is that measured passive side accelerations can contain extra inputs, which come from either road, or other auxiliary components. In a recent paper, Sottek et al. [104] offer another in situ measurement approach, which uses active side acceleration data and matrix inversion method together, to compute so called effective mount transfer functions. Unlike the former, this approach gives information about mount data, which can be used in a refinement study. Nevertheless, an important advantage of former method is lost, i.e. force data are dependent to specific case studied. To eliminate the disadvantage, Kelvin-Voigt type parameterization for mounts is offered. For many applications, es-

pecially for hydro and/or complex shaped mounts, assumptions of this modeling are not suitable. What is more, if the active part is not removed, as suggested by the method [104], it is hardly possible to access mounts for hammer impacts.

As the above discussion shows, current practice and new approaches have their own advantages and drawbacks, which force researchers to consider trade-offs, especially between accuracy and time cost, while making decisions. In what follows, current practice is briefly discussed and applicability of methods are also investigated, where the engine induced structure borne noise of vehicles L84 and L38 is studied. Methods are classified into two groups: force and transmissibility methods; first one (see Section 2.8.1) requires the knowledge of identified operational force vector and second one (see Section 2.8.2) uses transmissibility relationships to compute a target response.

2.8.1. Force Methods

Consider an assembled structure as sketched in Figure 2.53., which comprises active (source) and passive (receiver) substructures, linked by mount(s). According to TPA approach, a response ($\mathbf{y}$) at a selected target (i) can be computed as a linear superposition of separate vectorial contributions ($\mathbf{N_{ij}}$) from a defined set of force inputs ($\mathbf{f}$) entering to the structure over a known set of connections (j), as stated in Equation (2.18). Here, $\mathbf{N_{ij}}$ matrix is populated with noise transfer functions (a.k.a. propagation FRFs or vibro-acoustic transfer functions) that are estimated between a target location (i) and an excitation location (j). To solve Equation (2.18), matrix of noise transfer functions ($\mathbf{N_{ij}}$) and vector of operational forces ($\mathbf{f_j}$) have to be estimated.

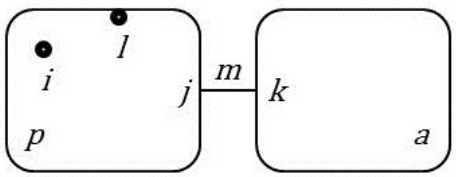


Figure 2.53. An assembled structure, where a and p denote the active (source) and passive (receiver) parts, respectively; m is a mount that links two substructures; j and k are passive and active side interfaces, respectively; i is a response point of interest; l is an extra measurement location.

$$\mathbf{y_i} = \mathbf{N_{ij}}\mathbf{f_j} \tag{2.18}$$

Estimation of noise transfer functions (NTFs) can be achieved directly, or reciprocally, on the account of linearity assumption, if it holds in the frequency bandwidth of interest. As it will be seen in Section 2.8.3, for some of the methods like in situ blocked force and OPAX, to use reciprocal measurements is a necessity rather than a preference, since they recommend not removing the source. NTFs can be measured directly, by exciting the body side of mounts, where operational forces enter to the structure, and by acquiring the response at the target receiver. As the name suggests, in reciprocal measurement, response data are acquired at mount locations, while the excitation is performed at the target location, using a low frequency volume source. The point is that results obtained using these two techniques do not often correlate well. In such a situation, one cannot intuitively find out which one is more reliable. Coster et al. [105] compared the two techniques and investigated the accuracy of them through a sensitivity analysis. Comparisons show that there are considerable differences in between two, which can affect results, and the low frequency bandwidth also gets its share. Note that, the source is removed in the direct measurement, while it is present in the reciprocal one. This incompatible change in boundary conditions may alter the dynamic properties of the system.

Advances in instrumentation technology give researchers an opportunity to measure operational forces ($\mathbf{f_j}$) directly, using thin, multi-axis sensors. These sensors are located between mounts and the structure, mostly using a tailored apparatus. To render a measurement possible, original mount bolts and required torque values have to be changed and what is more, prestress values and local stiffness deviate, which result in poor outcomes. Hence, instead of a direct measurement, operational forces are often estimated using following techniques.

Mount stiffness method requires the knowledge of complex dynamic stiffness of mounts, which can be measured using multi-axial test rigs. Mount data exhibit different characteristics, depending on static pre-load, frequency, temperature and up to some extent, on vibration amplitude [106]. Non-linear characteristics of data and variances among test specimens make this method impractical and confronting with linearity assumption of TPA methods. Estimation of operational forces using mount stiffness method is formulated in Equation (2.19), where $\mathbf{K_m}$ is the complex dynamic stiffness matrix of mount m; $\ddot{\mathbf{x}}_\mathbf{k}$ and $\ddot{\mathbf{x}}_\mathbf{j}$ are active and passive side acceleration vectors, respectively, which have to be measured, when the system is operating. Even mount data are reliable, identified forces contain some other information that is hard to decouple: measured acceleration vectors are also disturbed by road noise and other auxiliary components. Nevertheless, this approach is useful, especially in optimization studies of mounts, where $\mathbf{K_m}$ matrix is optimized subjective to a target response.

$$\mathbf{f_j} = \mathbf{K_m} \frac{\ddot{\mathbf{x}}_\mathbf{k} - \ddot{\mathbf{x}}_\mathbf{j}}{-\omega^2} \tag{2.19}$$

Matrix inversion method identifies operational forces using the passive side acceleration vector ($\ddot{\mathbf{x}}_\mathbf{j}$), as stated in Equation (2.20), where ($\mathbf{H}^+_\mathbf{mj}$) denotes the pseudo inverse of the accelerance matrix. Accelerance matrix ($\mathbf{H_{mj}}$) is populated with FRFs, which characterize modal properties of mount interfaces, measured when the source is decoupled. However, removal of source may change dynamic characteristics of the assembled structure, which result in deceptive information in measurements. Hammer tests that are achieved to measure complex FRFs, introduce leakage and unsubstantial damping effects, beside probable impact location and direction errors. What is more, measured FRFs contain data of same resonances, which are mathematically hard to decouple. For this reason, inversion operation of accelerance matrix may give wrong results, where condition number of inverted matrix gains considerably high values, especially at resonance frequencies.

$$\mathbf{f_j} = \mathbf{H}^+_\mathbf{mj} \ddot{\mathbf{x}}_\mathbf{j} \tag{2.20}$$

In decoupled passive substructure (p), hammer excitation at a mount location ($j = 1$) causes responses at other mount locations ($j = 2, 3, ..$), as well. Resulting FRFs are off-diagonal terms of $\mathbf{H_{mj}}$ matrix. One can assume that more FRF data mean more noise and error in the measurements. From this point of view, a diagonal version of matrix inversion method can also be used, which counts only on diagonal terms of $\mathbf{H_{mj}}$ matrix. This method can be formulated as follows.

$$\mathbf{f_j} = diag(\mathbf{H_{mj}^{+}})\ddot{\mathbf{x}}_\mathbf{j} \tag{2.21}$$

Pseudo force method [89, 90] is a variant of matrix inversion technique, where equivalent forces are identified instead of actual operating ones. Estimated pseudo forces are independent of the receiver structure, which means that they are theoretically valid even the source is mounted on a different structure other than used. Excitation locations can be chosen arbitrarily (not necessarily on mount interfaces), unlike the matrix inversion method. Non-uniqueness of pseudo forces is one of the important drawbacks. Moreover, as proposed by the method, to operate the source in a freely suspended state is hard if not unfeasible for some applications, like an engine of a vehicle.

$$\mathbf{f_{bl}} = \tilde{\mathbf{H}}_\mathbf{mj}^{+}\ddot{\mathbf{x}}_\mathbf{j} \tag{2.22}$$

Operational force vectors in Equations (2.20) and (2.21) are dependent on the dynamic properties of uncoupled receiver substructure. Notice that, this dependence is due to the accelerance matrix ($\mathbf{H_{mj}}$), which is constructed by measured FRFs, when the source is removed. If blocked forces can be estimated instead of them, then it is possible to characterize a vibration source independently. Special test rigs [95] render measurement of blocked forces possible, although this cannot be achieved ideally. In that case, Equation (2.18) can be used for different assemblies, on which the same source is mounted. Instead of a direct measurement, blocked forces can be estimated using an in situ method, i.e. without removing the source, as stated in Equation (2.22), where $\tilde{\mathbf{H}}_\mathbf{mj}^{+}$ denotes the pseudo inverse of accelerance matrix in the coupled state [102]. The matter in question with this approach is accessibility to excitation locations. As suggested by Moorhouse et al., it is also possible to identify the blocked force vector using the

operational acceleration of an extra measurement point (l) on the receiver substructure and by relating it to the passive side of mount (j). To define additional measurement points ($l = 1, 2, ..n$) is recommended, which can be used for over determination of the matrix ($\tilde{\mathbf{H}}_{\mathbf{jl}}$) to be inverted. To overcome the accessibility problem, reciprocity principle can be used and $\tilde{\mathbf{H}}_{\mathbf{jl}}$ is measured instead of $\tilde{\mathbf{H}}_{\mathbf{lj}}$, as stated in Equation (2.23), provided that the linearity assumption holds.

$$\mathbf{f_{bl}} = \tilde{\mathbf{H}}^{+}_{\mathbf{jl}} \ddot{\mathbf{x}}_{\mathbf{l}} \tag{2.23}$$

An alternative TPA approach, which proposes to identify operational forces by using parametric load models, is coined as OPAX [87,88]. The method tends to preserve the traditional TPA approach due to its widely accepted outcomes, while working out a solution for the time consuming FRF measurement step. The model essentially uses operational data, which have to be already measured for all TPA approaches. Additionally, instead of a full FRF measurement step, a limited number of FRFs are measured to be used in the construction of a parametric load model for the identification of operational forces, as offered in Equation (2.24). This scalable approach gives a chance for making trade-offs between accuracy and time cost, such that one can make decisions about the number of FRF measurements. In referred publications, it is recommended to increase number of FRF measurements and processed orders for a more accurate model. Note that, in comparison with traditional TPA, although time cost is considerably reduced, computational cost is significantly increased.

$$\mathbf{f_j} = f(\text{parameters}, \ddot{\mathbf{x}}_{\mathbf{k}}, \ddot{\mathbf{x}}_{\mathbf{j}}) \tag{2.24}$$

Accelerance matrix renders the identification of operational forces possible, by relating artificial excitations (e.g. a roving hammer) with measured operational passive side acceleration vector. Accelerance matrix consists of measured FRFs that characterize the receiver substructure. Actually, measured FRFs are estimated using H_1, H_2, or H_v algorithm, as formulated in Equations (2.25) to (2.27), where G_{jj} and G_{mm} denote one-sided auto spectral density functions of input and output, respectively; G_{mj} and G_{jm} denote one-sided cross spectral density functions, recorded during experimentation.

To access measurement locations and to prevent cross coupling of inputs, the active substructure (source) is necessarily removed. To minimize bias errors, measurements are achieved by using a shaker rather than a roving hammer, provided that the geometry of structure to be tested is convenient.

$$H_{1,mj} = \frac{G_{mj}}{G_{jj}} \tag{2.25}$$

$$H_{2,mj} = \frac{G_{mm}}{G_{jm}} \tag{2.26}$$

$$H_{v,mj} = \begin{bmatrix} G_{jj} & G_{mj} \\ G_{mj} & G_{mm} \end{bmatrix} \tag{2.27}$$

2.8.2. Transmissibility Methods

Yet another possibility is to accommodate MIMO transmissibility approach to TPA. Although, in principle transmissibility is a response-to-response relationship and different from force-to-response functions, both in terms of outcomes and their physical meanings, some proposals are available, which enable to get TPA like results, without removing the source. In what follows, different transmissibility based TPA approaches are formulated with a consideration on their applicability, using the thus far notation. One of them is OTPA method, which claims that there is no need to remove the source to predict a target response. Equations (2.18) and (2.20) can be rearranged as given in Equation (2.28), which defines a unique transmissibility matrix $\mathbf{T_{ij}}$, provided that $m = j$, $\mathbf{H_{mj}}$ is square and invertible. In that case, $\mathbf{N_{ij}}$ and $\mathbf{H_{mj}}$ matrices are replaced by $\mathbf{T_{ij}}$, which stands for transmissibility matrix, where entries can readily be estimated from an operational measurement, using one-sided auto and cross spectral density functions as stated in Equation (2.29). This formulation corresponds to an H_1 estimator, while H_2 or H_s estimators can also be used for construction of the

transmissibility matrix, as shown by Leclère et al [107]. That is to say, entries of NTF and accelerance matrices are FRFs, which are estimated using one of the H_1, H_2 and H_v algorithms, so why to remove the source? The point is that a response-to-response relationship is not causal, and has peaks at frequencies corresponding to zeros of one of the considered response, while force-to-response functions have peaks at the resonances of the structure. Hence, although they may give similar results in some cases, care must be taken and appropriacy of assumptions must be investigated for any particular application.

$$\mathbf{y_i} = \mathbf{N_{ij}}\mathbf{H^{+}_{mj}}\ddot{\mathbf{x}}_\mathbf{j} = \mathbf{T_{ij}}\ddot{\mathbf{x}}_\mathbf{j} \tag{2.28}$$

$$\mathbf{T_{ij}} = \mathbf{G_{ij}}\mathbf{G^{+}_{jj}} \tag{2.29}$$

Another transmissibility based approach is the GTDT method, which prescribes that force-to-response functions can be estimated from response-to-response functions, i.e. measured transmissibilities. Equation (2.30) states that response at i is the summation of blocked transmissibilities ($\hat{\mathbf{T}}_\mathbf{ij}$ and $\hat{\mathbf{T}}_\mathbf{ii}$), provided that $i \neq j$. Somehow, if all other paths can be blocked, the response at i would be equal to $\hat{\mathbf{T}}_\mathbf{ij}$, when the system is excited only at j. Following the same approach, if the system is excited only at i, $\hat{\mathbf{T}}_\mathbf{ii}$ would be the response at i, provided that all other responses of the system are blocked. To block a system physically hard, if not impossible and often may result in uncontrollable changes in the dynamic behavior of the system. Instead, GTDT method offers to estimate blocked transmissibilities from measured ones (see e.g. [97, 98]), using operational accelerations at j. However, the procedure requires a hammer test step, which cast doubt on any particular application. In other words, although the applicability of method is proven by another study [108], it may not be feasible for some applications, e.g. an engine induced structure borne noise of a vehicle, where access to interface is almost impossible without removing the source.

$$\mathbf{y_i} = \hat{\mathbf{T}}_\mathbf{ij}\mathbf{y_j} + \hat{\mathbf{T}}_\mathbf{ii}\mathbf{y_i} \tag{2.30}$$

2.8.3. Applicability of Methods

Here, applicability of above stated methods with respect to the defined problem (see Section 2.7) are given. Sources of errors, feasibility problems and resulting trade-offs are stated. Sources of errors force and motivate researchers to develop new techniques. Eventually, some of the trade-offs are caused by these errors, which are itemized as the following:

(i) Non-linear characteristics of mounts

Non-linearity of mounts is important in three ways; first, one of the TPA techniques, mount stiffness method uses mount data; second, in refinement studies mounts are one of the important targets; lastly, variability among measurements mostly introduced by mounts.

(ii) Removal of the source

Methods like matrix inversion require the removal of source, which changes boundary conditions.

(iii) Hammer excitation

Most of the TPA methods require hammer excitation to measure FRFs. Direction and location of applied force change the estimated FRFs. Among bias and variance type errors, leakage is the most important one. Force and exponential windows used as countermeasures introduce artificial damping effects to the estimated FRFs.

(iv) Inversion of an ill-conditioned matrix

Most of the TPA approaches require matrix inversion steps. Beside orthogonality, noise and artificial damping effects gain considerably high values during inversion process. To check the condition number is ever effective for orthogonality problem, but not enough for other effects.

(v) Effect of neglected paths

In TPA methods, paths are user defined. The point is that it is vital to reveal the effects of neglected paths, where it is not possible in some approaches such as OTPA.

(vi) Cross-coupling of inputs

Operational accelerations measured on the body side of a mount do not depend only on the force acting at this location, other forces acting on other mounts also made contributions. This is called cross-coupling of inputs, which cannot be neglected without computed.

(vii) Non-linearity of the system

The foremost assumption of TPA methods is the linearity, although it is not valid in real life structures, especially for complicated ones.

(viii) Contaminated information in acceleration signals

Beside noise, data coming from road and auxiliary components contaminate operational accelerations measured.

On the other hand, measurements are also restricted by some physical obstacles, which can be classified as feasibility problems that are itemized below:

(i) Access to excitation locations

Today, engines of vehicles are installed such that without partially, or in some cases completely removing the engine, even to locate sensors for an operational measurement is hard if not impossible. Some proposed methods cannot be applied, since excitation locations are inaccessible.

(ii) Space problem for a shaker

Almost all aforementioned problems associated with external excitation are eliminated, provided that a shaker is used instead of a hammer. Unfortunately, the irregular shape of automobile structures does not provide enough space for a shaker setup, especially to achieve excitations in x- and y-directions.

Sources of errors and feasibility problems cause the following trade-offs:

(i) If the source is removed, boundary conditions change and time cost increases. On the other hand, if the source is not removed, cross-coupling of inputs affects results. Response-to-response functions are used instead of force-to-response functions, e.g. for an OTPA work. To access excitation locations may not be possible,

e.g. for GTDT and in situ blocked force methods. Computational cost increases substantially and NTFs are needed to be measured reciprocally.

(ii) In cases, where a hammer is used for excitation, leakage affects results considerably, provided that force and exponential windows are not used. However, if these windowing functions are used, artificial damping effects are introduced to the measured responses.

Table 2.4. Summary of TPA methods for an engine induced low frequency noise of an automobile, where the symbols, $\surd$, $\times$ and n/a means yes, no and not applicable, respectively.

Method	Applicability	Source removal	Independent source	Time cost	Post process
BF	hard	$\surd$	$\surd$	very high	moderate
DMI	moderate	$\surd$	$\times$	high	moderate
GTDT	n/a	$\times$	$\times$	moderate	moderate
In situ BF	n/a	$\times$	$\surd$	high	moderate
MI	moderate	$\surd$	$\times$	high	moderate
Mount stiffness	easy	$\times$	$\times$	moderate	low
OPAX	moderate	$\times$	$\times$	moderate	high
OTPA	easy	$\times$	$\times$	low	high
Pseudo force	hard	$\surd$	$\surd$	high	high
Proposed method	moderate	$\surd$	$\times$	high	high

2.8.4. The Results of Transfer Path Analysis

Since excitation locations are inaccessible, GTDT and in situ blocked force methods are not applicable for the cases studied. Blocked force (BF) method and pseudo force methods require special test rigs and equipments. These methods are not so feasible for this particular problem, although they can be applied. Results obtained using OTPA method are not given here, but successful applications are reported in the literature. For OTPA method, post processing steps have a vital importance in

the sense of accuracy (see e.g. Refs. [109, 110] for a detailed framework). Likewise, OPAX results are not reported here, since outcomes change depending on the number and locations of defined extra measurement points (the number is 2 for this work). Additionally, in the post processing step, parameters used in identifying forces are obviously user defined. Hence, using the same data it is possible to get different outcomes in post processing steps. This situation can be assessed as another trade-off. In other words, the time gained in the experimental work can be spent out for complicated post processing steps. In what follows, an overview of results of calculations carried out for mount stiffness, matrix inversion (MI) and diagonal matrix inversion (DMI) methods are given, where they are compared with actual measurements. Next, derived results and contributions of defined paths are presented in detail for both of test vehicles (see Sections 2.8.4.2 and 2.8.4.3).

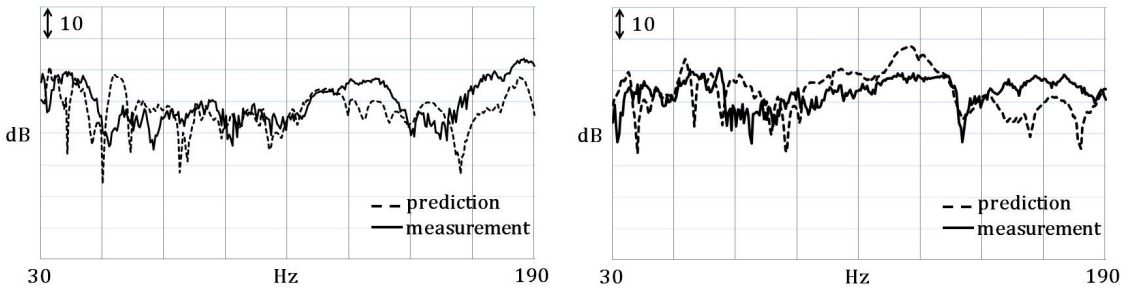
2.8.4.1. Overview. Employing mount stiffness method, operational forces are evaluated using Equation (2.19). To measure NTFs of Equation (2.18) directly, the engine of the vehicle is removed (see Figure 2.54.), since to access mount locations is impossible for the case studied. Available frequency dependent complex dynamic stiffness matrix data are put into calculation. Prediction and measurement results for the target microphone locations are given in Figure 2.55.



(a) Preparation (b) Operation

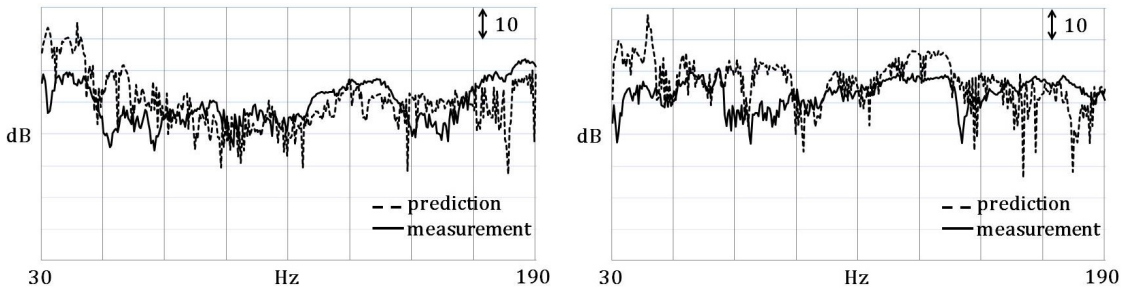
Figure 2.54. Removal of the engine, Vehicle L38

Matrix inversion method requires removal of source to achieve both FRF and NTF measurements. In these measurements, a roving hammer with an appropriate tip for low frequency applications is used and average of 10 impacts are put into calculation in Equation (2.20), where H_v estimator defined in Equation (2.27) is adopted due to its nearly perfect (above 0.95) ordinary coherence curves. Nevertheless, ordinary coherence values do not guarantee that measurements are free of errors, like leakage and artificial damping effects. Although an electromagnetic shaker would provide more accurate FRF estimates, as recommended in e.g. Ref. [76], the test structure is not appropriate for this type exciter due to lack of enough space. After inverting the accelerance matrix as formulated in Equation (2.20), condition number of matrix is also monitored. It reads values well below 100, in the corresponding frequency range of interest. Same data are also employed in the diagonal version of matrix inversion method to investigate whether if less data mean less measurement error, or not. The results of matrix inversion and diagonal matrix inversion methods are given in Figures 2.56. and 2.57., respectively. Observing these results, one can conclude that measurement errors are not less important than the effect of cross talk of mounts i.e., off-diagonal terms of $\mathbf{H_{ij}}$ matrix. *Prediction results presented in Figures 2.55. to 2.57. are calculated, using an in-house Matlab code.*



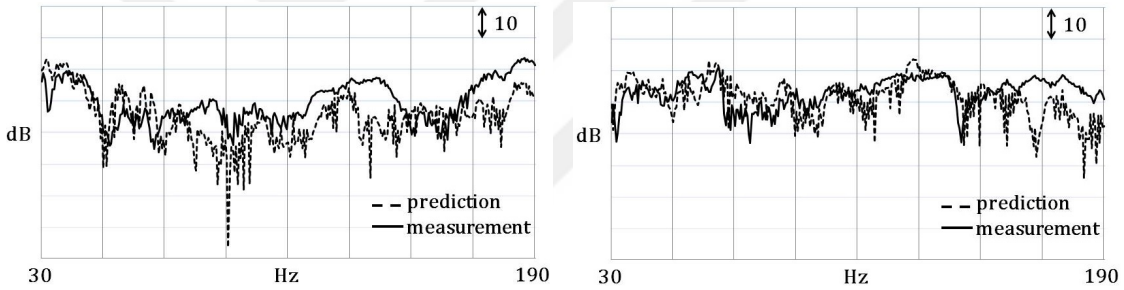
(a) BT :D (b) BT: K

Figure 2.55. Comparison of predicted and measured SPL curves using mount stiffness method, Vehicle L38. L_2 norm of difference (a) 9.317 dB, (b) 9.782 dB.



(a) BT :D (b) BT: K

Figure 2.56. Comparison of predicted and measured SPL curves using matrix inversion method, Vehicle L38. L_2 norm of difference (a) 10.523 dB, (b) 11.277 dB.



(a) BT :D (b) BT: K

Figure 2.57. Comparison of predicted and measured SPL curves using diagonal matrix inversion method, Vehicle L38. L_2 norm of difference (a) 9.006 dB, (b) 7.402 dB.

2.8.4.2. Detailed Results for the Vehicle L84. Measurements on the vehicle L84 are performed on 3 engine mounts in 3 translational directions through 2 targets, which populate 81 FRFs. Here, a roving hammer is used for impacts, i.e. a normalized unit impulse force is applied at the body side of engine mounts, as close as possible to the accelerometer locations. The vector of order tracked operational accelerations at the body side is readily available from either the road or the laboratory mock up test. For Vehicle L84 case, Equation (2.20) can be written more explicitly, as

$$\begin{Bmatrix} f_1 \\ \vdots \\ f_9 \end{Bmatrix}_{(9x1)} = \begin{bmatrix} \ddot{X}_1/F_1 & \cdots & \ddot{X}_1/F_9 \\ \vdots & \ddots & \vdots \\ \ddot{X}_9/F_1 & \cdots & \ddot{X}_9/F_9 \end{bmatrix}^{+}_{(9x9)} \begin{Bmatrix} \ddot{x}_1 \\ \vdots \\ \ddot{x}_9 \end{Bmatrix}_{(9x1)} \tag{2.31}$$

The accelerance ($\ddot{X}_M/F_N$) FRFs of L84 are given with the driving point coherence function plots in Figures 2.58. and 2.59., respectively. Knowing operational forces one can calculate resulting SPLs at the targets for all frequencies, providing that the coherence function for the measurement is in between 0.9 and 1, which indicates that the linear assumption of TPA is valid at the frequency band of point of interest. The calculation can be done using Equation (2.18), which can be written explicitly, as

$$\begin{Bmatrix} p_{(BT:D)} \\ p_{(BT:K)} \end{Bmatrix}_{(2x1)} = \begin{bmatrix} p_{(BT:D)}/F_1 & \cdots & p_{(BT:D)}/F_9 \\ p_{(BT:K)}/F_1 & \cdots & p_{(BT:K)}/F_9 \end{bmatrix}_{(2x9)} \begin{Bmatrix} f_1 \\ \vdots \\ f_9 \end{Bmatrix}_{(9x1)} \tag{2.32}$$

As seen in Figure 2.60., measured and calculated SPLs curves take different values at some intervals. Reasons are as follows: (i) only 9 structural paths are measured; although they are thought to be dominant, other paths like exhaust mounts also make some contributions to the calculated SPL, (ii) in some intervals, coherence problems exist and measured FRFs are too noisy, and (iii) only the translational paths are measured.

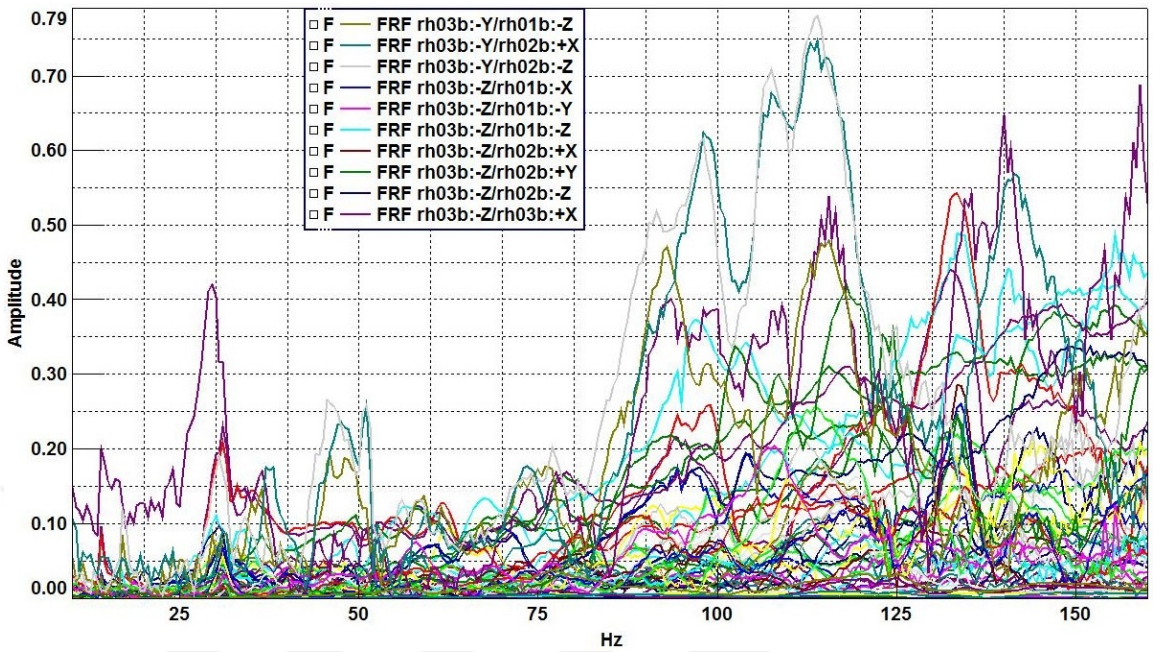


Figure 2.58. Accelerance FRFs (1/8 is shown in the legend)

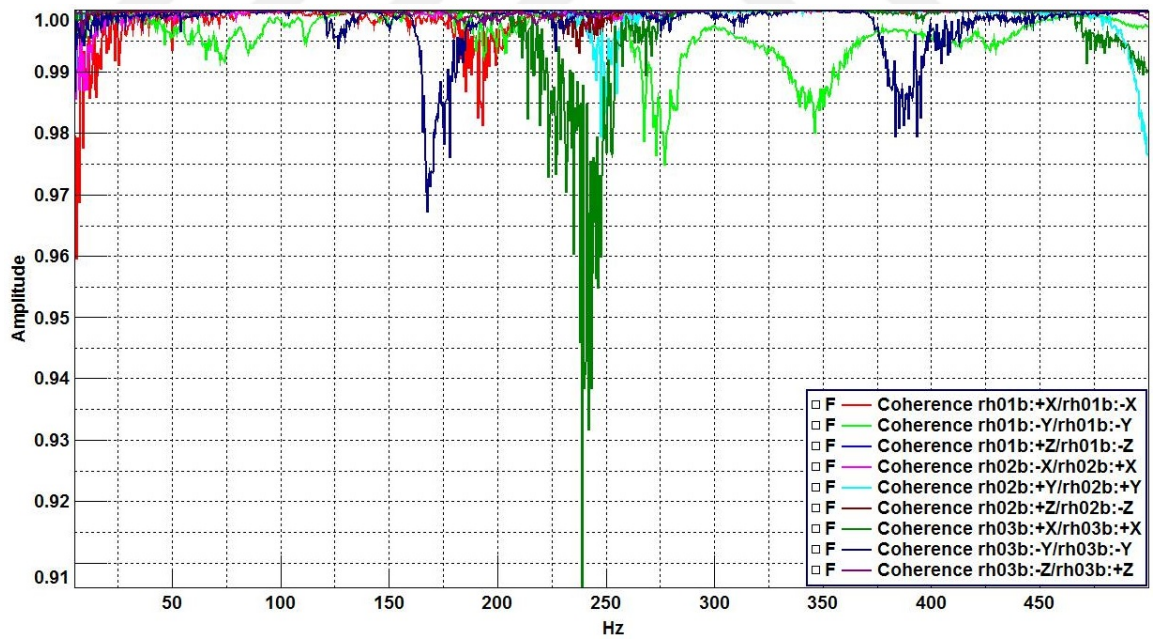


Figure 2.59. Coherence plots of the driving points (1/8 is shown in the legend)

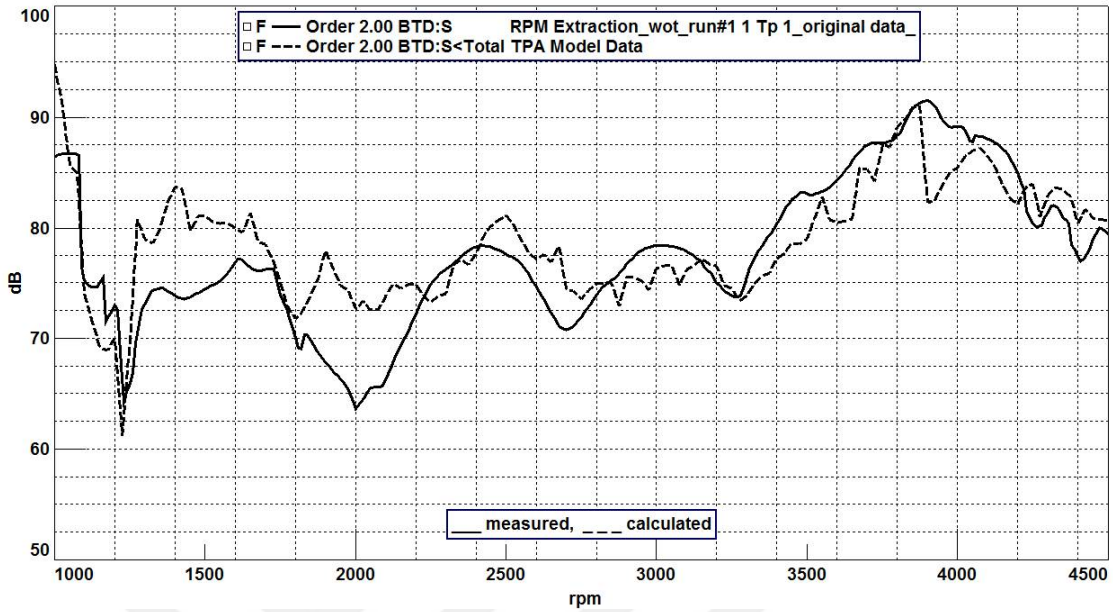


Figure 2.60. Measured and calculated SPLs at target BT:D

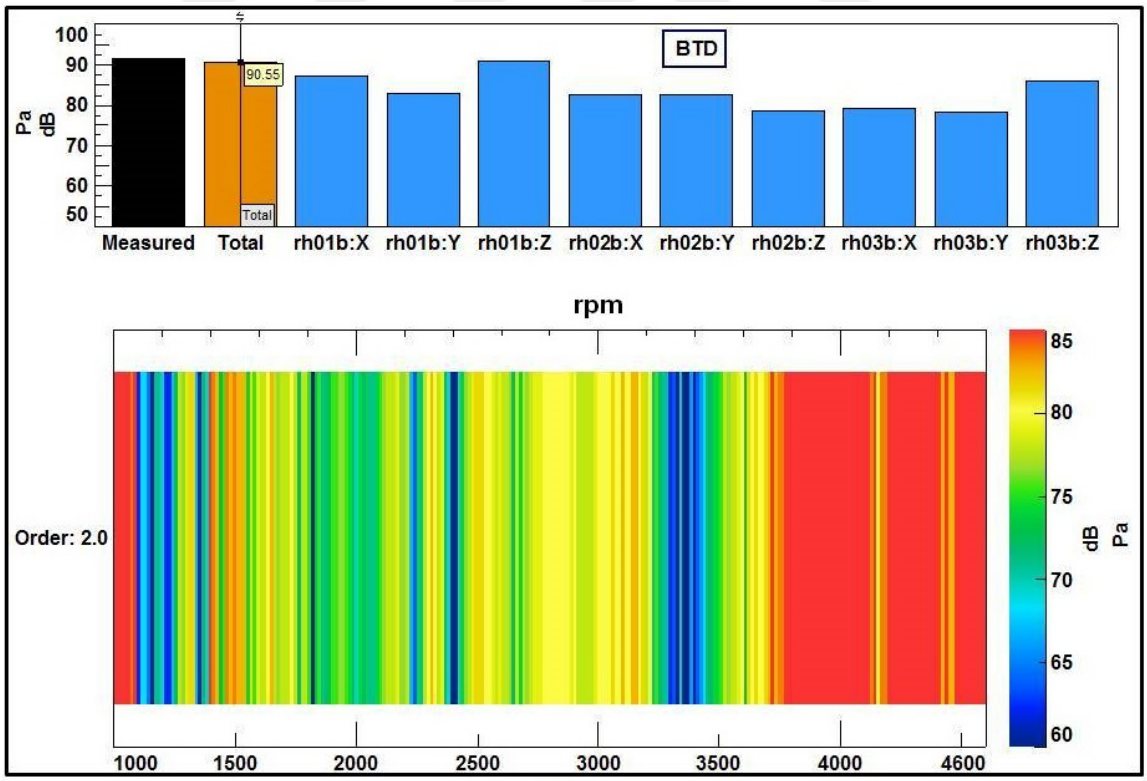


Figure 2.61. Measured TPA result, SPLs at target BT:D

As can be observed from the Figure 2.61. measured and calculated SPL terms quantitatively similar. Notice that, the black block indicates the measured value, whereas the orange one indicates the total calculated SPL term of the individual contributors, i.e. blue blocks. The engine of the test vehicle is hanged on RH:01 and RH:02, and there is no static loading on RH:03 at the z-direction, but since only translational paths are measured, the y-moment on that mount is added up to the RH:03:Z path.

The booming noise region is clearly seen in Figure 2.62. The main contributor is RH:01. The high SPL value observed before 1000 rpm is due to the start of engine. It is appeared exactly at 27 Hz, which indicates that *idle booming* also exists.

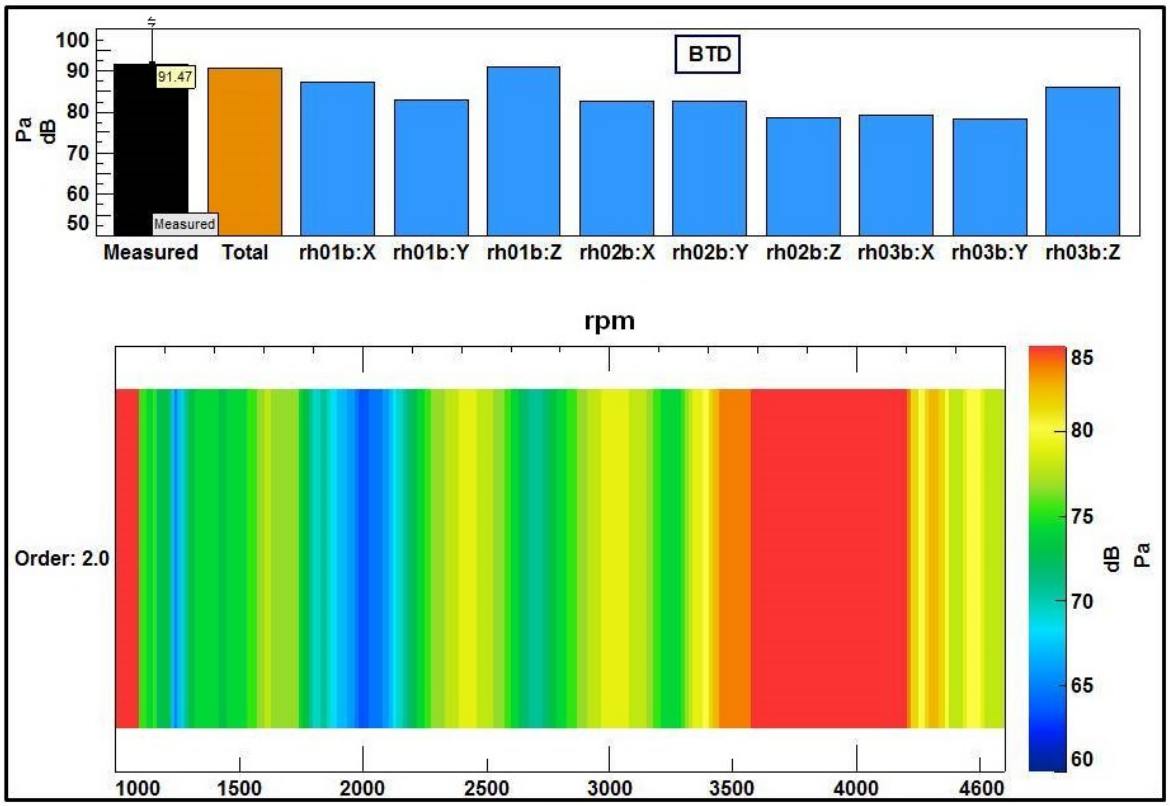


Figure 2.62. Calculated TPA result, SPLs at target BT:D

Note that, measured and calculated data exhibit some differences due to unmeasured paths, or nonlinearities. Therefore, interpretation of the results is not a straightforward task and requires a careful study on the model. Here, two important issues will be highlighted: (i) the condition number, and (ii) the problem oriented interpretation of

the results. Condition number is defined as the ratio of largest singular value of a matrix to the smallest one. For this system, there exist 81 accelerance FRFs, which belong to the same structure. This situation generally results in an ill-condition matrix, because measured FRFs contain data of same resonances. Putting a relative threshold is said to be a good solution, since mostly the singular values in the areas of resonance are taken away. It should be noticed that all operations to improve the condition number of a matrix cause the loss of information up to some extent, as well. In Figure 2.63. an improvement in the condition number of the 'FRFs to indicators' matrix is shown. This improvement is achieved by putting a relative threshold of 0.5 percent. In Figure 2.63 (a) the effects of various threshold values on the calculated sound pressure levels are shown. Contributions of other paths are ranked in Figure 2.64. The problem oriented interpretation of the results is critical; such that, if the whole bandwidth is considered, Figure 2.64. would be an answer for the problem. For the sake of clarity, recognize that in Figure 2.64., there exists an idle booming around 1000 rpm. What will happen if it is truncated? The answer is in Figure 2.65.: the ranking of the mounts is changed. It is observed that in the problem frequency interval, main contributors are RH:03:Z, RH:03:X and RH:01:Z. If one focus the 3000-4200 rpm interval, the ranking is not changing anymore (see Figure 2.66.).

As can be clearly seen in Figures 2.67. and 2.68., it is identified that the booming problem is mainly related to the RH03:Z and RH:03:X paths. Since it gives an insight and ability of ranking the engine mounts, this information is important on its own.

The dominant paths for the other target (BT:K) are stated and interpreted below:

(i) As shown in Figure 2.69. the booming problem that is observed at the target BT:D is also valid for the target BT:K and what is worse: in a larger band.
(ii) There exists a second booming, which has a peak around 2500 rpm.
(iii) As can be observed in Figure 2.70., main paths are RH:03:Z, RH:01:X and RH:03:X.
(iv) To check the problem frequency, again the interval is narrowed down in Figure 2.71.: the ranking is the same.

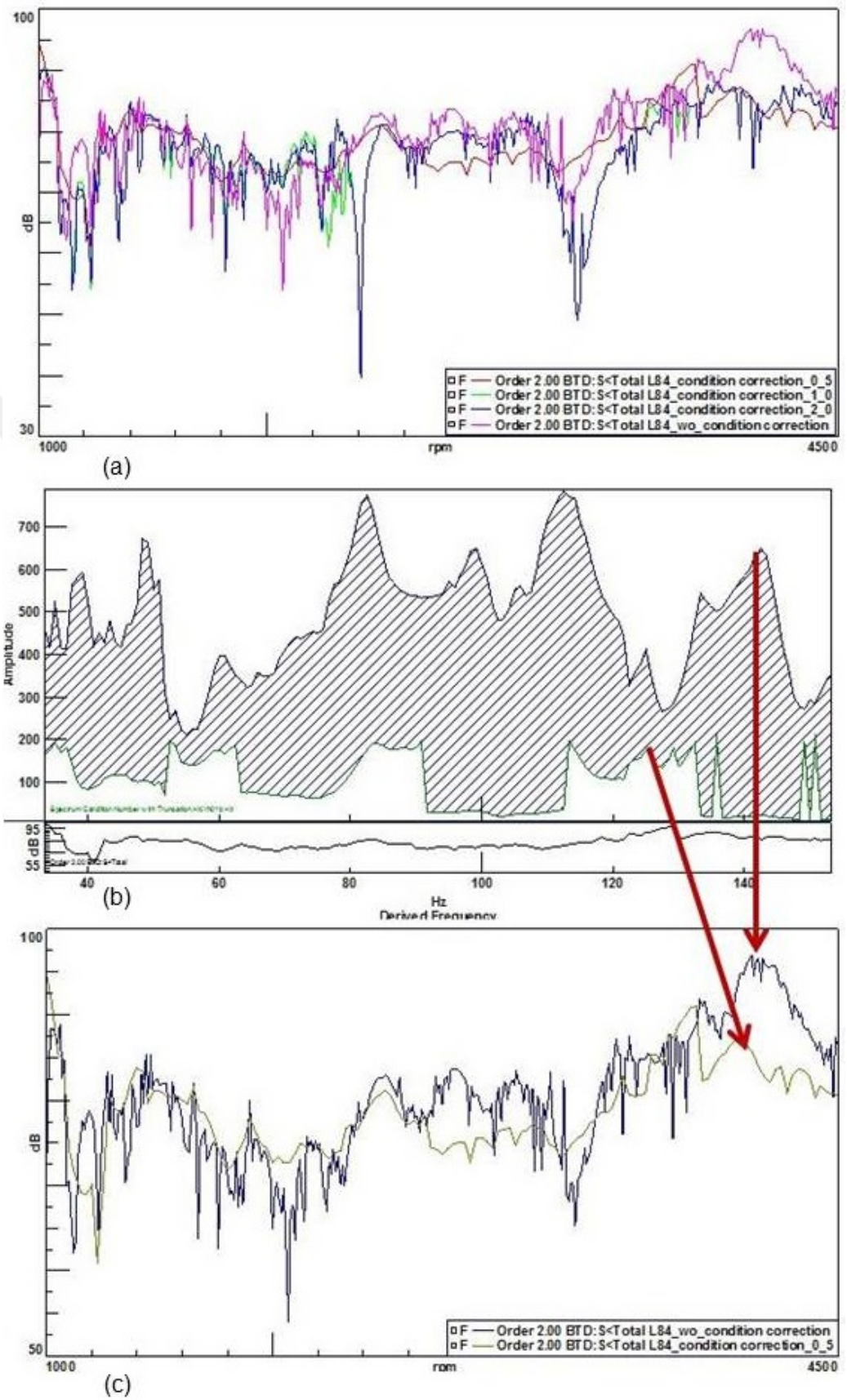


Figure 2.63. Improvement in the condition number: (a) condition number study, (b) achieved correction, (c) the resulting outcome.

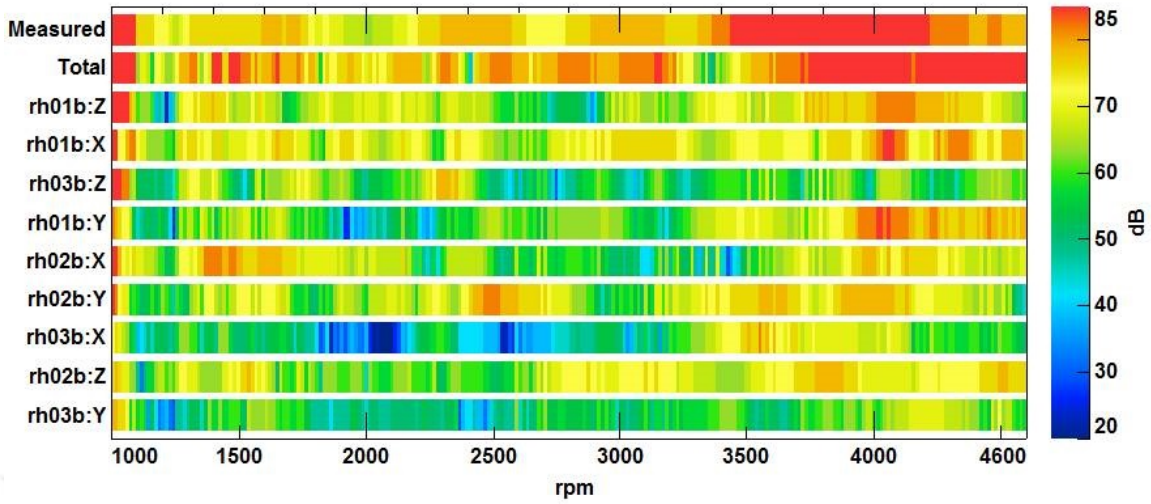


Figure 2.64. Contributions of all paths (1000-4600 rpm), BT:D

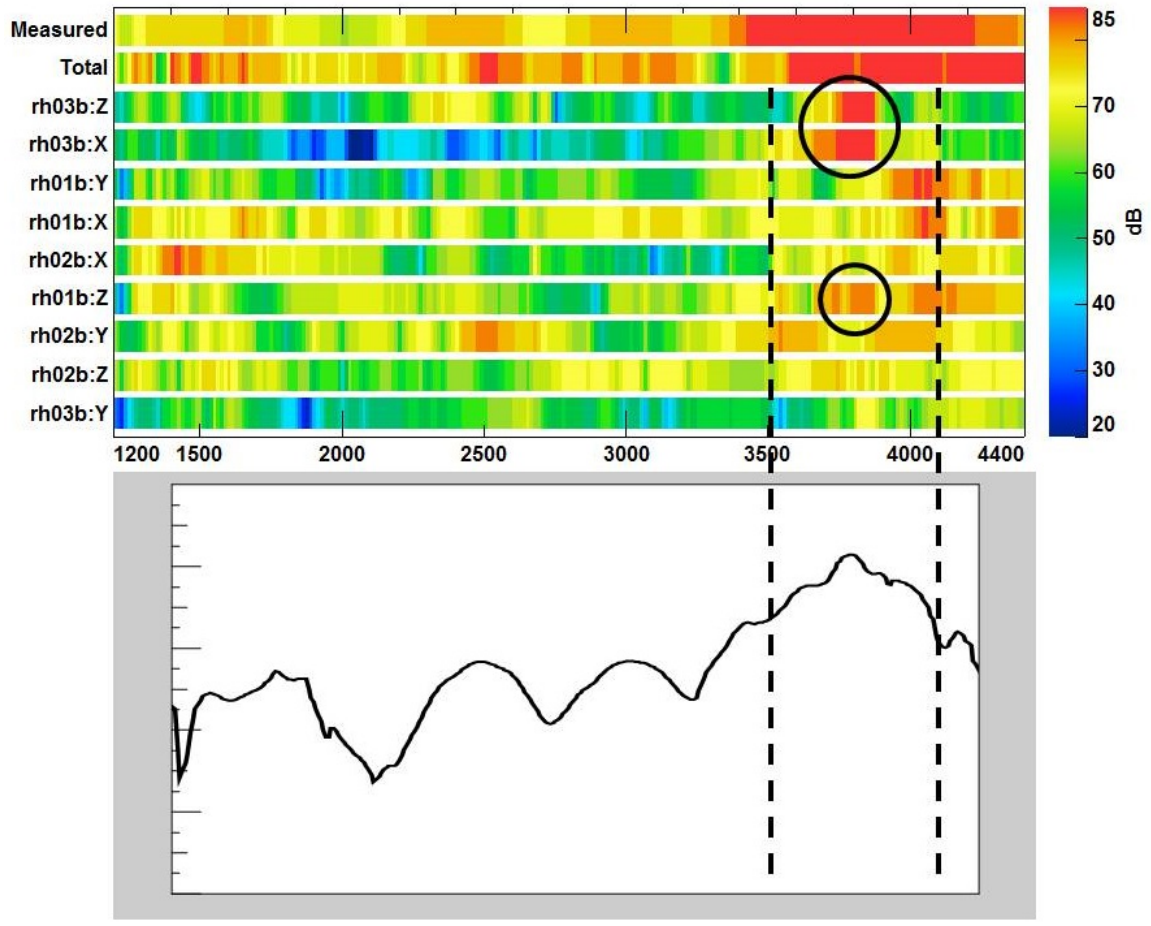


Figure 2.65. Contributions of all paths (1200-4400 rpm), BT:D

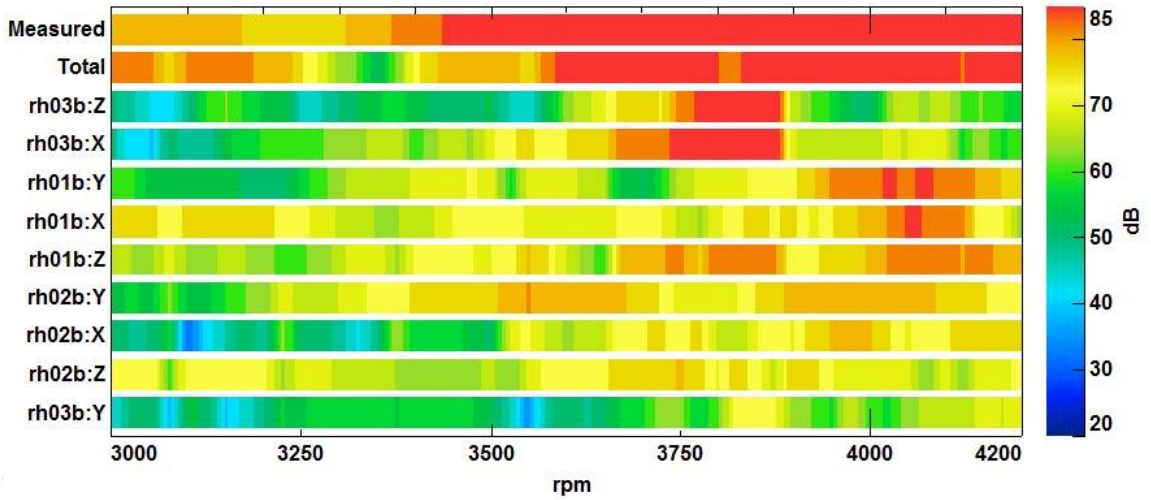


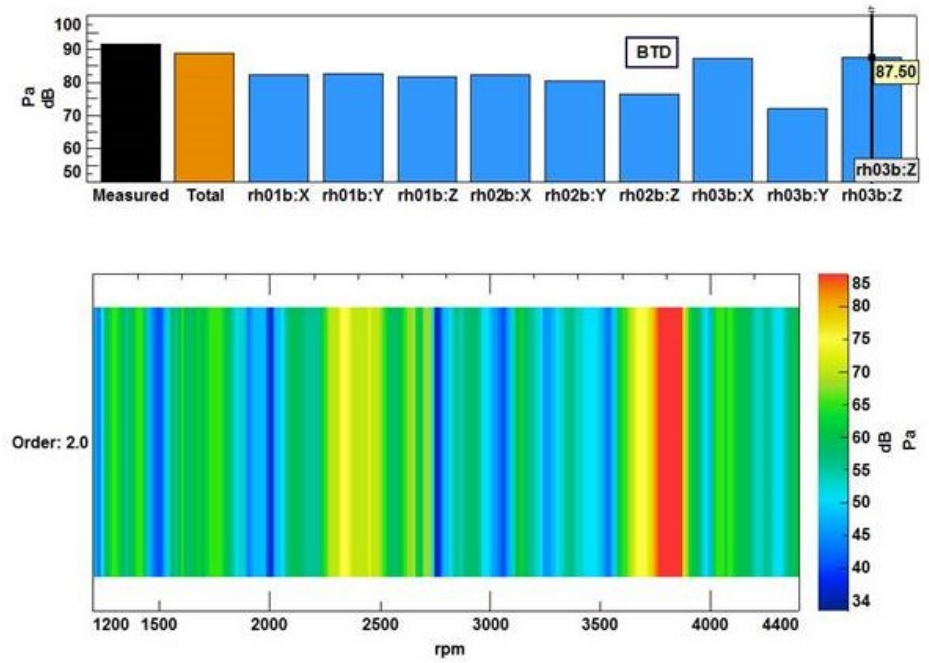
Figure 2.66. Contributions of all paths (3000-4200 rpm), BT:D

2.8.4.3. Detailed Results for the Vehicle L38. Force terms of Vehicle L38 are identified by populating the 'FRFs to indicator' matrix, which can be formulated as

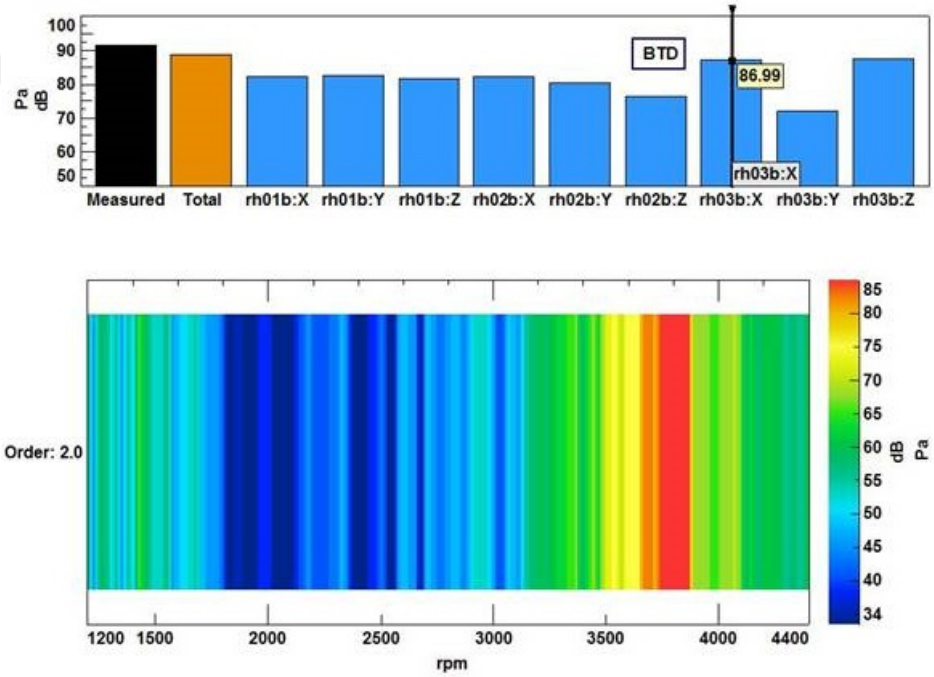
$$\begin{Bmatrix} f_1 \\ \vdots \\ f_{18} \end{Bmatrix}_{(18x1)} = \begin{bmatrix} \ddot{X}_1/F_1 & \cdots & \ddot{X}_1/F_{18} \\ \vdots & \ddots & \vdots \\ \ddot{X}_{18}/F_1 & \cdots & \ddot{X}_{18}/F_{18} \end{bmatrix}^{+}_{(18x18)} \begin{Bmatrix} \ddot{x}_1 \\ \vdots \\ \ddot{x}_{18} \end{Bmatrix}_{(18x1)} \tag{2.33}$$

For this case, 18 paths are defined from the engine and exhaust mounts through 3 targets. Impacts are carried out over 3 engine and 3 exhaust mounts in 3 translational directions, which populate 54 terms in the 'FRFs to targets' matrix. For the L38 test vehicle, the calculation is as follows:

$$\begin{Bmatrix} p_{(BT:D)} \\ p_{(BT:D1)} \\ p_{(BT:K)} \end{Bmatrix}_{(3x1)} = \begin{bmatrix} p_{(BT:D)}/F_1 & \cdots & p_{(BT:D)}/F_{18} \\ p_{(BT:D1)}/F_1 & \cdots & p_{(BT:D1)}/F_{18} \\ p_{(BT:K)}/F_1 & \cdots & p_{(BT:K)}/F_{18} \end{bmatrix}_{(3x18)} \begin{Bmatrix} f_1 \\ \vdots \\ f_{18} \end{Bmatrix}_{(18x1)} \tag{2.34}$$



(a) RH03:Z

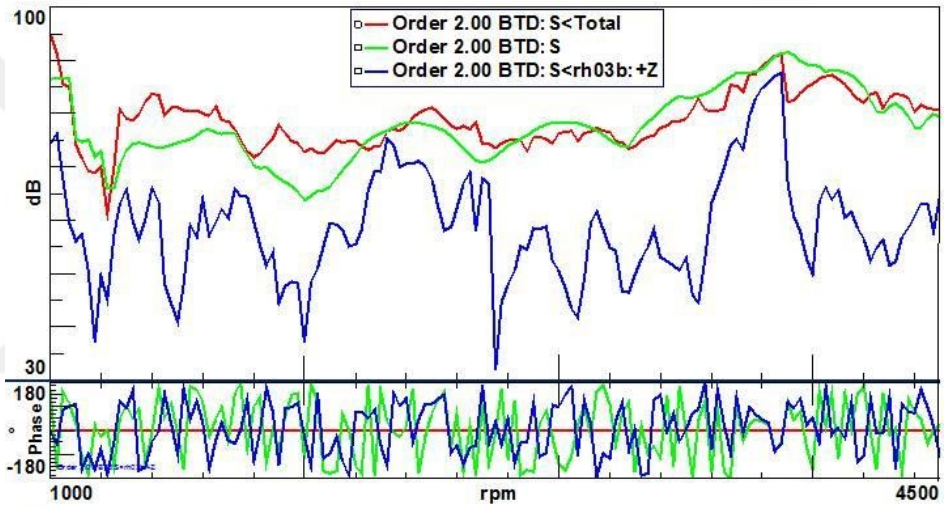


(b) RH03:X

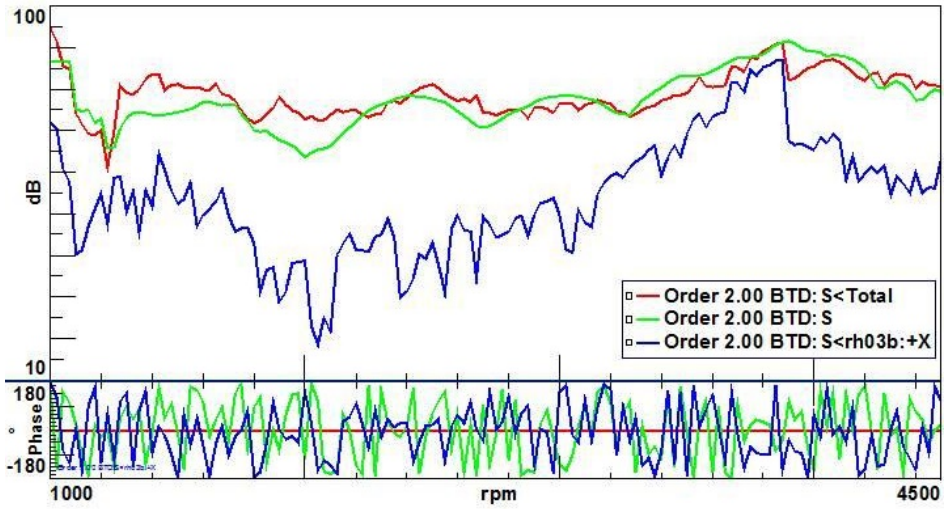
Figure 2.67. Main contributors of the booming

In TPA, beside the others, two important parameters are the FRF estimation algorithm and boundary conditions. Estimation algorithms, H_1, H_2 and H_v, are defined

in Equations (2.25) to (2.27). For comparison and getting insight, FRF measurements are performed, using all of the three algorithms. Two different boundary conditions are considered for the test vehicle: in one of them the vehicle is on its wheels, and in the other it is on the lift for the sake of easiness during the impact inputs. Here, in Figure 2.73. road test measurements and results of six different calculations are given for the L38 vehicle #170.



(a) RH03:Z



(b) RH03:X

Figure 2.68. The calculated (red), measured (green) and RH03:Z and RH03:X (blue) path SPLs. The summation of all paths is stated as 'total'.

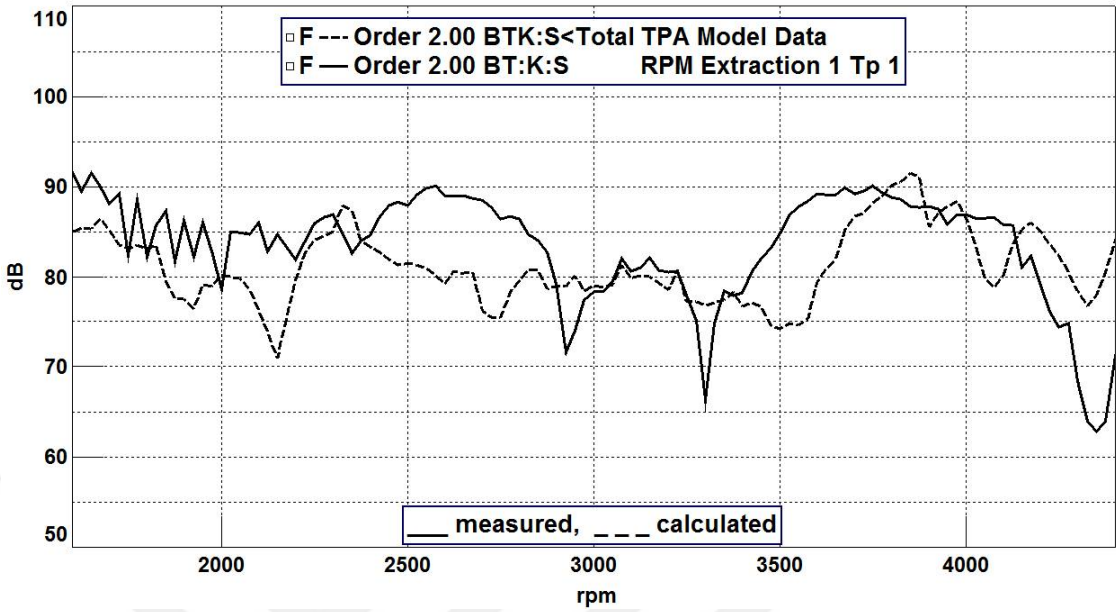


Figure 2.69. Measured and calculated SPLs at BT:K

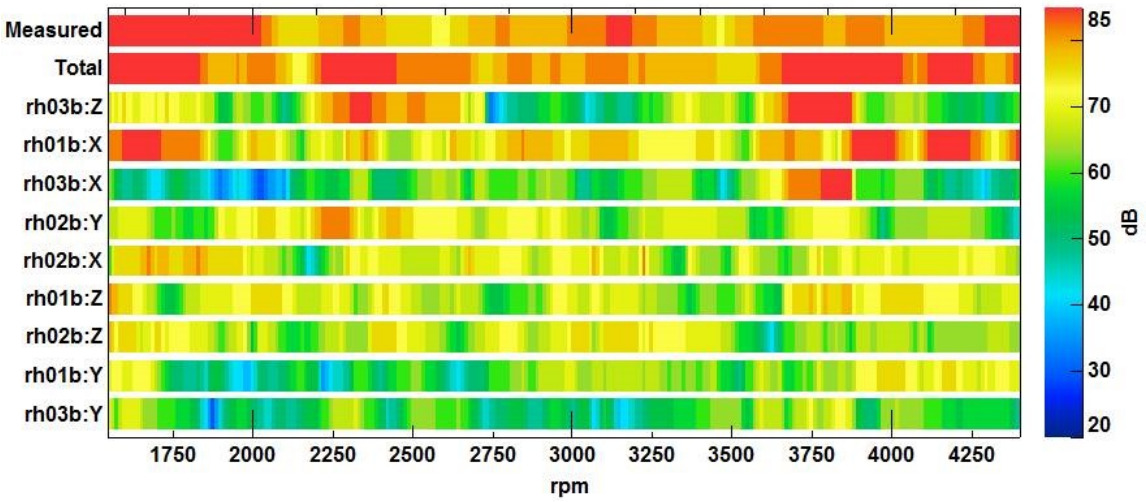


Figure 2.70. Contributions of all paths (1500-4500 rpm), BT:K

It is observed that like in the L84 case, the achieved best test result is "H_v on table". In Figure 2.74., the comparison of road test measurement and the TPA result obtained, when the vehicle is on its wheels is given. As mentioned, three targets are chosen for the L38 case; BT:D, BT:K and additionally BT:D1. Measured and calculated sound pressure levels for the others are shown in Figures 2.70. and 2.71., respectively.

One can say that measured and calculated results are compatible in general. When evaluating results, one has to consider the following issues:

(i) As mentioned, TPA is a linear analysis and has its own assumptions.

(ii) Probably the most important indicator of the test success is the coherence values of measured FRFs (see Figure 2.77.).

(iii) To increase the number of defined paths will always improve the accuracy of results. For this case, it is possible to define extra paths through the wheel suspension connections, differential, etc., provided that the channel number of the data acquisition system is enough.

(iv) Airborne paths and road inputs can be ignored; this assumption is valid due to the frequency band of interest, i.e. up to 200 Hz.

(v) Rotational paths are ignored, because of the operational difficulties. One can say that this assumption may lead to some mistakes.

(vi) One of the important requirements of TPA is the velocity difference at the active and passive sides, i.e. following condition must hold: $V_A >> V_P$ (see Figure 2.78.).

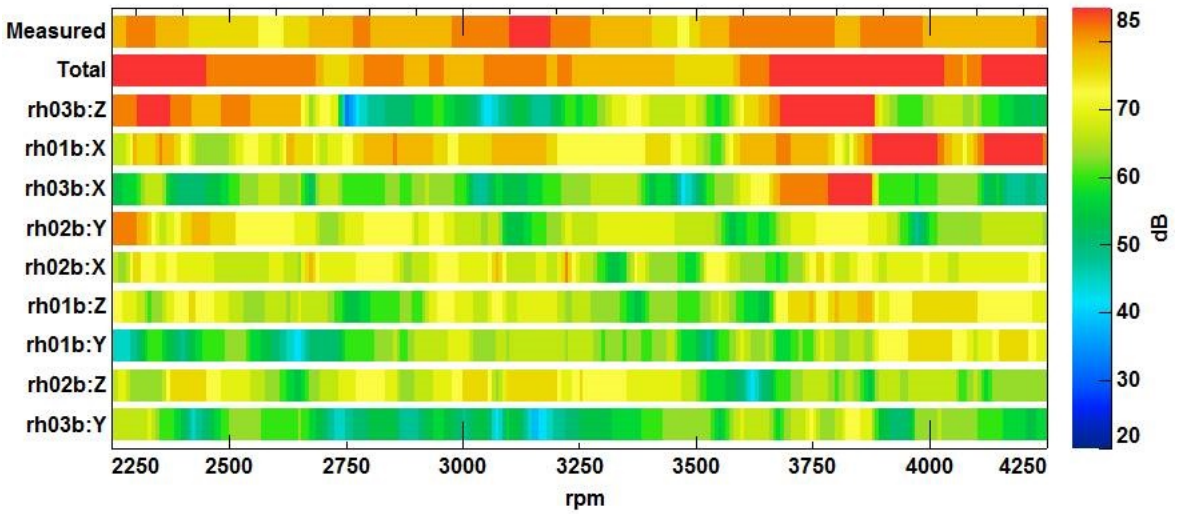


Figure 2.71. Contributions of all paths (2250-4250 rpm), BT:K



(a) L38, Vehicle #250



(b) L38, Vehicle #170

Figure 2.72. TPA test vehicles, where the photographs are taken in (a) NVH Laboratory of OYAK Renault Co. , and (b) in the Vibration and Acoustics Laboratory of Boğaziçi University, respectively. "Photo courtesy of OYAK Renault Co."

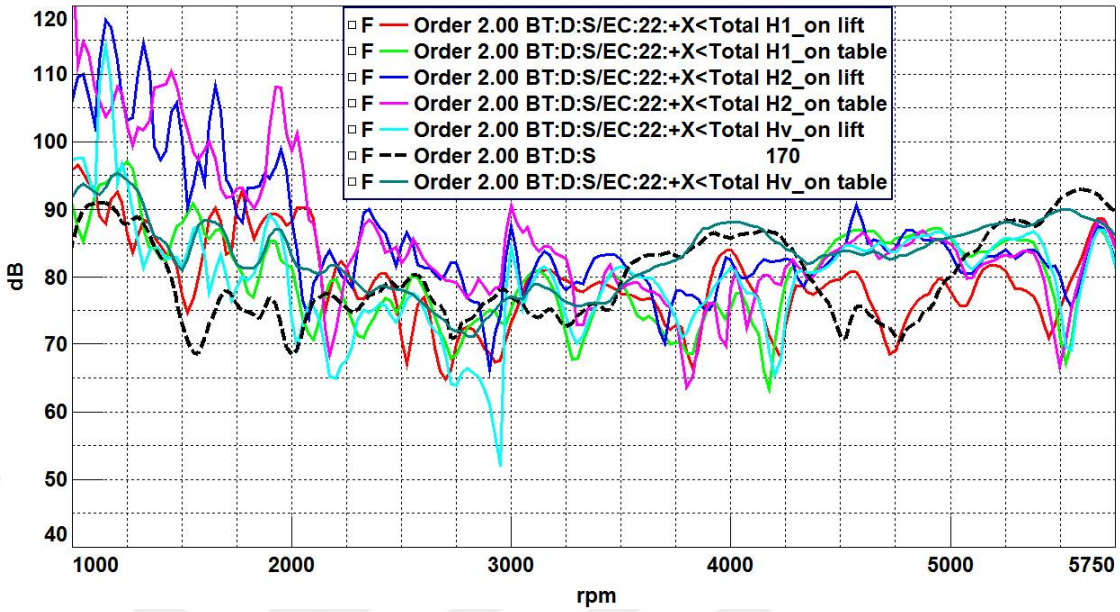


Figure 2.73. Measured and calculated SPLs at BT:D, 6 scenarios

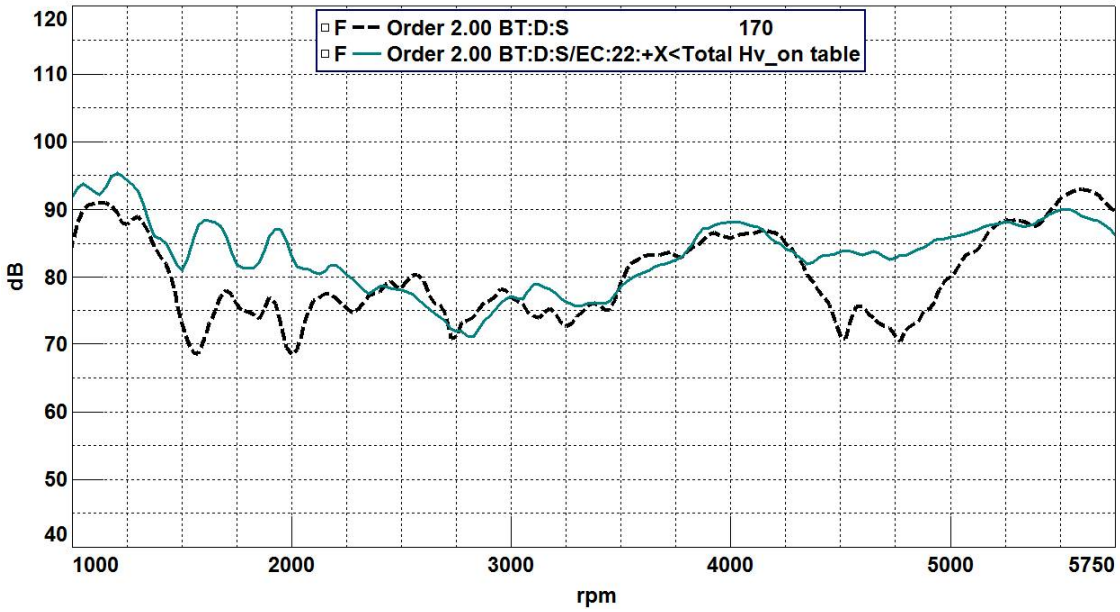


Figure 2.74. Measured and calculated SPLs at BT:D

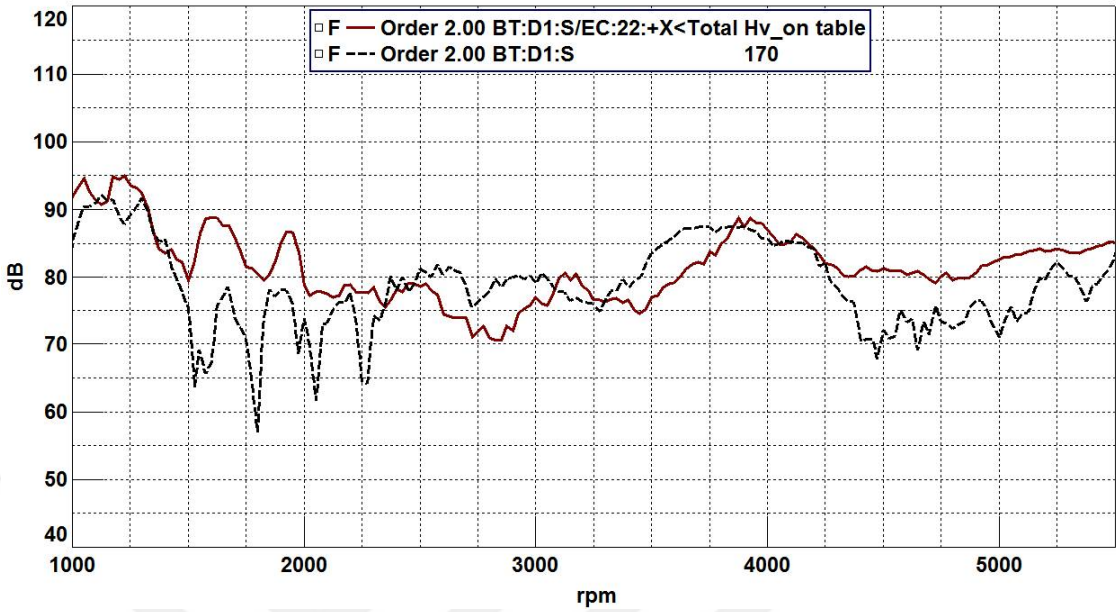


Figure 2.75. Measured and calculated SPLs at BT:D1

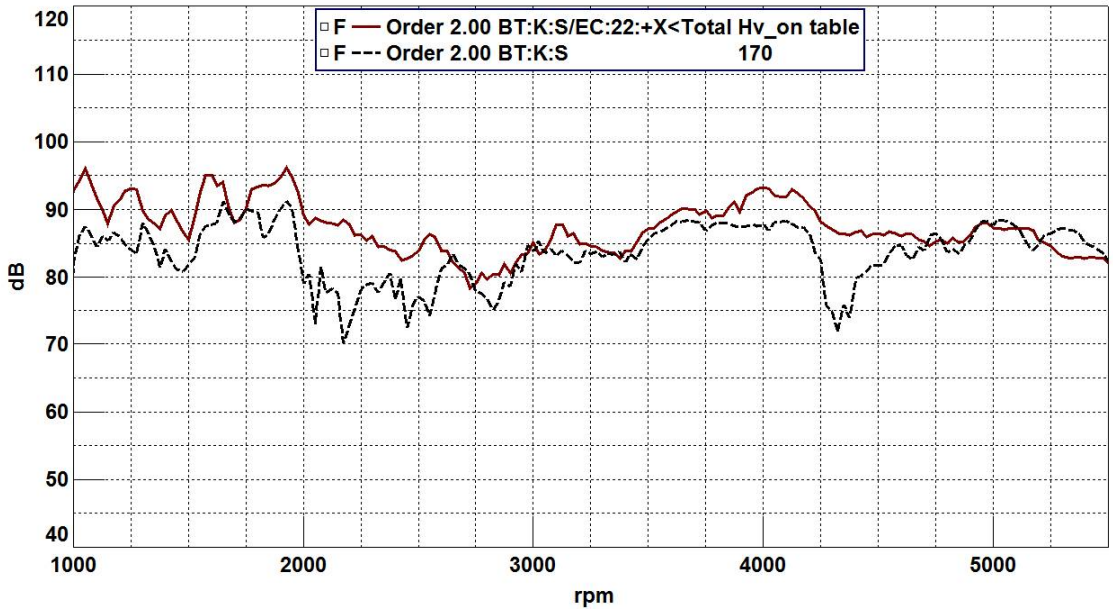


Figure 2.76. Measured and calculated SPLs at BT:K

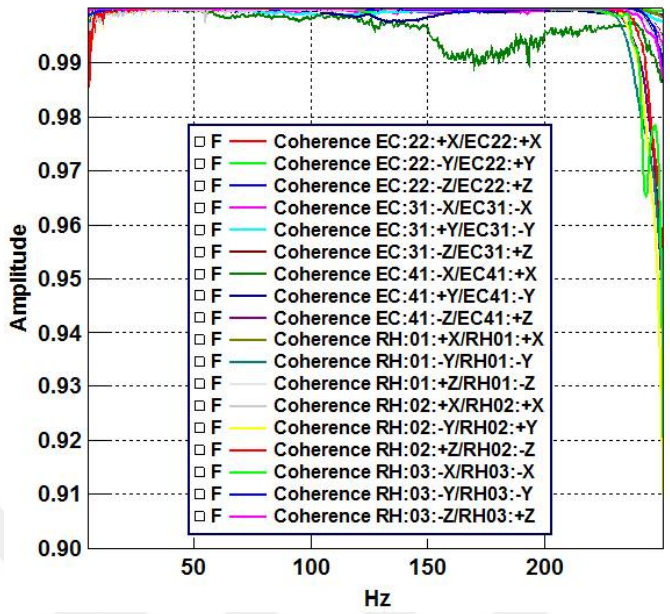
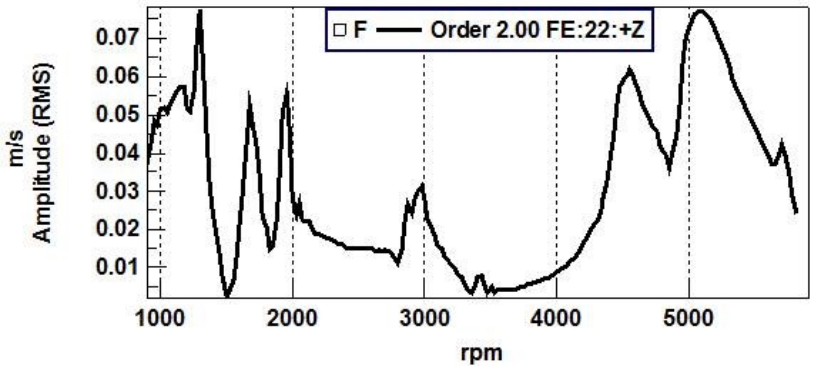
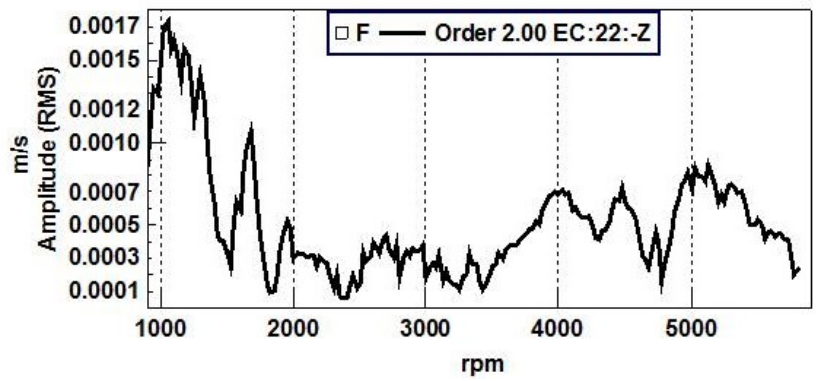


Figure 2.77. Coherence plots of driving points



(a) FE:22, Active side velocity (V_A)



(b) EC:22, Passive side velocity (V_P)

Figure 2.78. Exhaust hanger mount

Actually, the structures of the two test vehicles are not so different. Moreover, the engine installation type is identical for both. At this point, it will not be so surprising to encounter with similar results concerning the ranking of the mounts. Again, results in the whole bandwidth that the engine operates are checked, and to focus on the booming(s), it will narrow down. Figures 2.79. to 2.81. indicate the ranking in the whole bandwidth. One can observe that this ranking is changed in the relatively frequency band of interest, namely 1500-4500 rpm, as shown in Figures 2.82. to 2.84. For the L38 case, the problem frequency is in between 3500-4300 rpm, when targets concerning the driver are considered. In Figures 2.85. and 2.86., this bandwidth is checked out for BT:D and BT:D1 respectively. For the BT:K position, two booms are present: one is in between 1600-2000 rpm, while the other is in the 2950-4250 rpm bandwidths. Figures 2.87. and 2.88. are referred to these two booms.

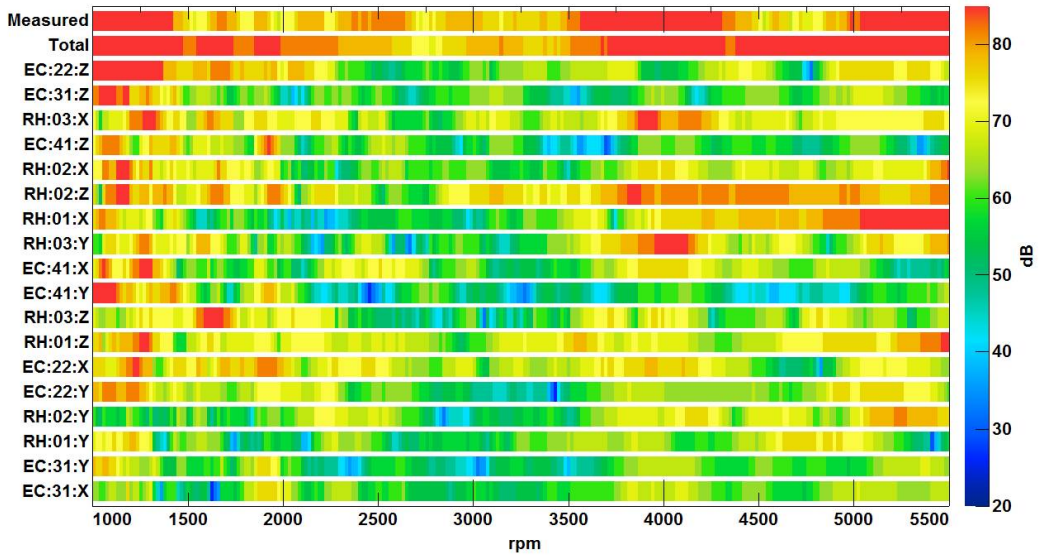


Figure 2.79. The contributions of all paths (1000-5500 rpm), BT:D

To come up with verification, the method is also applied to the identical test vehicle # 250. Again, the measurements are taken, while the vehicle is on its wheels, and the method for the estimation of FRFs is chosen as H_v. Results are as follows:

(i) The compatibility with the road test measurement and TPA calculation are similar to the vehicle #170 case, but *worse*. (see Figures 2.89. to 2.91.)

(ii) Results show that in the problem frequency dominant paths are not completely same with the ones in the case #170. (see Figures 2.92. to 2.95.)

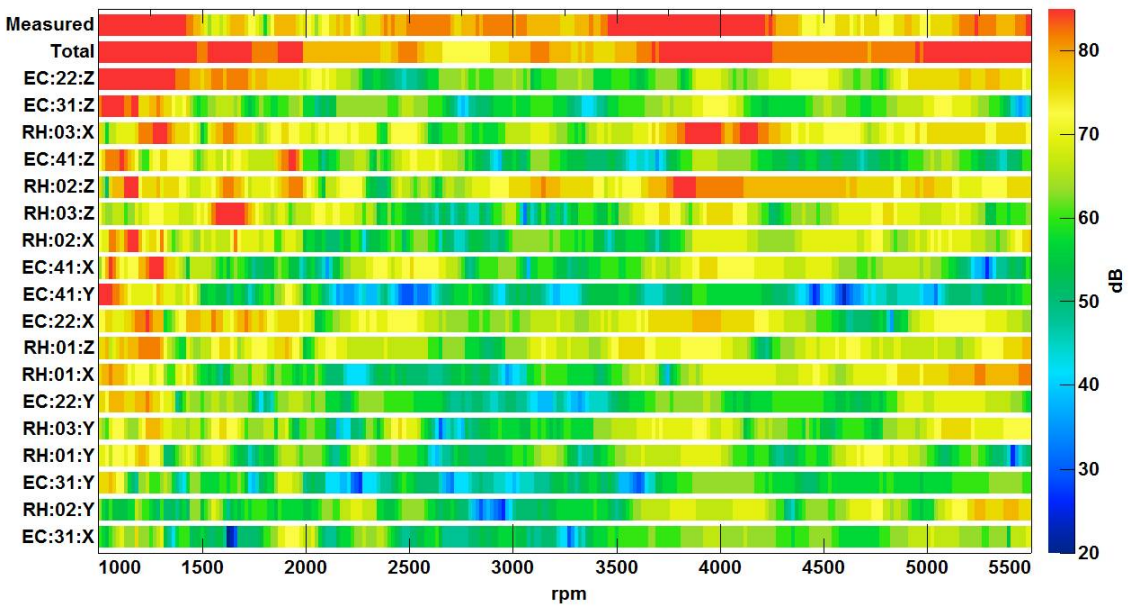


Figure 2.80. The contributions of all paths (1000-5500 rpm), BT:D1

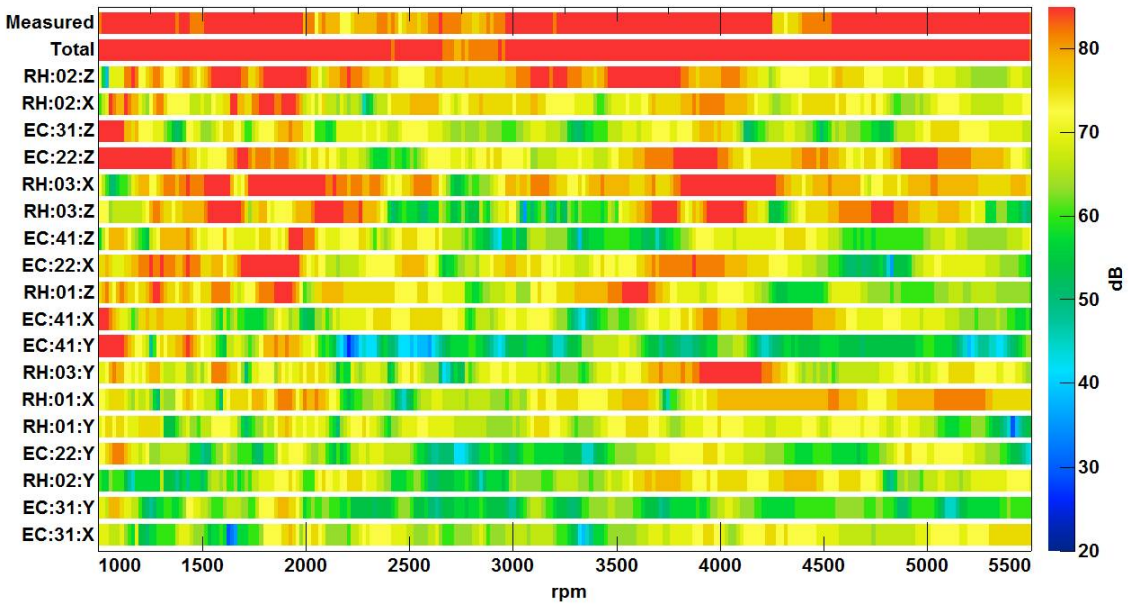


Figure 2.81. The contributions of all paths (1000-5500 rpm), BT:K

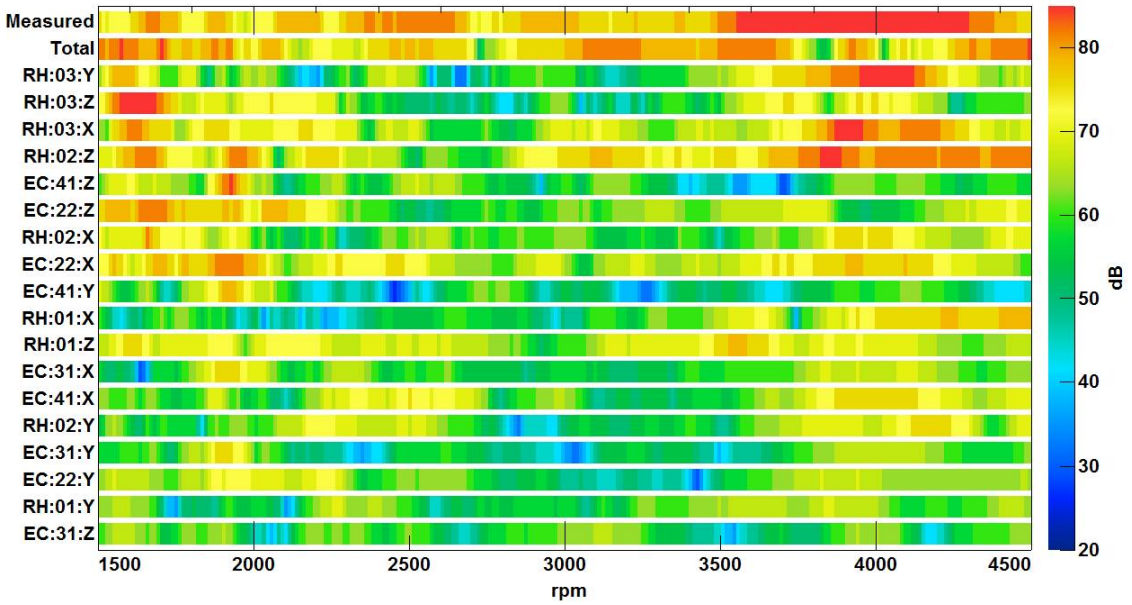


Figure 2.82. The contributions of all paths (1500-4500 rpm), BT:D

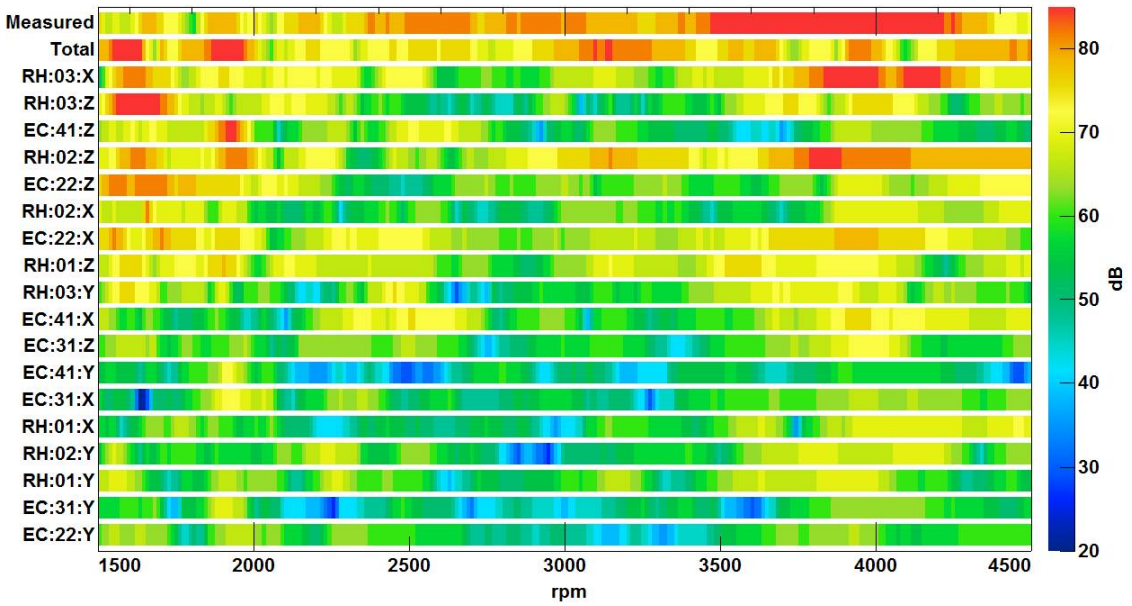


Figure 2.83. The contributions of all paths (1500-4500 rpm), BT:D1

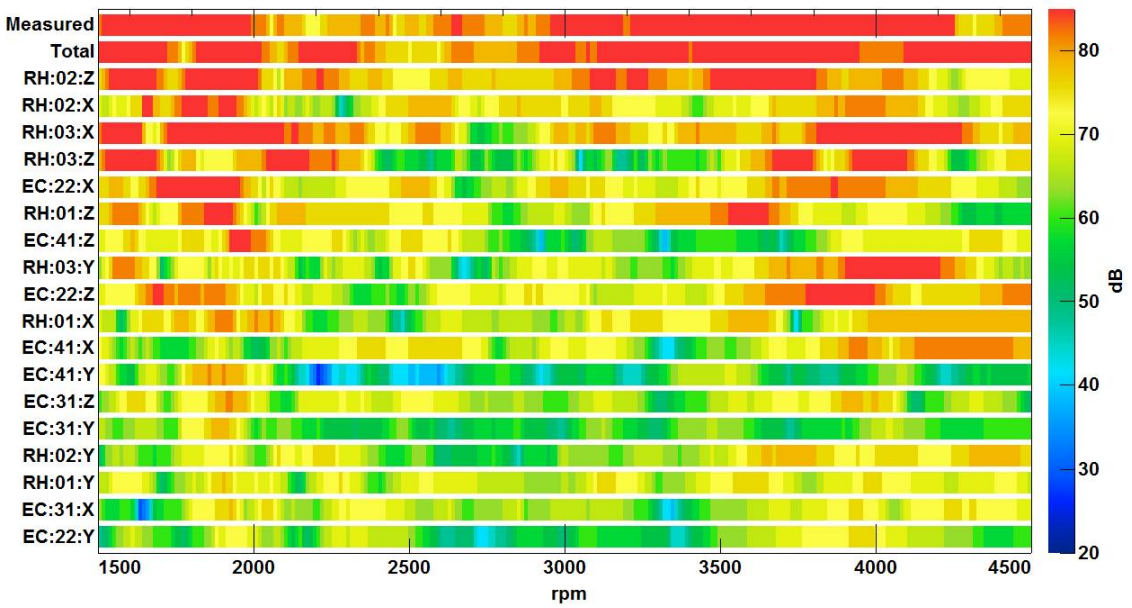


Figure 2.84. The contributions of all paths (1500-4500 rpm), BT:K

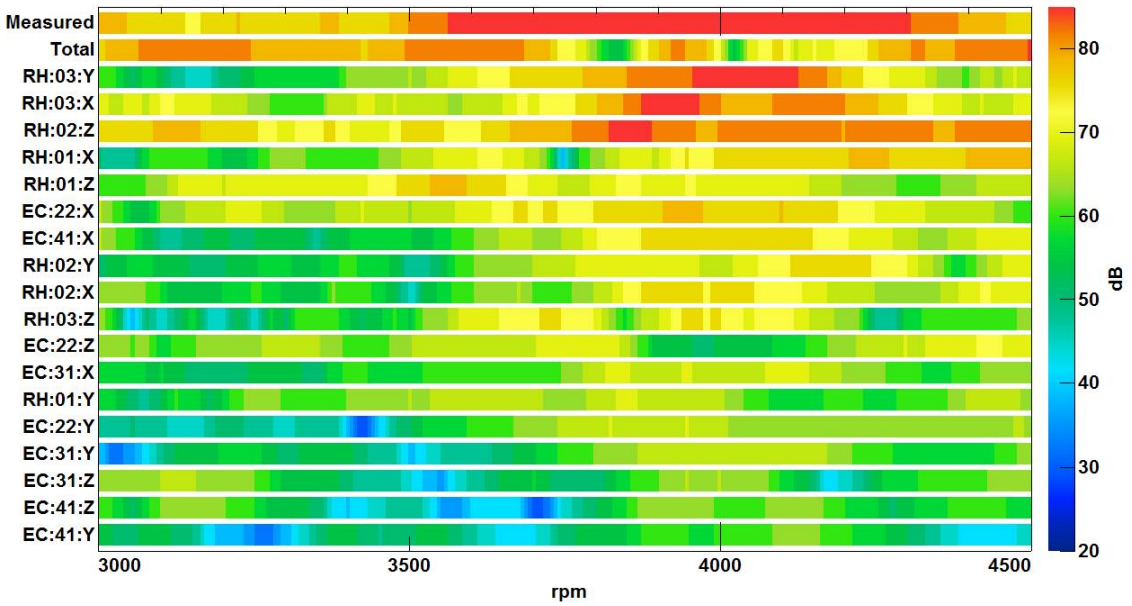


Figure 2.85. Contributions of all paths (3000-4500 rpm), BT:D

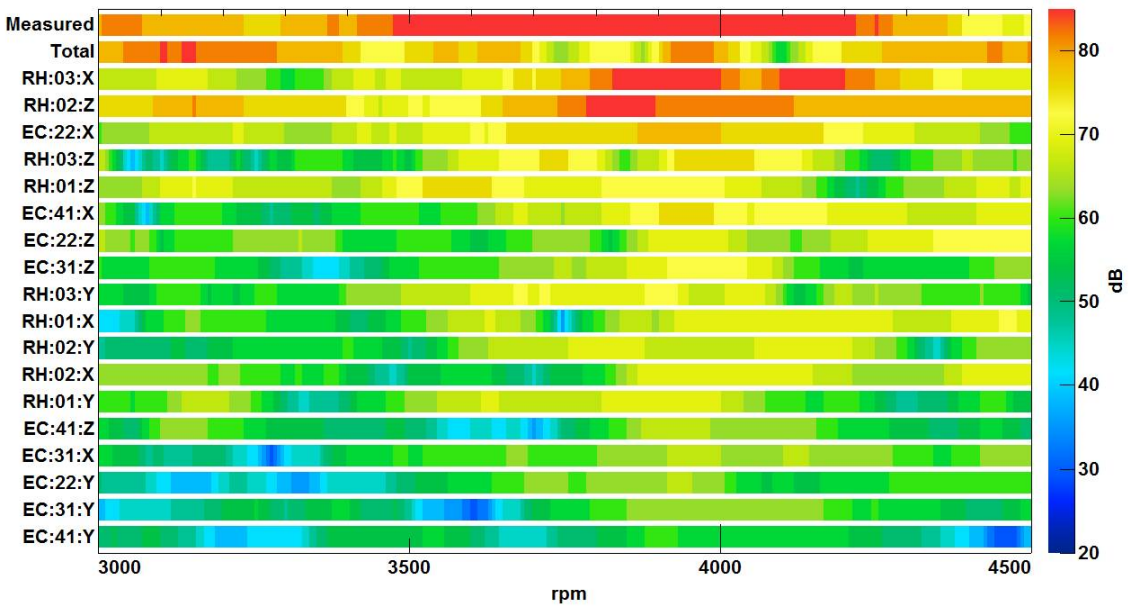


Figure 2.86. Contributions of all paths (3000-4500 rpm), BT:D1

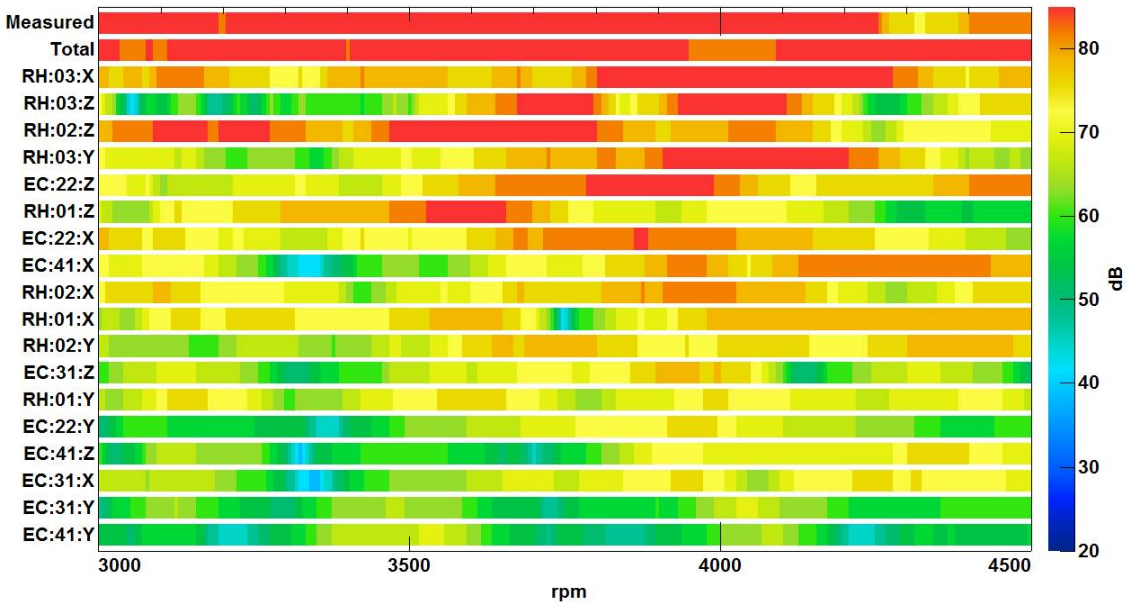


Figure 2.87. Contributions of all paths (3000-4500 rpm), BT:K

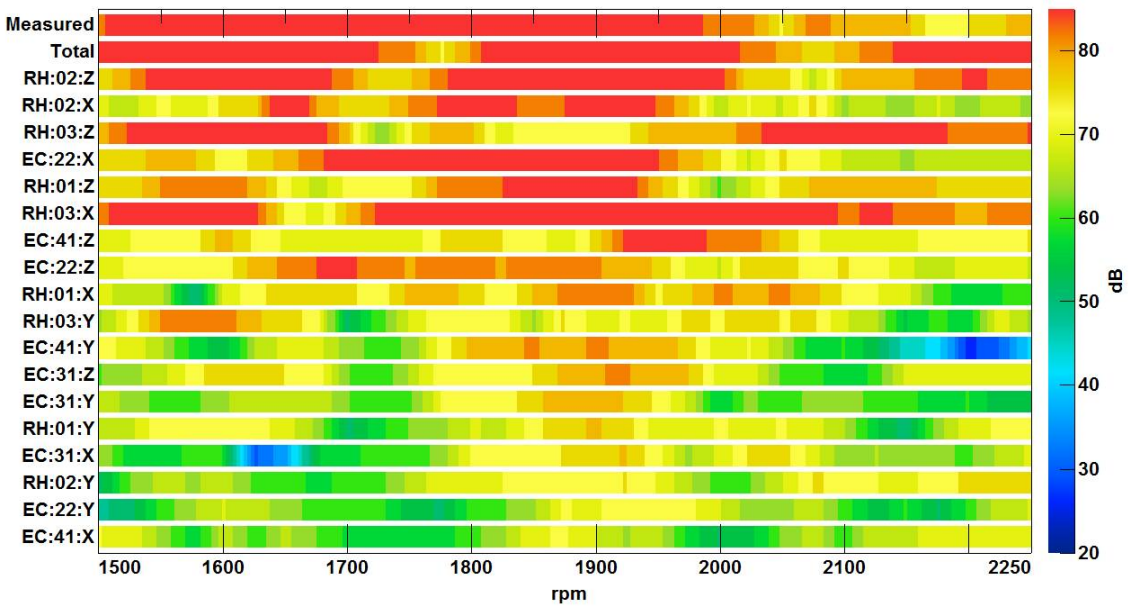


Figure 2.88. Contributions of all paths (1500-2250 rpm), BT:K

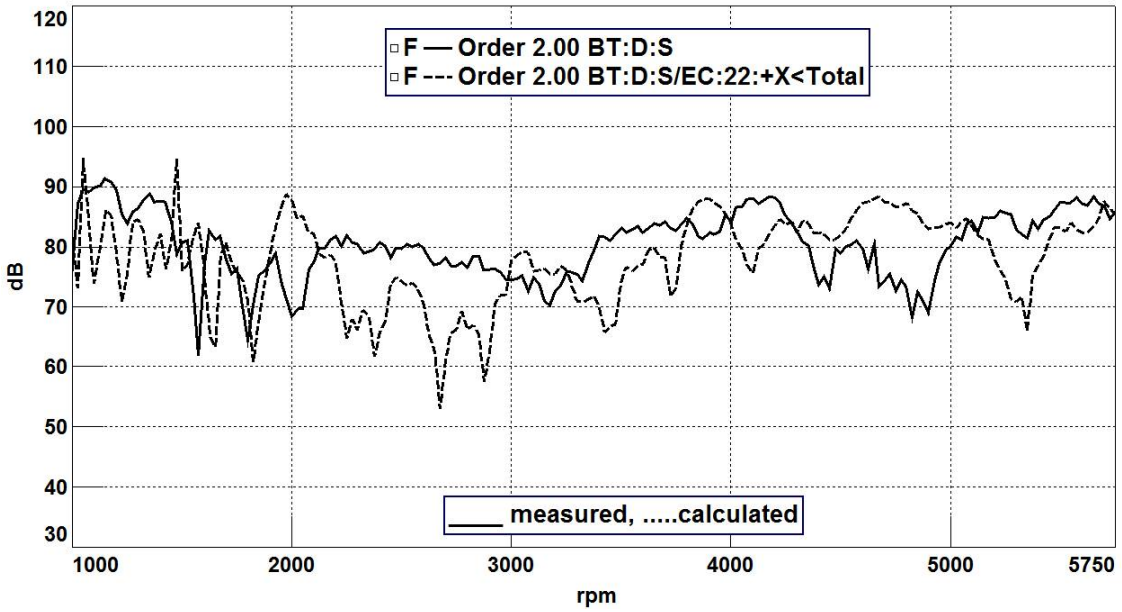


Figure 2.89. Measured and calculated SPLs at BT:D, Vehicle#250

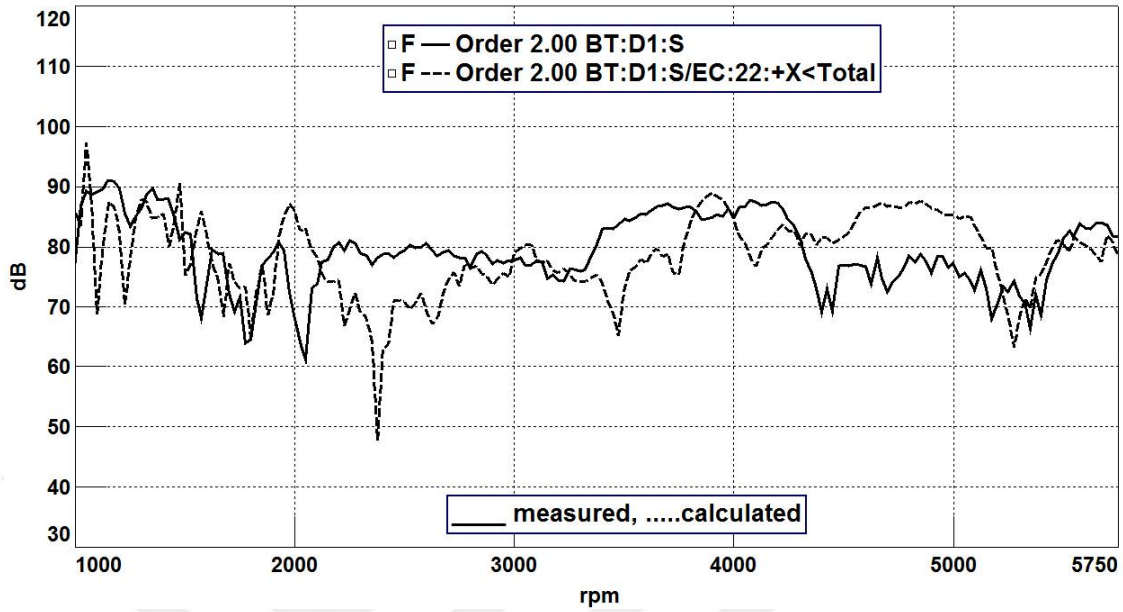


Figure 2.90. Measured and calculated SPLs at BT:D1, Vehicle#250

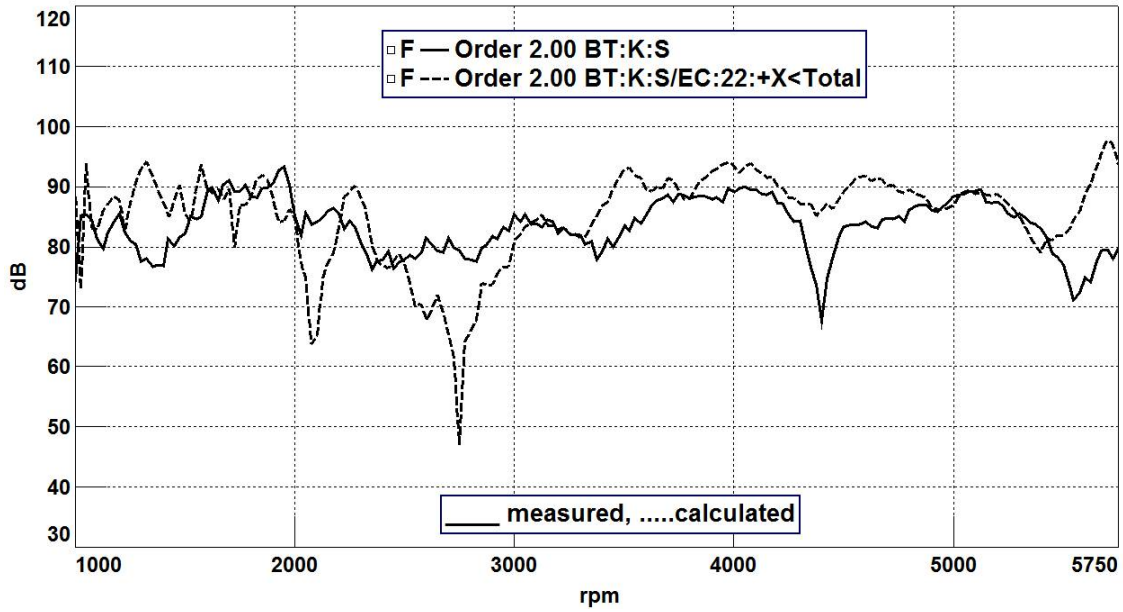


Figure 2.91. Measured and calculated SPLs at BT:K, Vehicle#250

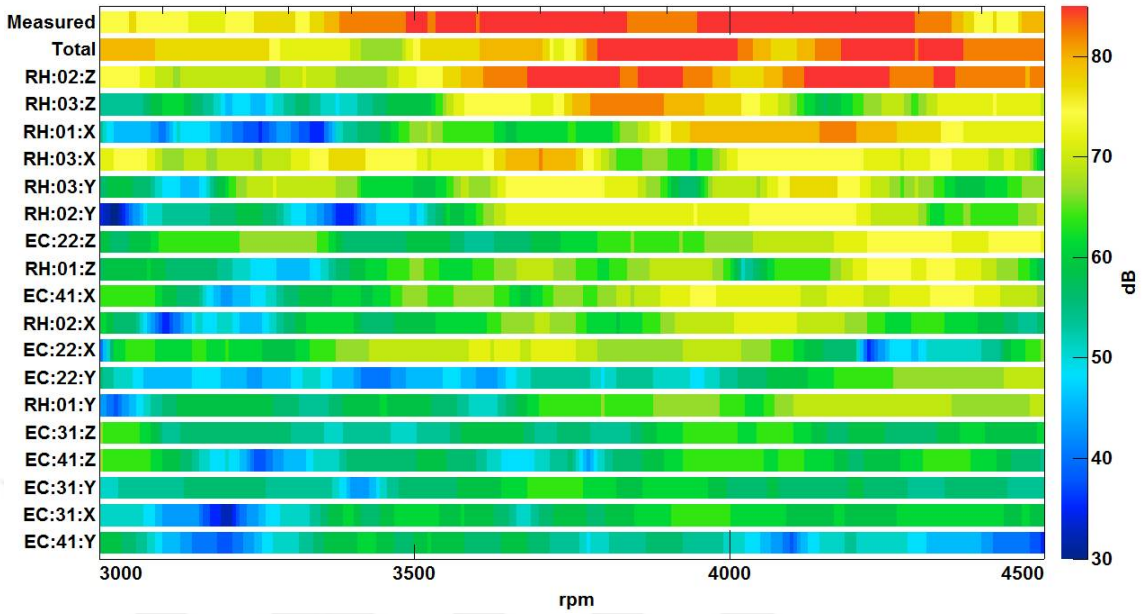


Figure 2.92. Contributions of all paths (3000-4500 rpm), BT:D, Vehicle#250

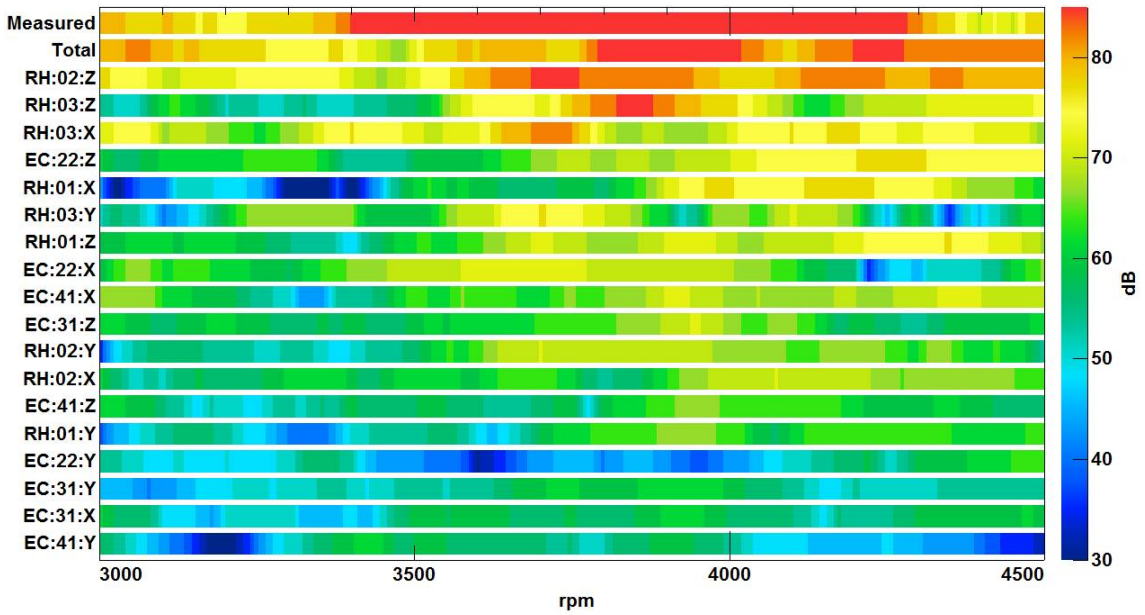


Figure 2.93. Contributions of all paths (3000-4500 rpm), BT:D1, Vehicle#250

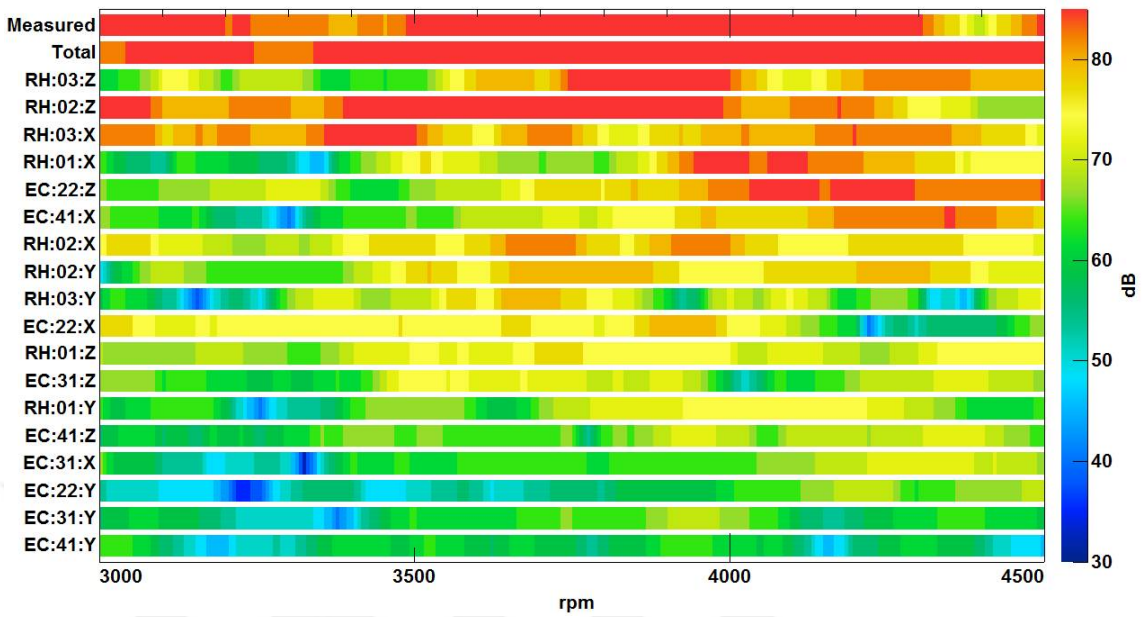


Figure 2.94. Contributions of all paths (3000-4500 rpm), BT:K, Vehicle#250

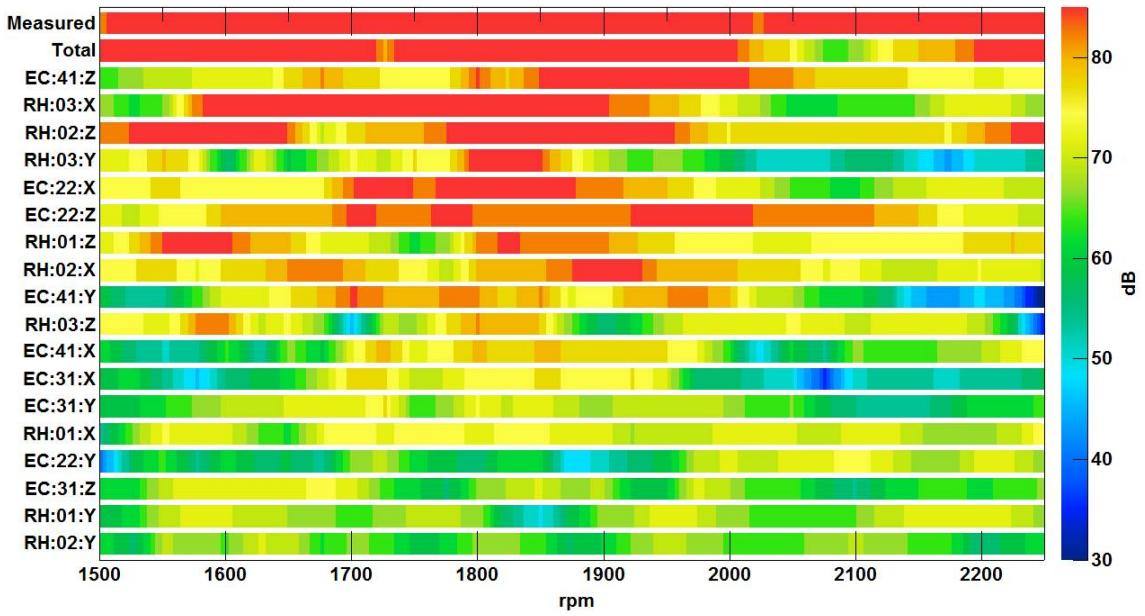


Figure 2.95. Contributions of all paths (1500-2250 rpm), BT:K, Vehicle#250

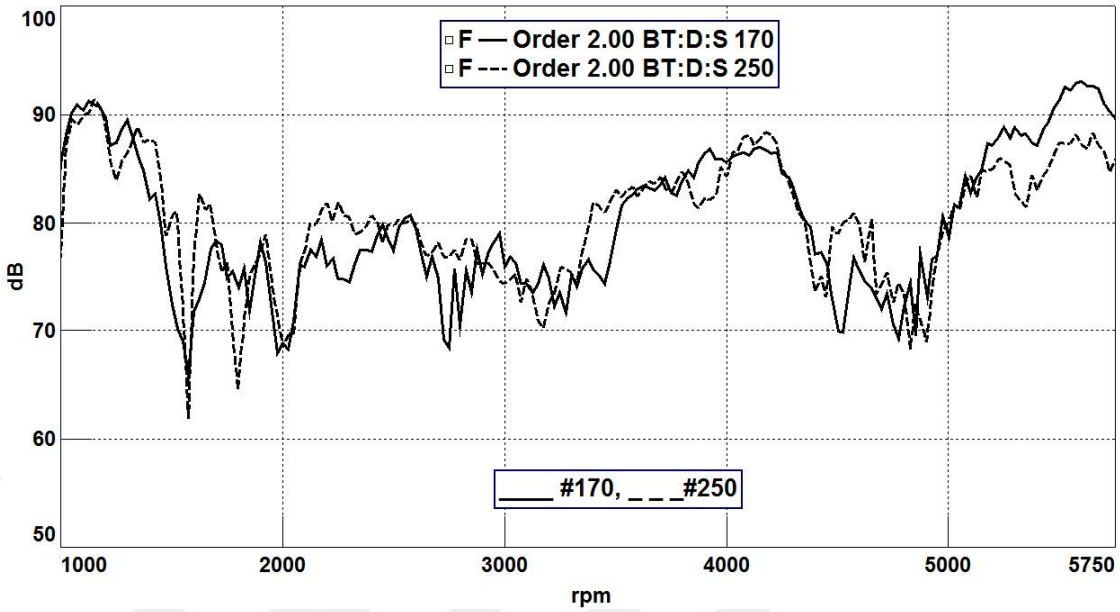


Figure 2.96. Road test results for the vehicles #170 and #250, BT:D

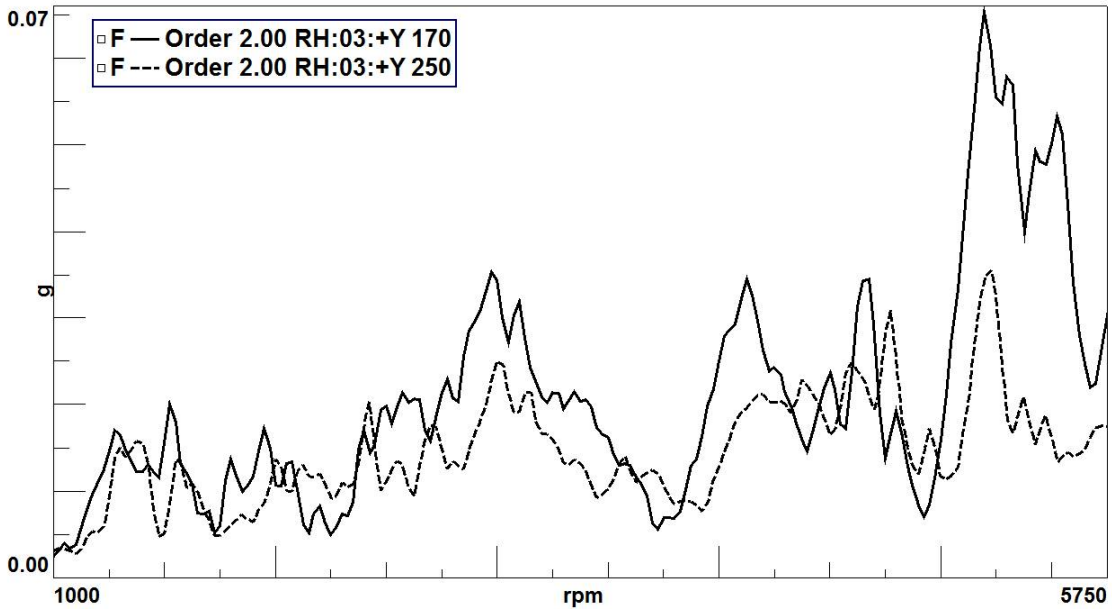


Figure 2.97. Road test results for the vehicle #170 and #250, RH:03:Y

Conflicting results are found, instead of verification! As seen in this particular application again, the variability in manufacturing process [12] and the complexity of

the structure makes the problem even harder and confusing. Probable reasons for these conflicting results can be outlined as follows:

(i) As seen in Figure 2.15., road tests do not give identical results for five identical vehicles. For a comparison, in Figure 2.96., BT:D measurements taken during road tests are given for the vehicles #170 and #250.

(ii) Although reference engine block signals are similar, acceleration signals from the engine mounts are considerably different, which in turn cause deviations in TPA results. An example that indicates the situation is given in Figure 2.97., where acceleration signals of two vehicles taken from RH:03:Y is compared.

(iii) The difference in acceleration signals, which is distinctly observed at the body side of the mounts, can be caused either *by the mount itself, or it may be due to the response of the structure.*

Half of the defined paths are belong to the exhaust system. The fourth order is also considerable, although it is not dominant like the second order. Contributions of orders are shown in Figure 2.98., where second order and harmonics are considered.

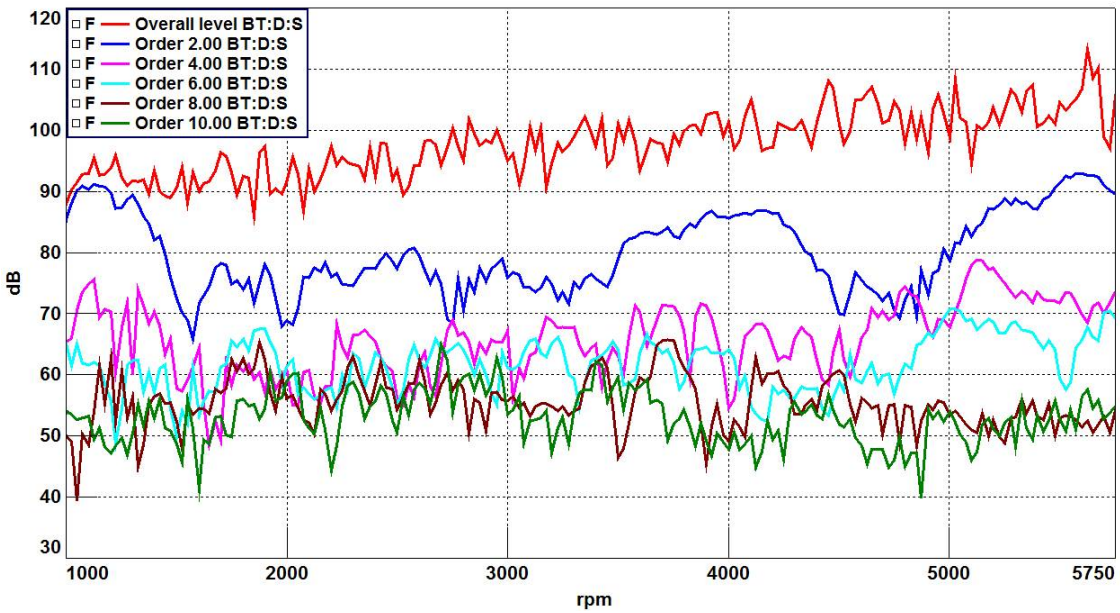


Figure 2.98. Overall and harmonics of second order, BT:D, L38 #170

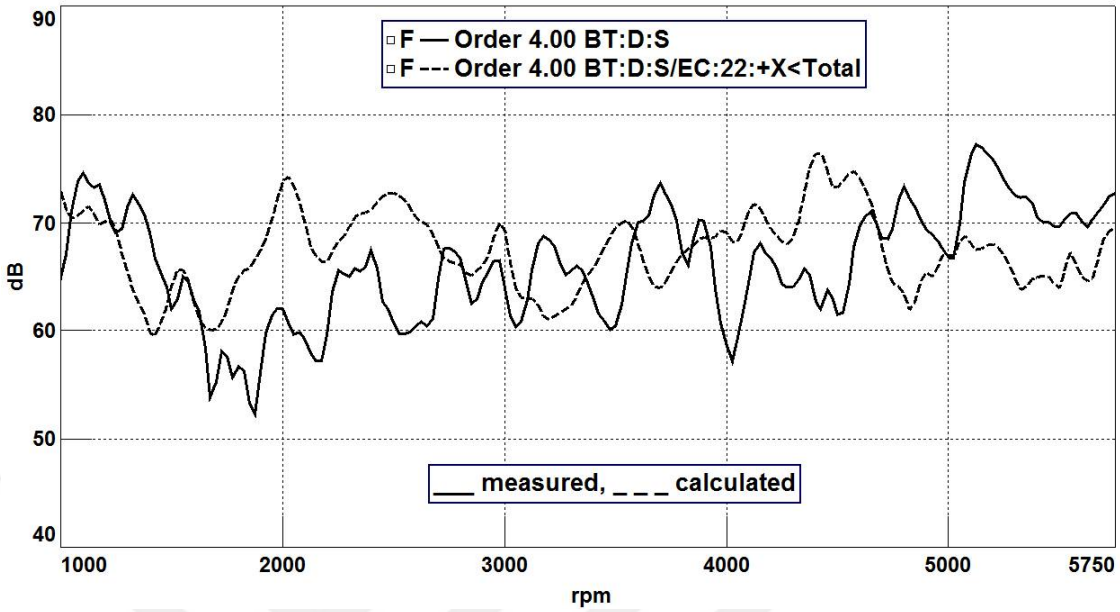


Figure 2.99. Measured and calculated 4^{th} order SPLs at BT:D, Vehicle# 170

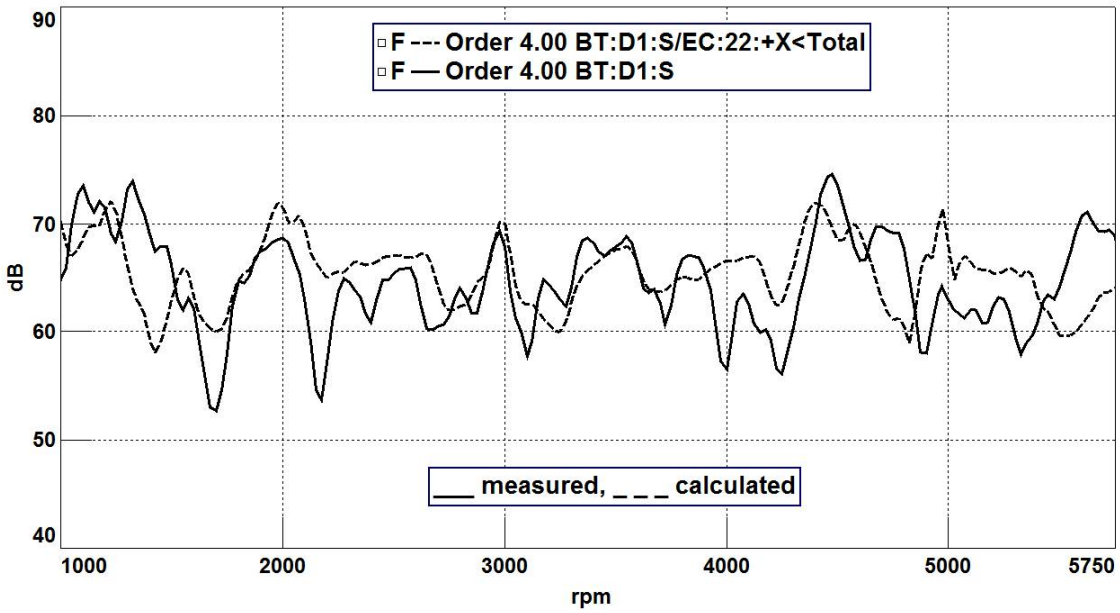


Figure 2.100. Measured and calculated 4^{th} order SPLs at BT:D1, Vehicle# 170

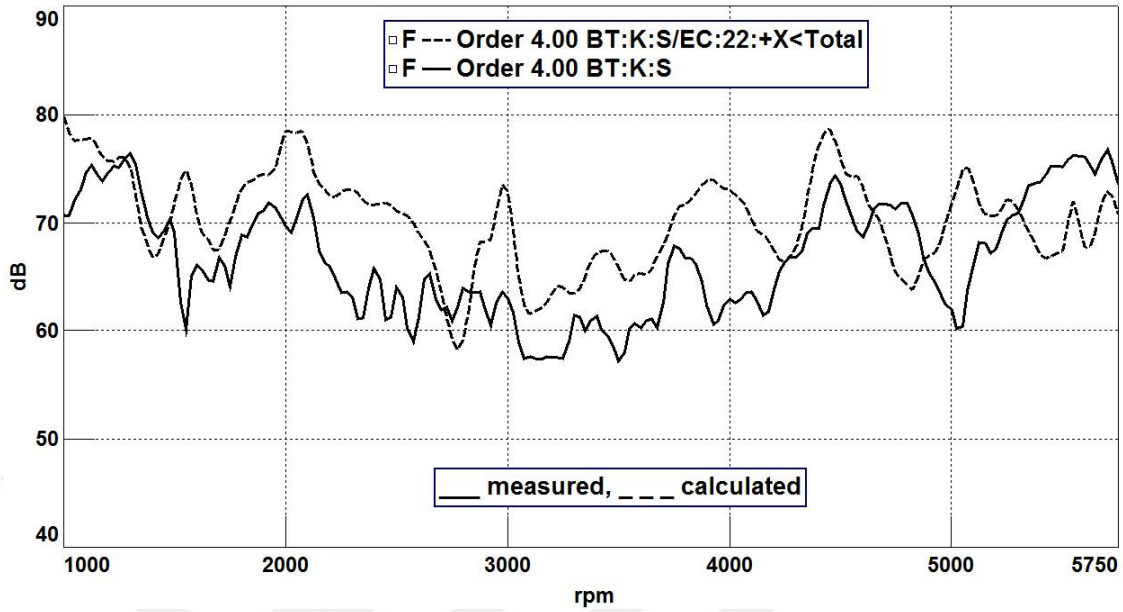


Figure 2.101. Measured and calculated 4^{th} order SPLs at BT:K, Vehicle# 170

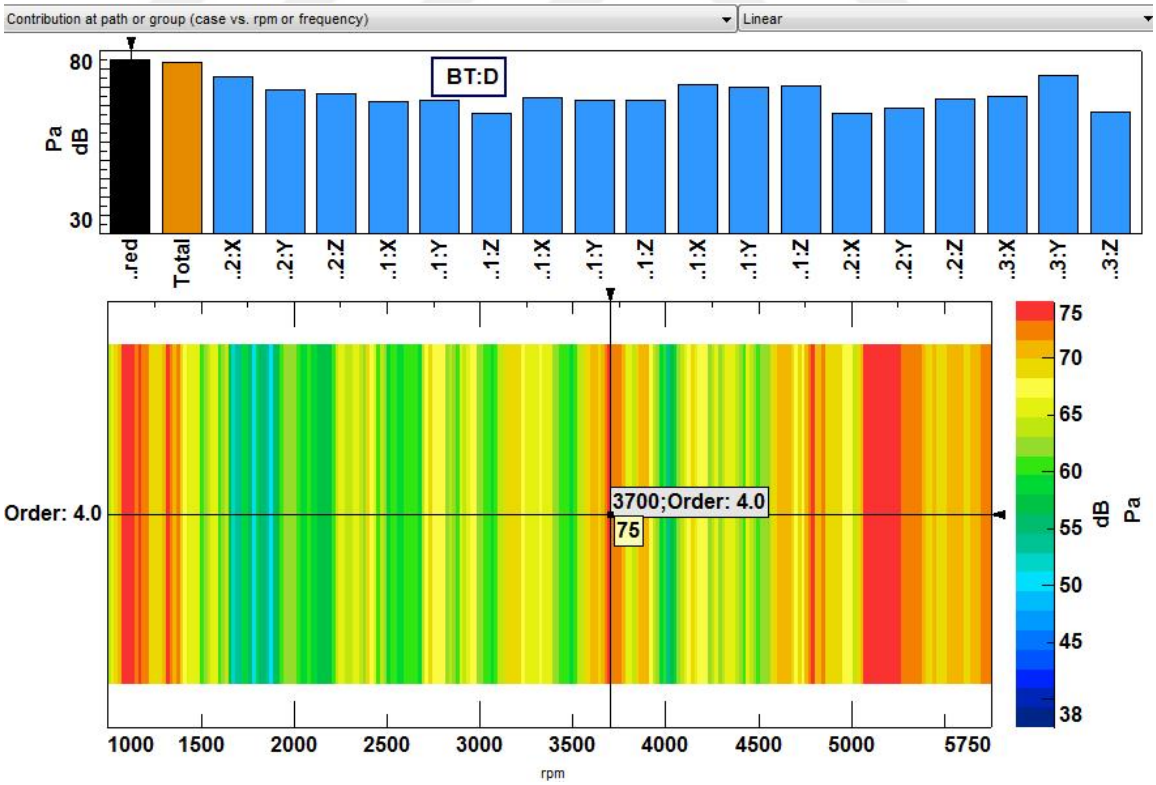


Figure 2.102. Measured TPA result, 4^{th} order SPLs at BT:D, Vehicle# 170

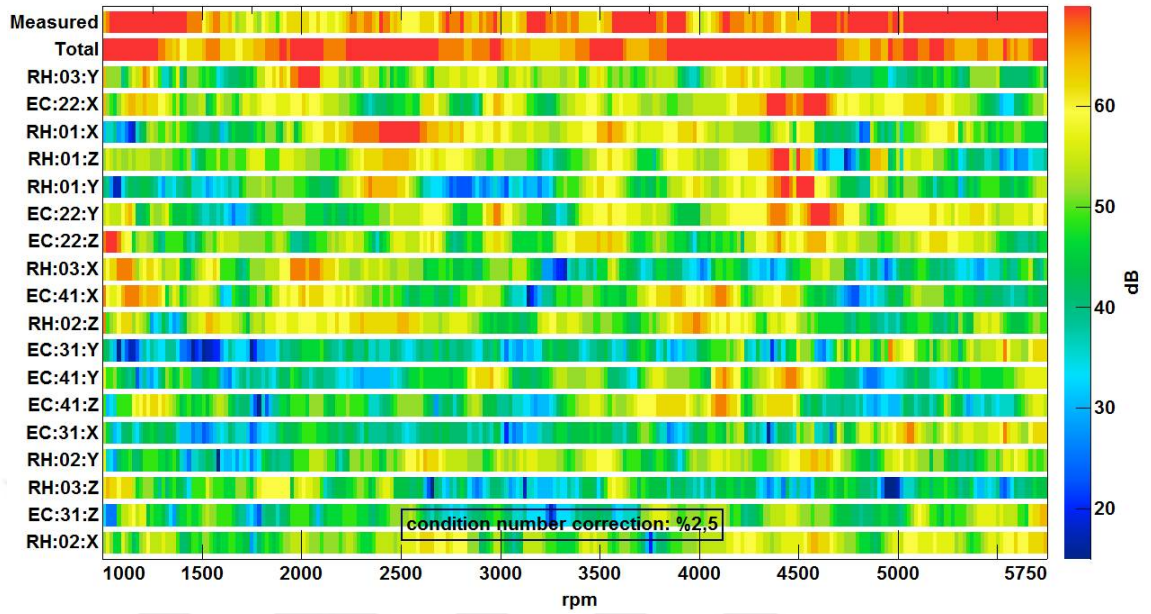


Figure 2.103. Contributions of all paths, BT:D, 4^{th} order, Vehicle# 170

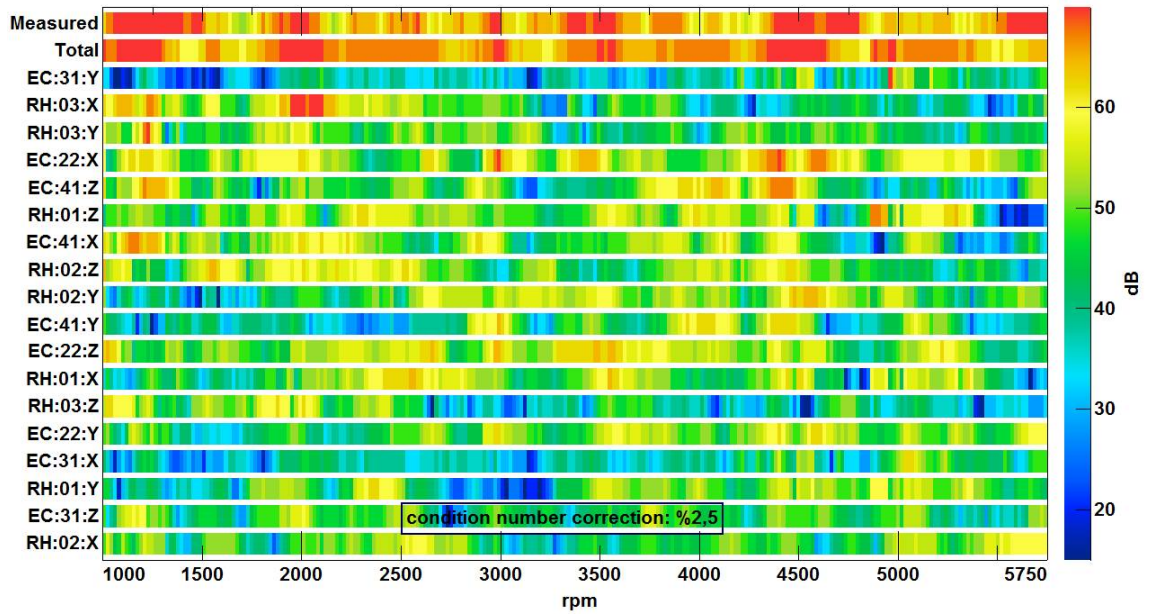


Figure 2.104. Contributions of all paths, BT:D1, 4^{th} order, Vehicle# 170

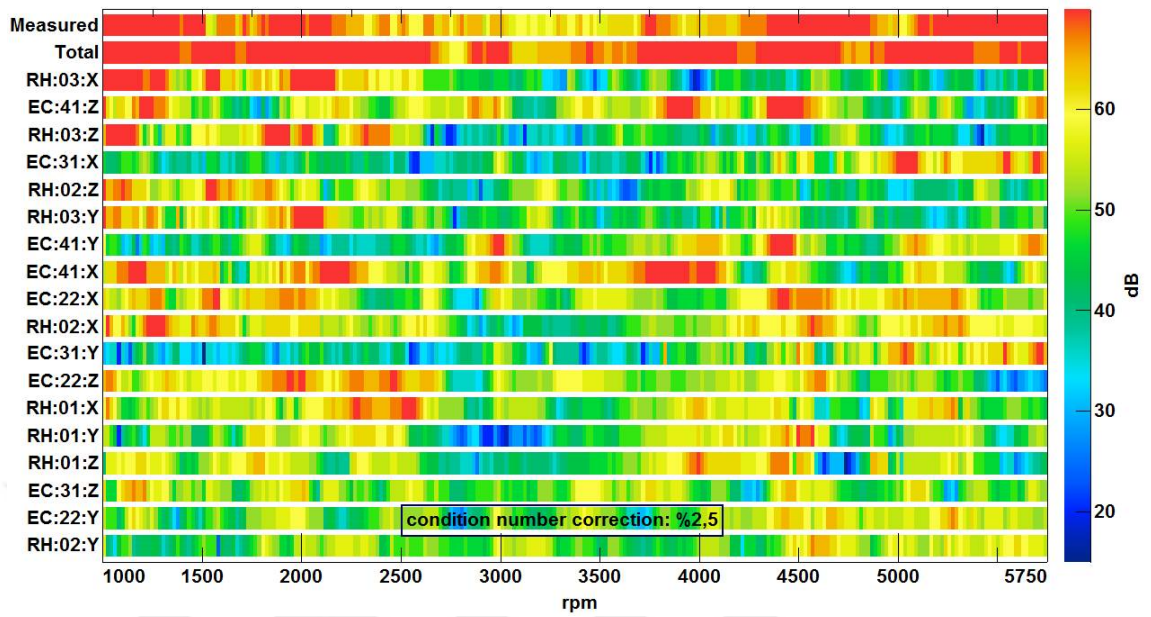


Figure 2.105. Contributions of all paths, BT:K, 4^{th} order, Vehicle# 170

2.9. An Approach to the Assessment of Inter Variability

In this section, an experimental procedure is proposed and its applicability is examined. In a source-path-receiver concept, inter variability problem can be broken down as in the following sequence. Variations might have been caused by the engine, i.e., vibrational inputs entering to the structure may be different; if not, differences between engine mounts may alter forces transmitted, which in turn affect sound pressure levels. Yet another possibility is that variability might have been caused by structural differences in between studied passive subsystems, which had unavoidably occurred during manufacturing processes. Structural differences obviously alter the sound pressure levels perceived by the receivers. In that case, it is recommended to inspect structural differences through measured frequency response functions by means of an experimental modal analysis (EMA) study (see Section 4.1 for a detailed framework).

In the defined collocation, we primarily compare phase reference signals, which are acquired through accelerometers attached to the engine block. In Figure 2.16., by giving amplitudes of measured accelerations, it is shown that the source inputs of test vehicles are matched, except a slight difference observed in the engine of vehicle # 251.

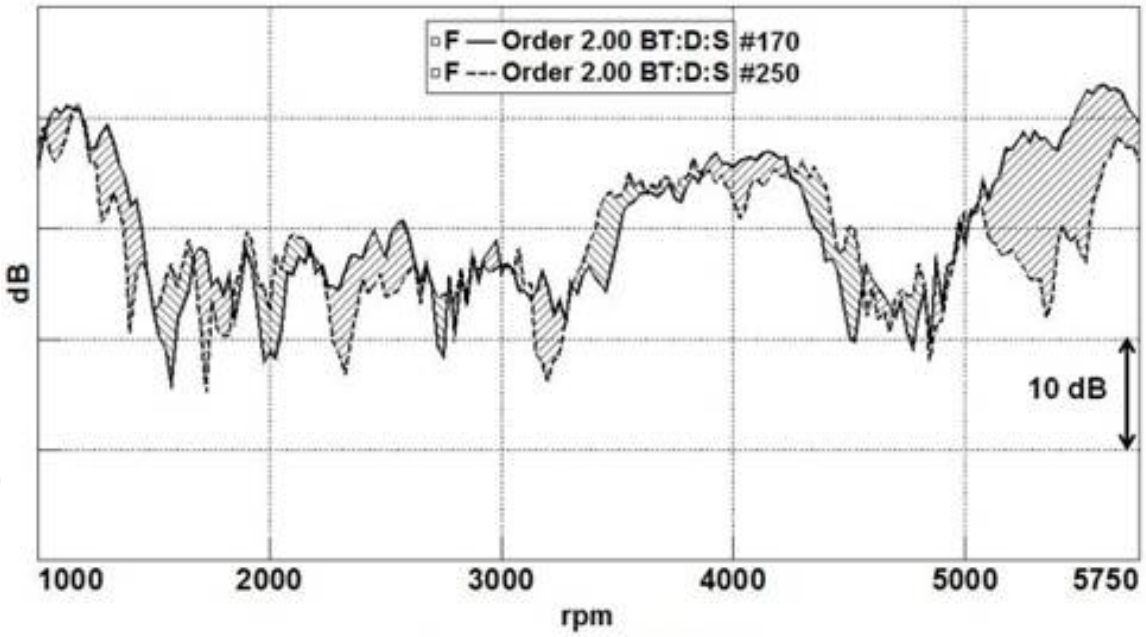


Figure 2.106. Comparison of sound pressure levels measured at BT: D for test vehicles # 170 and # 250

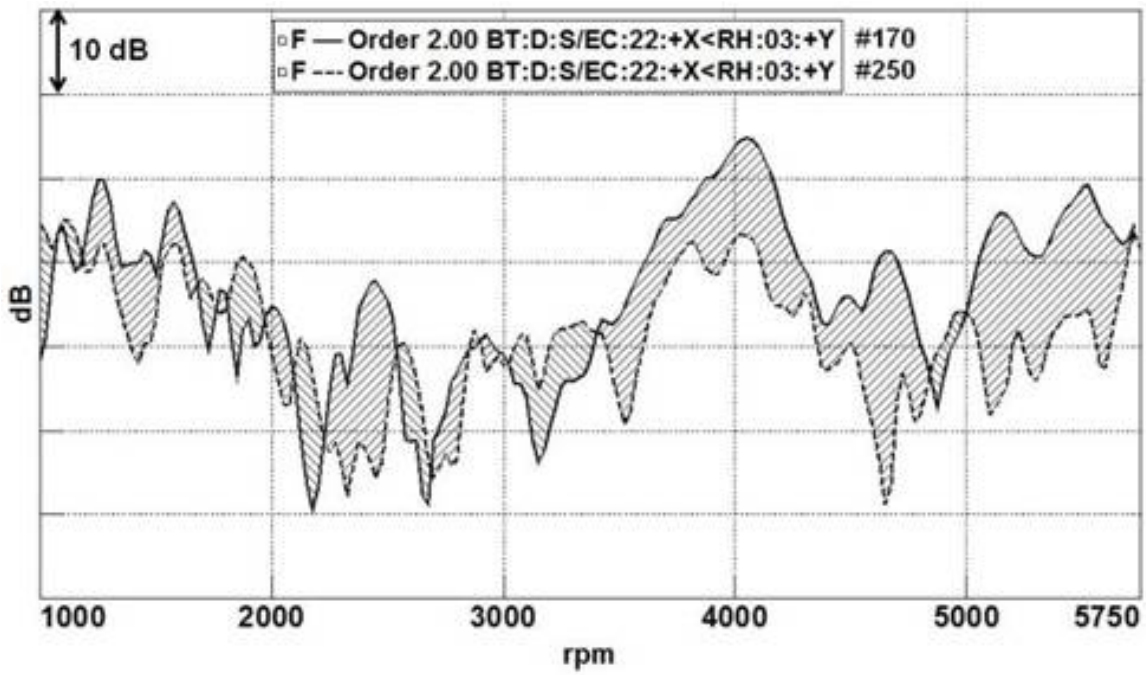


Figure 2.107. Contributions of the predominant path RH:03:Y predicted at BT: D for test vehicles # 170 and # 250

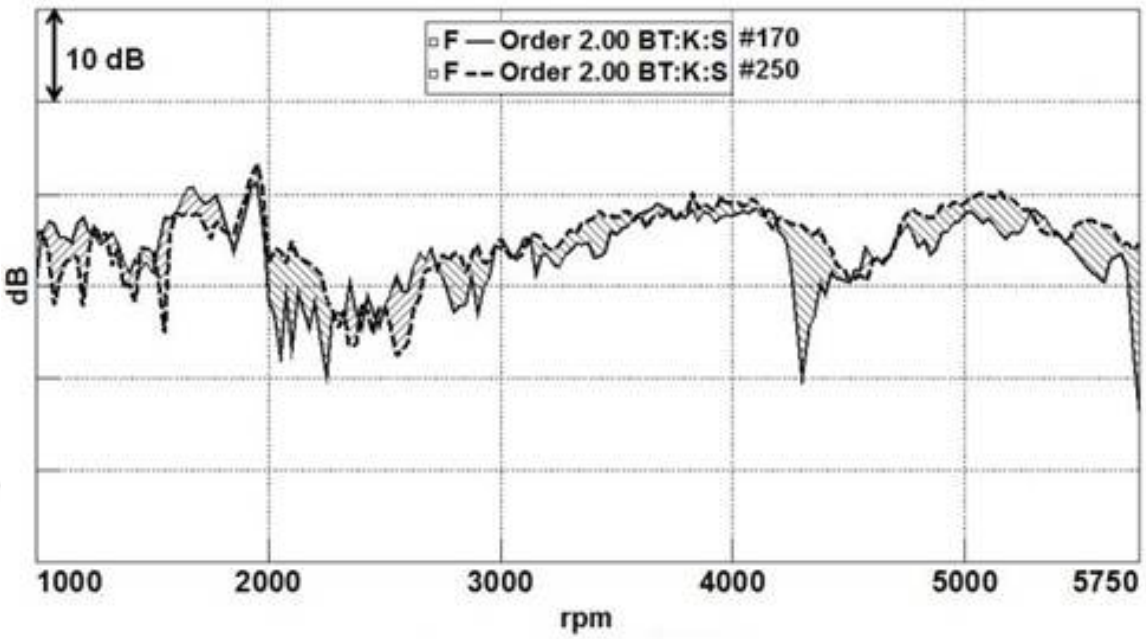


Figure 2.108. Comparison of sound pressure levels measured at BT: K for test vehicles # 170 and # 250

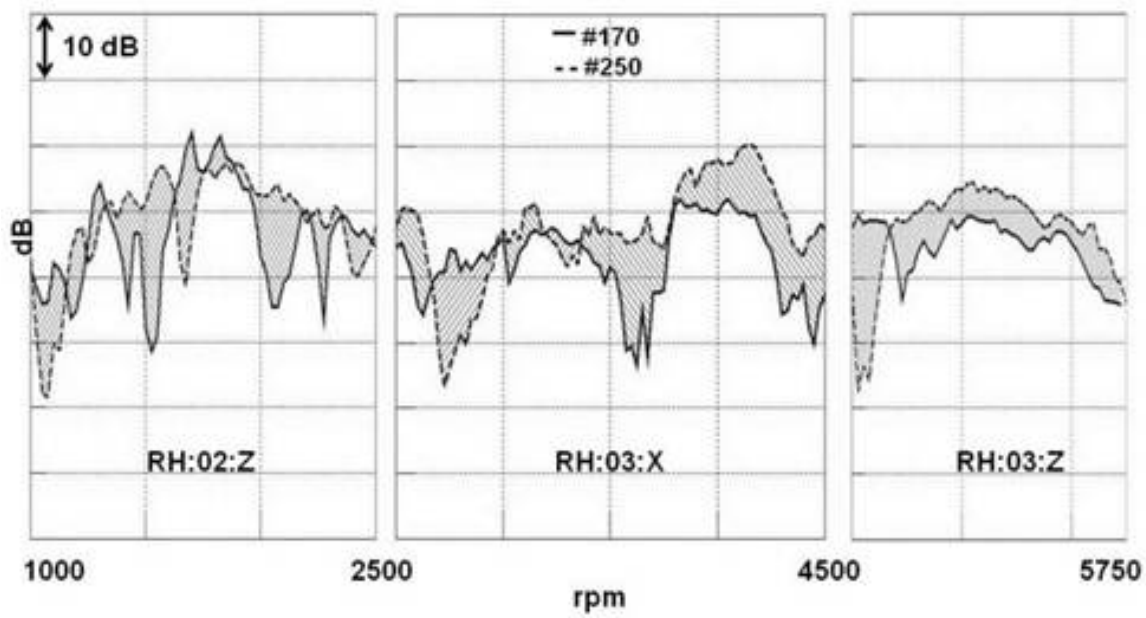


Figure 2.109. Contributions of dominant paths: RH:02:Z, RH:03:X and RH:03:Z predicted at BT: K for test vehicles # 170 and # 250

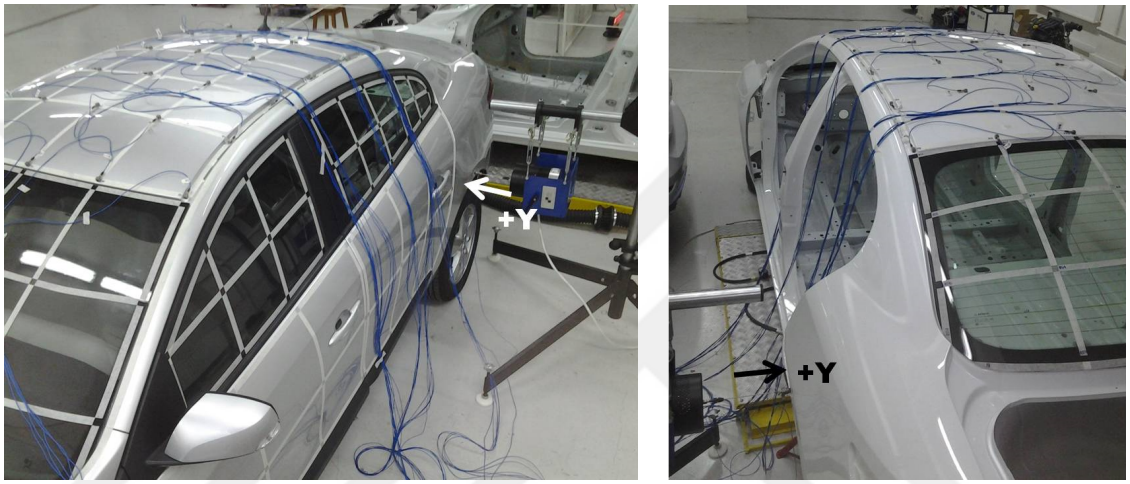
Next, data taken from engine and exhaust mounts are inspected in the following way. Since the contributions of mounts are identified, one can compare the differences between predominant paths. It can be observed from Figure 2.82. that the predominant path for the first booming is the contribution of the mount RH:03 at y-axis. Measured sound pressure levels at target BT: D of two vehicles are compared in Figure 2.106., whereas the predominant contributor path (RH: 03: Y) curves of the two vehicles are given in Figure 2.107. When the curves in Figures 2.106. and 2.107. are observed, it is clearly seen that the SPL variability is introduced by the primer contributor path. Path RH:03:Y is not only the root cause of the first booming, but it is also the cause of inter variability. Moreover, it is seen that the similarities observed at variances are not only valid in the booming region frequency interval. Actually, deviations caused by this contributor affect the whole bandwidth, i.e., not only the amplification differences, but also the resonance and anti-resonance frequencies are ruled by this main contributor.

Inter variability at the other target (BT: K) is assessed in a similar approach. Measured SPL curves of the two vehicles are compared in Figure 2.108. For target BT: K, we have three different dominant paths for the whole bandwidth. As shown in Figure 2.109., the dominant paths are RH:02:Z, RH:03:X and RH:03:Z, in the order of frequency interval.

2.10. Panel Contribution Analysis

Panel contribution analysis is important in the following way. It is assumed that air inside the vehicle cavity is stationary; pressure fluctuations in air generate the sound, if they exist. Actually, the stationary air is excited by means of body panels. Complex frequency response functions and acceleration signals acquired from the body panels are critical, in characterization of vibro-acoustic behavior of the structure. What is more to analyze body panels are also essential in the sense of design modification practices, such as adding extra mass, designing vibration pads and changing interior trims, etc.

For panel contribution analysis, panels surrounding the vehicle cavity are considered; these are roof, windscreen, back screen, doors, floor, fire wall, parcel shelf, and mudguards. A fictitious wireframe is constructed on the vehicle, where panels are treated as independent plates. The same wireframe is also adopted in latter studies, e.g. experimental modal analysis (see Section 4.1). The wireframe that is used to locate sensors is pictured in Figure 2.110.



(a) L38, full vehicle (b) L38, BIW

Figure 2.110. Wireframe used for sensor locations and shaker configuration, where the excitation direction is $+y$-axis

Electro-magnetic shakers (see Section 2.4) are used to excite the structure, in both of BIW and full vehicle tests. In full vehicle test, the engine is also used as an exciter, where all engine rpm are spanned. To use the vehicle's own engine as an exciter is considerable, since the real operating condition is achieved. On the other hand, this test is uncontrollable in the sense of applied forces, i.e. there is no control on exciting forces, so inputs are unknown. In the shaker case, excitation type and applied force is controllable, although it is different from the real operating conditions. The user can generate a specific signal, or use well accepted signal types, such as burst random, sine swept, periodic chirp, etc. The time period for the signal and magnitude of forces are also user defined. Consequently, engine and shaker driven tests have advantages and drawbacks; hence, it is determined to use both of them. One more basic difference is the boundary conditions applied during tests. In full vehicle case, tests are performed,

when the vehicle is on its wheels, and the whole bandwidth (i.e. up to 200 Hz=6000 rpm) is spanned, using road test mock up explained in Section 2.6. In BIW case, the structure is supported by four air springs to achieve a free boundary condition. Free boundary condition is important in the following way: experimental modal analysis and computational analysis are also performed under free boundary conditions, where reasons are explained Sections 3.3.2 and 4.1. In Figure 2.111. air springs and the shaker that excites the system in z-direction are shown.



Figure 2.111. BIW test configuration, air springs and the shaker that excites the system in z-direction

For full vehicle test, seats, carpet, in brief the whole interior trim is removed. The aim is to gain access to sheet parts to locate sensors. At this point, the question in mind is the loss of originality, i.e. the vehicle is changed. This is true; if sound pressure levels are acquired, results will be slightly different, but this is not the case. In this state, only panel accelerations are measured. As expected, and partially verified (only roof sheet is considered) by previous mock up test, acceleration results are identical,

whether interior trim parts are present, or removed.



Figure 2.112. Full vehicle test configuration, interior trim parts are removed

For both structures, same driving point chosen on the left mudguard of test structure is used. As shown in Figure 2.110., excitation is applied through the stinger of shaker in y-direction. The driving point is selected depending on the results of various tests, after the following requirements are met: (i) the location of driving point must be identical in full vehicle and BIW tests; (ii) excitation of all structural modes must be achieved in the frequency bandwidth of interest; (iii) ordinary coherence value should be read at least 0,7. Shaker is driven, using burst random signal, where the average of 100 excitations is accepted. Measurements are performed up to 1024 Hz, with a 0,5 frequency resolution, i.e. 2048 spectral lines are sampled. In engine run up test, signals are weighted, using Hanning window, whereas uniform windowing is adopted in shaker driven measurements. Accelerometers are fixed to sheet using a special purpose wax, which is effective in measurements up to 2 kHz. In BIW tests, a second shaker is

employed to achieve excitation at z-direction, as indicated in Figure 2.111. The number of measurement locations is stated in Table 2.5., whereas results of engine driven full vehicle test are given in Figures 2.113. to 2.123.

Table 2.5. Number of measurement locations in engine driven full vehicle test

Back floor	20	Front floor	14	Parcel shelf	28
Back screen	20	Front left door	23	Front right door	23
Rear left door	32	Rear right door	32	Roof	30
Windscreen	20	Rear mudguard	2	Total	244

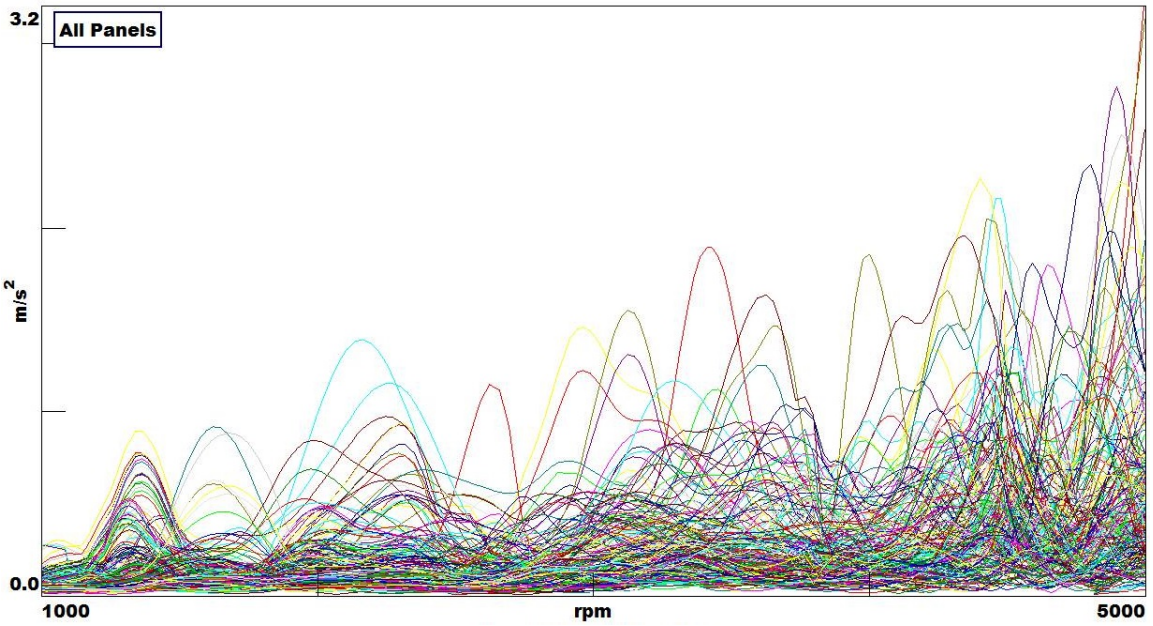


Figure 2.113. Engine driven full vehicle test, acceleration of body panels: all of the panels

The results of shaker driven full vehicle test are given in Figures 2.124. to 2.134. The number of measurement locations is identical to engine driven test. To assess the reliability of the test, ordinary coherence functions are monitored. As shown in Figures 2.135. to 2.144., coherence functions take values well above 0.9.

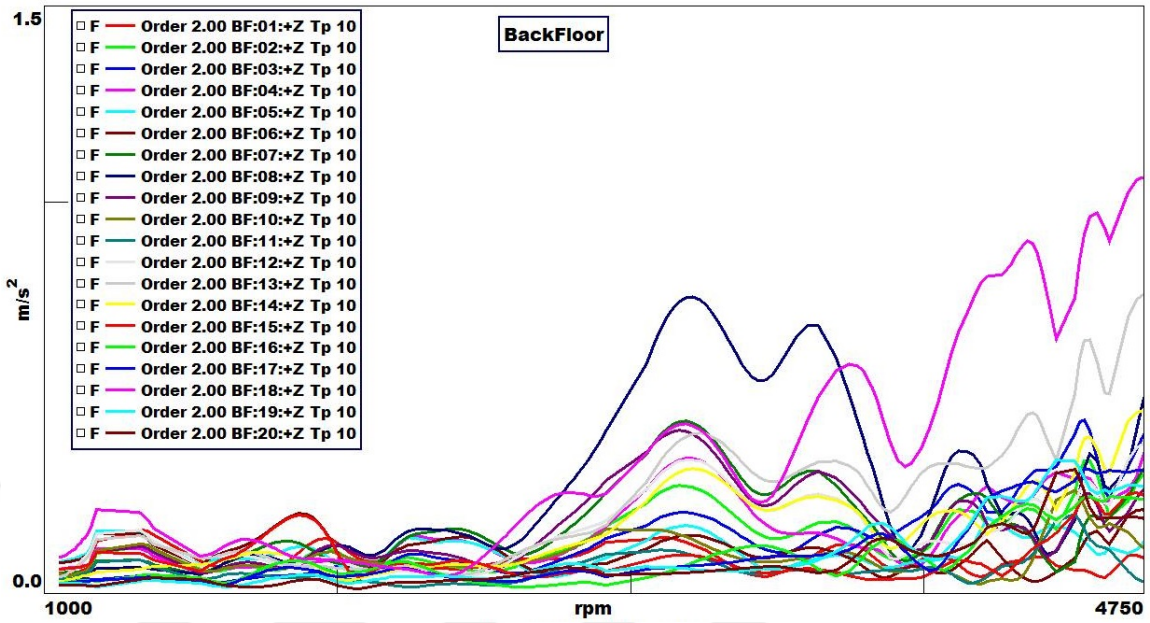


Figure 2.114. Engine driven full vehicle test, acceleration of body panels: back floor

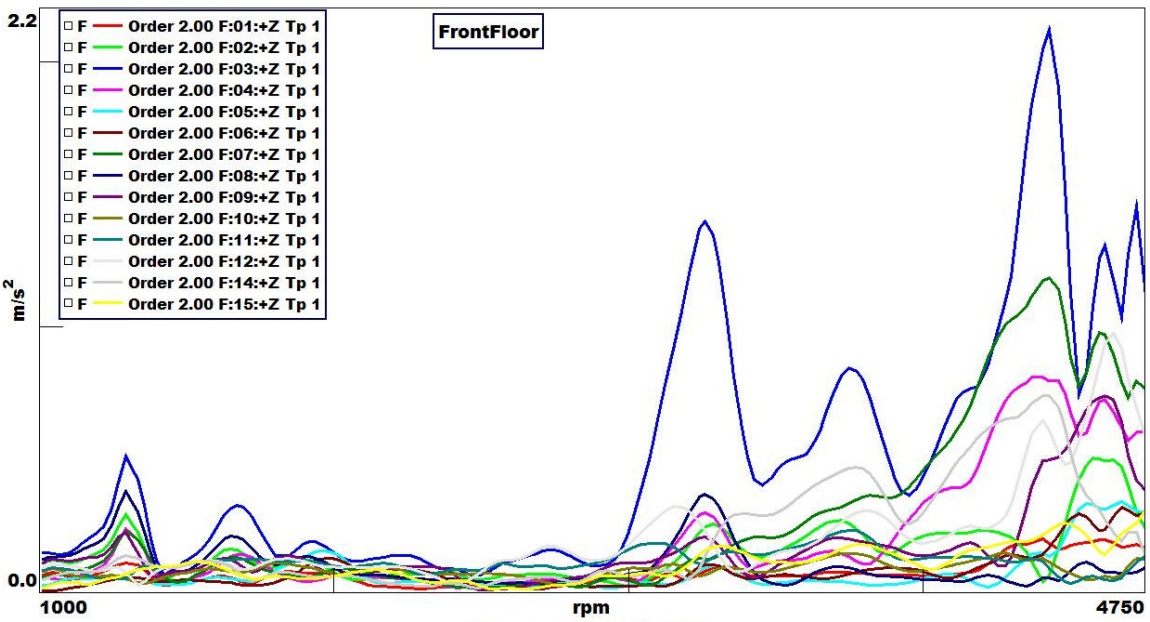


Figure 2.115. Engine driven full vehicle test, acceleration of body panels: front floor

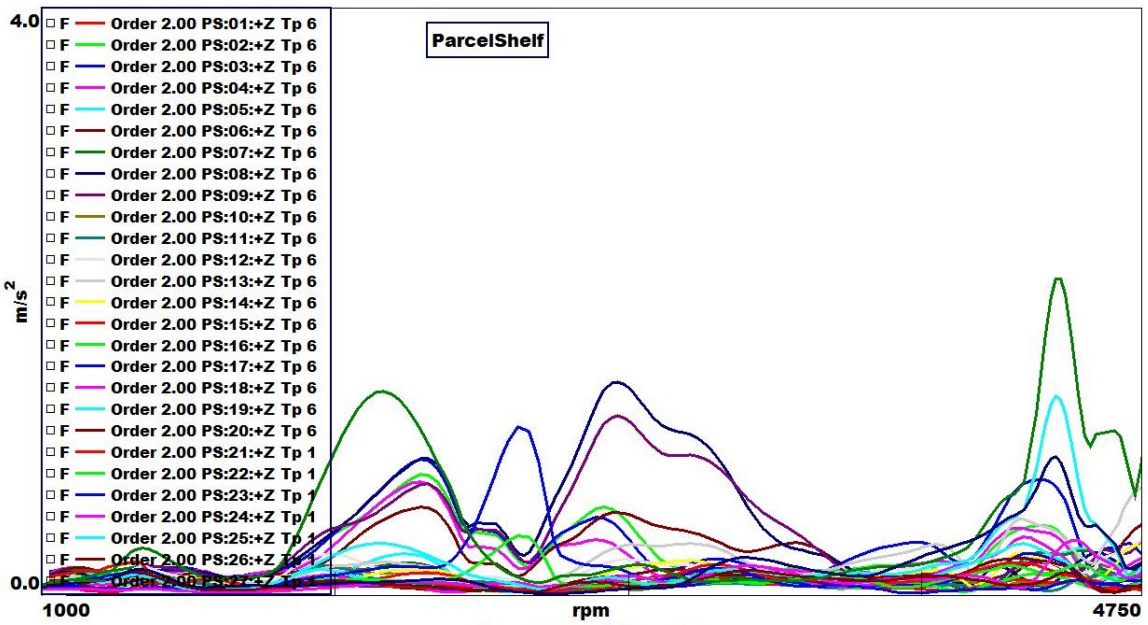


Figure 2.116. Engine driven full vehicle test, acceleration of body panels: parcel shelf

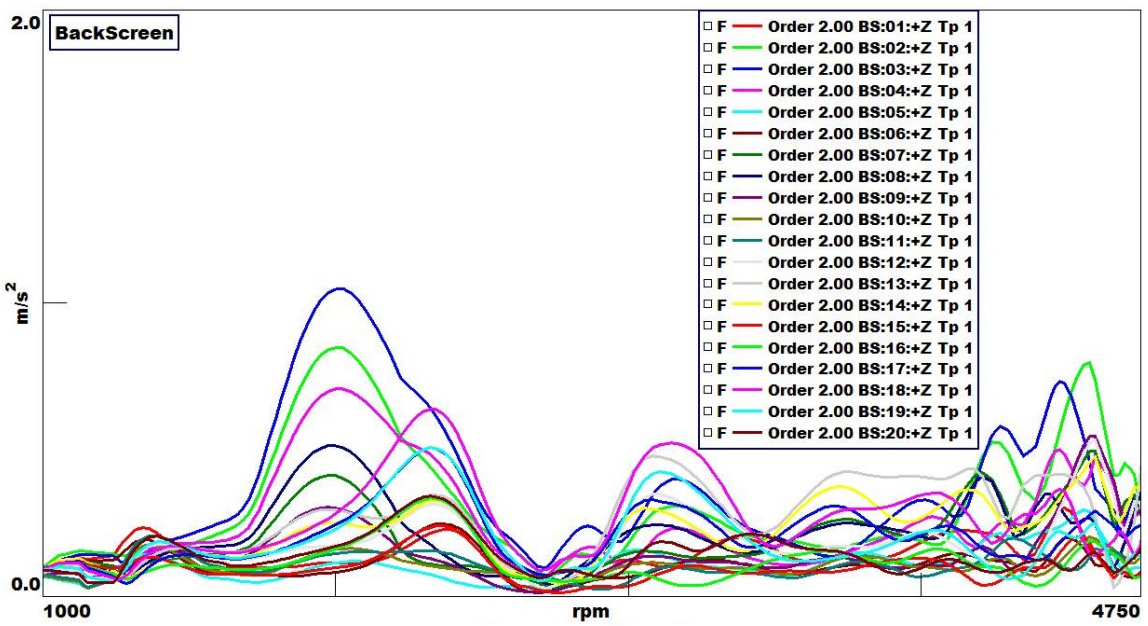


Figure 2.117. Engine driven full vehicle test, acceleration of body panels: back screen

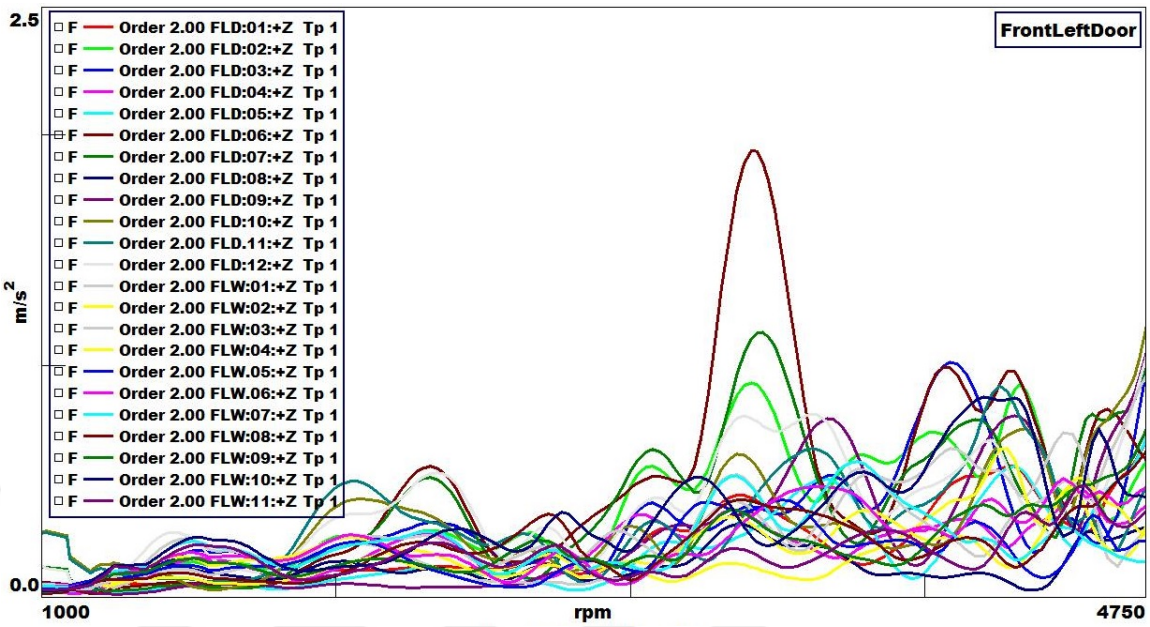


Figure 2.118. Engine driven full vehicle test, acceleration of body panels: front left door

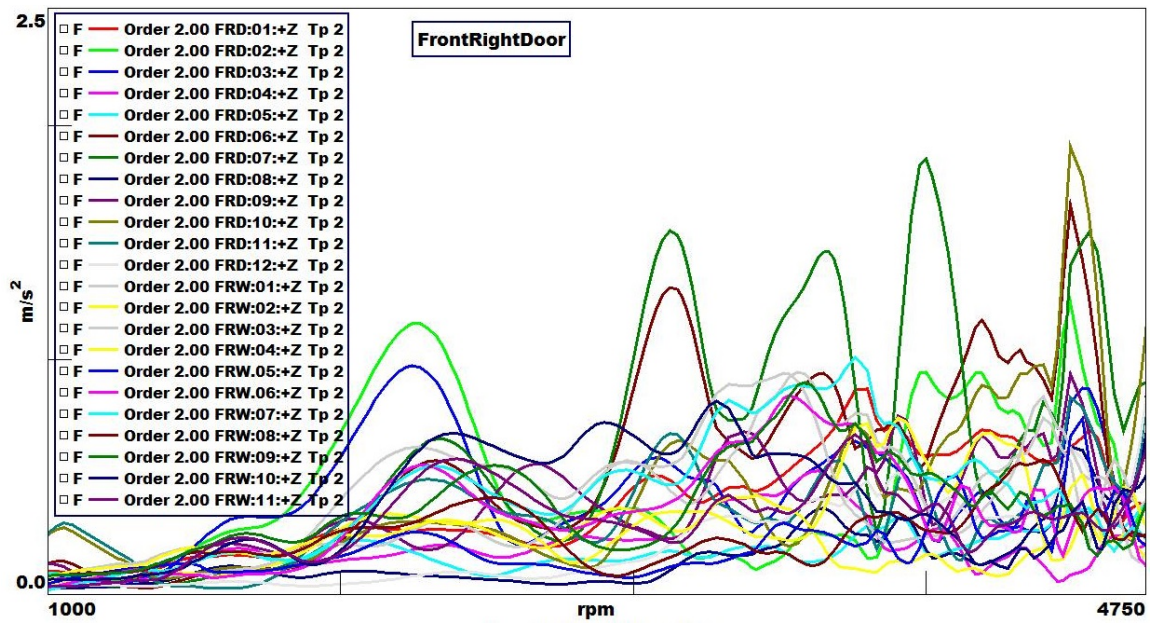


Figure 2.119. Engine driven full vehicle test, acceleration of body panels: front right door

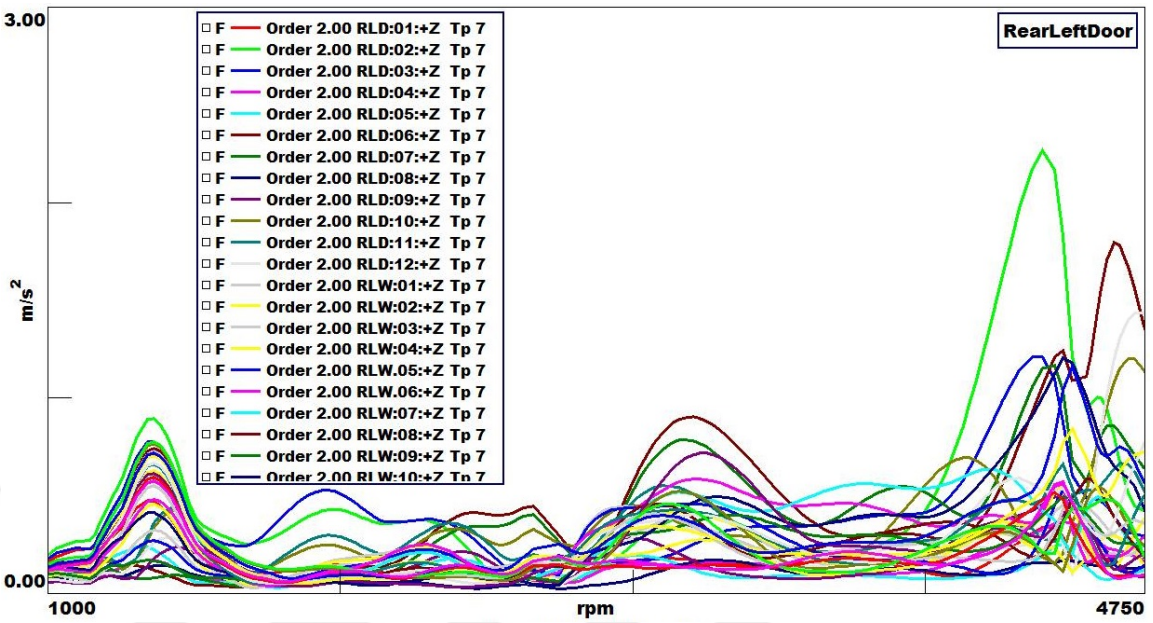


Figure 2.120. Engine driven full vehicle test, acceleration of body panels: rear left door

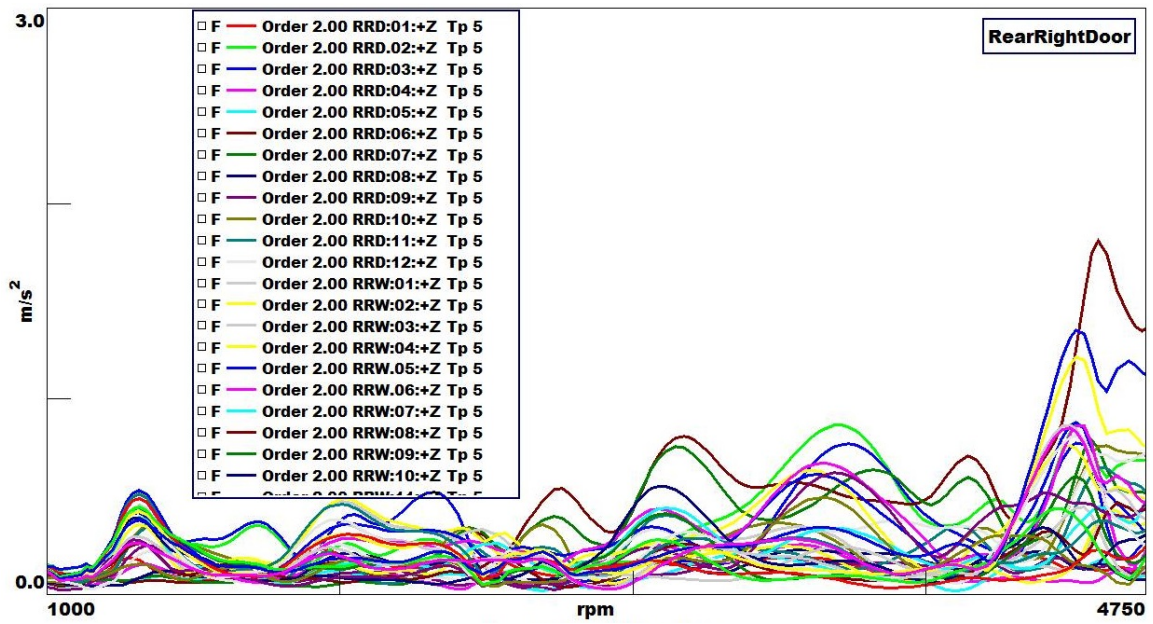


Figure 2.121. Engine driven full vehicle test, acceleration of body panels: rear right door

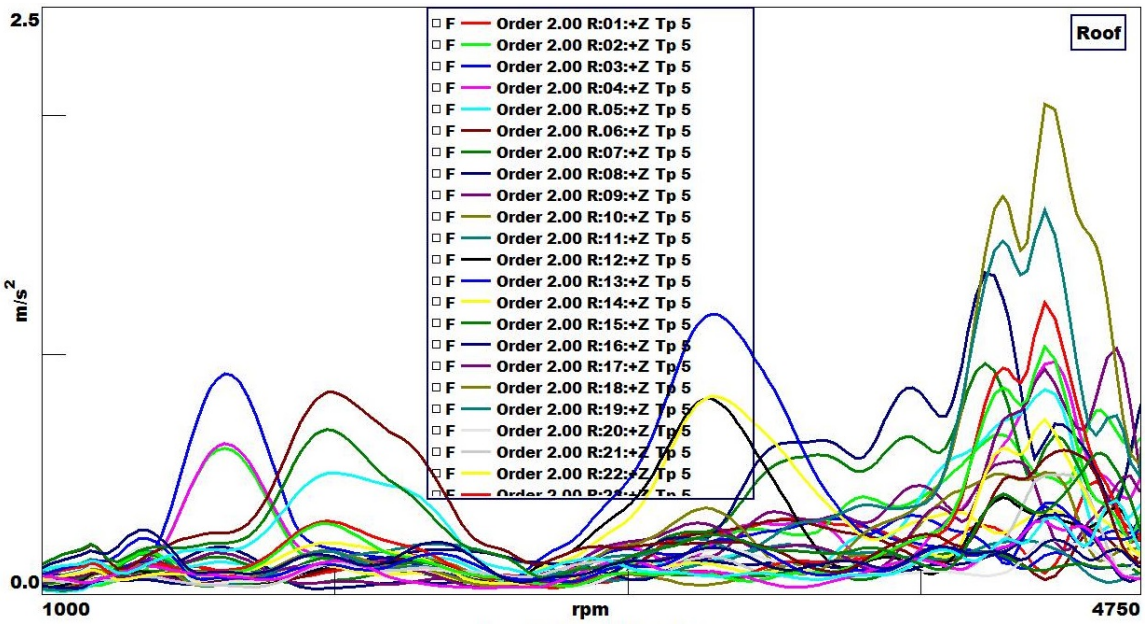


Figure 2.122. Engine driven full vehicle test, acceleration of body panels: roof

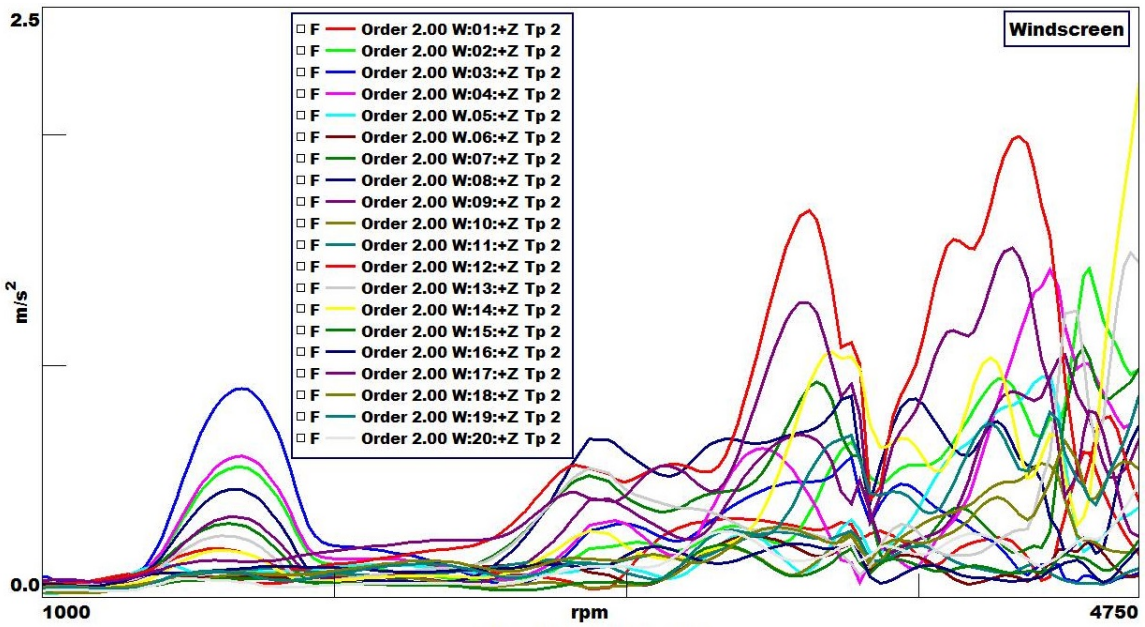


Figure 2.123. Engine driven full vehicle test, acceleration of body panels: windscreen

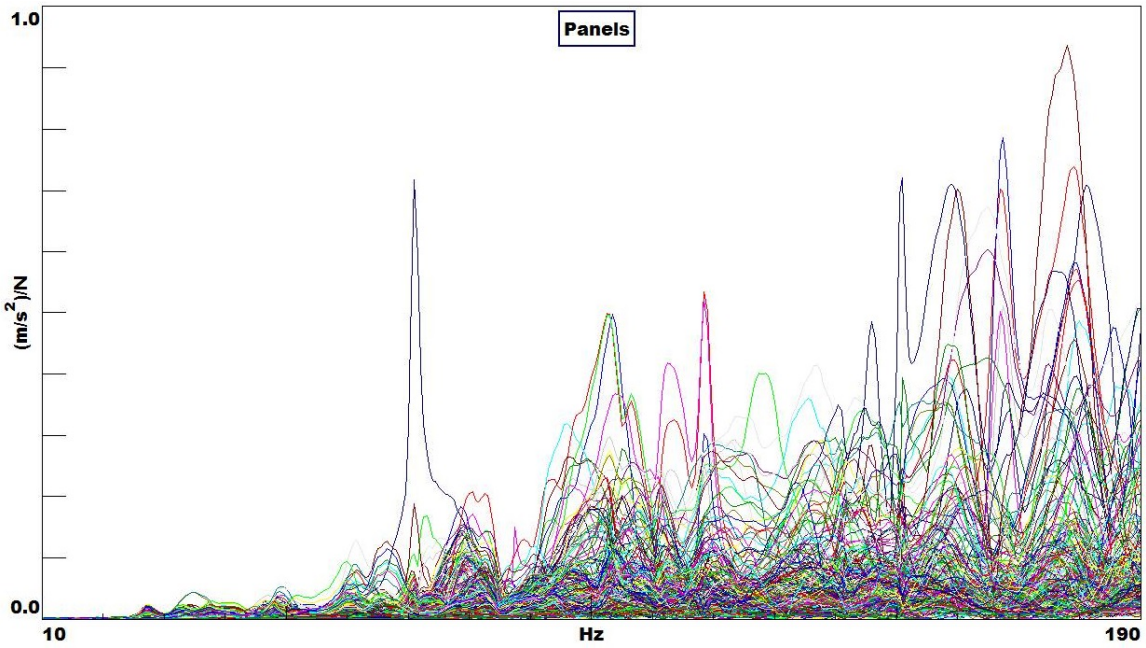


Figure 2.124. Shaker driven full vehicle test, acceleration of body panels: all of the panels

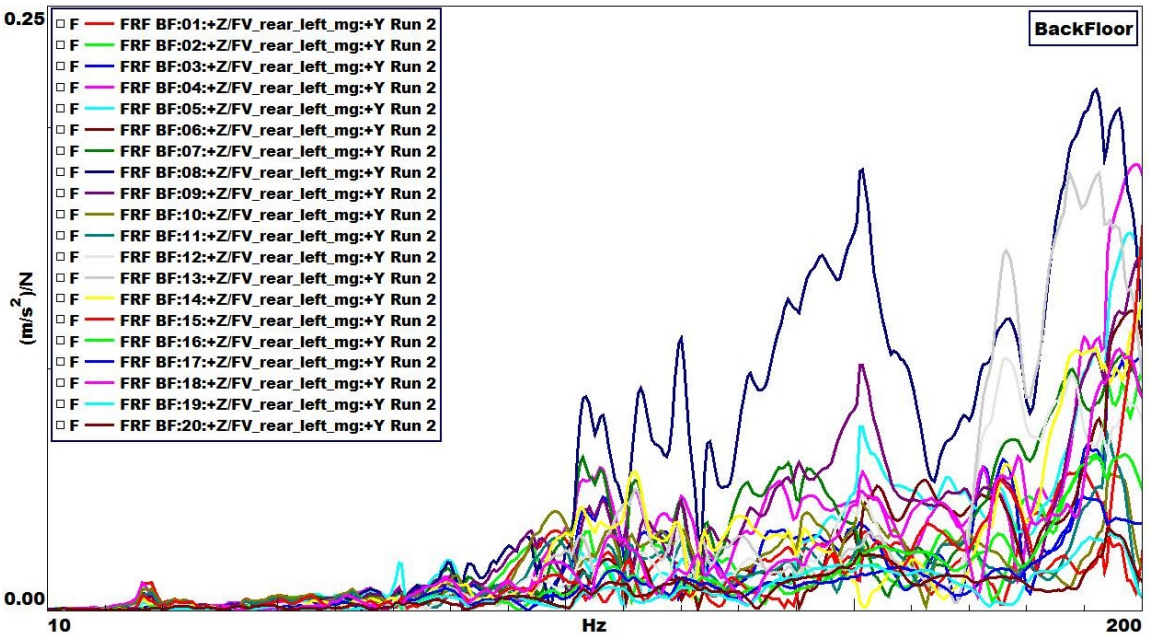


Figure 2.125. Shaker driven full vehicle test, acceleration of body panels: back floor

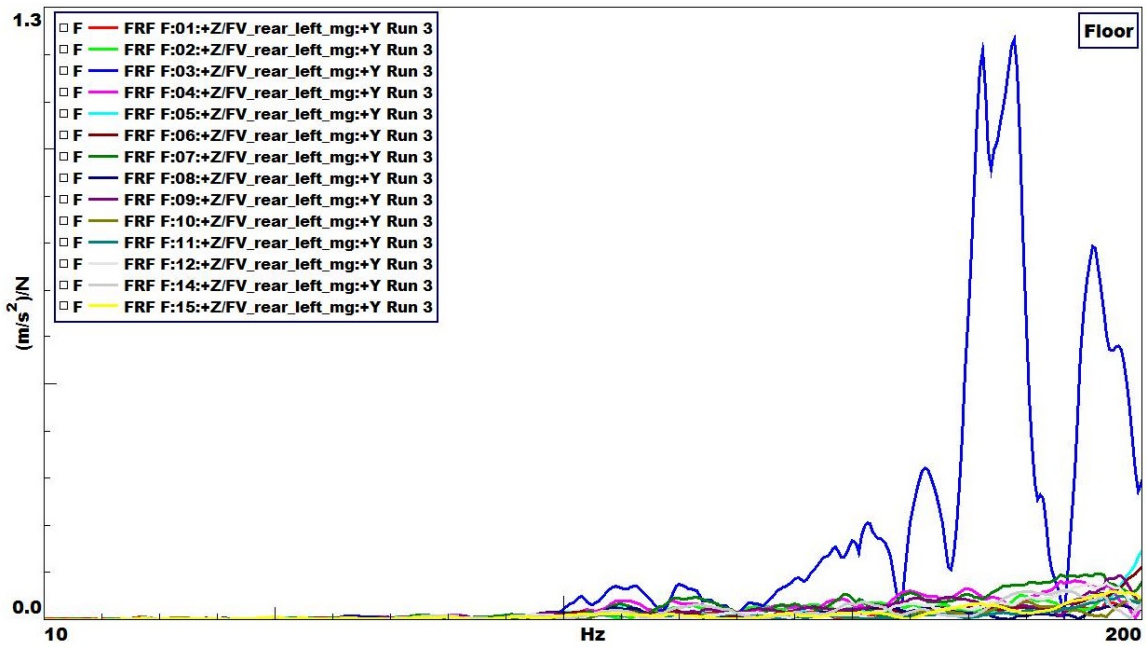


Figure 2.126. Shaker driven full vehicle test, acceleration of body panels: front floor

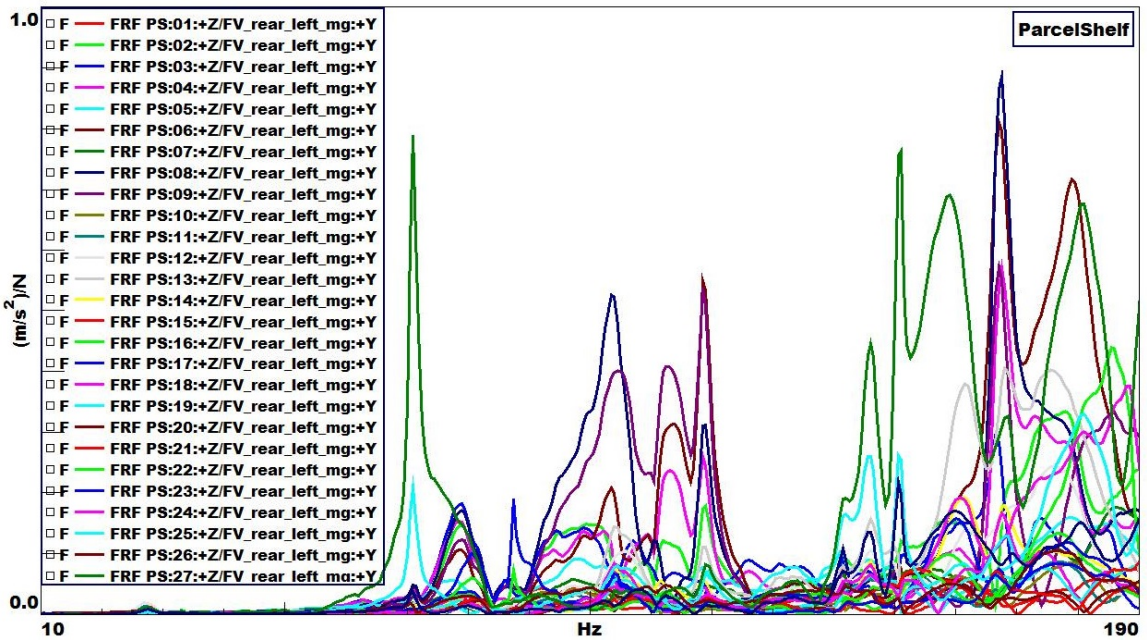


Figure 2.127. Shaker driven full vehicle test, acceleration of body panels: parcel shelf

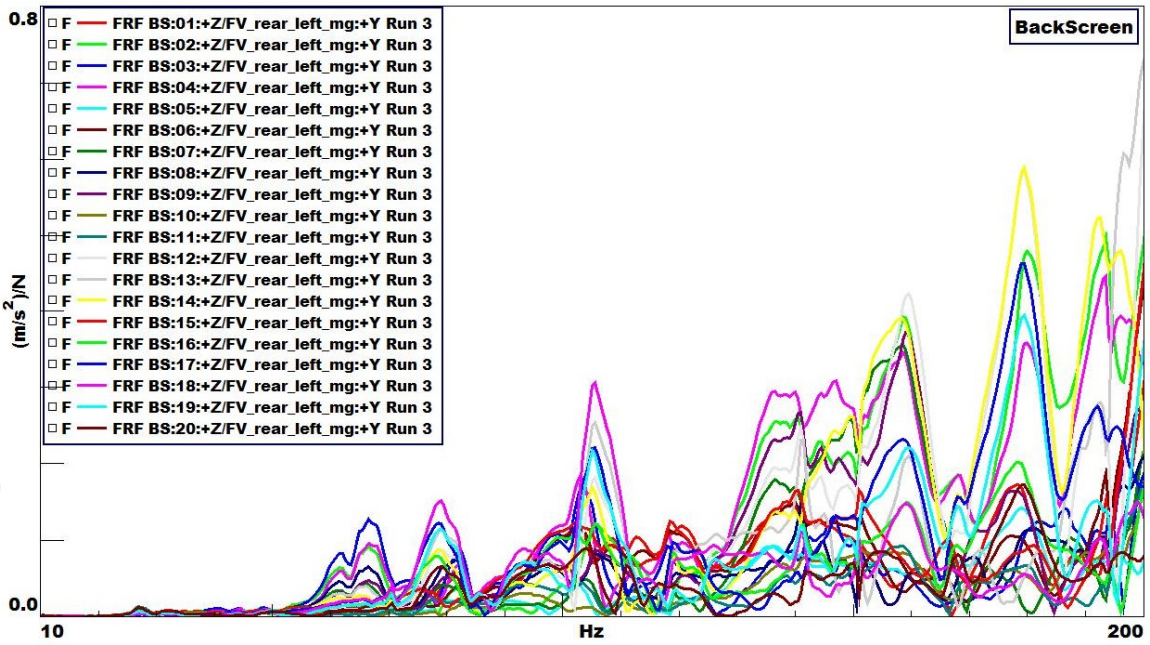


Figure 2.128. Shaker driven full vehicle test, acceleration of body panels: back screen

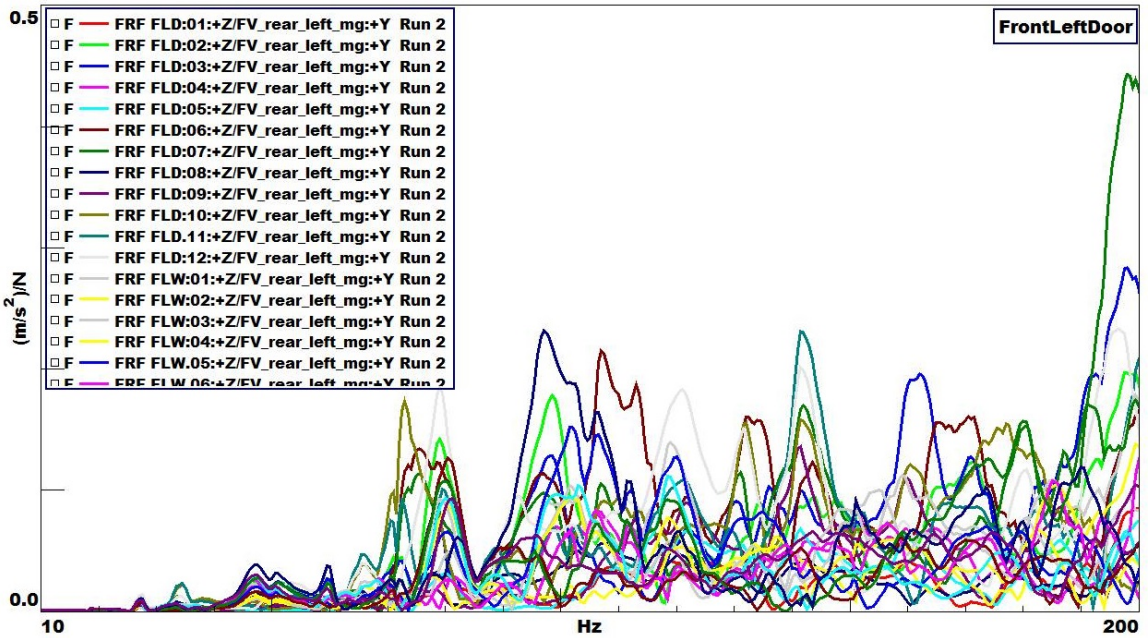


Figure 2.129. Shaker driven full vehicle test, acceleration of body panels: front left door (FLD)

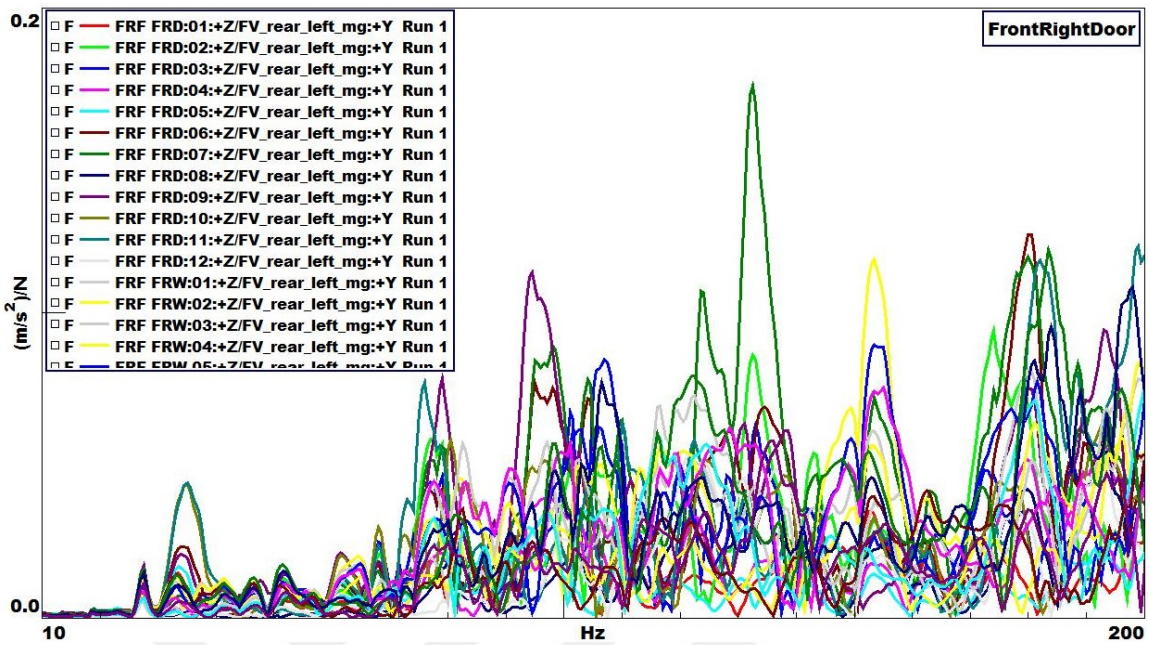


Figure 2.130. Shaker driven full vehicle test, acceleration of body panels: front right door (FRD)

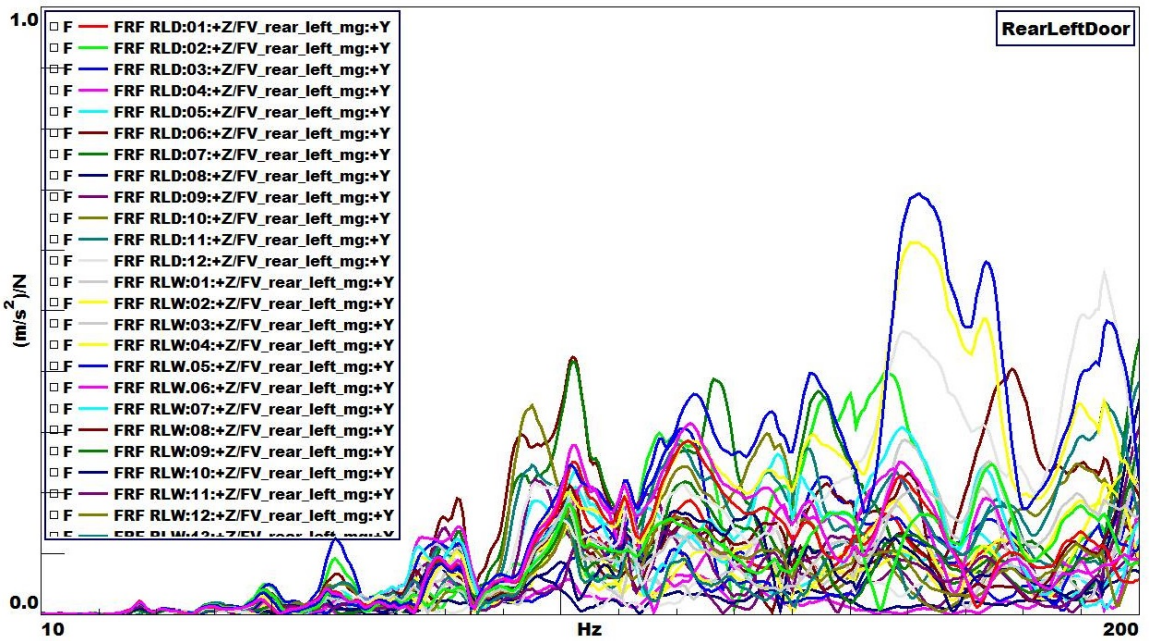


Figure 2.131. Shaker driven full vehicle test, acceleration of body panels: rear left door (RLD)

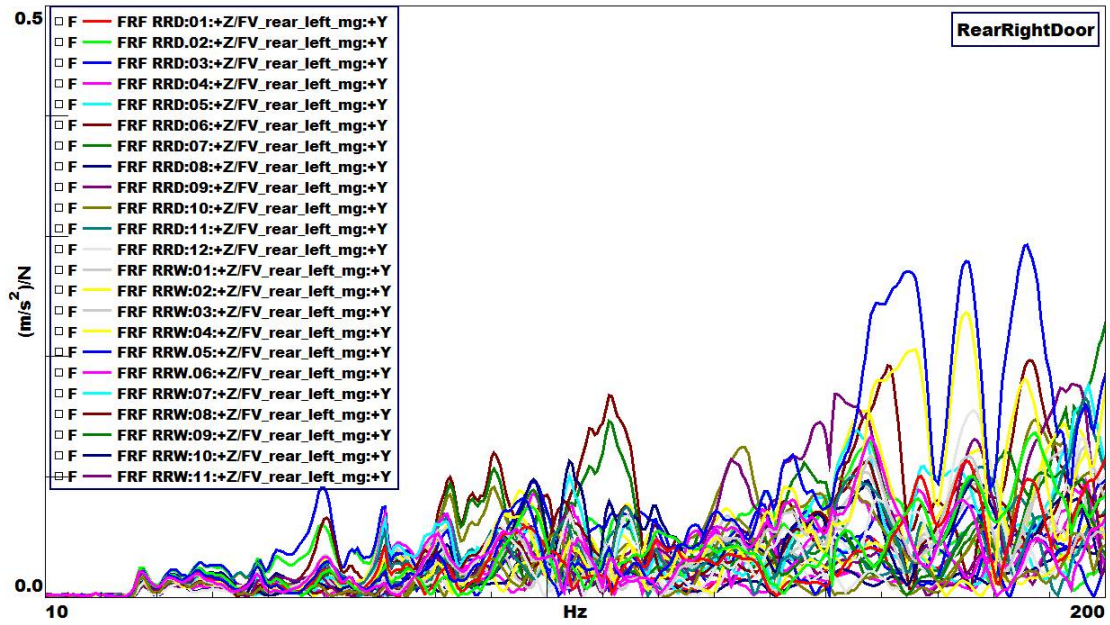


Figure 2.132. Shaker driven full vehicle test, acceleration of body panels: rear right door (RRD)

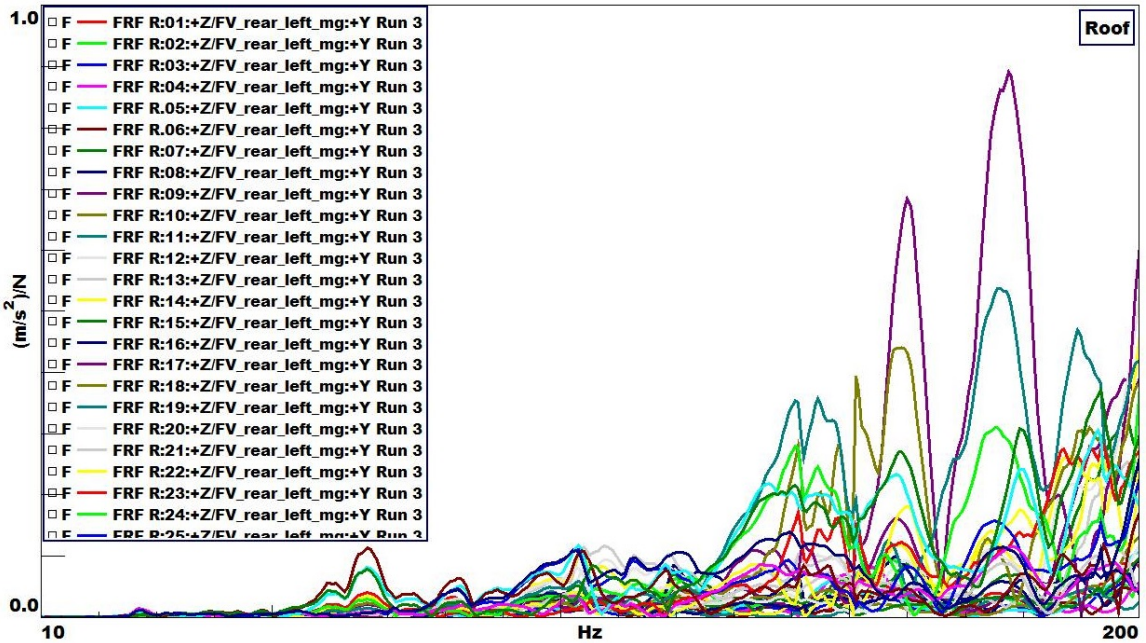


Figure 2.133. Shaker driven full vehicle test, acceleration of body panels: roof

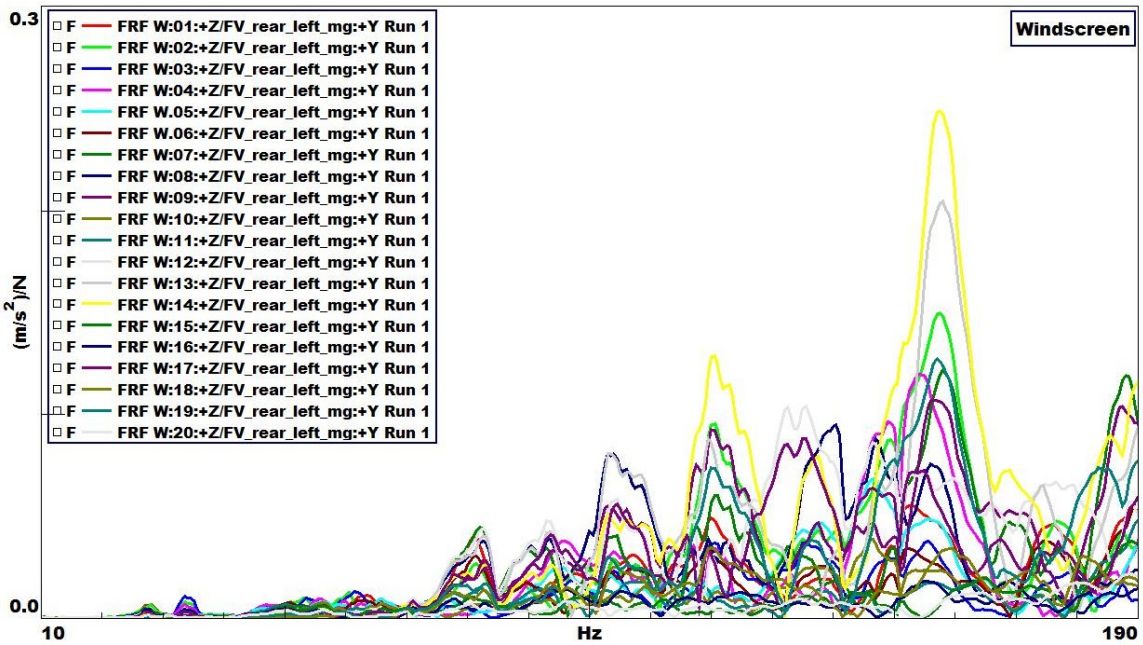


Figure 2.134. Shaker driven full vehicle test, acceleration of body panels: windscreen

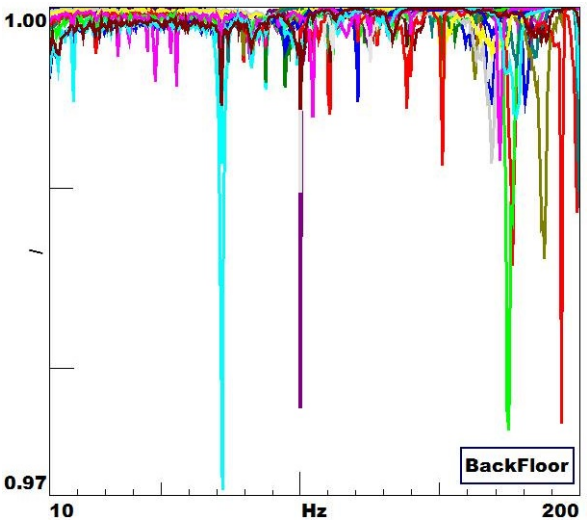


Figure 2.135. Coherence, back floor

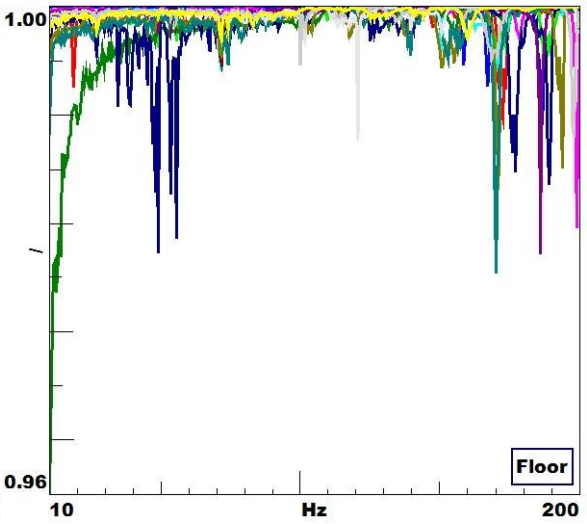


Figure 2.136. Coherence, front floor

The results of shaker driven BIW test are given in Figures 2.145. to 2.151. The number of measurement locations is tabulated in Table 2.6. To assess the reliability of the test, ordinary coherence functions are monitored. As shown in Figures 2.152. to 2.158., coherence functions take values well above 0.9.

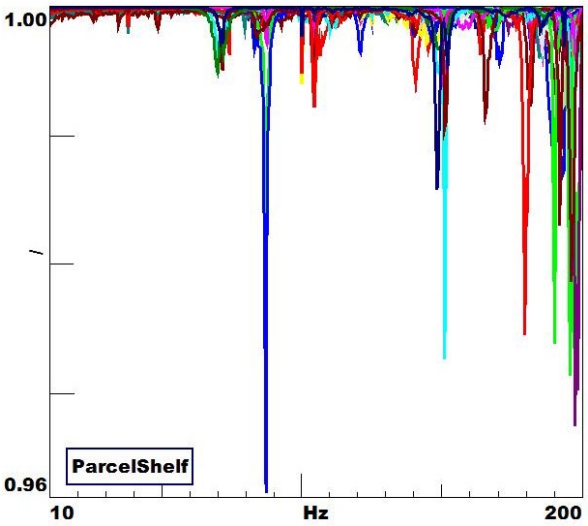


Figure 2.137. Coherence, parcel shelf

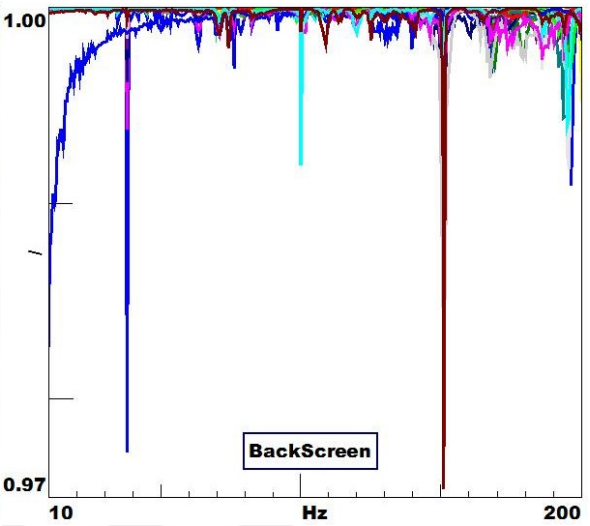


Figure 2.138. Coherence, back screen

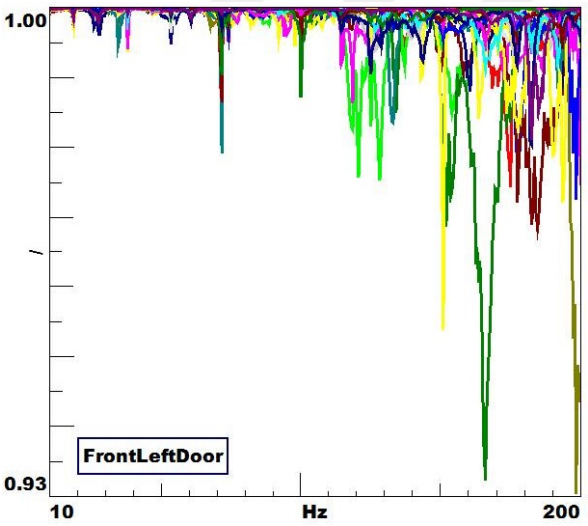


Figure 2.139. Coherence, front left door

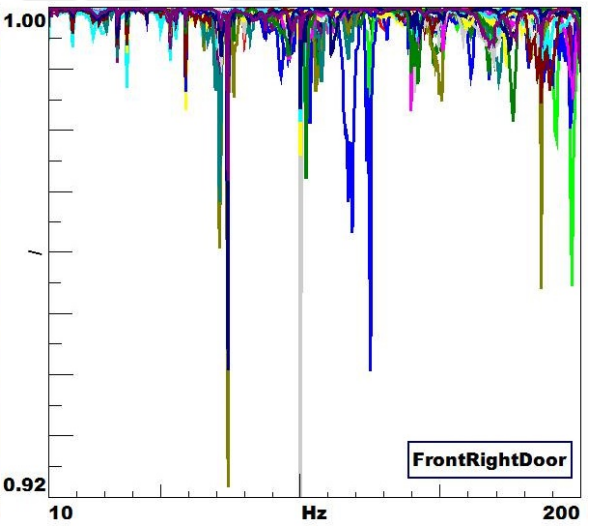


Figure 2.140. Coherence, front right door

Table 2.6. Number of measurement locations in shaker driven BIW test

Back floor	20	Front floor	20	Parcel shelf	28
Back screen	20	Firewall	23	Roof	30
Windscreen	20	Rear mudguard	2	Total	163

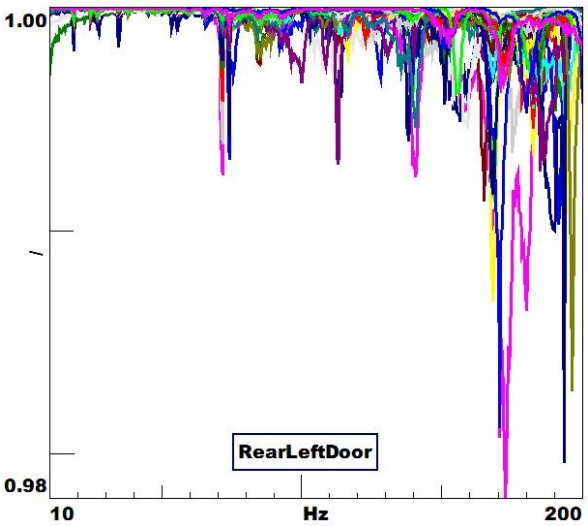


Figure 2.141. Coherence, rear left door

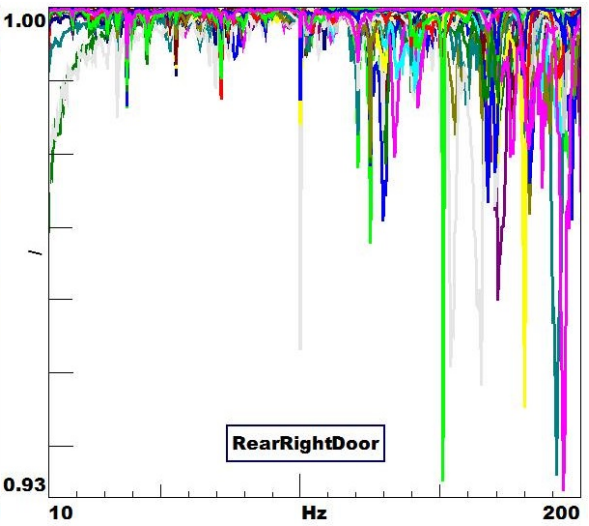


Figure 2.142. Coherence, rear right door

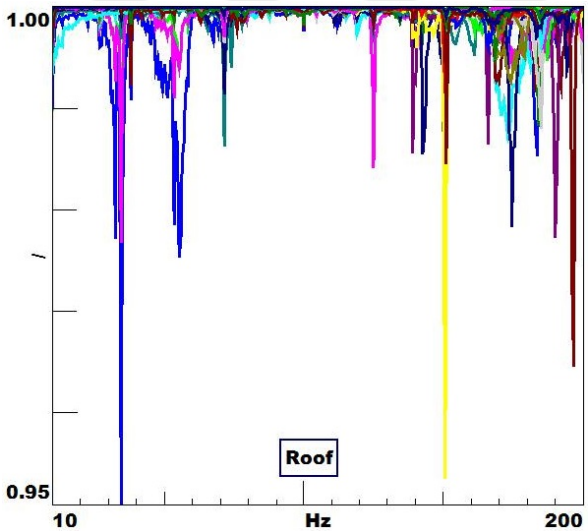


Figure 2.143. Coherence, roof

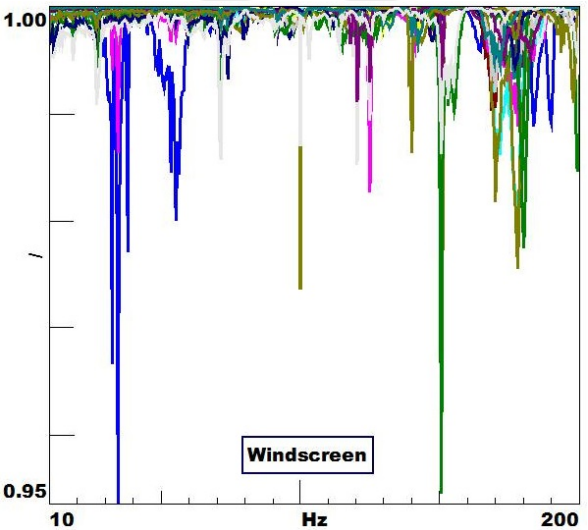


Figure 2.144. Coherence, windscreen

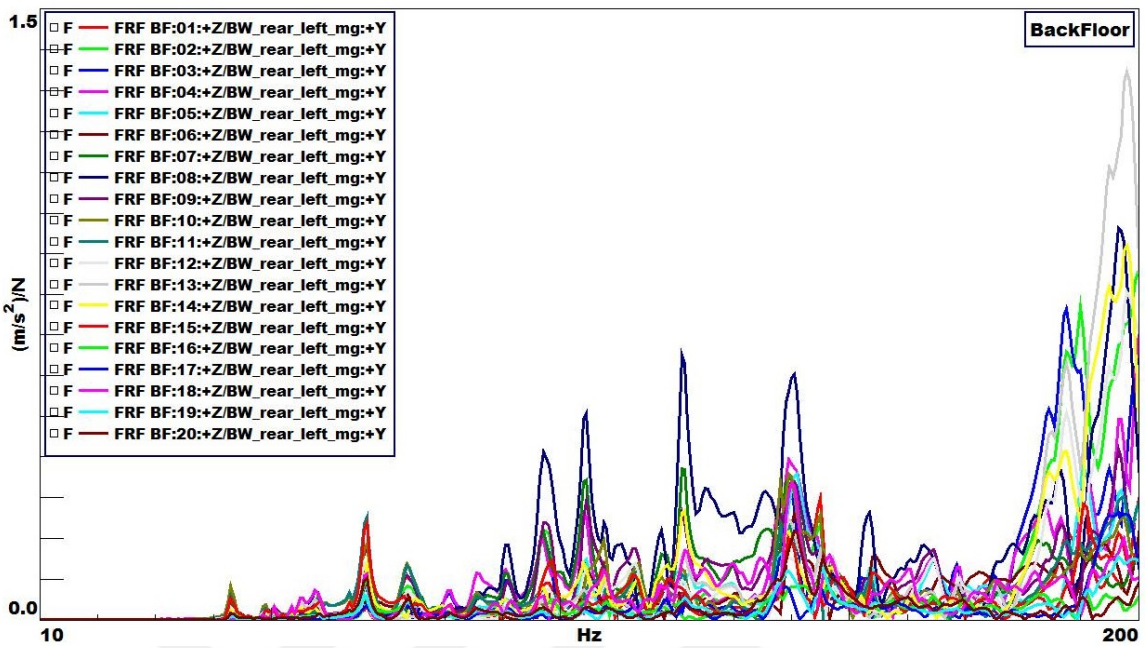


Figure 2.145. Shaker driven BIW test, acceleration of body panels: back floor

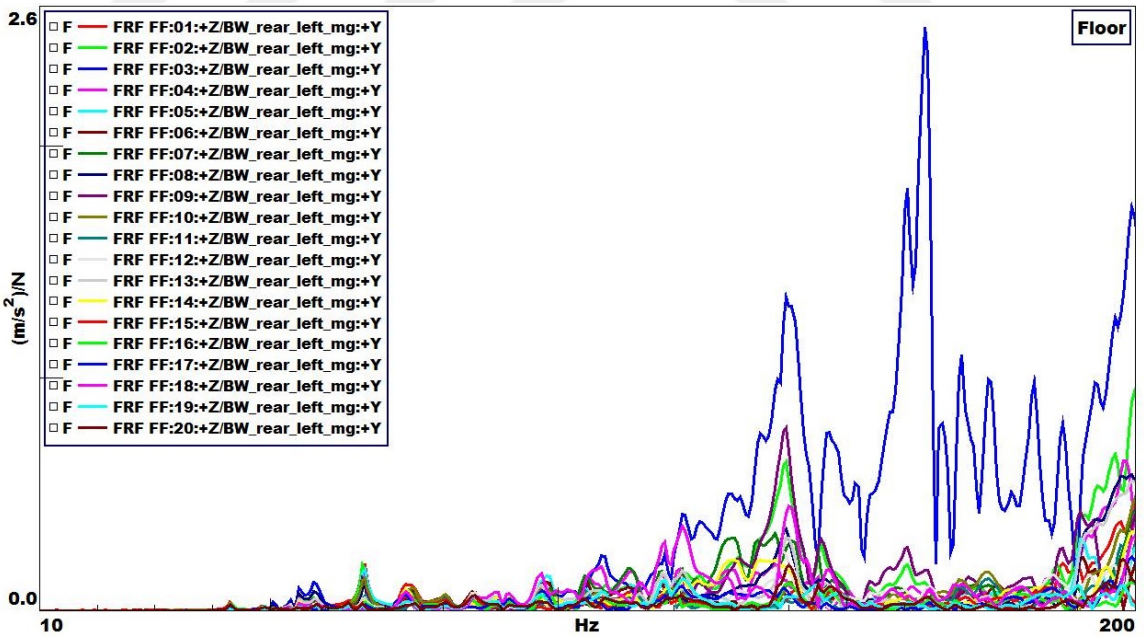


Figure 2.146. Shaker driven BIW test, acceleration of body panels: front floor

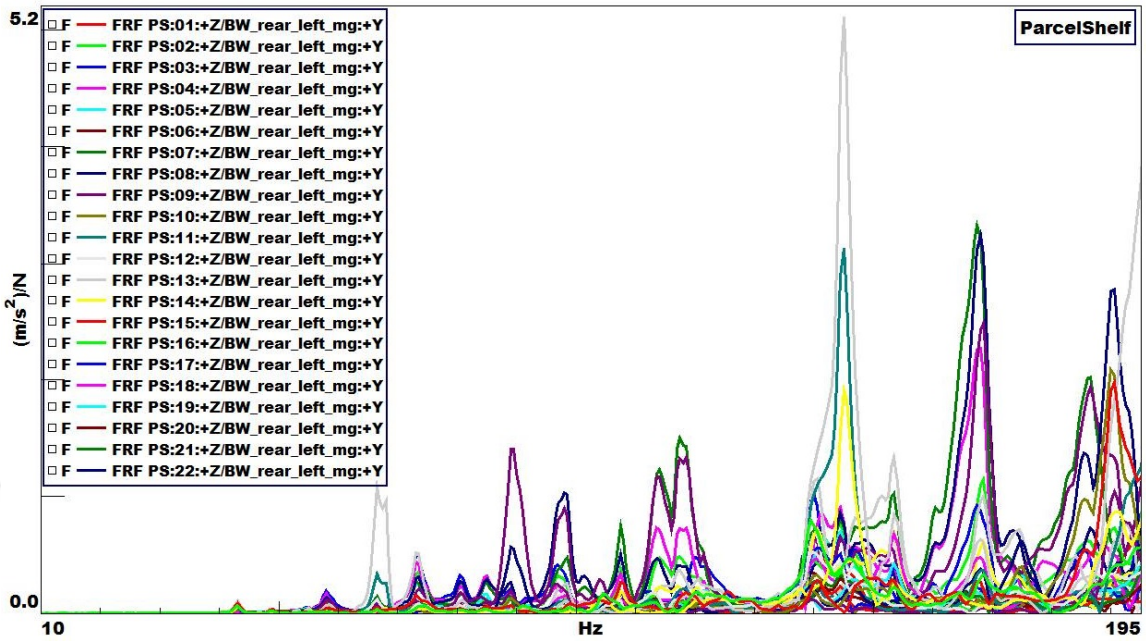


Figure 2.147. Shaker driven BIW test, acceleration of body panels: parcel shelf

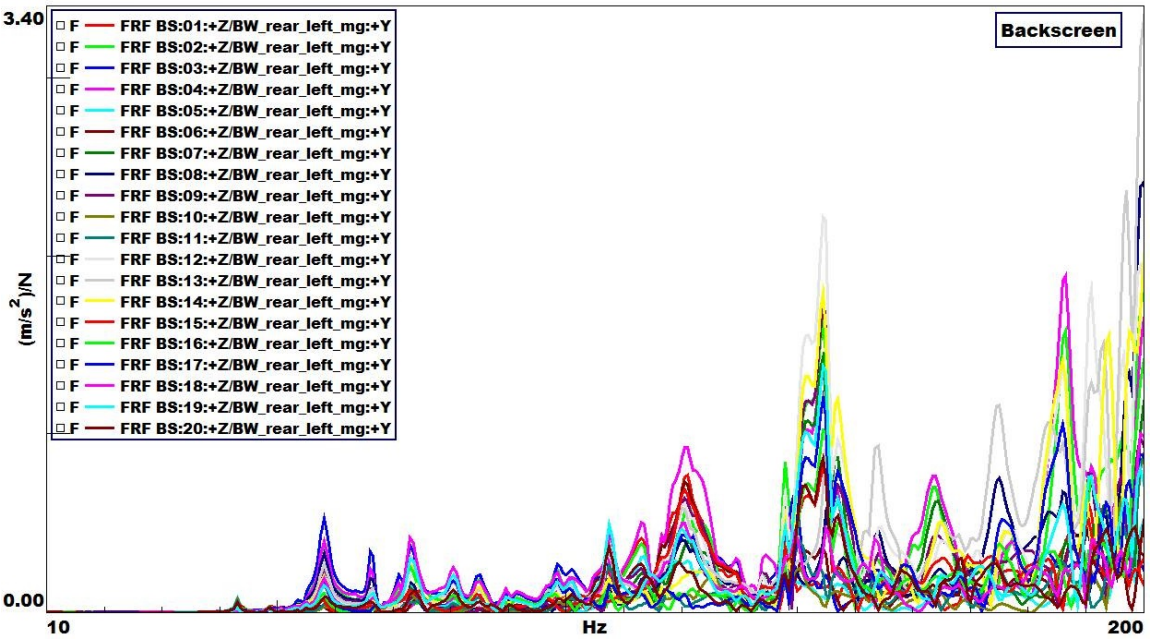


Figure 2.148. Shaker driven BIW test, acceleration of body panels: back screen

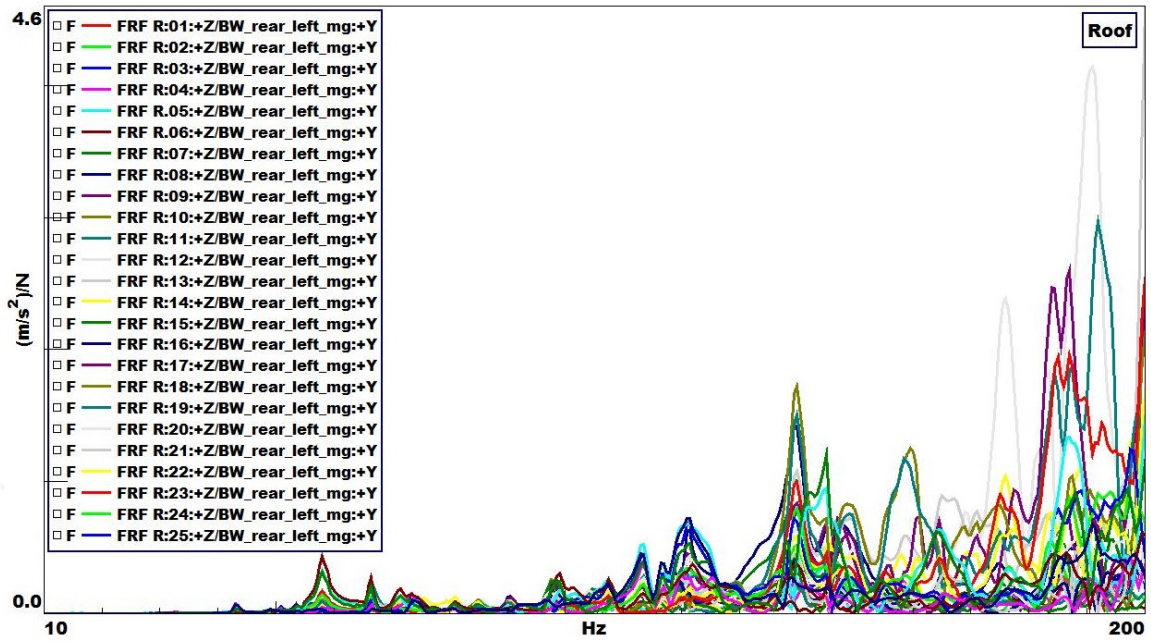


Figure 2.149. Shaker driven BIW test, acceleration of body panels: roof

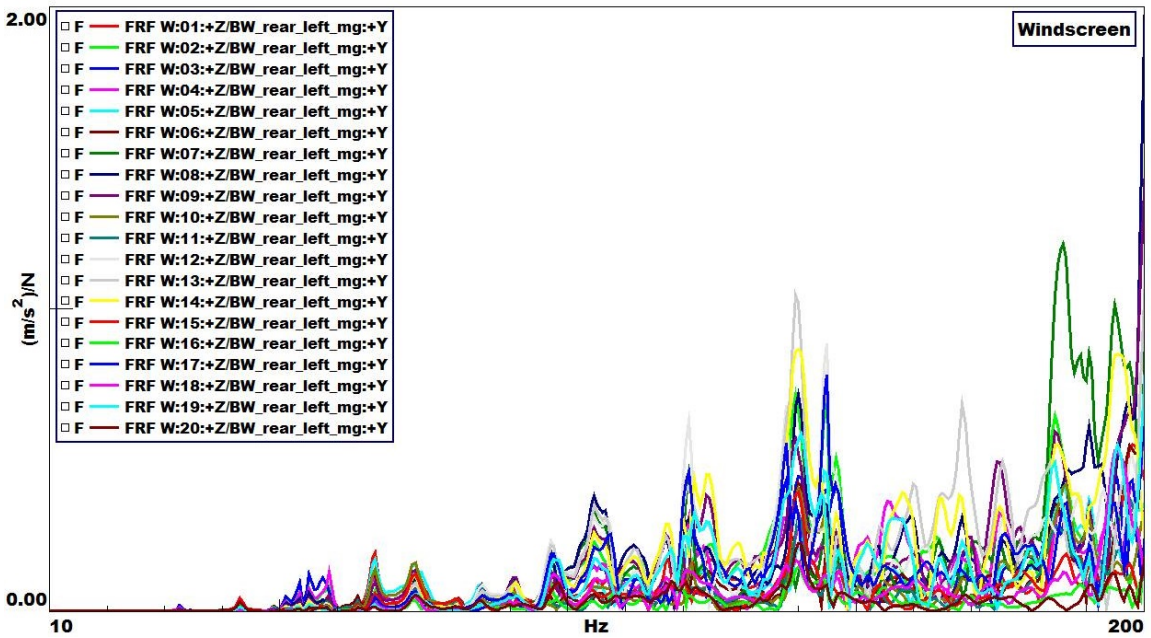


Figure 2.150. Shaker driven BIW test, acceleration of body panels: windscreen

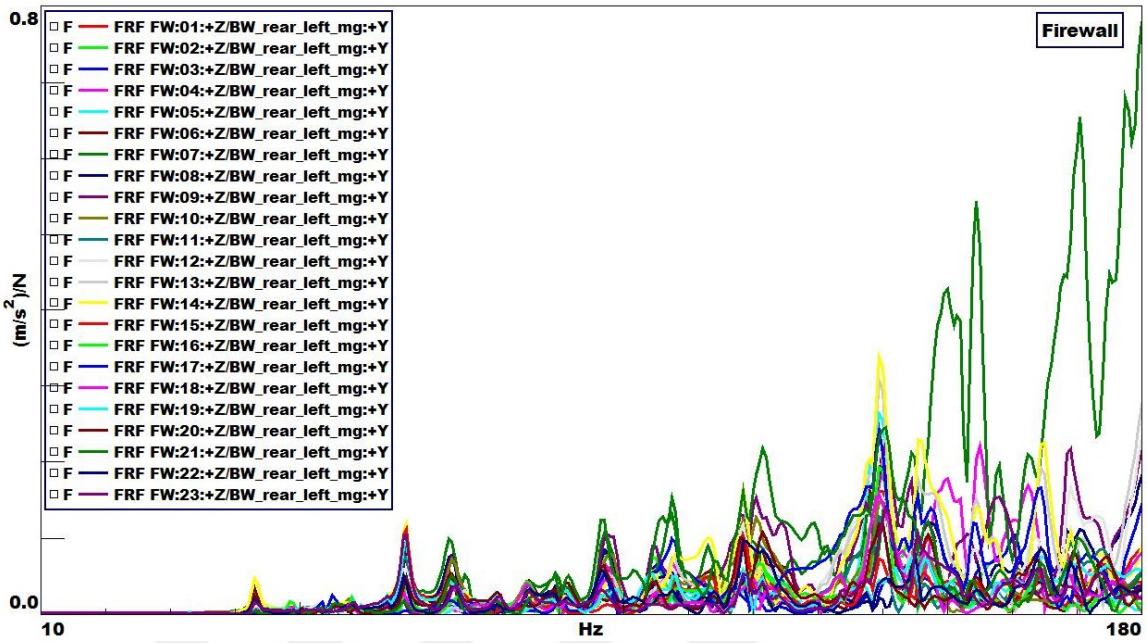


Figure 2.151. Shaker driven BIW test, acceleration of body panels: firewall

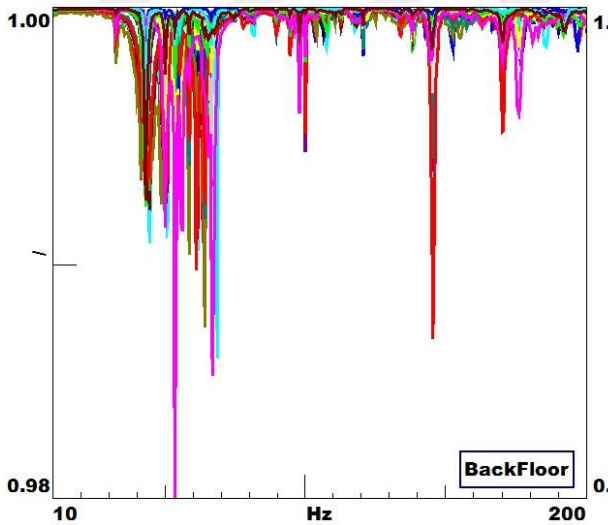


Figure 2.152. Coherence, back floor

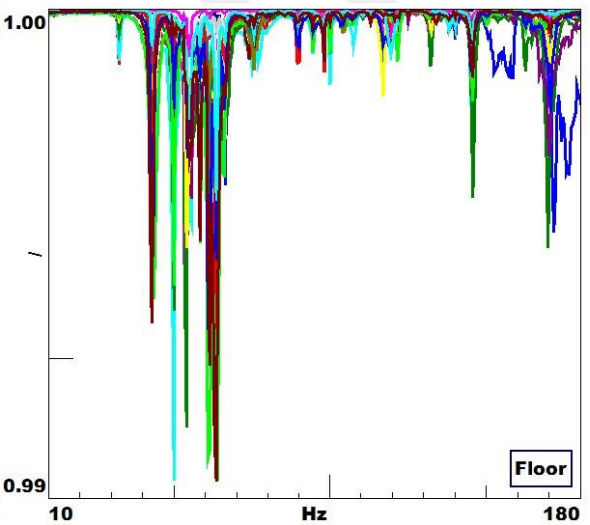


Figure 2.153. Coherence, front floor

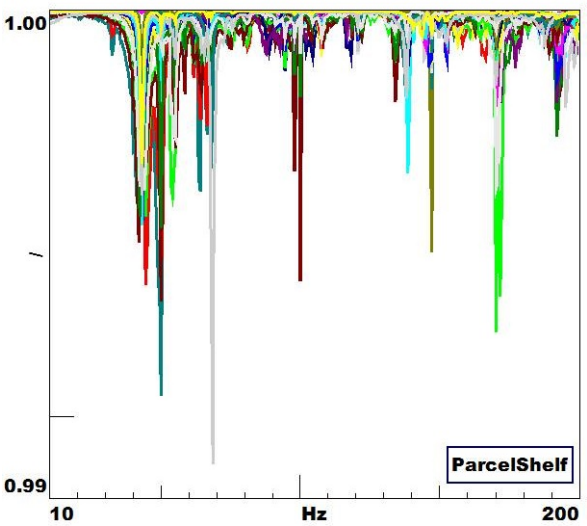


Figure 2.154. Coherence, parcel shelf

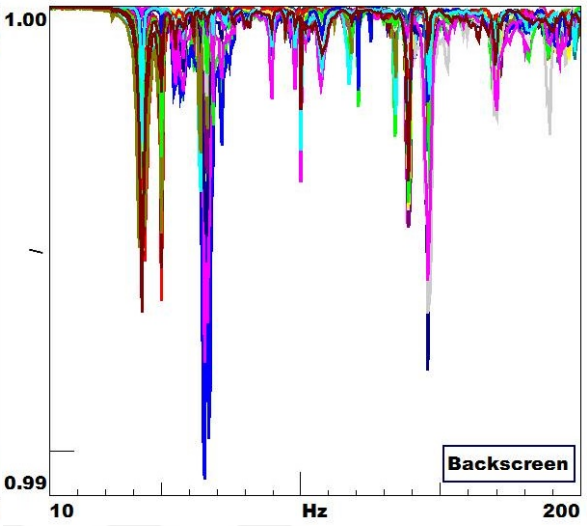


Figure 2.155. Coherence, back screen

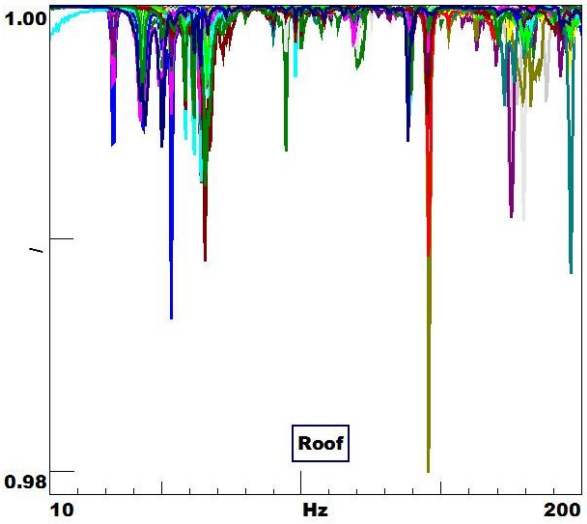


Figure 2.156. Coherence, roof

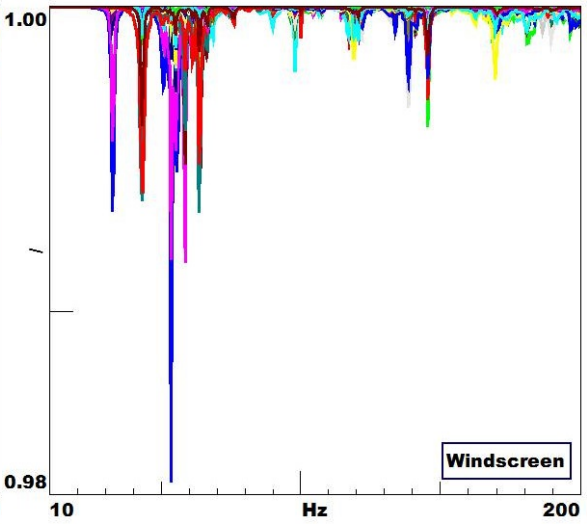


Figure 2.157. Coherence, windscreen

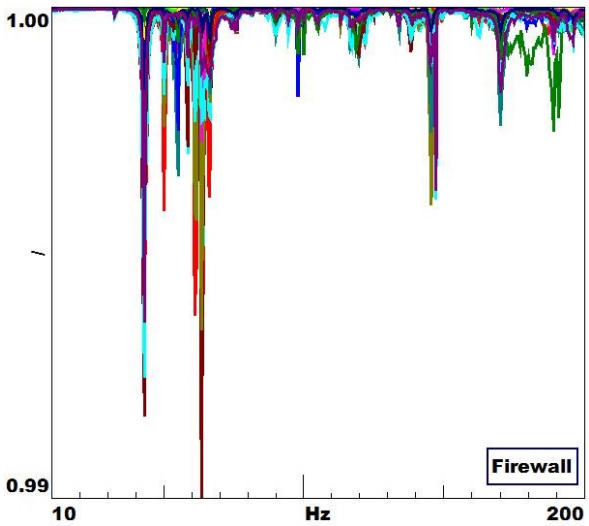


Figure 2.158. Coherence, firewall

2.11. Hybrid Transfer Path Analysis

In this section, improvement of the accuracy of FRF based TPA methods is investigated in what concern damping in measured responses, where a roving hammer is used as an excitation source. As discussed in Section 2.8.3, hammer tests are prone to some measurement errors, like leakage, even applied perfectly (see e.g. Ref [75]). Hence, force and exponential windows are used in hammer tests, where the former and latter are applied to input and outputs, respectively. Measured complex FRFs have real and imaginary parts, where the latter is associated with damping and has smaller signal to noise ratio due to its respectively small magnitude. The real part that represents the mass and stiffness effect is relatively more reliable, since it is known that the exponential window used during impact tests specifically increases apparent damping [77, 111]. Inversion of matrix $\mathbf{H_{mj}}$ (see Section 2.8.1) further increases these errors, which results in poor outcomes. Hence, it is reasonable to analyze damping in the estimated FRFs, before inverting the accelerance matrix.

2.11.1. Identification of structural and viscous damping

In time domain, the governing equations of motion of a multi degree of freedom (MDOF), finite dimensional, linear structure can be written as

$$\mathbf{M}\ddot{\mathbf{x}}(t) + \mathbf{C}\dot{\mathbf{x}}(t) + (\mathbf{K} + j\mathbf{D})\mathbf{x}(t) = \mathbf{f}(t) \tag{2.35}$$

where $\mathbf{M}$, $\mathbf{C}$, $\mathbf{K}$ and $\mathbf{D}$ matrices indicate the mass, viscous damping, stiffness, and structural damping of the system, respectively; $j = \sqrt{-1}$, $\mathbf{f}$ and $\mathbf{x}$ are force and displacement vectors, respectively. Assuming harmonic excitation, Equation (2.35) becomes

$$\left(\mathbf{K} - \mathbf{M}\omega^2\right)\mathbf{x} + j\omega\mathbf{C}\mathbf{x} + j\mathbf{D}\mathbf{x} = \mathbf{f} \tag{2.36}$$

in the frequency domain. Rearranging, we get

$$\left[\mathbf{K} - \mathbf{M}\omega^2 + j(\omega\mathbf{C} + \mathbf{D})\right]\mathbf{x} = \mathbf{f} \tag{2.37}$$

where the statement in curly brackets is the complex dynamic stiffness matrix. As stated in Equation (2.38), it is nothing but the inverse of complex receptance type FRF matrix ($\mathbf{H}^C$), which is estimated using hammer, or shaker test. That is

$$\left(\mathbf{H}^C\right)^{-1} = \left[\mathbf{K} - \mathbf{M}\omega^2 + j\left(\omega\mathbf{C} + \mathbf{D}\right)\right] \tag{2.38}$$

In the way that offered by Lee and Kim [112], it is possible to separate damping from the measured FRF as shown in Equations (2.39) and (2.40):

$$\left(\mathbf{H}_R^C\right)^{-1} = \mathbf{K} - \mathbf{M}\omega^2 =: \left(\mathbf{H}^N\right)^{-1} \tag{2.39}$$

$$\left(\mathbf{H}_I^C\right)^{-1} = \omega\mathbf{C} + \mathbf{D} \tag{2.40}$$

where subscripts R and I denote real and imaginary parts, respectively. Here, the real part that represents the mass and stiffness characteristics is also called as normal frequency response function (NFRF), and will be denoted as $\mathbf{H}^N$. Since, all structures have damping up to some extent, NFRF cannot be measured directly; instead, it is calculated using the measured complex FRFs. Structural and viscous damping can be calculated as

$$\begin{bmatrix} \mathbf{D} \\ \mathbf{C} \end{bmatrix}_{2nxn} = \begin{bmatrix} \hat{\mathbf{I}} & \omega_1\hat{\mathbf{I}} \\ \vdots & \vdots \\ \hat{\mathbf{I}} & \omega_s\hat{\mathbf{I}} \end{bmatrix}^{+}_{snx2n} \begin{bmatrix} \left(\mathbf{H}_I^C(\omega_1)\right)^{+} \\ \vdots \\ \left(\mathbf{H}_I^C(\omega_s)\right)^{+} \end{bmatrix}_{snxn} \tag{2.41}$$

where $\hat{\mathbf{I}}$ is the identity matrix and s are the spectral line indices. Alternatively, using Equations (2.37) and (2.39), we have

$$\left(\mathbf{H}^N\right)^{-1}\mathbf{x} + j(\omega\mathbf{C} + \mathbf{D})\mathbf{x} = \mathbf{f} \tag{2.42}$$

pre-multiplying both sides with $\mathbf{H}^N$ gives

$$\mathbf{x} + j\mathbf{H}^N(\omega\mathbf{C} + \mathbf{D})\mathbf{x} = \mathbf{H}^N\mathbf{f} \tag{2.43}$$

and defining the following transformation matrix, after Chen et al. [113]

$$\mathbf{G} = \mathbf{H}^N(\omega\mathbf{C} + \mathbf{D}) \tag{2.44}$$

we have

$$\mathbf{x} + j\mathbf{G}\mathbf{x} = \mathbf{H}^N\mathbf{f} \tag{2.45}$$

From experimental modal analysis, we know that

$$\mathbf{x} = \mathbf{H}^C\mathbf{f} \tag{2.46}$$

which can be written as

$$\mathbf{x} = \left(\mathbf{H}_R^C + j\mathbf{H}_I^C\right)\mathbf{f} \tag{2.47}$$

Comparing Equations (2.45) and (2.47), we get

$$\mathbf{H}_R^C + j\mathbf{H}_I^C + j\mathbf{G}\left(\mathbf{H}_R^C + j\mathbf{H}_I^C\right) = \mathbf{H}^N \tag{2.48}$$

Rearranging Equation (2.48) yields

$$\mathbf{H}_R^C - \mathbf{G}\mathbf{H}_I^C + j\left(\mathbf{G}\mathbf{H}_R^C + \mathbf{H}_I^C\right) = \mathbf{H}^N \tag{2.49}$$

where right hand side of Equation (2.49) has only real part, which implies that the imaginary part of the expression on the left hand side must be zero for all frequencies; hence,

$$\mathbf{G}\mathbf{H}_R^C + \mathbf{H}_I^C = 0 \tag{2.50}$$

Substituting Equation (2.44) into Equation (2.50), we get

$$\mathbf{H}^N\left(\omega\mathbf{C} + \mathbf{D}\right) = -\mathbf{H}_I^C\left(\mathbf{H}_R^C\right)^{-1} \tag{2.51}$$

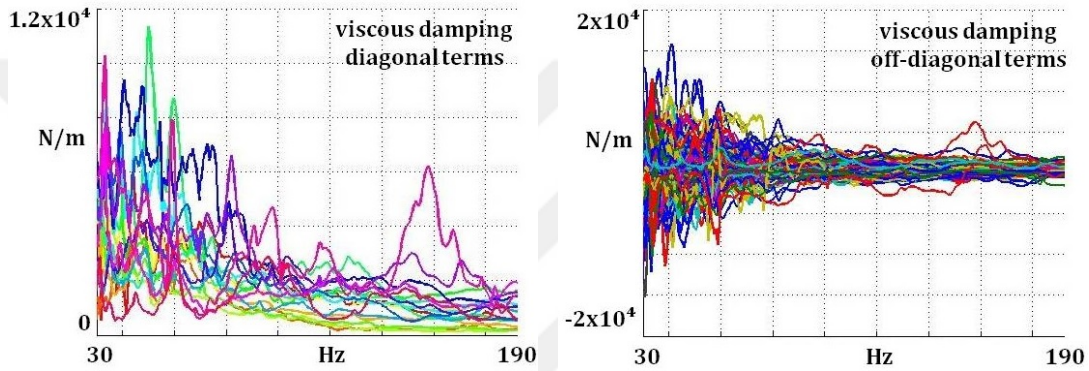
Finally, structural and viscous damping can be calculated by

$$\begin{bmatrix}\mathbf{D}\\ \mathbf{C}\end{bmatrix}_{2nxn} = -\begin{bmatrix}\mathbf{H^N} & \omega_1\mathbf{H^N}\\ \vdots & \vdots\\ \mathbf{H^N} & \omega_s\mathbf{H^N}\end{bmatrix}^+_{snx2n}\begin{bmatrix}\mathbf{H_I^C}(\omega_1)\\ \vdots\\ \mathbf{H_I^C}(\omega_s)\end{bmatrix}_{snxn}\begin{bmatrix}\left(\mathbf{H_R^C}(\omega_1)\right)^+\\ \vdots\\ \left(\mathbf{H_R^C}(\omega_s)\right)^+\end{bmatrix}_{snxn} \tag{2.52}$$

where resulting damping matrices are both symmetric and positive definite.

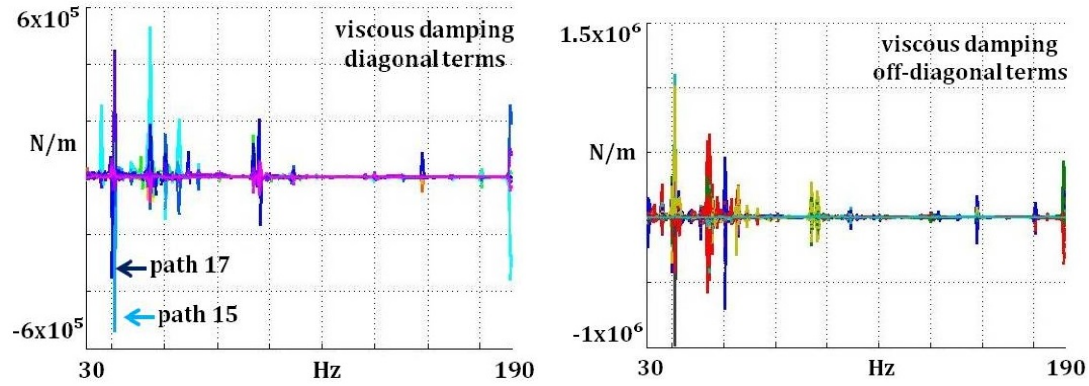
2.11.2. Proposed procedure

Viscous damping calculations are performed for the vehicle L38 # 170, using Equations (2.41) and (2.52). 18 paths described are used to calculate damping in 30-192 Hz bandwidth with 0.5 Hz resolution, i.e. $n = 18$ and $s = 325$. Results are plotted in Figures 2.159. and 2.160., where diagonal and off-diagonal elements of viscous damping matrix are shown separately.



(a) Diagonal terms (b) Off-diagonal terms

Figure 2.159. Plots of elements of viscous damping matrix



(a) Diagonal terms (b) Off-diagonal terms

Figure 2.160. Plots of elements of viscous damping matrix calculated using the proposed procedure. In Figure 2.160(a), viscous damping curves of paths 15 and 17 are plotted in cyan and dark blue colors, respectively.

Identified damping characteristics of all paths are examined in detail. It is observed that among diagonal paths, two of them exhibit strong damping characteristics: Paths 15 and 17. The essential observation related to damping characteristics of these paths is that they take negative damping values, which means that they create energy, rather than dissipating. This situation indicates a measurement error, provided that the calculation procedure of damping characteristics is true.

A similar observation is revealed in Ref [76], where it is suggested to employ a MIMO testing, instead of an impact hammer test to resolve such measurement errors. Unfortunately, the case study of present work is not appropriate for a MIMO test, as explained in Section 2.8.3. Exponential windowing that introduces artificial damping is necessarily used to compensate leakage, through hammer test [111]. To quantify the effects of damping on the problem studied, a transfer path analysis is performed through normal frequency response function matrix, $\mathbf{H}^N$ (see Equations (2.39) and (2.51)). Considering the outcomes of Section 2.8.4.1, and to minimize variance type errors, Equation (2.21), which counts only on diagonal elements of $\mathbf{H_{mj}}$ is employed for the analysis. Differently, instead of $diag(\mathbf{H_{mj}})$, $diag(\mathbf{H^N_{mj}})$, which is populated using normal frequency response functions is put into calculation, i.e.,

$$\mathbf{f_j} = diag\left(\mathbf{H^N_{mj}}\right)^{+} \ddot{\mathbf{x}}_\mathbf{j} \tag{2.53}$$

The aim is to reveal the effect of damping in the foregoing analysis. Then, identified force vector is used in Equation (2.18), to calculate SPLs at $\mathbf{y}_1$ and $\mathbf{y}_2$ (i.e. mic.1 and mic.2). Like formers, predicted and measured SPLs at the targets are compared, where results are plotted in Figure 2.161. As expected, predicted SPL curves take higher values than measured ones, nearly in the whole bandwidth of interest, although a few exceptions are present.

The foregoing discussion suggests that the damping effect, which is embedded in the measured complex frequency response functions, is needed to be analyzed in the post processing step. The need arises due to errors in measured FRFs, which cannot

be avoided depending on trade-offs and physical obstacles faced in application, where expressed in detail, through Section 2.8.3. It is apparent that Paths 15 and 17 exhibit large measurement errors, and among them artificial damping effects introduced by the exponential windowing function are dominant. To further inspect the situation, an analysis is conducted as described in the following:

(i) All diagonal paths are put into calculation in force identification step as suggested in Equation (2.21).

(ii) Among them, Paths 15 and 17 are selected for a further post processing operation depending on the identified viscous damping outcomes presented in Figure 2.160(a). Damping information embedded in the measured frequency response functions of these paths is decontaminated.

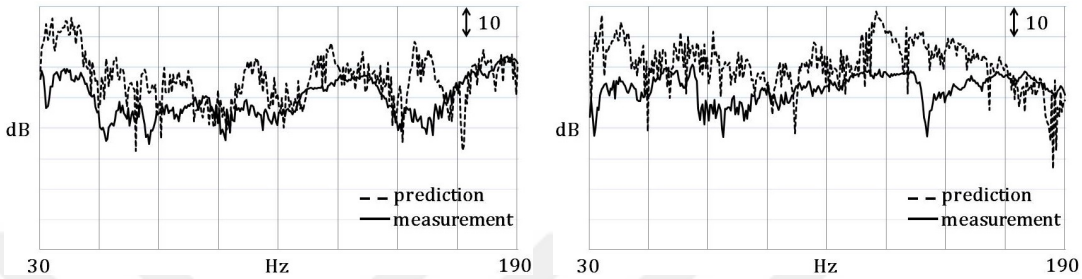
(iii) Finally, sound pressure level calculations are performed through the manipulated diagonal matrix ($diag(\tilde{\mathbf{H}}_{\mathbf{mj}})$), i.e.

$$diag(\tilde{\mathbf{H}}_{\mathbf{mj}}) = \begin{bmatrix} H_{1,1} & 0 & & \cdots & & 0 \\ 0 & \ddots & & & & \\ & & \ddots & & & \\ \vdots & & H_{14,14} & & & \vdots \\ & & & H^{N}_{15,15} & & \\ & & & & H_{16,16} & \\ & & & & & H^{N}_{17,17} \\ 0 & & & \cdots & & H_{18,18} \end{bmatrix} \tag{2.54}$$

The described procedure is successfully applied to the reference problem. The procedure proposed increases the accuracy of results, as observed in Figure 2.162.

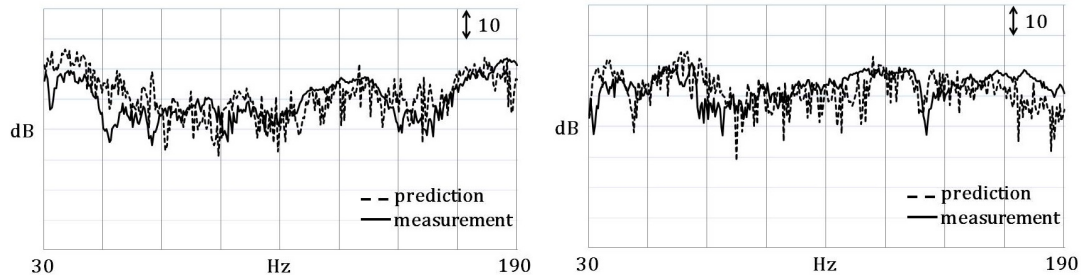
Note that, although the proposed procedure provides better accuracy, it introduces new trade-offs, and has its own drawbacks. First of all, to ignore the damping effect in some specific paths seems unrealistic. Another drawback is the time cost of the detailed post processing step.

On the other hand, the damping effect in the passive side acceleration vector ($\ddot{\mathbf{x}}_\mathbf{j}$) is not ignored. This vector is measured under operational conditions, and put into calculations as it is. Hence, only the damping information in the determined paths is ignored with respect to the measurement errors, which cannot be decoupled.



(a) mic.1 (b) mic.2

Figure 2.161. Comparison of predicted and measured SPL curves, where diagonal NFRF matrix method is used for prediction. L_2 norm of difference (a) 10.416 dB, (b) 11.741 dB.



(a) mic.1 (b) mic.2

Figure 2.162. Comparison of predicted and measured SPL curves, where the described procedure is used for prediction. L_2 norm of difference (a) 7.045 dB, (b) 6.825 dB.

2.12. Remarks

(i) Next to identifying booms and observing inter variability (see Sections 2.5 to 2.7), a structural transfer path analysis is followed out (see Section 2.8) for test vehicles chosen. Root causes of diagnosed booms are identified. Results are tabulated in Table 2.7. The booming around 1800 rpm (Vehicle L38) is important, since this

speed is downshifting and stop-and-go rpm in traffic. The booming cantered around 4000 rpm (Vehicle L38 and L84) is certainly critical in the sense of being the cruise speed at the top gear.

Table 2.7. Summary of first three contributor paths, where L38 results are belong to Vehicle #170 and L84 results are based on engine mount contributors only.

Test vehicle	Order	Target	Bandwidth (rpm)	Booming contributors
L84	2	BT:D	2950-4300	RH:03:Z, RH:03:X, RH:01:Y
L84	2	BT:K	2950-4300	RH:03:Z, RH:01:X, RH:03:X
L38	2	BT:D	3000-4500	RH:03:Y, RH:03:X, RH:02:Z
L38	2	BT:D1	3000-4500	RH:03:X, RH:02:Z, EC:22:X
L38	2	BT:K	3000-4500	RH:03:X, RH:03:Z, RH:02:Z
L38	2	BT:K	1500-2250	RH:02:Z, RH:02:X, RH:03:Z
L38	4	BT:D	1000-5750	RH:03:Y, EC:22:X, RH:01:X
L38	4	BT:D1	1000-5750	EC:31:Y, RH:03:X, RH:03:Y
L38	4	BT:K	1000-5750	RH:03:X, EC:41:Z, RH:03:Z

(ii) Several parameters are investigated to find out a reliable prediction result and to observe effects of measurement variability. Benchmark shows that reliable predictions are achieved provided that (i) frequency response function estimations are performed, when the active part, i.e., powertrain is removed; (ii) the test vehicle is on ground and (iii) the H_v estimator is used (see Figure 2.73.). Additionally, it is shown that prediction results can be improved by managing the condition number of the matrix, which is populated by measured accelerance frequency response functions (see Figure 2.64.).

(iii) A systematic approach is introduced to find out cause of inter variability. Eventually, it is shown that predominant paths, which are said to be the main contributors of diagnosed booms, are also the causes of variability.

(iv) The proposed procedure (see Section 2.9) promise a solution in examining the cause of a widespread problem, which takes up an important part quality control and customer satisfaction departments of vehicle manufacturers: inter variability. Further, proposed procedure make use of a well-known and a common experimental tool: transfer path analysis.

(v) In Section 2.10, panels of the structure are analyzed. Results obtained from 3 different scenarios are found to be consistent. Resonance frequencies of panels tabulated in Table 2.8., give insight into booms defined in Section 2.7.

Table 2.8. Resonance frequencies of the body panels

Panel name	Frequency (Hz)
Back floor	106, 120
Back screen	67, 78, 105, 150
Firewall	66, 73, 96, 107, 118, 140
Front floor	43, 108, 125, 147
Front left door	75, 104, 150
Front right door	78, 113
Parcel shelf	76, 98, 148
Rear left door	45, 106, 147
Rear right door	44, 105, 123
Roof	54, 67, 110, 148
Windscreen	55, 97, 120, 145

(vi) In TPA, the complained time cost is actually caused by the following issues: (i) removal of the source; (ii) to locate sensors and cables; (iii) to measure frequency response functions (FRFs) and noise transfer functions (NTFs) by applying a known force (shaker), or a normalized impact force (hammer). Today, engines of automobiles are installed such that without partially, or in some cases completely removing the engine, even to locate sensors for an operational measurement is

hard, if not impossible. Once the source is removed, and sensors are located, to apply an external force is no more a big deal in terms of time cost.

(vii) During the population of FRF matrix, unavoidable measurement errors introduce to results. Artificial damping, measurement noise, finite record length, phase, variance and bias errors certainly affect the outcomes of transfer path analysis. Although many of these measurement errors are reported in the literature, damping and its effects are not considered in detail. This dissertation suggests considering the effects of damping in any TPA framework.

(viii) Dynamic stiffness matrix is the inverse of experimental FRF matrix. During inversion process, measurement errors of FRFs are highly amplified in the dynamic stiffness matrix, since it is dominated by weakest modes. Whether measured directly or reciprocally, all FRFs contain the damping information, and in any method that inverts the FRF matrix, same problem is valid.

(ix) In many studies, predictions of proposed methods are compared with traditional transfer path analysis (TPA) results. In fact traditional TPA has its own assumptions and drawbacks, which motivate new research. In this work, unlike many reported results in the literature, comparisons are made between calculated and measured sound pressure levels. Current practice is studied on a reference problem, and results are presented. Validity is the greatest for the procedure proposed (see Table 2.9.).

Table 2.9. Assessment of TPA results

TPA method	L_2 norm of difference(dB)	
	BT:D	BT:K
Mount stiffness (see Figure 2.55.)	9.317	9.782
Matrix inversion (see Figure 2.56.)	10.523	11.277
Diagonal matrix inversion (see Figure 2.57.)	9.006	7.402
Diagonal NFRF (see Figure 2.161.)	10.416	11.741
Proposed procedure (see Figure 2.162.)	7.045	6.825

3. COMPUTATIONAL ANALYSIS

3.1. Construction of the Finite Element Model

Finite element method has three steps: pre-processing, processing and post-processing. It is possible to perform these steps in different software environments through import-export features. Pre-processing is to write a mathematical model, in a format that the solver can read out. Actually, this model is created by breaking down the complex geometry into simple regular shapes, i.e. meshing. Pre-processing is the critical and troublesome step for commercial software users. To create the meshed model, CAD data are subjected to many procedures, like geometry simplifications, material definitions, constraint definitions, assembling, etc. In this dissertation, HyperMesh is used to create an FE model, and employed solvers are Radioss, Nastran and SysNoise. Post-processing procedures and analysis are performed using VirtualLab.

Body-in-white (BIW) CAD data of test vehicles are received in Catia format, as a part of a university-industry collaboration project. The BIW is an industrial term that refers to the metallic structure only, i.e. no engine, no doors and no trim parts are present (see Figure 2.111. for the one used in this study). In automotive industry, there are various BIW definitions, like so-called 'stripped', 'closed' and 'trimmed' BIW [114]. In this study, BIW term refers to the structure that has no openings (doors, trunk lid, etc.), and has only a windscreen and a rear glass, as shown in Figure 3.1. The reason to keep them is the dominant effect of longitudinal waves in acoustic behavior of vehicles, where details are explained in Section 3.2.

Considering noise and vibration analysis, there are often many unnecessary details that have to be eliminated in this type of received CAD Data. One has to eliminate bolts, some of wedges, hinges and housings, etc. Eventually, one needs a 2D mid-surface mesh that contains no holes, and continually covers the vehicle cavity. Due to topography and mass optimization studies, nowadays vehicles have a very detailed geometric shape, e.g. at the floor part. After reduced, the CAD data studied have around

50,000 surfaces; still a very complex shape! Although this surface number will result in a huge DOF at the FE model, further eliminations are not performed to preserve the bead patterns, which strongly affect damping values. Similarly, CAD data of vehicle L38 received have many unnecessary details. The drawing shown in Figure 3.2. has 2,201 components. Next to comparing the drawing to real BIW structure, component number is reduced to 249 (see Figure 3.3.) Reduced drawings of Vehicles L84 and L38 are exported to HyperMesh, in IGES format.

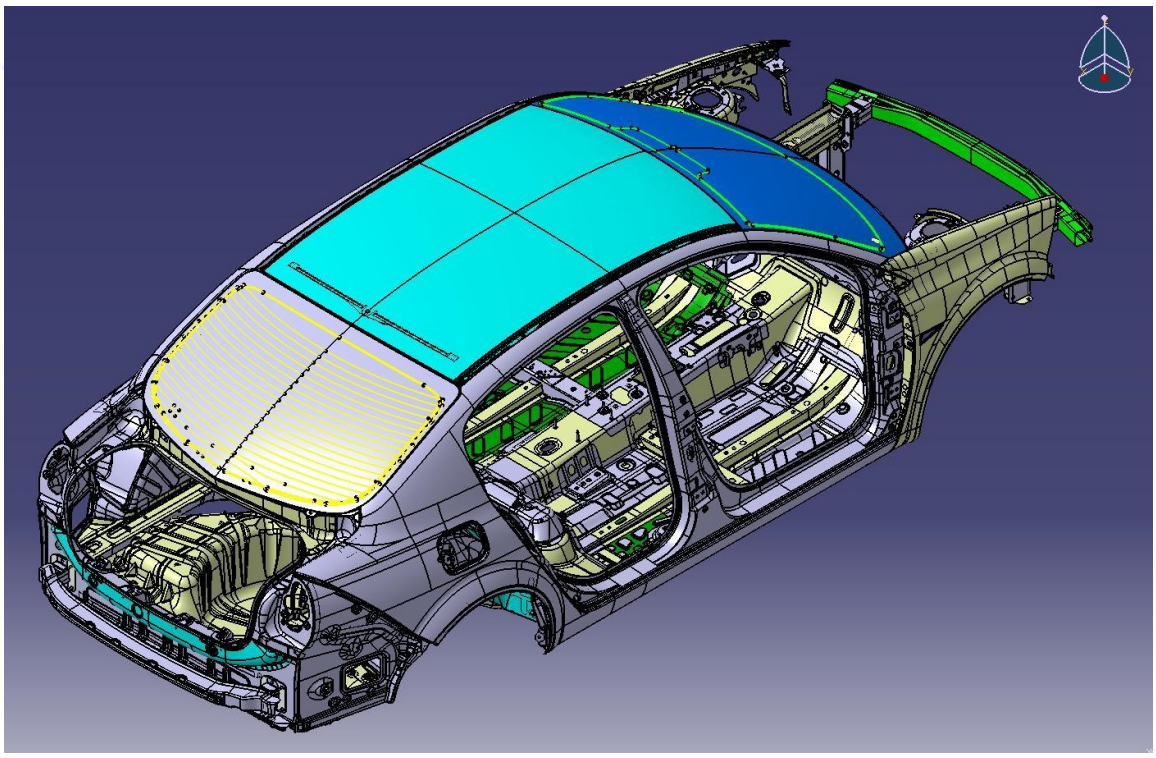


Figure 3.1. L84 BIW CAD in Catia V5

Pre-processing steps are explained as in the following sequence:

(i) Geometry Cleaning

For complex geometries, importing operation may cause some errors, like missing or duplicated surfaces, which result in connectivity (topology) problems. Before meshing, geometry is reviewed and repaired. Although, there are automated procedures for finding duplicated surfaces in pre-processing suite of commercial FEA packages, missing surfaces and edges can be found and fixed manually. For details, readers can refer to help files of commercial FE packages.

Since BIW is a complex structure, geometry cleaning procedures are applied by breaking down the body into small parts. Actually, these small parts are predefined panel objects used in panel contribution analysis, as well (see Section 2.10). After the geometry cleaning step, the model is ready for mid-surface extraction.

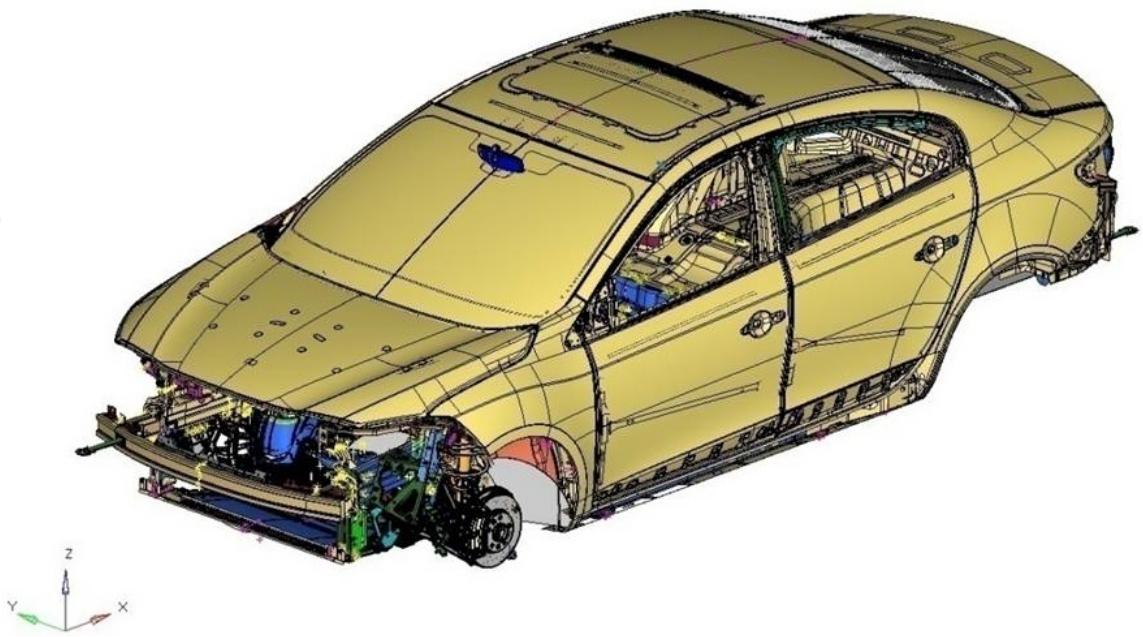


Figure 3.2. L38 BIW CAD received, 2201 components

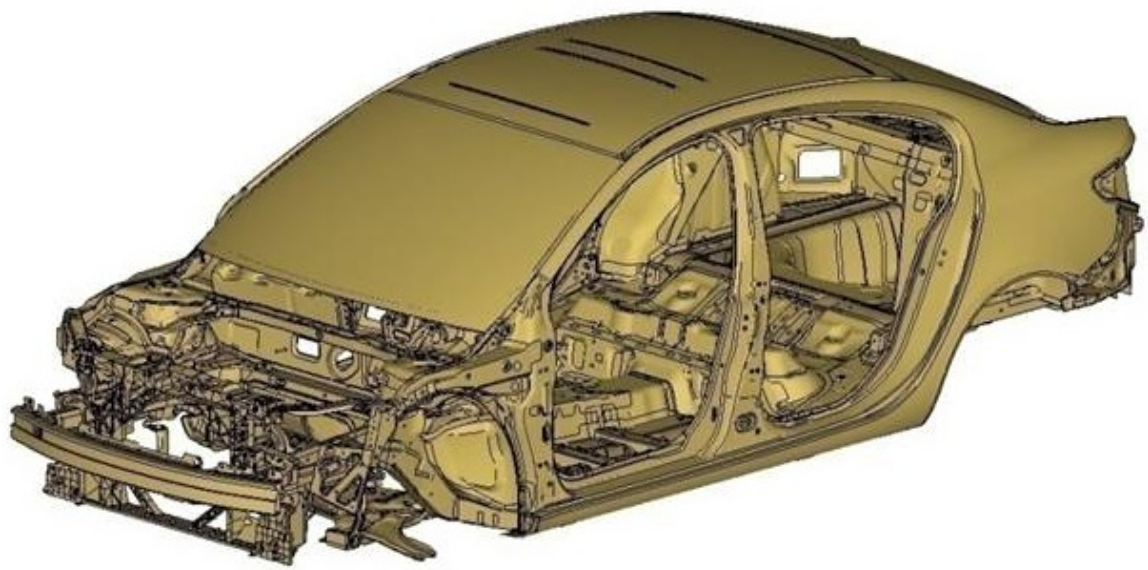


Figure 3.3. L38 BIW CAD reduced, 249 components

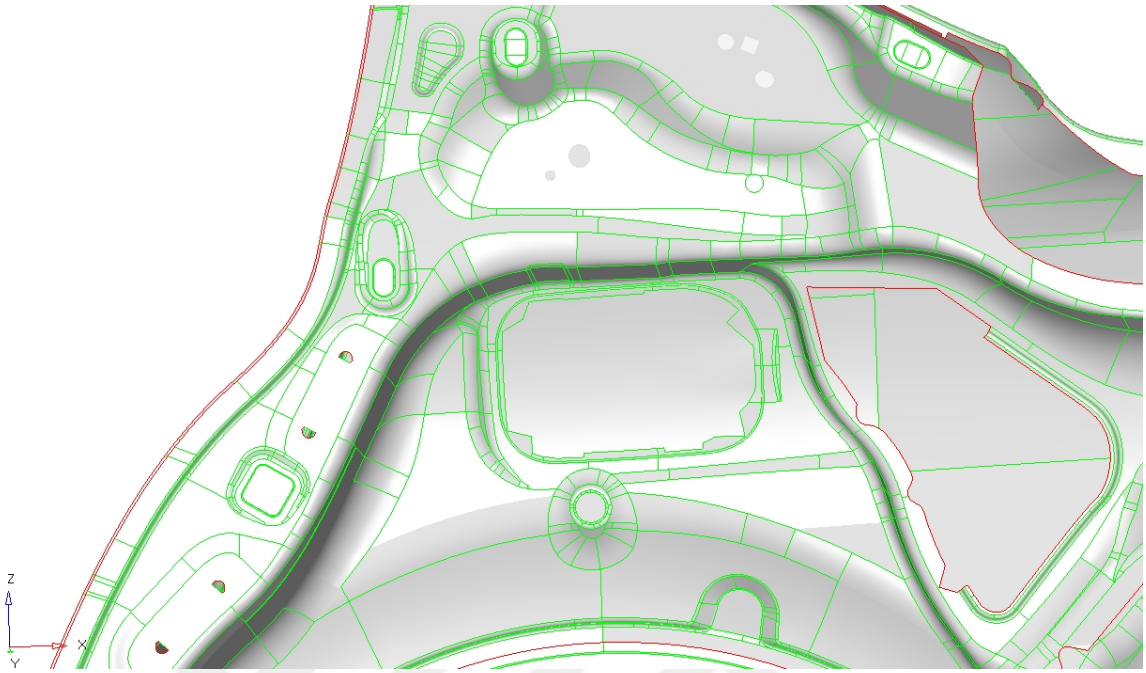


Figure 3.4. Right mudguard geometry, edge view

(ii) Creating Mid-surfaces

Shell elements are often used in vehicle body meshing, because they are appropriate to describe thin panel parts that have very big surface areas compared to their thickness. Shell elements are displayed as 2D objects, but thickness values are assigned to provide information to the solver. FE solvers assume that shell elements are located at mid-plane of the geometry meshed; that is why the name is *mid-surface*. Although mid-surface extraction is an automated procedure in commercial softwares, some corrections have to be made manually, when performed for complex geometries.

(iii) Geometry Simplifications

Since many unnecessary details are still present, mid-surface geometry is subjected to some other simplification procedures. Resulting from mass optimization studies, the model has many holes that have to be closed. For a better mesh quality, edge and surface fillets are also reviewed and simplified. Since a closed volume is needed for NVH analysis, holes of housings, pinholes and screw sockets are closed.

(iv) Topology Refinement

Topological details of the mid-surface geometry may alter the mesh quality. At this point there is a trade-off between fidelity to geometry and mesh quality. It is better to check the quality of mesh by means of predefined *criteria files*, before refinement attempts. Topology refinements, such as suppressing small edges, splitting some surfaces, and removing some of the interior fixed points are done.

(v) Shell Meshing

While preparing FE models of test vehicles, the aim is to create shell elements that have four nodes for all panel geometries. Due to complexity of the geometry, relatively a little number of elements that have three nodes are consented for the sake of general mesh quality. All FE preprocessing softwares have automated mesh algorithms, which are very successful for geometries that have regular shapes. Following the procedures explained above, automated mesh algorithm of the aforementioned software is employed to get a meshed model. For BIW components, maximum element size values are determined to be in between 5 and 10 cm, where elements have linear shape functions. The model is constructed by 1,231,152 QUAD4 and 62,390 TRIA3 elements. When the element quality is examined, it is observed that % 98 of elements is in accordance with the dictated criterion file. % 2 of elements, i.e. 25,000 are corrected manually and forced to obey the dictated criterion file. Since solver algorithms are different, for Nastran and Radioss, two distinct FE models are prepared.

(vi) Card Editing

Next to the FE model preparation, material properties and thicknesses of the panels are defined. All components of the models have their own identity cards. Assumptions adopted are:

(a) defined thickness value is constant at every point on the panel,

(b) described materials are isotropic, and

(c) elastic modulus and density values are valid at every point on the panel.

Material properties are tabulated in Table 3.1. L38 body weight is measured physically, which reads out 360 kg. Identical value is achieved for the FE model, after the card editing procedure is followed. Resulted body weight of model is shown in Figure 3.5., in tonnes.

Table 3.1. Material properties used in computational analysis

Material	E (N/mm^2)	ν	ρ ($tonne/mm^3$)
steel	2.1 x 10^5	0.30	7.9 x 10^{-9}
rigid PVC	1.5 x 10^3	0.42	1.4 x 10^{-9}
glass	7.4 x 10^4	0.20	2.5 x 10^{-9}
adhesive	3.0 x 10^4	0.30	1.4 x 10^{-9}

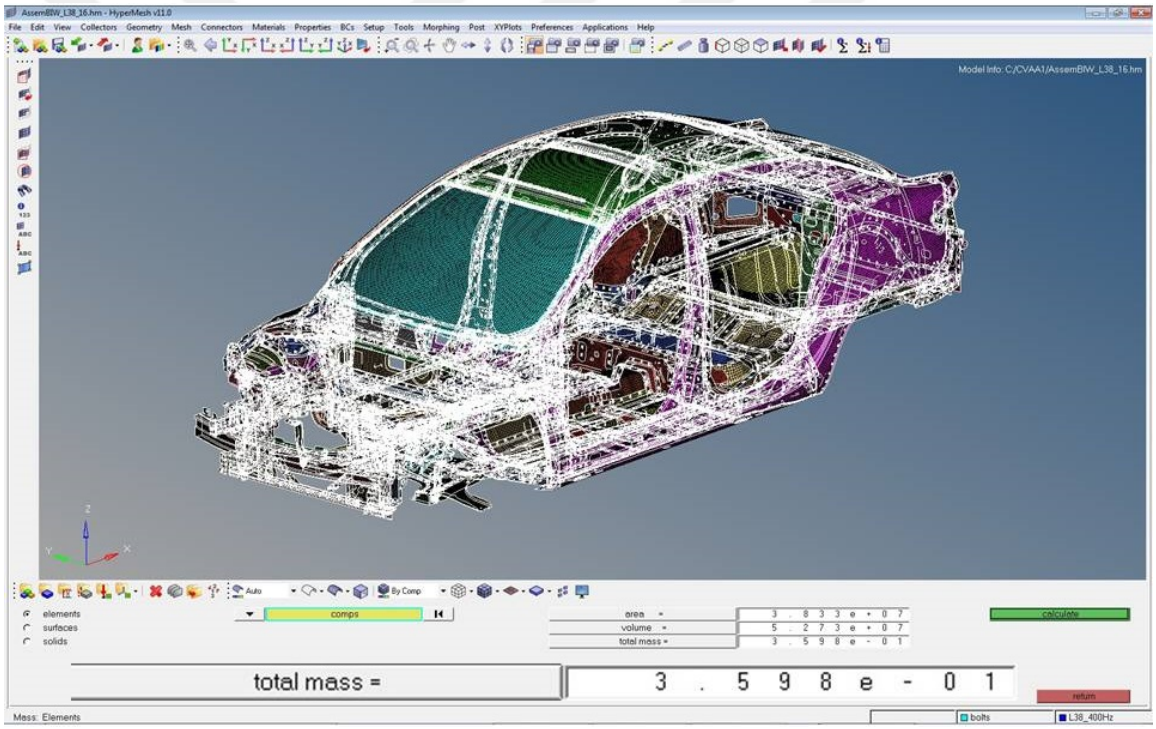


Figure 3.5. L38 BIW, confirmed weight

(vii) Element Refinement

Element types and quantities used in finite element model of test vehicles are tabulated in Table 3.2. After all, elements still have to be corrected for a robust calculation. Some of the dictated criterions and achieved values are tabulated in Table 3.3.

Table 3.2. Element types and quantities used in finite element model of vehicles

Element type	Vehicle L84	Vehicle L38
QUAD4	1,231,152	483,866
TRIA3	62,390	24,799
HEXA8	1,655	9,127
TET10	0	11,787
Rigid-Spider	777	692
Interpolation	11,281	6,990
BEAM	0	10

Table 3.3. Criterions used in mesh refinement

Criterion	Worst value
warpage	25.00
aspect	11.74
skew	66.78
chord deviation	1.10
jacobian	0.41
taper	0.53
area skew	0.68

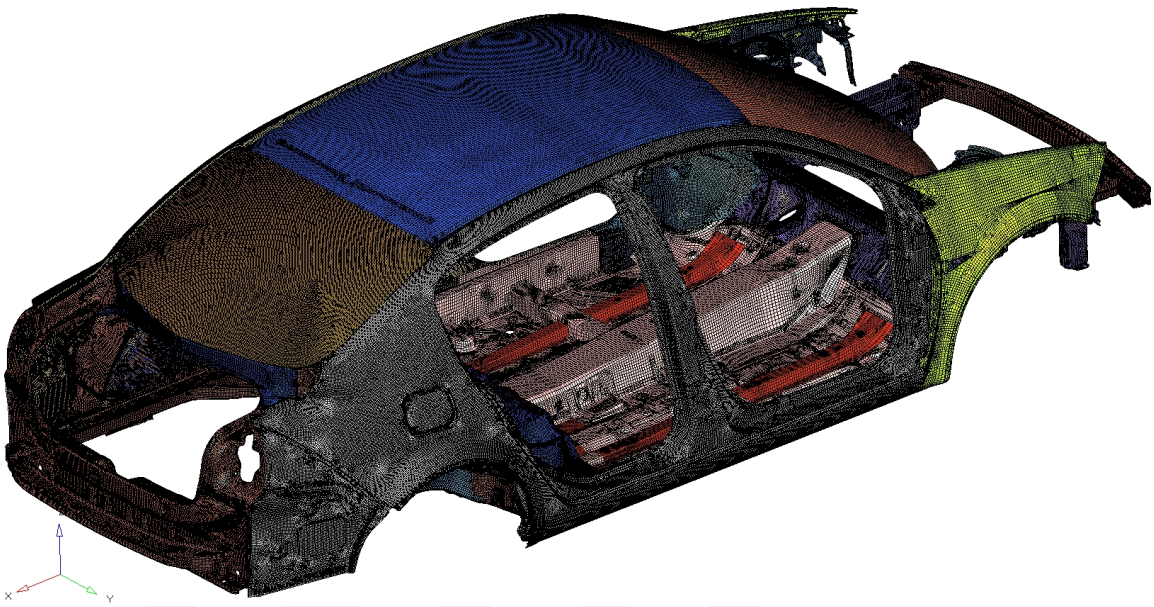


Figure 3.6. FE model of L84 BIW

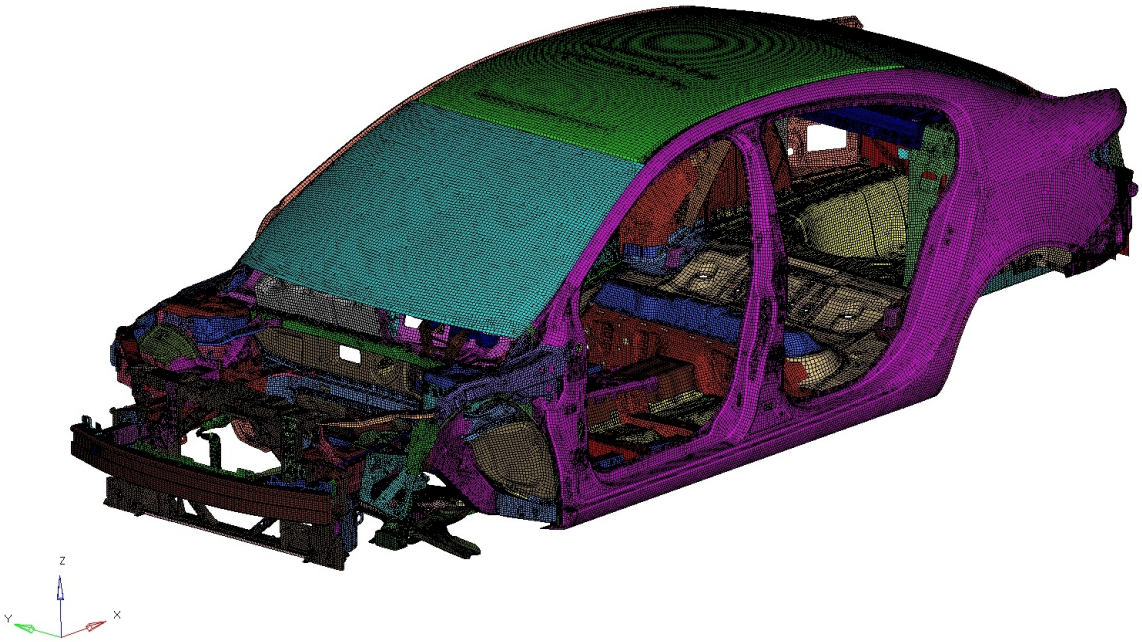


Figure 3.7. FE model of L38 BIW

(viii) Assembling

FE models of two vehicles are assembled through rigid connections, bolts, glue, spot and seam welds. Assembly locations and properties are given by OEM, in the collaboration of project conducted. Locations of connectors, where the number is around 2,500 are shown in Figure 3.8.

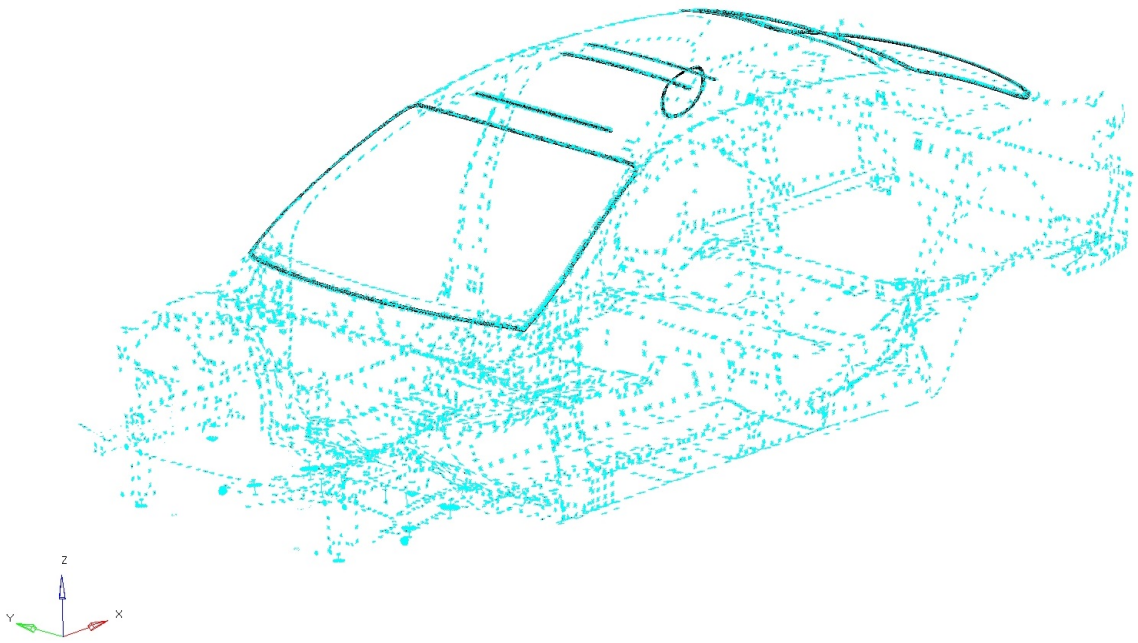


Figure 3.8. Connector locations for assembling of L38 BIW

3.2. Computation of Acoustic Modes

The theory of linear computational acoustics is based on the fundamental equations of continuum mechanics. While propagating, sound waves cause variations of pressure, particle velocity, density, and temperature in the medium. Hence, the wave equation is formulated using relations between these physical quantities, in terms of physical laws. In the following derivation of wave equation, Eulerian representation is used [115].

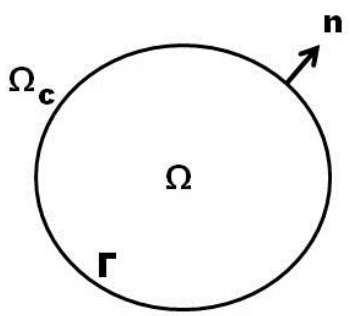


Figure 3.9. Domains Ω, Ω_c and boundary Γ

Conservation of mass and balance of momentum principles are fundamentals of continuum mechanics. The principle of conservation of mass states that total mass M in the domain Ω is constant within measurable limits, during motion, i.e.

$$M(t) = \int_{\Omega} \rho(\mathbf{x}, t) d\Omega \tag{3.1}$$

where ρ, $\mathbf{x}$ and t denote density, position vector and time. The principle of conservation of mass implies that

$$\dot{M} = \frac{dM}{dt} = \int_{\Omega} \left(\frac{\partial \rho}{\partial t} + \rho \nabla \cdot \mathbf{v} \right) d\Omega = 0 \tag{3.2}$$

where material derivative introduces the flow velocity vector, $\mathbf{v}$. For an arbitrary small neighborhood of a particle,

$$\frac{\partial \rho}{\partial t} + \rho \nabla \cdot \mathbf{v} = 0 \tag{3.3}$$

which can be taken as 'local conservation of mass'. Balance of momentum principle dictates that

$$\dot{\mathbf{P}} = \frac{d\mathbf{P}}{dt} = \mathbf{F}_R \tag{3.4}$$

where $\mathbf{F}_R$ is the resultant force acting on the body. It combines volume and external forces as

$$\mathbf{F}_R = \int_{\Omega} \mathbf{b} \rho d\Omega - \int_{\Gamma} p \mathbf{n} d\Gamma \tag{3.5}$$

where b is external body force and p is pressure. Momentum vector is given by

$$\mathbf{P} = \int_{\Omega} \rho \mathbf{v} d\Omega \tag{3.6}$$

Neglecting gravity and employing Gauss' theorem, we have

$$\int_{\Gamma} p\mathbf{n}d\Gamma = \int_{\Omega} \nabla p d\Omega \tag{3.7}$$

Material derivative of momentum is

$$\begin{aligned} \frac{d\mathbf{P}}{dt} &= \frac{d}{dt}\left(\int_{\Omega} \rho\mathbf{v}d\Omega\right) = \int_{\Omega} \frac{d(\rho\mathbf{v})}{dt}d\Omega \\ &= \int_{\Omega} \left[\frac{\partial\rho}{\partial t}\mathbf{v} + \rho(\nabla\cdot\mathbf{v})\mathbf{v} + \rho\frac{\partial\mathbf{v}}{\partial t} + \rho(\mathbf{v}\cdot\nabla)\mathbf{v}\right] d\Omega \end{aligned} \tag{3.8}$$

Considering Equations (3.2) and (3.3),

$$\frac{d\mathbf{P}}{dt} = \int_{\Omega} \left[\rho\frac{\partial\mathbf{v}}{\partial t} + \rho(\mathbf{v}\cdot\nabla)\mathbf{v}\right] d\Omega \tag{3.9}$$

Substituting Equations (3.5), (3.7) and (3.9) into Equation (3.4) and rearranging, so-called Euler equation is obtained, i.e.

$$\int_{\Omega} \left[\rho\frac{\partial\mathbf{v}}{\partial t} + \rho(\mathbf{v}\cdot\nabla)\mathbf{v} + \nabla p\right] d\Omega = 0 \tag{3.10}$$

or, in local form

$$\rho\frac{\partial\mathbf{v}}{\partial t} + \rho(\mathbf{v}\cdot\nabla)\mathbf{v} + \nabla p = 0 \tag{3.11}$$

Equation (3.11) is also known as 'balance of angular momentum' equation. Notice that, when shear effects are not considered ∇p term can be neglected. In computational linear acoustics, physical quantities, such as pressure, density and particle velocity exhibit small variations. A medium in an equilibrium state, in which there exists no sound wave, has equilibrium pressure p_0 and equilibrium density ρ_0. When a sound wave propagates, the pressure and density in the medium are changed to p' and ρ', respectively. For interior acoustics problems, we assume that air inside the closed domain Ω_c, (e.g. passenger cavity) is in steady state; hence, there is no ambient flow,

i.e. $\mathbf{v}_0 = 0$. Pressure, density and particle velocity are given as

$$\begin{aligned} p &= p_0 + p' \\ \rho &= \rho_0 + \rho' \\ \mathbf{v} &= \mathbf{v}_0 + \mathbf{v}' \end{aligned} \tag{3.12}$$

Considering Equation (3.3) with only first order terms, we have

$$\frac{\partial \rho'}{\partial t} + \rho_0 \nabla \cdot \mathbf{v}' = 0 \tag{3.13}$$

If ρ_0 and p_0 is assumed to be independent of time and spatial coordinates, Equation (3.11) is reduced to a linear form as

$$\rho \frac{\partial \mathbf{v}'}{\partial t} + \nabla p' = 0 \tag{3.14}$$

Note that, when a wave propagates, particles perform elastic oscillations, only about their equilibrium positions. These fluctuations result in sound, through pressure waves. Sound propagation occurs so fast that there is no time for the temperature to equalize itself with the medium; hence, this is an adiabatic process. How fast the wave travels is measured by speed of sound c. Considering ideal gases only, an adiabatic process implies that

$$(p_0 + p')(\rho_0 + \rho')^{-\kappa} = (p_0 \rho_0)^{-\kappa} \tag{3.15}$$

where κ is defined as specific heat ratio, then

$$1 + \frac{p'}{p_0} = \left(1 + \frac{\rho'}{\rho_0}\right)^{\kappa} \tag{3.16}$$

Linearizing the right hand side of Equation (3.16) gives

$$\left(1 + \frac{\rho'}{\rho_0}\right)^{\kappa} = 1 + \kappa \frac{\rho'}{\rho_0} \tag{3.17}$$

therefore,

$$p' = \left(\kappa \frac{p_0}{\rho_0}\right) \rho' = c^2 \rho' \tag{3.18}$$

Herein, c (speed of sound) is defined as a constant that relates pressure fluctuations and density, i.e.

$$p' = c^2 \rho' \tag{3.19}$$

Introducing adiabatic bulk modulus K, we have

$$c = \sqrt{\frac{K}{\rho_0}} = \sqrt{\frac{\kappa p_0}{\rho_0}} \tag{3.20}$$

With respect to time, differentiating the constitutive relation of Equation (3.19) twice, we get

$$\frac{\partial^2 p'}{\partial t^2} = c^2 \frac{\partial^2 \rho'}{\partial t^2} \tag{3.21}$$

Using the local conservation of mass equation (Equation (3.3)), we have

$$\frac{\partial^2 p'}{\partial t^2} = -c^2 \rho_0 \frac{\partial (\nabla \cdot \mathbf{v}')}{\partial t} = -c^2 \rho_0 \nabla \left(\frac{\partial \mathbf{v}'}{\partial t}\right) \tag{3.22}$$

Expressing the velocity vector by linearized Euler equation (Equation (3.14)) gives the wave equation, i.e.

$$\frac{\partial^2 p'}{\partial t^2} = c^2 \nabla \cdot \nabla p' \tag{3.23}$$

where the derivation is made in terms of pressure as the dependent field variable. Be aware that, this hyperbolic partial differential equation also holds for ρ and $\nabla \cdot \mathbf{v}$.

3.2.1. Analytical Box Model

Consider a box cavity of dimensions L_x, L_y, L_z as shown in Figure 3.10. This box represents a reverberant room, a simple model of a rectangular volume that has rigid walls. If all walls of this box are assumed to be perfectly rigid, which implies that

$$\begin{aligned}\left(\frac{\partial p}{\partial x}\right)_{x=0} &= \left(\frac{\partial p}{\partial x}\right)_{x=L_x} \\ \left(\frac{\partial p}{\partial y}\right)_{y=0} &= \left(\frac{\partial p}{\partial y}\right)_{y=L_y} \\ \left(\frac{\partial p}{\partial z}\right)_{z=0} &= \left(\frac{\partial p}{\partial z}\right)_{x=L_z}\end{aligned} \tag{3.24}$$

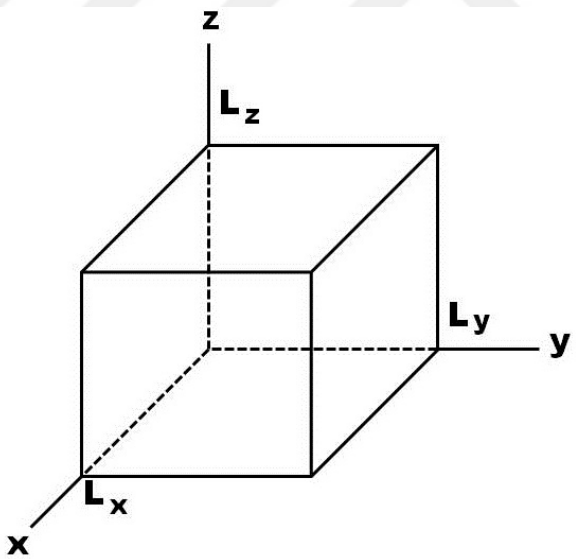


Figure 3.10. Box cavity

Then, an appropriate solution of Equation (3.23) results in so-called standing waves. Employing separation of variables, substitution of

$$p(x, y, z, t) = X(x)Y(y)Z(z)e^{j\omega t} \tag{3.25}$$

into Equation (3.23) gives

$$\begin{aligned} \frac{\partial^2 X}{\partial x^2} + k_x^2 X = 0 \\ \frac{\partial^2 Y}{\partial y^2} + k_y^2 Y = 0 \\ \frac{\partial^2 Z}{\partial z^2} + k_z^2 Z = 0 \end{aligned} \tag{3.26}$$

where separation constants are related by

$$k^2 = k_x^2 + k_y^2 + k_z^2 \tag{3.27}$$

Imposing boundary conditions stated in Equation (3.24) gives

$$p_{lmn}(x, y, z, t) = A_{lmn} \cos(k_{xl} x) \cos(k_{ym} y) \cos(k_{zn} z) e^{j\omega_{lmn} t} \tag{3.28}$$

where $k_{xl} = l\pi/L_x; \quad k_{ym} = m\pi/L_y; \quad k_{nz} = n\pi/L_z \quad (l, m, n = 0, 1, 2, ..)$.

Hence, eigenfrequencies (a.k.a. normal or resonance frequencies) of a rectangular volume is computed by

$$\omega_{lmn} = ck = c\sqrt{\left(\frac{l\pi}{L_x}\right)^2 + \left(\frac{m\pi}{L_y}\right)^2 + \left(\frac{n\pi}{L_z}\right)^2} \tag{3.29}$$

or

$$f_{lmn} = \frac{c}{2}\sqrt{\left(\frac{l}{L_x}\right)^2 + \left(\frac{m}{L_y}\right)^2 + \left(\frac{n}{L_z}\right)^2} \tag{3.30}$$

Considering the literature (e.g. Ref. [116]), analytical solution of acoustic eigenfrequencies of Vehicle L84 is studied. The aim is to compare analytical and computational results. Since, there is no analytical solution for complex geometries; the box geometry with appropriate dimensions is constructed, such that the cavity of vehicle fits into. Vehicle cavity and the box geometry depicted are shown in Figure 3.11. FEM

of the cavity is composed of 122,421 HEXA8 elements. Using Equation (3.30), first five acoustic eigenfrequencies are computed analytically. For verification purposes and more importantly to examine the commercial software used, eigenfrequencies of the box are computed through FE model, as well. Results are sketched in Figures 3.12. to 3.16. and tabulated in Table 3.4.

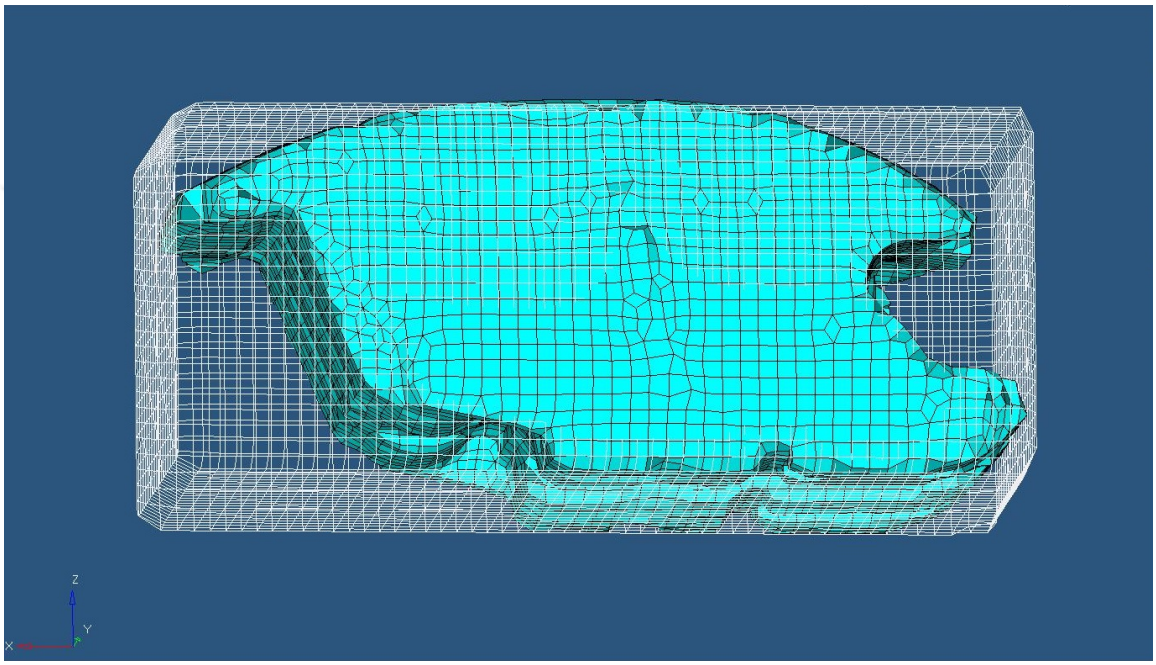
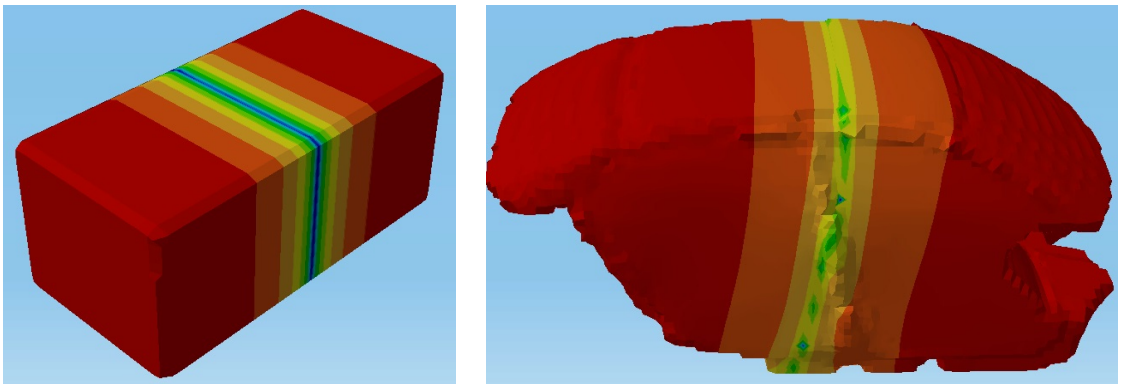
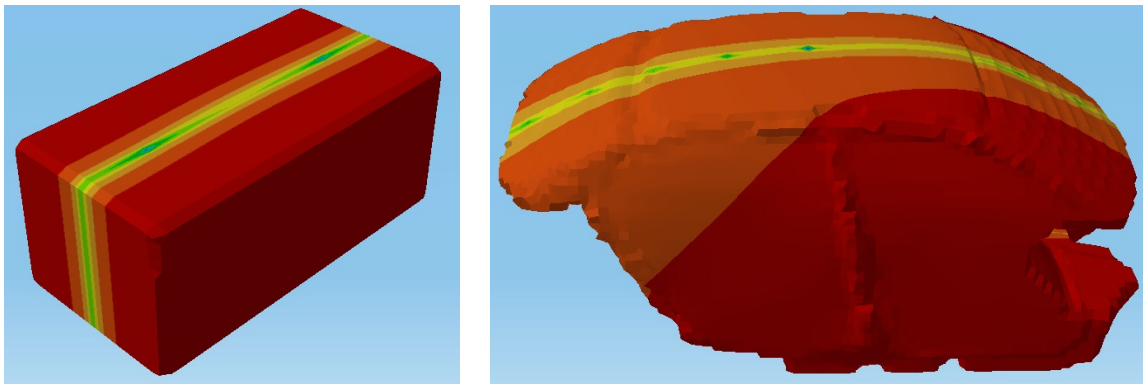


Figure 3.11. Vehicle L84 cavity and the box depicted



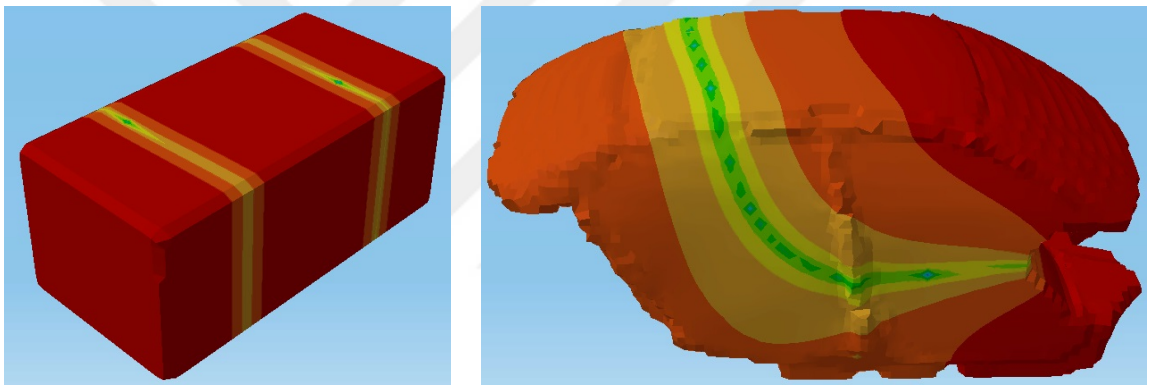
(a) 60.9 Hz, (1,0,0) (b) 83.1 Hz

Figure 3.12. Comparison of the 1st eigenfrequencies of the box and Vehicle L84 cavity



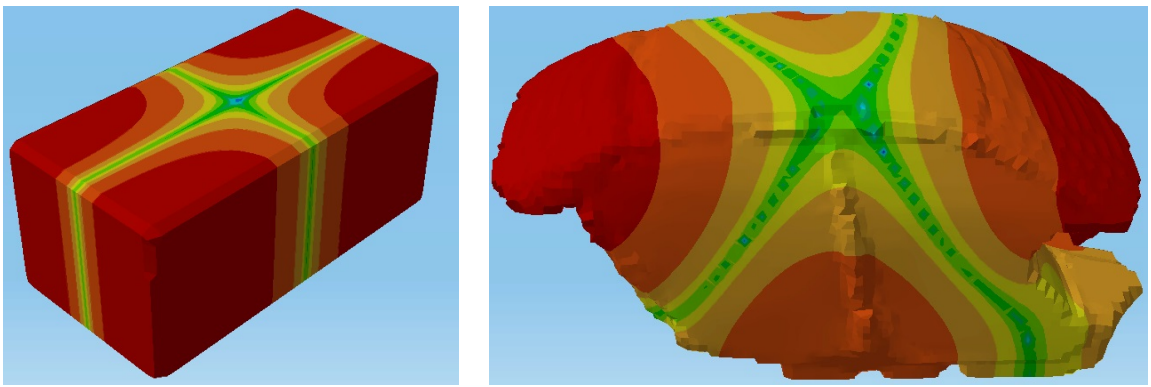
(a) 121.8 Hz, (2,0,0) (b) 116.7 Hz

Figure 3.13. Comparison of the 2nd eigenfrequencies of the box and Vehicle L84 cavity



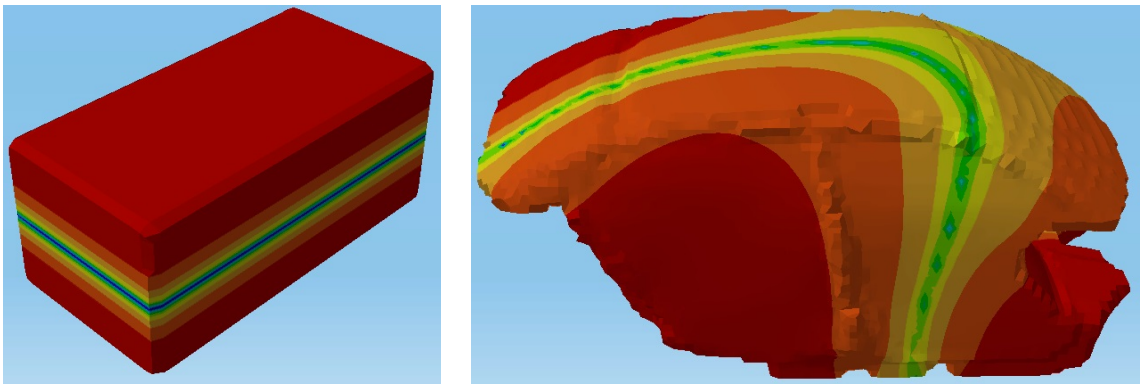
(a) 121.8 Hz, (0,1,0) (b) 127.6 Hz

Figure 3.14. Comparison of the 3rd eigenfrequencies of the box and Vehicle L84 cavity



(a) 136.5 Hz, (1,1,0) (b) 142.9 Hz

Figure 3.15. Comparison of the 4th eigenfrequencies of the box and Vehicle L84 cavity



(a) 142.3 Hz, (0,0,1) (b) 146.1 Hz

Figure 3.16. Comparison of the 5th eigenfrequencies of the box and Vehicle L84 cavity

Table 3.4. Comparison of the first five eigenfrequencies of the box and Vehicle L84 cavity

Eigenfrequency	The box	Vehicle cavity
1st	60.9	83.1
2nd	121.8	116.7
3rd	121.8	127.6
4th	136.5	142.9
5th	142.3	146.1

In related references (e.g. Ref. [116]), the analytical solution is offered for the computation of eigenfrequencies, but comparison of results show that acoustic eigenfrequencies and mode shapes of the box and actual cavity do not match well enough. The point is the approximation of actual cavity geometry to a rectangular shape; while some geometry, such as mini vans or buses are appropriate for this type approximation, some geometries are not, as in the case studied.

3.2.2. Coupling of Adjacent Cavities

Acoustic comfort of passenger vehicles has become a significant competition factor in the market, as much as the others, i.e. styling, power, fuel consumption and budget [117]. Vibro-acoustic response studies play an important role in developing countermeasures to noise problems, before or after vehicle launch [118]. Unforeseen noise problems are often revealed during quality tests [119], or due to customer complaints. In most cases, sound pressure level predictions and measurements do not match well.

Harrison [50] stated that first longitudinal acoustic eigenfrequency (i.e. 1,0,0) is around 70 Hz for a typical sedan. Experimental studies show that the value is far less than expected, which indicates a short-coming in the application of theory, or something is missed while determining assumptions. For such low values, e.g. around 35 Hz, the length of acoustic cavity must be obviously longer.

In sedans, cabin and trunk cavities are separated by a parcel shelf and a plate that supports the rear seat. The effect of trunk cavity is noticed; Kang et al. [120] handled the rear seat as an artificial elastic boundary to explain the differences between computational and experimental results. Lim [121] claimed that the rear seat is transparent to noise transmission; hence, trunk and cabin cavities can be treated as a single cavity. Even so, total cavity length is still not enough for low eigenfrequencies revealed during tests. There are holes on the parcel shelf providing space for loudspeakers, ventilation and cables. Effects of holes on the parcel shelf of a sedan are investigated [122]. Acoustic response is measured, when the holes are open and closed. In their follow up study, [123] reported a low frequency acoustic mode that should not be appeared, provided that the effect of trunk cavity is ignored.

Besides holes on the parcel shelf, there exist some other apertures between trunk and cabin cavities, like in the case of folding rear seats. The back rest of these seats are made of two separate parts, which are supported by two independent plates. Nowadays, almost all of the sedans have this type of rear seats, which can be folded either in 1/3, or

2/3 position. The air, confined inside cabin and trunk cavities, is excited by structural displacements of panels, causing a volume change and creating high impedance [124]. Under load, the confined air in the cabin moves to additional cavities, such as the trunk volume, provided it finds a way.

In their computational study, Sung et al. [125] noticed and considered leakages, between trunk and cabin cavities. They construct a very detailed acoustic cavity model, which also counts for front and rear seats, door volumes, and instrument panel volume. Like former studies [126,127], experiments are achieved through loudspeaker excitation, where roving microphone arrays are used to characterize acoustic behavior of the cavity. Seats are modeled through so-called heavy air assumption [126], or using equivalent-acoustic properties, determined from impedance-tube sample tests [127]. Nevertheless, in studies concerning leakages, the effect of apertures is not shown explicitly, since leakages and apertures are different. The former is modeled using a direct connection of equivalent grids at the assumed leakage locations, where material properties are adjusted, accordingly [125]. For the latter, a single acoustic volume that contains two cavities has to be constructed to explicitly enable the effect in the model. In other words, acoustic mesh has to be continuous through the aperture.

Through discontinuities, coupling effects of the trunk on acoustic modes are also reported in the literature. By developing an analytical model, Lee et al. [128] claimed that such discontinuities generate evanescent waves in addition to standing waves, resulting in a change in computed acoustic modes. Ahn et al. [129] modeled those holes as an equivalent spring damper system. Experimental results of the forced vibration response of a simplified car-like structure are presented, where a sound source is employed for excitation [130].

Actually, since mentioned discontinuities behave as if necks of a Helmholtz resonator, acoustic cavity becomes longer. The length of acoustic cavity is determined by adding an extra length term, which is calculated in compliance with the aperture geometry. In this work, with regard to its formation mechanism, the mentioned term is called as *reactance length*. Note that, a similar mass reactance also forms at the

open end of pipes and wave guides, and generally referred as *end correction* term. Helmholtz [131] developed a resonance equation considering an acoustic cavity with a circular aperture. Rayleigh [132] offered an end correction term for a plate with a hole. Nielsen [133] developed a transcendental equation for the Helmholtz resonator. Ingard [134] extensively studied the theory and design of Helmholtz resonators. Panton and Miller [135] developed a corrected Helmholtz equation, which gives more accurate results and extends the region of wavelength of validity. Chanaud [136, 137] improved Ingard's work and derived an explicit end correction formula for apertures placed asymmetrically. Selamet [138] investigated the acoustic performance and effect of specific cavity dimensions of resonators theoretically and experimentally.

It is well known that in low frequency region, where booming frequently occurs, there exist a few acoustic modes. The vibro-acoustic response of a vehicle is essentially ruled by them, and the planar ones are the strongest. In what follows, a simplified cavity model of the sedan that consists of two adjacent boxes connected by an aperture is presented in Figure 3.17. Planar eigenfrequencies are calculated analytically considering the *reactance length*, and results are compared to ones obtained from computational model of the box. Next, uncoupled acoustic eigenfrequencies of the sedan are computed using the commercial code Sysnoise™. Computational results obtained from acoustic cavity model of the sedan and calculated results of its simplified model are compared.

Table 3.5. Dimensions of the simplified model given in Figure 3.17.

parameter	d_1	d_2	w	h	w_1	w_2	w_a
size (cm)	219	117	134	141	44	88	2

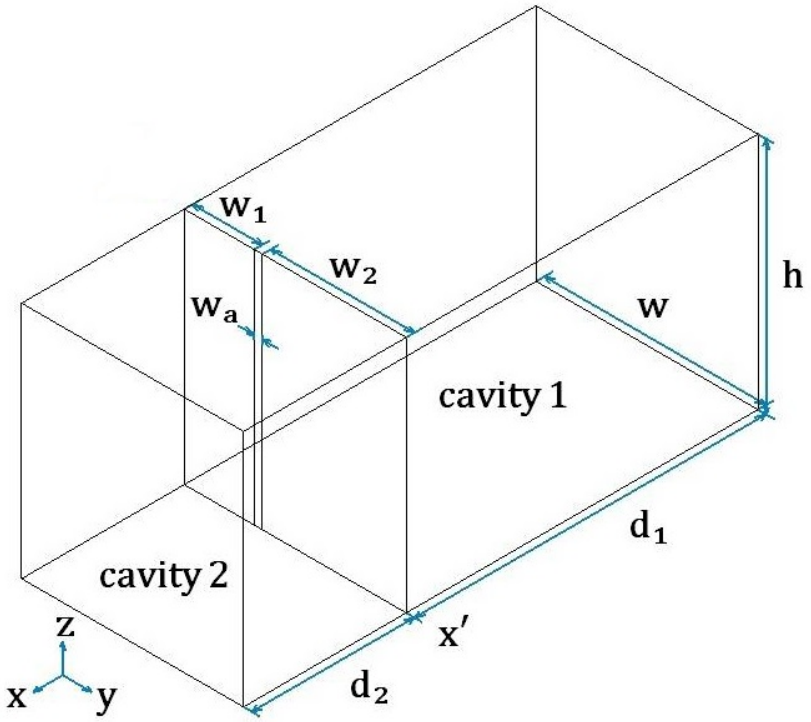


Figure 3.17. A simplified model of trunk and passenger cavities of Vehicle L38 (cavity 1: passenger volume, cavity 2: trunk volume).

As distinct from a regular rectangular volume (see Figure 3.10.), the geometry given in Figure 3.17. has a partition at x'. It is assumed that the aperture on the partition is replaced by a rectangular piston in the same dimensions, with a uniform velocity amplitude u_p, as suggested by [134]. Like other walls of the geometry, the partition is assumed to be perfectly rigid, so that only the axial velocity at x' is contributed by the piston. The average velocity of the piston can be written as

$$u_0 = (w_a/w)u_p \tag{3.31}$$

In that case, the acoustic pressure is

$$p(x,\omega) = A\cos(k_y y)\cos(k_z z)e^{ik_x x} \tag{3.32}$$

where k_y and k_z are identical with those appear in Equation (3.27). In the fundamental mode (p_0), acoustic pressure is uniform and

$$k_x = k = \omega/c \tag{3.33}$$

Depending on the mentioned assumptions, the velocity in the fundamental mode is equal to the average piston velocity. In that case pressure amplitude is

$$p_0 = \rho c \frac{w_a}{w} u_p e^{ikx} \tag{3.34}$$

Normalized reactance of the piston is expressed by

$$\chi = \frac{i\omega M}{w_a h \rho c} \equiv ik\delta \tag{3.35}$$

where M stands for mass. The acoustic radiation impedance of the piston is expressed by

$$\varphi = \frac{p_0}{\rho c u_p} = \frac{w_a}{w} - ik\delta \tag{3.36}$$

where the imaginary part, $ik\delta$ is the mass reactance [139]. In what concern the physics of problem, this term can be thought as if the length of an air column through the aperture, since there is no piston in the actual case. Regarding the geometry given in Figure 3.17., it is assumed that the reactance length δ is effective only in longitudinal direction. In this way, the problem can be separated into two parts. In the first part, acoustic eigenfrequencies of planar modes in y- and z-directions can be calculated using Equation (3.27). For the second part, an analytical solution, which takes the mass reactance occurred in the x-direction into account can be used. To express such a solution requires the computation of reactance length for higher orders. In such a computation reactance length depends only on the dimensions of the geometry, rather than frequency, provided that the low frequency limit approximation (i.e. $k_x w_a \ll 1$)

is valid. Then, axial velocity field is obtained as

$$u_x = \sum_{mn=0}^{\infty} \frac{k_x}{k} \frac{P_{mn}}{\rho c} \cos(k_y y) \cos(k_z z) e^{ikx} \tag{3.37}$$

accordingly. Expanding the velocity distribution, using orthogonality ($m \neq n$), and integrating over the area of aperture,

$$U_{mn} = \iint\limits_{aperture} U \cos(k_y y) \cos(k_z z) dy dz = U \frac{w_a h}{wh} \gamma_{mn} \frac{\sin(k_y w_a)}{k_y w_a} \frac{\sin(k_z h)}{k_z h} \tag{3.38}$$

for $m, n > 0$. Herein, $\gamma_{0,0} = 1$, $\gamma_{m,0} = \gamma_{0,n} = 2$ and $\gamma_{m,n} = 4$. The velocity distribution at $x = x'$ can be taken as

$$u = \sum_{mn}^{\infty} U_{mn} \cos(k_y y) \cos(k_z z) \tag{3.39}$$

Velocities in Equations (3.37) and (3.39) must be equal at $x = x'$, hence

$$P_{mn} = \rho c U_{mn} \frac{k}{k_x} \tag{3.40}$$

Below cut off frequency $k_x \simeq k_{mn}$, and the transverse contribution P_{mn} corresponds to the mass reactance part of Equation (3.36). Thus, reactance length is expressed by

$$\delta = \sum_{mn}^{\infty\prime} \frac{1}{k_{mn}} \frac{w_a}{w} \gamma_{mn} \frac{\sin(k_y w_a)}{k_y w_a} \frac{\sin(k_z h)}{k_z h} \tag{3.41}$$

Reactance length is contributed by all transverse modes (m, n) except the fundamental mode ($m = n = 0$); thus, it is excluded in the summation above, where a prime symbol is used for distinction. Defining the ratio of widths as $\xi = w_a/w$,

$$\delta = \sum_{mn}^{\infty\prime} \frac{\xi}{k_{mn}} \gamma_{mn} \frac{\sin(m\pi\xi) \sin(n\pi)}{mn\xi\pi^2} \tag{3.42}$$

Recall the geometry given in Figure 3.17.; it is assumed that air inside the adjacent cavities is driven by the piston located instead of aperture. As the piston moves, plane waves will form in both of the cavities [135]. Considering plane waves formed in x and $-x$ directions, acoustic impedance can be written as

$$Z = \frac{\rho c}{wh} \frac{\alpha e^{ik_x x} + \beta e^{-ik_x x}}{\alpha e^{ik_x x} - \beta e^{-ik_x x}} \tag{3.43}$$

provided the mentioned assumptions hold. Theoretically, at $x = d_1$ and at $x = d_2$ acoustic impedance is infinite, which in turn yields

$$Z = \frac{\rho c}{iwh} \cot(k_x d_n) \tag{3.44}$$

where $n = 1, 2$. It is reasonable to assume that at $x = x'$ the impedance is purely reactive, and can be written as

$$Z = i\omega \frac{M}{w_a^2 h^2} \tag{3.45}$$

Using Equations (3.35) and (3.45), acoustic impedance is expressed by

$$Z = i \frac{\delta \rho c k_x}{w_a h} \tag{3.46}$$

Substitution of Equation (3.46) into Equation (3.44) results in a transcendental equation that can be used to calculate higher orders of k_x, i.e.

$$\frac{\delta k_x}{\xi} = \cot(k_x d_1) + \cot(k_x d_2) \tag{3.47}$$

Employing Equations (3.42) and (3.47), first three values of k_x are calculated (see Figure 3.18.). Then, longitudinal planar acoustic eigenfrequencies are calculated by

$$f_l = c k_x / 2\pi \tag{3.48}$$

where results are given in Table 3.6. Although reactance length is contributed by all transverse modes, summation of a few number of terms is enough due to the frequency of interest; the upper limit of summation stated in Equation (3.42) can be taken as 10, for instance.

A finite element model of the geometry is constructed using HEXA8 type elements. Through the commercial code, eigenfrequencies are extracted, where both of Lanzcos [140] and Arnoldi [141] algorithms are used to perform a double check. Number of elements per wave length is defined as 6 [121], whereas the speed of sound (c) and air density (ρ) are taken as 340 m/s and 1.225 kg/m^3, respectively. All the walls of the geometry are defined to be perfectly rigid, as in the analytical solution. Results are tabulated in Table 3.7., where f_l and f_c denote analytical and computational acoustic eigenfrequencies, respectively.

Table 3.6. Comparison of first three eigenfrequencies of longitudinal acoustic modes of the simplified model, where f_l and f_c denote analytical and computational results, respectively. (Results are in Hz.)

mode	f_l	f_c
($\underline{1}$ 0 0)	33,8	33,1
($\underline{2}$ 0 0)	84,2	83,9
($\underline{3}$ 0 0)	161,4	161,4

First three longitudinal planar acoustic modes are given in Figure 3.19. Planar modes at y- and z-directions are not altered by the aperture; hence, Equation (3.30) can be used in calculation. In Figure 3.20., first planar modes at y- and z-directions are presented, respectively.

Acoustic cavity model of the sedan is shown in Figure 3.21. Uncoupled acoustic modes of the model are computed in a similar way, using the commercial software. Eigenfrequencies of planar and non-planar acoustic modes are tabulated in Table 3.7.

A comparison is made between the analytical results of the simplified model and computational results of the actual model. When energy density is considered, effective acoustic modes are obviously the planar ones. Planar modes are two times stronger than the tangential ones. Likewise, tangential modes are two times stronger than the oblique ones [49]. Energy density of acoustic modes is related to the mean square sound pressure in the volume. Thus, it is reasonable to assume that if present, booms diagnosed are ruled by the planar acoustic modes, which can be approximately predicted by the analytical procedure proposed.

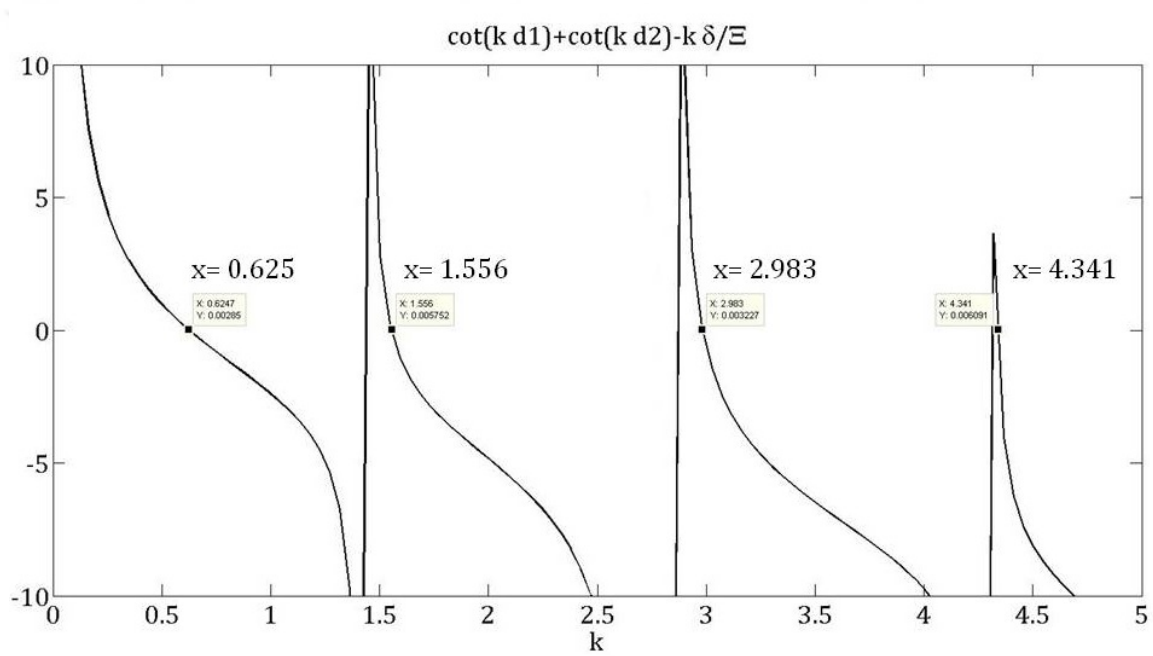


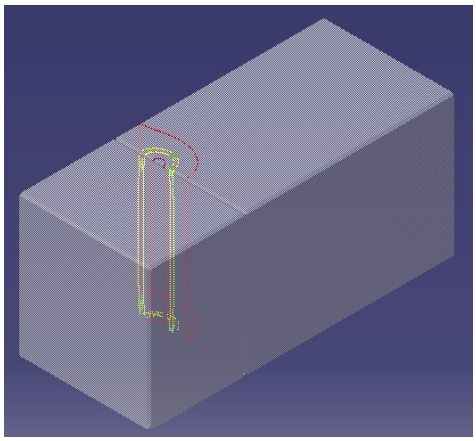
Figure 3.18. First three values of k_x are determined by root finding: k_1 =0.625, k_2 =1.556, k_3 =2.983. (k_4 is not used, since its associated frequency value is beyond the interest of analysis.)

For further investigation and validation, acoustic response of the sedan is computed in determined target microphone locations, i.e. BT:D and BT:K (see Figure 3.21.). A coupled vibro-acoustic analysis, where all steps are described in Chapter 4 is conducted. What is more, to reveal the importance of determination of acoustic cavity, three case studies are defined: i) trunk and cabin cavities are modeled as two acoustic volumes connected with an aperture; ii) trunk and cabin cavities are modeled as a single acoustic volume; iii) the acoustic volume is taken to be only the cabin cavity

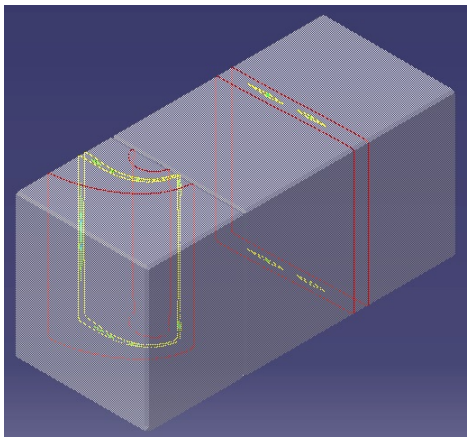
ignoring the trunk. Results up to 200 Hz are computed and tabulated in Table 3.8. This bandwidth is the low frequency region, and the pulse frequency can be calculated using Equation (2.17). First two longitudinal and one of the transverse acoustic modes of Case 1 are shown in Figures 3.22. to 3.24., respectively.

Table 3.7. Computed uncoupled acoustic eigenfrequencies of the actual cavity, and comparison of planar eigenfrequencies of the simplified and actual models, where f_l and f_c denote analytical and computational results, respectively. (Results are in Hz.)

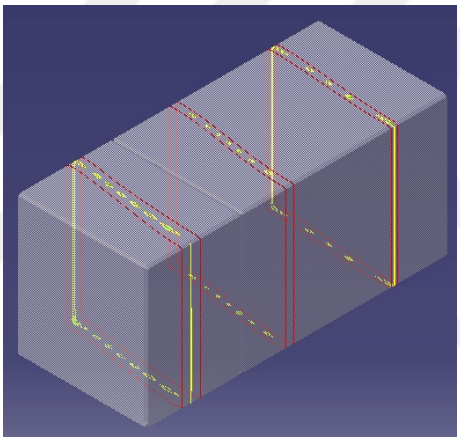
number	mode	direction	f_c	f_l
1	planar	x	35	34
2	planar	x	83	84
3	planar	z	118	121
4	planar	y	127	127
5	tangential		136	
6	oblique		139	
7	tangential		144	
8	tangential		147	
9	planar	x	166	161
10	oblique		175	
11	tangential		182	
12	oblique		185	
13	oblique		194	



(a) 33.1 Hz

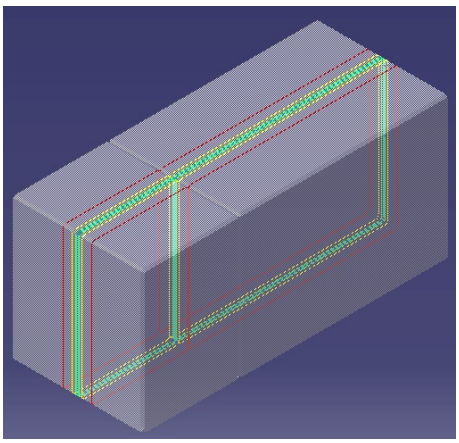


(b) 83.9 Hz

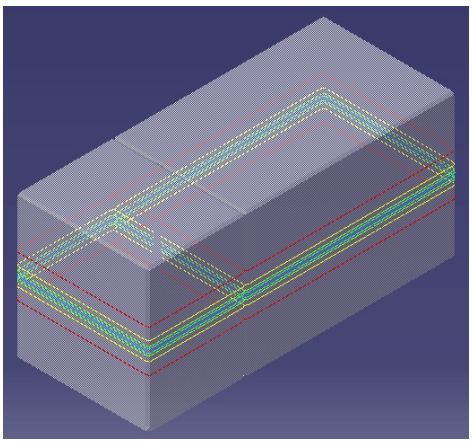


(c) 161.4 Hz

Figure 3.19. First three longitudinal acoustic mode shapes of the box in x-direction



(a) y-direction, $(0\underline{1}0)$, 126.9 Hz



(b) z-direction, $(00\underline{1})$, 120.6 Hz

Figure 3.20. First planar mode shapes of the box along y- and z-directions

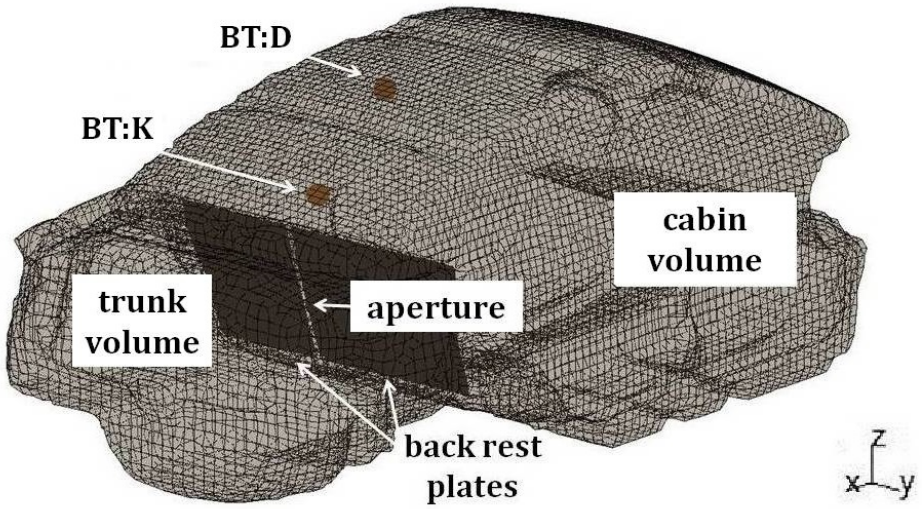


Figure 3.21. Two cavities in Vehicle L38 are connected by an aperture

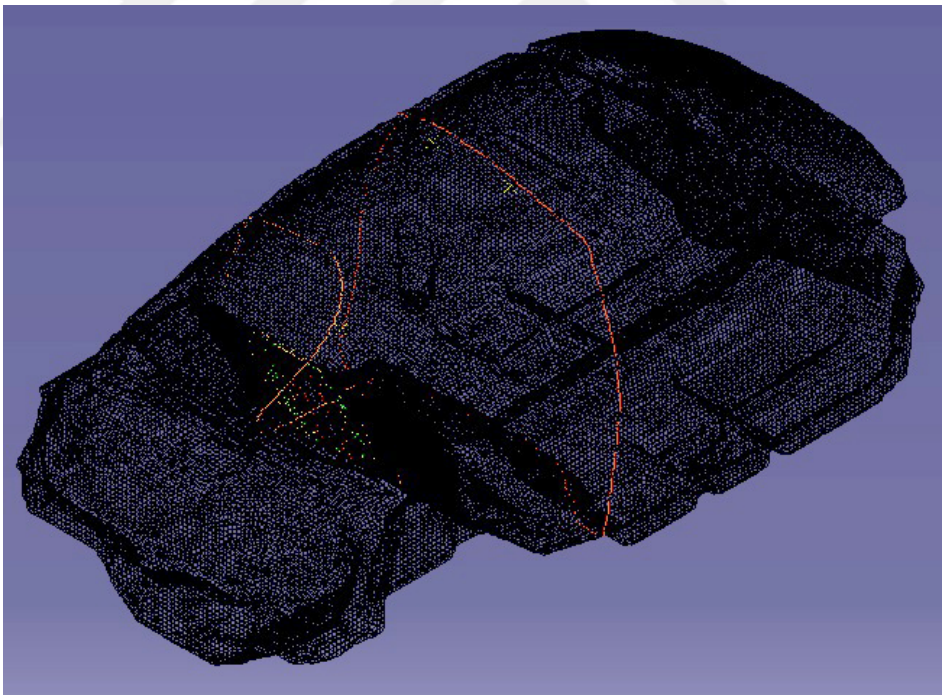


Figure 3.22. First longitudinal acoustic mode shape of the sedan, x-dir., 35 Hz, Case1.

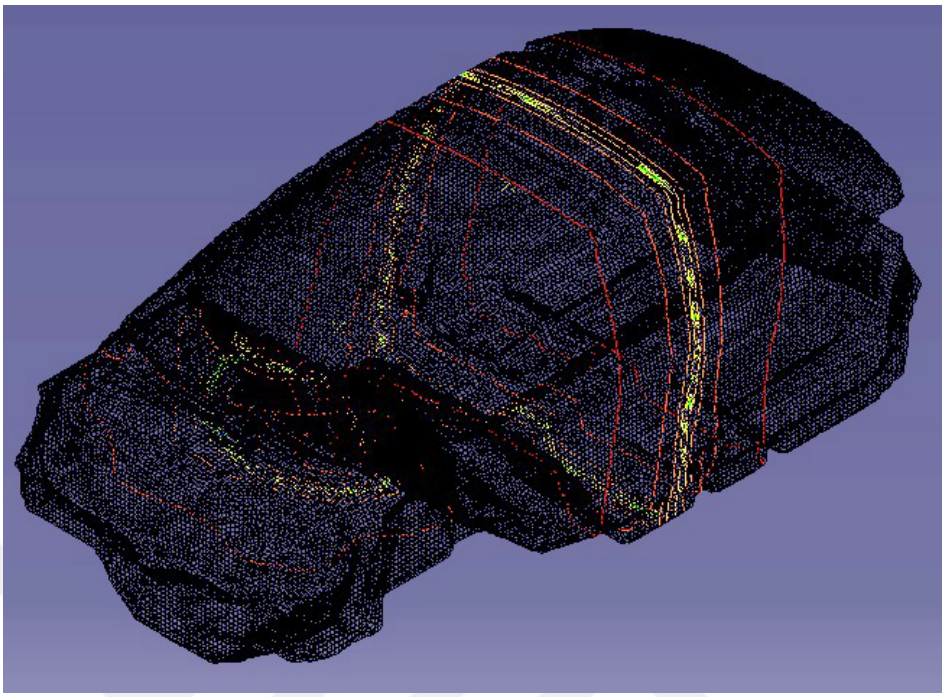


Figure 3.23. Second longitudinal acoustic mode shape of the sedan, x-dir., 83 Hz, Case1.

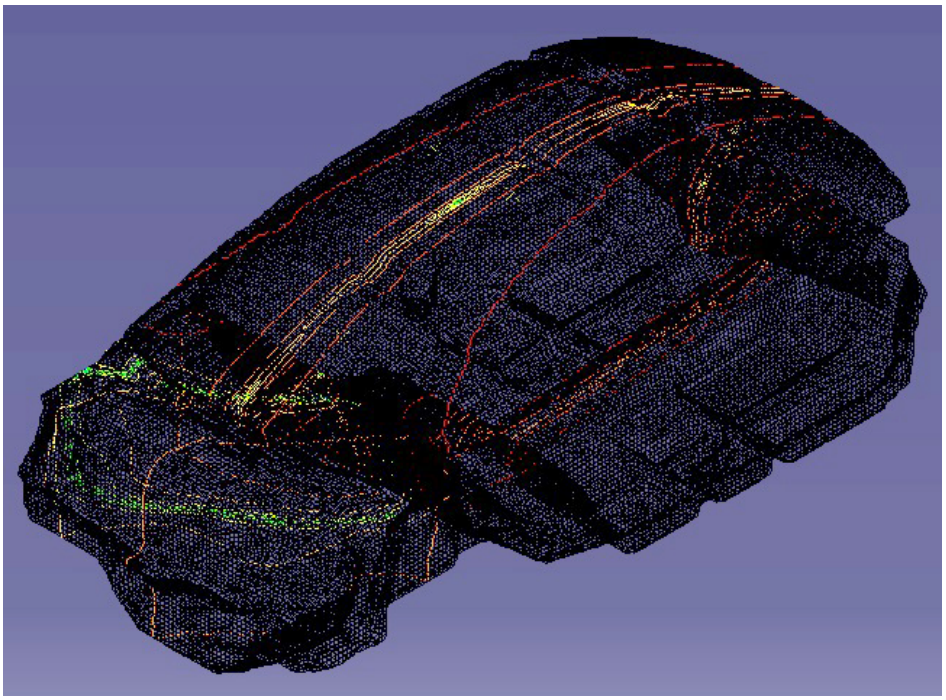
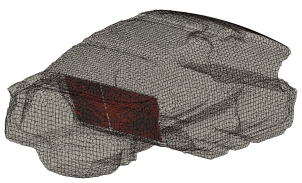
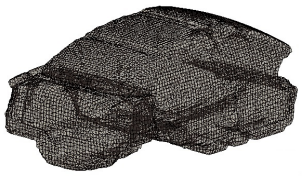
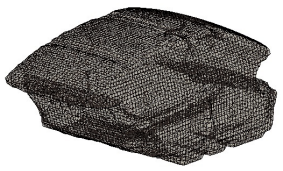


Figure 3.24. First planar acoustic mode shape of the sedan, y-dir., 127 Hz, Case1.

Table 3.8. Computed uncoupled acoustic eigenfrequencies of the sedan for the defined three cases up to 200 Hz.

modes			
	Case 1	Case 2	Case 3
1	35	55	80
2	83	97	118
3	118	119	127
4	127	130	144
5	136	132	147
6	139	146	177
7	144	154	182
8	147	177	187
9	166	183	196
10	175	187	
11	182	194	
12	185	197	
13	194		

Case 1 Trunk and passenger cavities are modeled as two acoustic volumes connected with a slit (68,231 elements)

Case 2 Trunk and passenger cavities are modeled as a single acoustic volume (68,395 elements)

Case 3 The acoustic volume is taken to be only the passenger cavity ignoring the trunk (53,616 elements)

3.3. Computation of Structural Modes

Computation of structural modes is critical in two folds: i) results of the computation are used in experimental modal analysis (EMA) studies (Section 4.1) to determine locations of sensors; ii) in coupled vibro-acoustic simulations (Section 4.3), the interaction between flexible shell and acoustic cavity incident upon this computation. FEA is commonly used for the computation, in which the structure is theoretically divided into contiguous linear elements that are substantially smaller than structural wavelength at the highest frequency of interest [142]. Mentioned requirement is actually analogous to the Shannons sampling theorem given in Equation (2.13), which states that the sampling rate must be greater than twice the maximum frequency of interest. For the very reason, it is determined to perform computations up to 400 Hz, since the highest frequency of interest is 200 Hz, in low frequency noise region.

3.3.1. Normal Modes Analysis

Normal Modes Analysis (a.k.a. eigenvalue analysis or eigenvalue extraction) is a procedure used to calculate the displacement patterns and associated frequencies of a structure. Computed frequencies are natural frequencies at which the structure naturally tends to vibrate, provided a disturbance is present. In the literature, natural frequency is also called as resonance, normal, characteristic, or fundamental frequency. Resonance, or resonant frequency term arises from the fact that if cyclic loads are applied at these frequencies, the structure can go into a resonance condition that will lead to failure. The displacement pattern, or say deformed shape of the structure at a specific natural frequency of vibration is known as 'normal mode'. Natural frequencies and normal modes are functions of characteristics of structure and boundary conditions. Natural frequencies and normal modes are determined from the reduced form of the equation of motion for dynamic systems. In the absence of damping and load

$$[M]\{\ddot{w}\} + [K]\{w\} = 0 \tag{3.49}$$

where $[M]$, $[K]$ are mass and stiffness matrices,respectively, and $\{w\}$ is the displacement vector. The free vibration solution is mathematically the non-trivial solution of Equation (3.49). It takes the form as

$$\{w\} = \{\Phi\} \sin \omega t \tag{3.50}$$

where $\{\Phi\}$ is the eigenvector, or mode shape and ω is the circular natural frequency. Here, the harmonic form of Equation (3.50) has also an important physical meaning, i.e. all the DOF of the structure move in a synchronous manner. The structural configuration does not change in shape during motion; only its amplitude changes. Substitution of solution form into Equation (3.49) gives

$$\begin{aligned} &- \omega^2[M]\{\Phi\} \sin \omega t + [K]\{\Phi\} \sin \omega t = 0 \\ &\Rightarrow \left([K] - \omega^2[M]\right)\{\Phi\} = 0 \end{aligned} \tag{3.51}$$

For Equation (3.51) to have non-zero solution $\{\Phi\}$, matrix $([K] - \omega^2[M])$ has to be singular so that

$$\left|[K] - \omega^2[M]\right| = 0 \tag{3.52}$$

where '$|\cdot|$' refers to determinant. Actually, Equation (3.52) represents an eigenvalue problem, where ω^2 and $\{\Phi\}$ is the eigenvalue and the eigenvector, respectively. The eigenvalue is the square of the natural frequency of the system, and the eigenvector is the associated mode shape. Note that, mode shape $\{\Phi\}$ is not unique, since any multiples of it satisfy Equation (3.52). Both the mass and the stiffness matrices are symmetric. The mass matrix is positive definite, while the stiffness matrix may be semi-positive definite, provided the system has rigid body modes.

The generalized eigenvalue problem of test vehicles is solved following the automated multi level substructuring (AMLS) method [41, 143], rather than Lanczos algorithm. Commercial solvers, Nastran and Radioss are both using AMLS type algorithms to provide fast solutions [144]. Both solvers are used in the calculation of

generalized eigenvalue problem to ensure results. Although solution procedure is theoretically identical, due to different algorithms of the solvers, two distinct models are prepared for each. The finite element model of Vehicle L38 used in the analysis is given in Figure 3.25. Normal modes analysis is performed up to 400 Hz, and the number of eigenfrequencies extracted is 1,209.

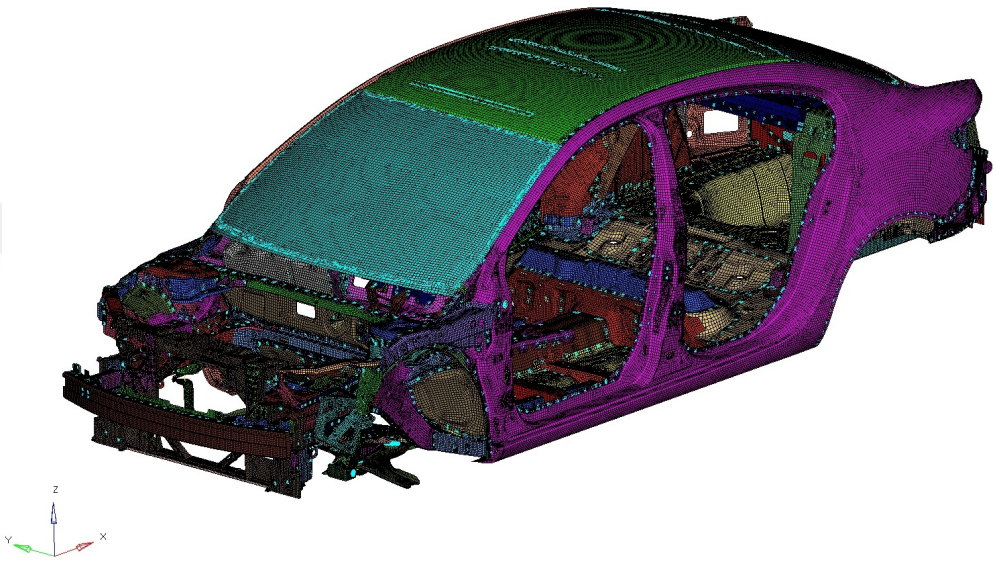


Figure 3.25. FEM of assembled Vehicle L38, # of DOF 3,620,607

3.3.2. Preparation for EMA

Before setting up of an experimental modal analysis (EMA), the critical question that must be answered is where excitation and response locations should be. In Ref. [145], an overview is given of the commonly used techniques to address the target mode selection, the accelerometer location and the placement of the shaker(s). Since it is impossible to instrument the test vehicle in all DOF corresponding to those of the computational model, the challenge is to use a minimum number of sensors. On the other hand, limited number of sensors may lead to an incomplete displacement pattern of mode shapes, even their locations are optimum. The term 'optimum' implies that there is a single best solution to the problem, which is rarely the case in most modal testing, especially for complex structures, such as a BIW [146]. A reduced model is needed to correlate experimental modal analysis and finite element analysis results. This reduced model, which is used in experimental modal analysis studies, is

prepared through the FE model. The reduced model is generally called as test-analysis-model (TAM), although many other names are available coined by commercial code developers. From the industrial perspective, the complexity of the sensor placement problem requires an automated procedure [147].

The most common reduction techniques are: Guyan (static), Generalized Dynamic, and SEREP. These reduction techniques are described in detail, in Refs. [148–150]. For ordinary models, massless DOF for instance, can be effectively removed using Guyan reduction, without altering the final result. If the model to be reduced has a huge DOF, some other reduction techniques are also available, but any reduction, apart from the massless DOF possibly alters the final solution.

So-called 'driving point residues' (DPRs) are stated as being equivalent to 'modal participation factors' (MPFs), and are a metric to assess how much a mode is excited, or participates in global response of the structure, at the driving point, i.e. excitation location [151]. In theory, DPRs are proportional to the magnitudes of normal frequencies in a driving point frequency response function. Many other methods of optimal sensor placement are proposed. Fisher information matrix (FIM) that uses mode shapes of the structure is one of the common methods. Similar studies derived from FIM are proposed: to maximize the norm of the FIM, the determinant of the FIM, or the smallest eigenvalue of the FIM; or, to minimize the trace of inverse of the FIM, or the condition number of the FIM are some of them. Another way is to use the Kinetic Energy Optimization Technique (KEOT). One of the common techniques is the modal assurance criterion (MAC): a correlation coefficient for modal vector analysis [152]. In Ref. [147], a new technique based upon 'Effective Independence', that places accelerometers as single units in an optimal fashion, is presented.

All techniques mentioned above make use of available finite element model. The critical point is to take the computational model as a reference for further studies. Nevertheless, it must be understood that this model is suitable for 'real analysis', where many assumptions are made. Recall that damping free assumption is the most outstanding one. On the other hand, the test model is a physical subject, where

results cannot be managed through assumptions. Importantly, experimental modal analysis is a 'complex analysis', where we get complex frequency response functions that have damping information embedded in. Above all, the engineer should be aware about differences of real and complex analysis, before set to work on test-analysis-model (TAM). The challenge is to compute normal modes from identified complex modes [153–155].

Using commercial software, optimal excitation and response locations are determined. Many attempts are made, and results are compared. In related studies, the number of excitation locations is determined as 1, or 2, whereas various response location sets are tested. The number of response locations is increased from 50 to 400 for different sets. Apart from the software recommendations, an independent approach is also put into experimentation, where explained in detail, in Section 4.1.

3.4. Remarks

(i) In Section 3.2.1, a well known analytical solution offered for the determination of acoustic eigenfrequencies of rectangular geometries is applied to the cavity of test vehicle. It is observed that results do not match well. Although promising outcomes are available for vehicle cavities, which have geometries convenient to approximate to a rectangular geometry, it is deduced that this analytical solution is not appropriate for sedans.

(ii) In Section 3.2.2, effect of folding rear seat aperture is studied. Trunk and passenger cavities are simplified into two adjacent boxes connected by an aperture. An analytical solution is proposed. Analytical and computational results showed that as the confined air in the vehicle is allowed to pass between the trunk and passenger cavities, the acoustic response changes substantially. It is shown that planar acoustic eigenfrequencies of the sedan can approximately be calculated using the analytical solution proposed. To further clarify the impact of folding rear seat aperture, three case studies are examined. It is concluded that proposed analytical solution can be effectively used in calculation of planar acoustic eigenfrequencies.

4. SYNTHESIS

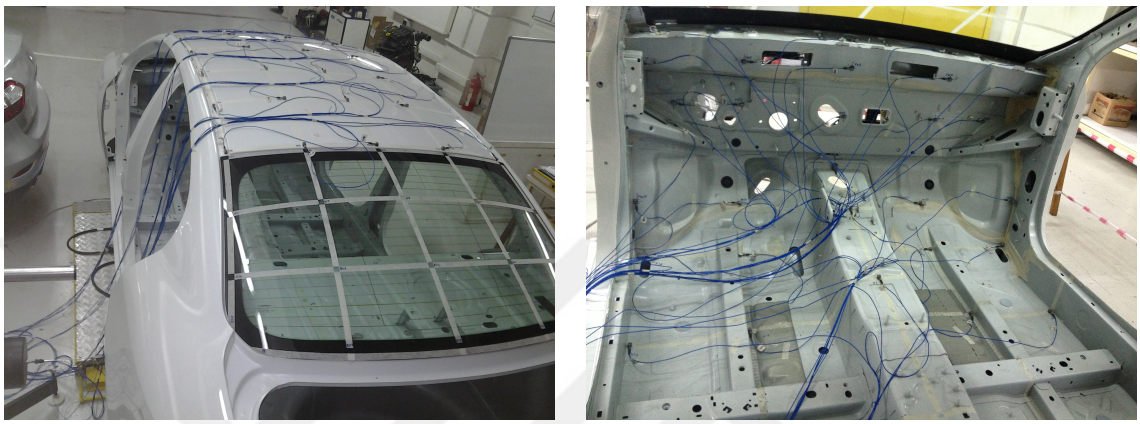
4.1. Experimental Modal Analysis

Experimental modal analysis (a.k.a. modal analysis or modal testing) is the procedure of determining natural frequencies, damping ratios, and mode shapes of a linear time invariant (LTI) system, through vibration testing. The vibration problem studied is a function of both forces applied, and system characteristics described by the modal parameters [156, 157]. Hence, experimental modal analysis (EMA) alone is not the answer to the whole problem, but is often an important part of the procedure. In general, mass and stiffness matrices are robustly constructed through finite element (FE) models. When it comes to damping matrix, FE model is needed to be updated using outcomes of modal tests. There is no practical way of damping identification, other than experimentation, although some alternatives, such as strain energy method are available. Therefore, EMA is not only beneficial in verification/correlation analysis, but it also complements the modal model. Theory of modal analysis is outlined well in Refs. [25, 52]. The steps of EMA can be broken down as (i) modal data acquisition, (ii) modal parameter estimation, and (iii) modal data validation.

4.1.1. Modal Data Acquisition

BIW of the test vehicle is employed for experimental modal analysis. Four air springs are used to provide a free boundary condition, like in panel tests, where described in Section 2.10. A very coarse physical mesh is formed on the structure, where a paper tape is used for marking. This physical mesh is a coarse mock up of the computational model, which is constructed for normal modes analysis (see Section 3.3.1). Every element has four nodes, and the locations of nodes are tagged in computational model to construct a wireframe. Mentioned physical mesh and the nodes tagged are shown in Figures 4.1. and 4.2., respectively. To acquire modal data, a roving uniaxial accelerometer array is used, where sensors are located at every node point determined. In exact node locations, the paper tape is removed, and sensors are attached directly

to the sheet metal, or on the glass using a special purpose wax. As explained in Section 3.3.2, various sets of response locations are studied, where the number of sensors is increased from 50 to 400. Finally, a number of 380 output locations are determined for the analysis presented.



(a) Roof and backscreen (b) Firewall and floor

Figure 4.1. The physical mesh

The wireframe is constructed in VirtualLab™ through the computational model, by combining the tagged nodes. The wireframe is a reduced computational model of the BIW, and it has the all information assigned to the FE model, i.e. material properties, thickness, etc. This reduced model, where shown in Figure 4.3. is used in correlation and model update studies. To excite the system, same driving points used in panel tests are adopted. To excite both bending and torsional modes, two excitation locations in y- and z-directions are determined. These driving points are selected after many attempts, where results are monitored with respect to the following criterions: (i) excitation of all structural modes must be achieved in the frequency bandwidth of interest; (ii) ordinary coherence value should be read at least 0,7. Note that, SIMO and MIMO tests have their own advantages and drawbacks depending on the structure to be tested. There is no single best solution offered for the application of EMA on vehicle structures. Consequently, many test parameters have to be reviewed, before attempting any model updating study. A benchmark is given in Section 4.1.1.1, where various parameters are analyzed for the particular application presented in the current work.

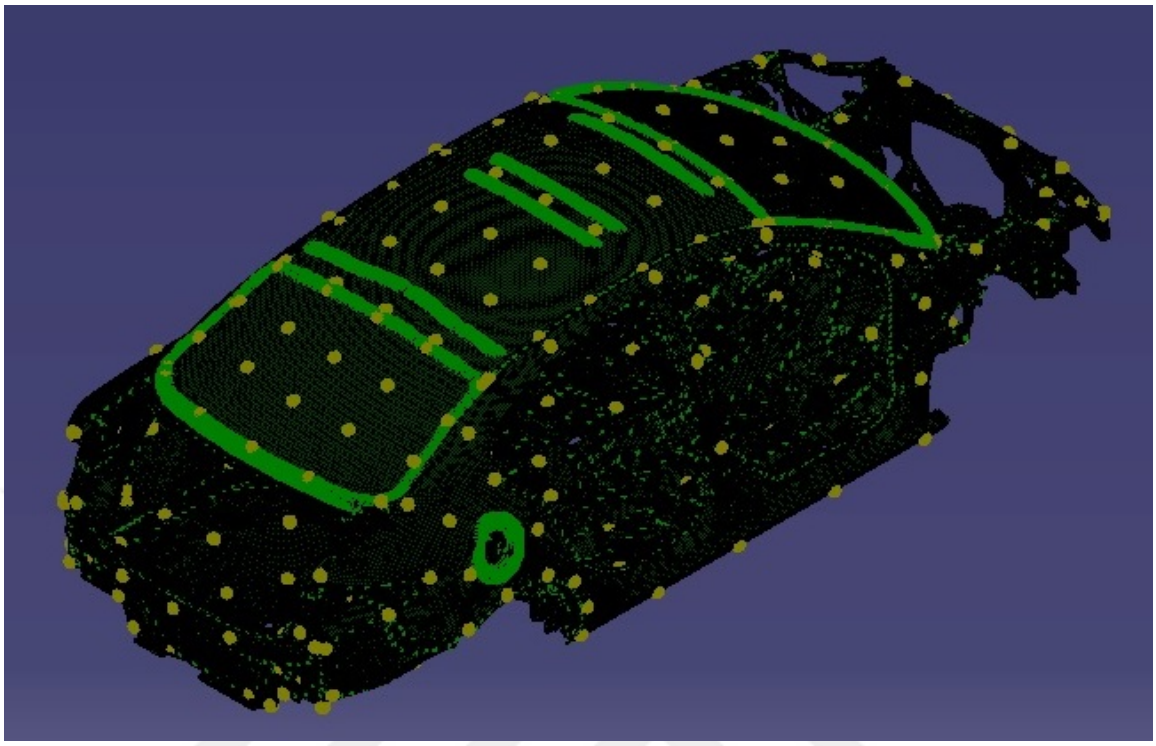


Figure 4.2. Nodes tagged on the computational model

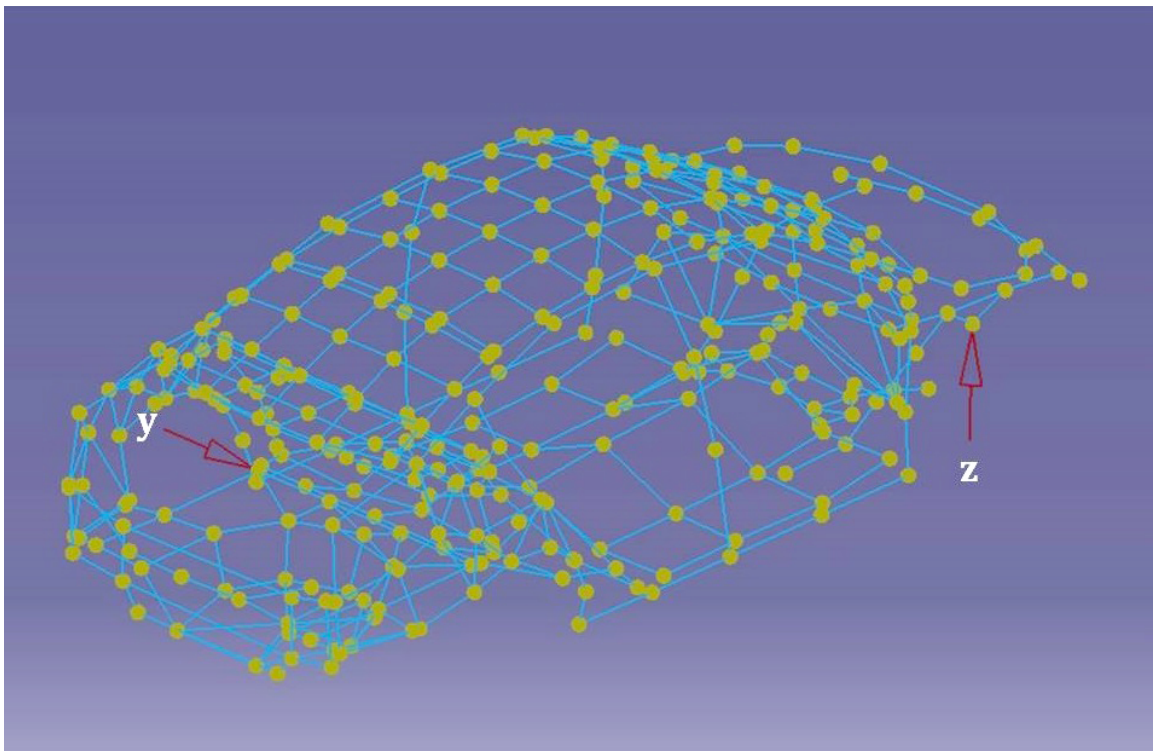


Figure 4.3. The wireframe constructed using 380 output locations (nodes tagged). The two arrows indicate the input locations determined for excitation.

4.1.1.1. Benchmark for BIW Excitation. Next to the determination of output points, appropriate locations for driving points are investigated, apart from suggestions of the commercial software used. In operational conditions, the BIW is excited by engine and exhaust. Hence, it is decided to choose locations nearby the connections, where engine and exhaust mounts are fixed (see Figure 2.37. for the locations of mounts). After many attempts and assessments, two locations and directions are specified: engine mount RH:02 in z-direction and exhaust mount EC:31 in y-direction. Notice that, z- and y-directions are related to bending and torsional modes, respectively.

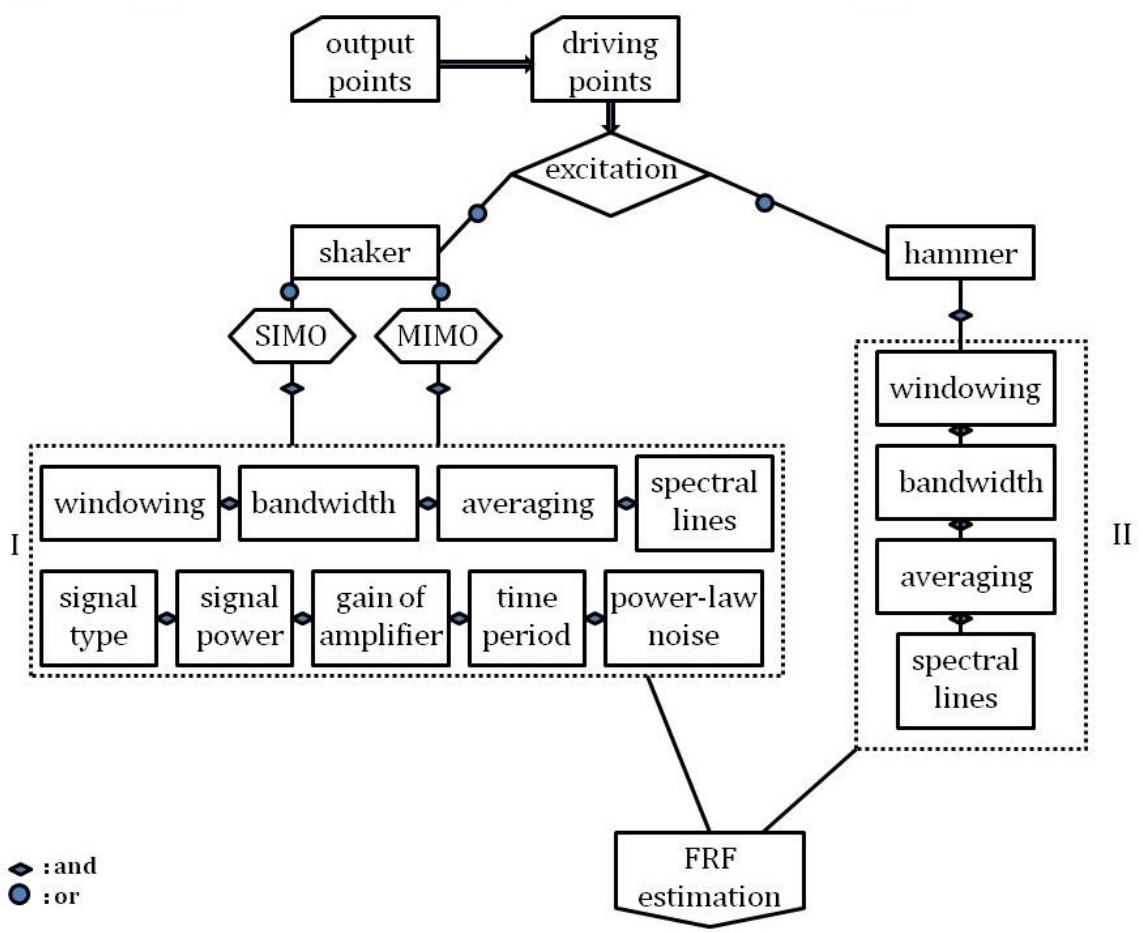


Figure 4.4. Excitation flowchart and Parameter sets I and II

Theoretically, there is no obligation for using an impact hammer as an exciter, except a troublesome spectral error: leakage[1] . The practical problem associated with the hammer excitation is the repeatability, i.e. the errors caused by deviations at

[1]This phenomenon is discussed in Section 2.8.

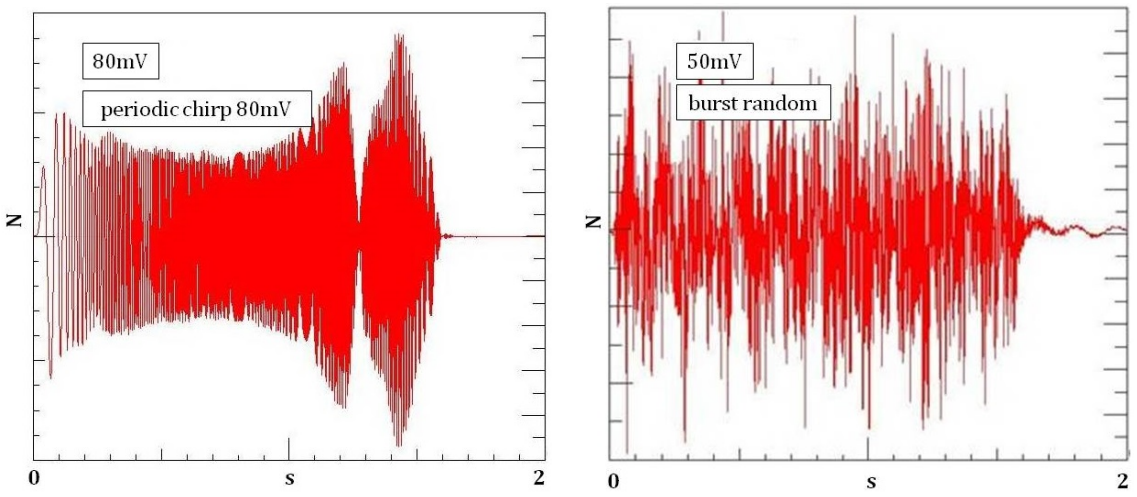
excitation locations and directions (see e.g. Ref [75]). Nevertheless, such a test is conducted for benchmarks. The Parameter set II mentioned in Figure 4.4. is determined as follows. Force and exponential windows are used, where the former and latter are applied to inputs and outputs, respectively. Having regarded to low energy excitation values of impact hammers, a bandwidth of 512 Hz is selected with a 0.5 Hz resolution. The average of 20 impacts is recorded for the FRF estimation step, where all of the three estimation techniques (i.e. H_1, H_2, and H_v) explained in Section 2.2 are used for comparisons.

Beside mentioned problems, the ones faced in the impact hammer application are the following. The energy produced by the hammer is observed to be insufficient to excite all modes in the frequency range of interest. What is more artificial damping effects are observed in the FRFs estimated, and ordinary coherence values are not successful enough, at least in some critical frequency intervals associated with global structural modes.

Following the procedure described in Figure 4.4., single input multi output (SIMO) and multi input multi output (MIMO) shaker excitation techniques are also employed. The determined excitation locations are shown in Figure 4.3.; they are RH:02:Z and EC:31:Y. Arranging the Parameter set I mentioned in Figure 4.4., three sets of modal test for every parameter is recorded, i.e. the structure is excited in (i) y-direction only, (ii) z-direction only, and (iii) both of y- and z-directions. Results are assessed, and parameters tabulated in Table 4.1. are determined for the final test whose results are used in the correlation analysis (Section 4.2). Shaker excitation signals used in tests are plotted in Figure 4.5. The signals are driven at $t_1 = 2ms$ - $t_2 = 1.6s$ period, where windowing time is $2s$. An indicator that plays an important role in specifying the parameters determined is the coherence value of estimated FRFs. To give an idea, three plots are presented in Figures 4.6. to 4.8., where coherence values of an identical FRF set is obtained through different excitations. Note that, the MIMO test result shown in Figure 4.8. has the highest coherence values.

Table 4.1. Parameters determined for experimental modal analysis

parameter	option or value
excitation	MIMO
windowing	uniform
bandwidth	1,024 Hz
number of spectral lines	2,048
number of averages	100
signal type (input: $+z$)	periodic chirp
signal type (input: $+y$)	burst random
signal power of $+z$ input	80 mV
signal power of $+y$ input	50 mV
voltage gain of amplifier	-4 dB
time period	2 s
power-law	white noise



(a) Periodic chirp (b) Burst random

Figure 4.5. Input signals

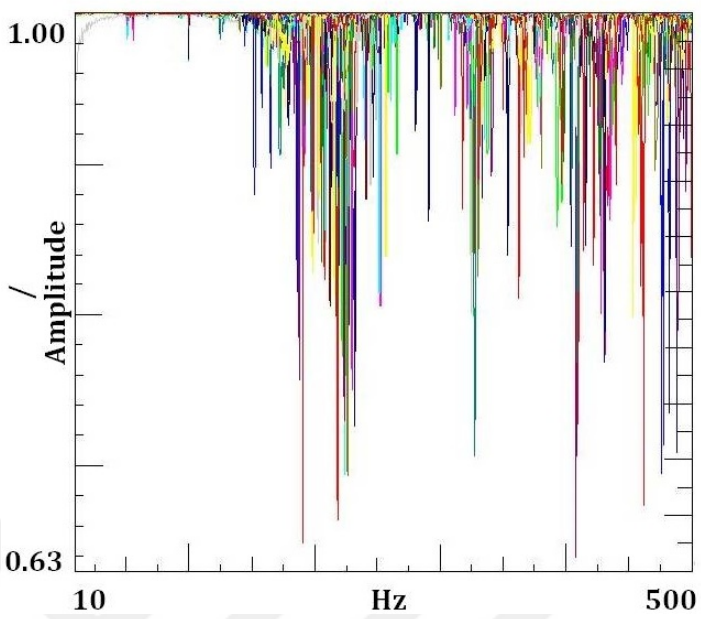


Figure 4.6. Ordinary coherence plots of estimated FRFs through impact hammer test. Parameters: $+y$, force and exponential window, 512 Hz, average of 20 impacts H_v.

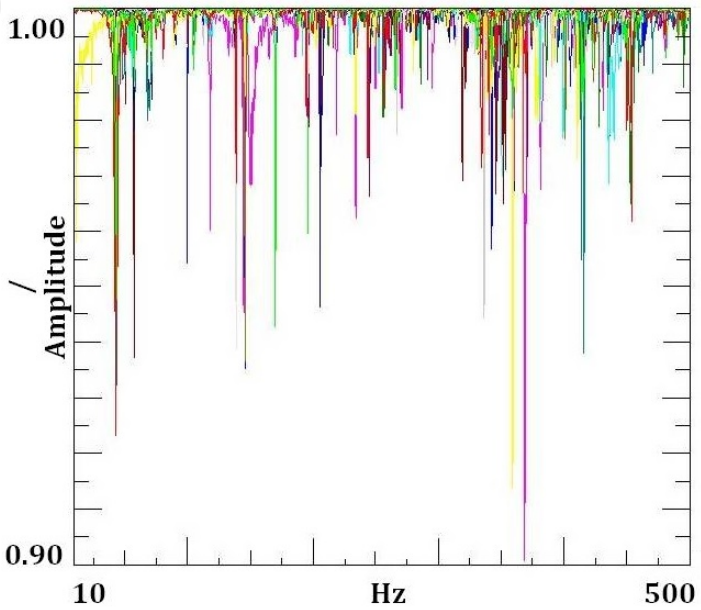


Figure 4.7. Ordinary coherence plots of estimated FRFs through SIMO test. Parameters: $+y$, uniform window, 1,024 Hz, H_v, average of 100 excitations, 50 mV, 2 ms, burst random.

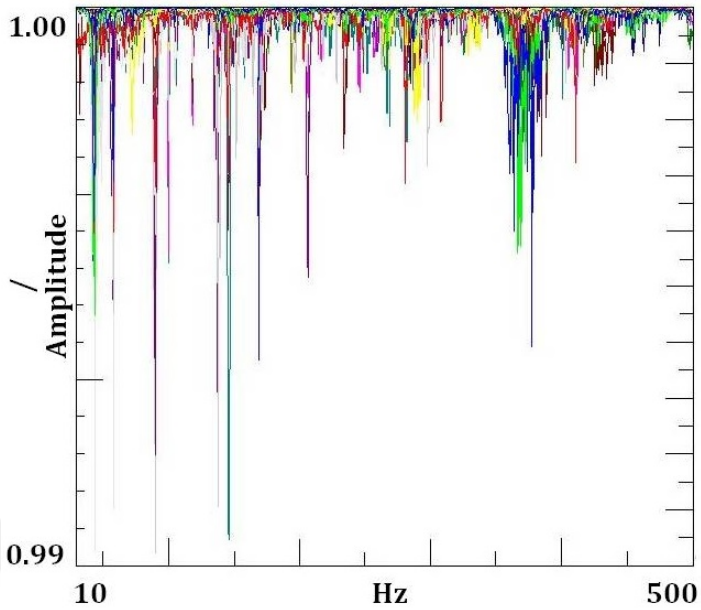


Figure 4.8. Multiple coherence plots of estimated FRFs through MIMO test.

Parameters: Table 4.1.

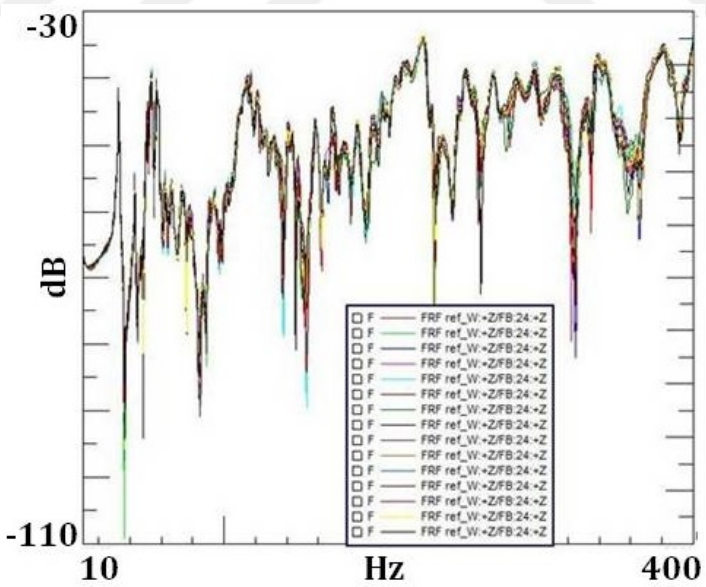


Figure 4.9. FRFs estimated through one of the reference accelerometers (15 sets).

Sensor measurements should be acquired simultaneously at all of the output locations determined. Since the number of analyzer channels and sensors are not enough for such a measurement, a roving array of 30 uniaxial accelerometers is employed. To ensure the repeatability, three reference accelerometers are also used throughout the experimental modal analysis studies. FRFs given in Figure 4.9. belong to one of these reference accelerometers, which are attached to an arbitrary location on the windscreen of the test vehicle. Results of 15 sets of measurements match well enough, which means that the repeatability condition is satisfied.

4.1.2. Modal Parameter Estimation

Modal data acquired are processed using the polyreference least-squares complex frequency-domain method. The method is outlined well in Refs. [52, 158, 159]. A commercial code derived from this approach is presented in Refs. [160,161], where comparisons with time domain methods, like least squares complex exponential (LSCE) are also given. Modal parameters are estimated through the measured frequency response functions. These fundamental parameters are complex modal frequencies (λ_r), modal vectors (ψ_r), and modal mass (A). Current algorithms also extract modal participation vectors (L_r) and residues (A_r). Polyreference parameter estimation algorithms identify modal participation vectors. These vectors scale how well each modal vector is excited from each of the driving points determined for the modal test. Combination of the modal participation and modal vectors yields the residue for a mode, i.e.

$$A_{pqr} = L_{qr}\psi_{pr} \tag{4.1}$$

Modal participation and modal vectors are supposed to have the information about right and left eigenvectors of a structural mode, respectively. If the assumptions outlined in Section 2.2 hold for the system, left and right eigenvectors are expected to be proportional to each other. Following the notation used by Allemang, and recalling

Equation (2.5), for MIMO systems

$$[H(\omega)]_{N_o \mathrm{x} N_i} = \sum_{r=1}^{N} \frac{[A_r]_{N_o \mathrm{x} N_i}}{j\omega - \lambda_r} + \frac{[A_r^*]_{N_o \mathrm{x} N_i}}{j\omega - \lambda_r^*} \tag{4.2}$$

which can be split into

$$[H(\omega)]_{N_o \mathrm{x} N_i} = [\psi]_{N_o \mathrm{x} 2N} \left[\frac{1}{j\omega - \lambda_r}\right]_{2N \mathrm{x} 2N} [L]^T_{2N \mathrm{x} N_i} \tag{4.3}$$

and

$$[H(\omega)]^T_{N_i \mathrm{x} N_o} = [L]_{N_i \mathrm{x} 2N} \left[\frac{1}{j\omega - \lambda_r}\right]_{2N \mathrm{x} 2N} [\psi]^T_{2N \mathrm{x} N_o} \tag{4.4}$$

where N is the number of spectral lines; i and o denote input and output, respectively. The model presented has 2x380 DOFs and 2048 spectral lines. For one spectral line, Equation (4.4) can be written as

$$[H(\omega_i)]^T_{N_i \mathrm{x} 1} = [L]_{N_i \mathrm{x} 2N} \left[\frac{1}{j\omega_i - \lambda_r}\right]_{2N \mathrm{x} 2N} [\psi]^T_{2N \mathrm{x} 1} \tag{4.5}$$

Residues are related to mode shapes, whereas poles are associated with the frequency and damping of the system. Residues can be calculated from modal participation vectors and the modal coefficients by Equation (4.1). Modal vector coefficients (ψ_r) are equal to residues for an associated reference (A_{pqr}), and these coefficients can be calculated by normalizing one column of the modal participation factor matrix (L) to unity.

The number of modal frequencies (λ_r) can be found by counting the number of peaks in the frequency response functions measured. However, closely spaced modes, or repeated roots may be present. What is more the resolution selected may not be appropriate to render close modal frequencies. A more reliable procedure is the summation of FRF power, since such a summation includes the peaks that are present

in several frequency response functions. The FRF power is formulated as

$$H_{\text{power}}(\omega) = \sum_{p=1}^{N_o} \sum_{q=1}^{N_i} H_{pq}(\omega) H_{pq}^{*}(\omega) \tag{4.6}$$

and represents the auto power of the FRFs summed over a number of response measurements. Model order is defined as the highest power in a matrix polynomial equation. Equation (4.6) does not provide an accurate estimate of model order, when repeated roots, or close modes are present. A method offered to find out the model order is the error chart, where the error in the model is plotted as a function of increasing model order. The error chart quantifies the normalized error, and reveals the ability of the model in predicting data, which are not comprised in the estimate of the modal parameters. If the model order is not sufficient to predict next data points, the normalized error value will increase. On the other hand, if there is incompleteness in the observation of the model, to increase the model order will not decrease the normalized error.

The stability plot is a further interpretation of the error chart, where stable (i.e. physical) poles are identified as a function of the model order. In these plots, more modal frequencies are estimated as the model order is increased. Identified modal parameters stabilize and converge, when the correct model order is found. Poles of well excited modes are identified at low model orders, whereas the poles of poorly excited modes will not stabilize, till the model order is increased up to a certain value. When the correct model order is reached, convergence is noticed, i.e. the number of identified modes will not increase anymore, provided that the experimental modal analysis study is successful. Such a certain value is found for the analysis presented, where the correct model order is observed to be 200. In Figure 4.10., the stabilization plot of Vehicle L38 is given. Note that, the stability diagram identifies structural damping and modal participation factors as a function of model order, besides tracking the estimates of modal frequencies. Commercial algorithms derived from polyreference least-squares complex frequency-domain method use the damping ratio estimations to

separate physical and computational poles, where a negative value indicates a computational pole [160]. These type algorithms exclude such poles from the diagram to provide more clear stabilization plots.

In the analysis, the complex mode indicator function (CMIF) is used to investigate the existence of normal, and/or complex modes. Peaks determined by the CMIF indicate the corresponding frequencies of associated modes. Then, damped natural frequencies for each identified mode can readily be calculated. These frequencies are calculated by taking the singular value decomposition (SVD) of the constructed FRF matrix at each spectral line (N), i.e.

$$[H(\omega)] = [U(\omega)]_{N_o \mathrm{x} N_e} [\Sigma(\omega)]_{N_e \mathrm{x} N_e} [V(\omega)]^H_{N_d \mathrm{x} N_i} \tag{4.7}$$

where $[U(\omega)]$ and $[V(\omega)]$ are the left and right singular matrices, respectively. $[\Sigma(\omega)]$ is the diagonal singular value matrix, and $[\,\cdot\,]^H$ denotes the Hermitian matrix. N_e denotes the number of effective modes; i and o input and output, respectively. For a mode, the closest modal frequency to the spectral line takes the larger singular value. Hence, by Equation (4.7), damped natural frequencies can be identified. Eigenvalues are calculated for every spectral line, i.e.

$$\mathrm{CMIF}_{N_e}(\omega) = \Sigma_{N_e}(\omega)^2 \tag{4.8}$$

and the CMIF is the plot of these eigenvalues, where the calculated one for the present study is shown in Figure 4.11., as a function of frequency. Every detected peak corresponds to an eigenvector, and these eigenvectors are equivalent to modal participation factors, provided that the measured FRFs are free of noise and leakage. Note that, the effect of leakage can be decreased by increasing the number of spectral lines of data in Equation (4.8). In the 20-200 Hz bandwidth, 54 damped natural frequencies and associated percent damping values (i.e. % of critical damping) are measured. Results of experimental modal analysis are tabulated in Table 4.2. Bode diagram of the results are given in Figure 4.12.

Table 4.2. Experimental modal analysis results; damped natural frequencies (ω_d) in Hz and corresponding percent damping (ζ) values. 54 damped eigenfrequencies are measured in the 20-200 Hz bandwidth.

#	ω_d	ζ	#	ω_d	ζ	#	ω_d	ζ
1	32,75	0,61	19	91,24	1,06	37	139,79	1,36
2	34,37	4,82	20	94,25	1,36	38	142,12	1,49
3	43,19	0,53	21	95,68	1,53	39	142,80	1,34
4	47,24	3,28	22	97,72	0,94	40	144,77	1,00
5	49,18	0,76	23	101,10	1,44	41	147,21	1,16
6	50,91	0,92	24	102,68	2,59	42	153,84	1,05
7	52,89	1,57	25	105,25	1,08	43	155,56	1,06
8	57,05	0,94	26	107,85	1,52	44	156,55	0,91
9	58,59	0,58	27	110,87	1,45	45	158,30	0,85
10	61,88	0,79	28	114,68	1,76	46	162,67	1,33
11	66,37	0,68	29	116,78	0,88	47	167,10	0,99
12	67,88	1,35	30	117,00	1,17	48	168,62	0,74
13	72,35	1,31	31	120,76	1,45	49	173,72	1,39
14	75,10	1,03	32	122,52	1,67	50	180,37	1,36
15	76,55	1,18	33	126,64	1,30	51	181,87	1,35
16	80,76	1,10	34	128,35	1,51	52	185,91	0,83
17	84,56	1,49	35	131,14	1,32	53	187,47	1,28
18	88,48	1,11	36	136,80	1,35	54	194,98	0,76

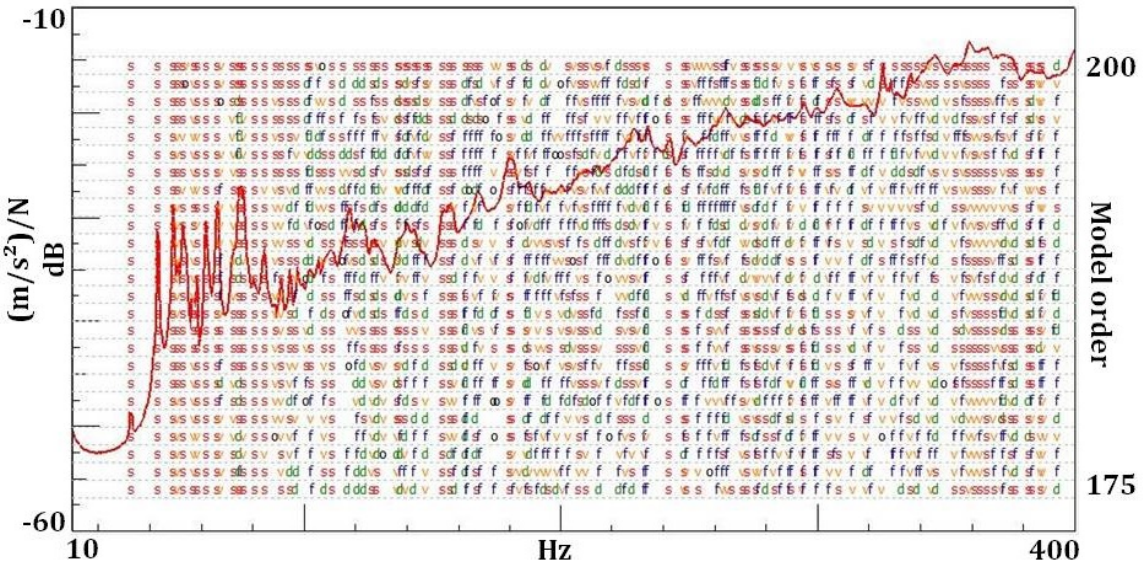


Figure 4.10. Stabilization plot is obtained by applying polyreference least-squares complex frequency-domain method to the Vehicle L38 data. The order of model is 200. The letter 's' in red indicates a stable pole.

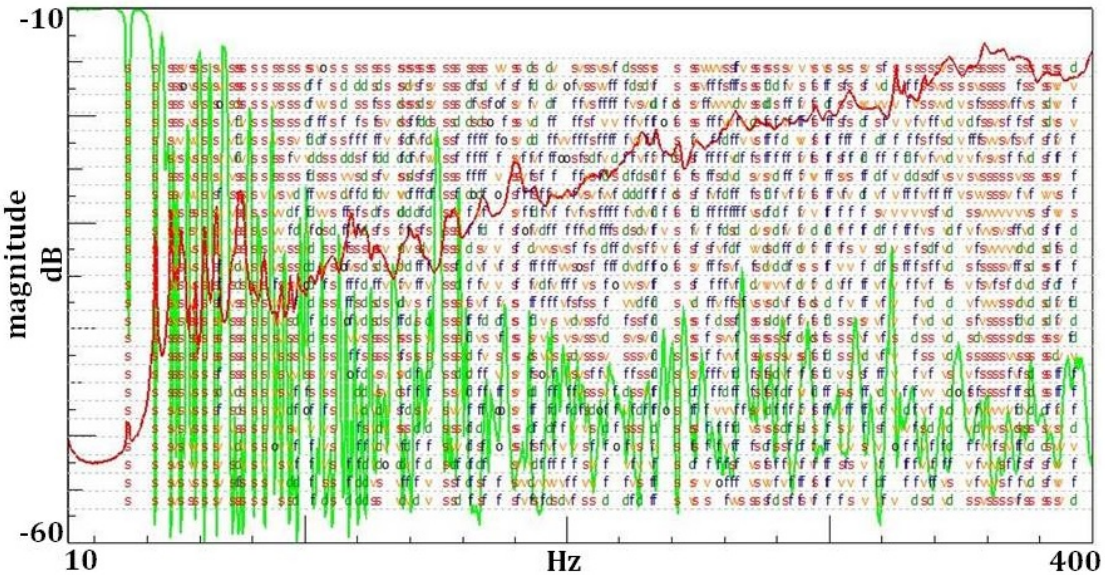


Figure 4.11. Complex mode indicator function (CMIF), the green curve, is shown on the stabilization plot, as a function of frequency.

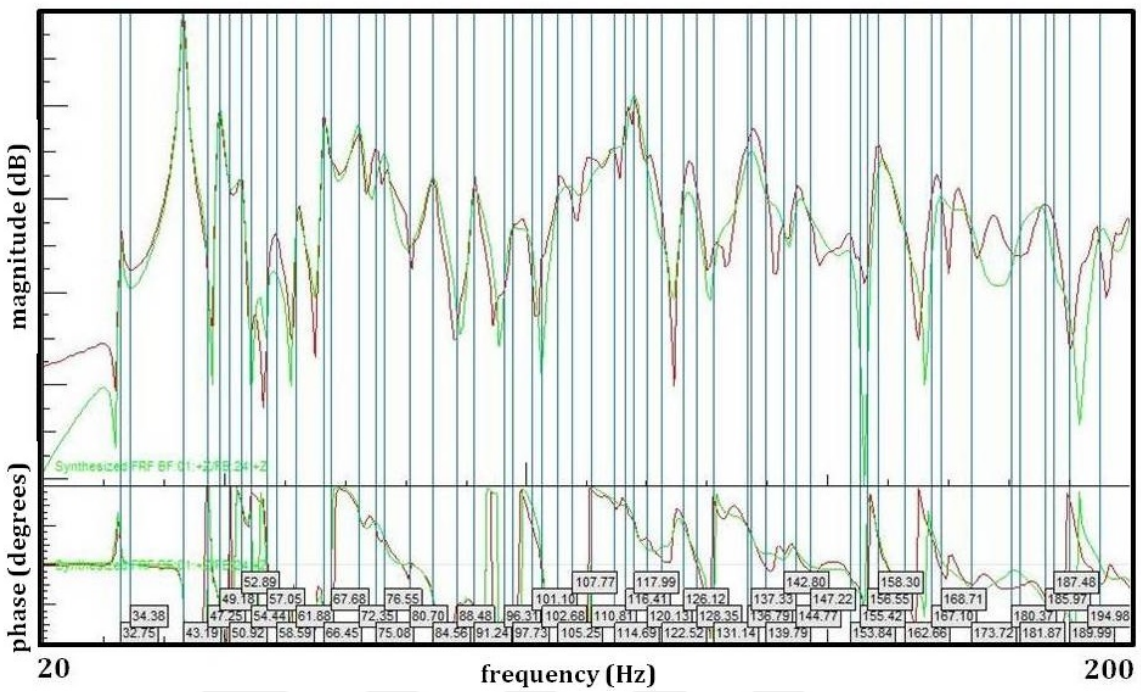


Figure 4.12. Bode diagram of identified damped natural frequencies in 20-200 Hz bandwidth.

4.1.3. Modal Data Validation

Experimental modal analysis results and outcomes of the computational studies given in Chapter 3 are used to validate and to complement each other. Actually, this is not a straightforward synthesis as suggested by theoretical considerations. It is often used to pair experimentally extracted eigenvectors with computationally derived ones. The common practice is to use modal assurance criterion (MAC), which is a simple function of the angle α between the two eigenvectors, i.e.

$$\mathrm{MAC}(\alpha) = \cos^2 \alpha \tag{4.9}$$

This criterion is first offered by Allemang and Brown [152]. Later on, many similar criterions are offered in the area of structural dynamics [162]. As criterions are used in applications, limitations and shortcomings of them are realized. Unsatisfactory results motivate researchers to come up with new statistical considerations. Various methods

are offered:

(i) Weighted Modal Analysis Criterion (WMAC) [162],
(ii) Partial Modal Analysis Criterion (PMAC) [163],
(iii) Modal Assurance Criterion Square Root (MACSR) [164],
(iv) Scaled Modal Assurance Criterion (SMAC) [165],
(v) Modal Assurance Criterion Using Reciprocal Vectors (MACRV) [166],
(vi) Modal Assurance Criterion with Frequency Scales (FMAC) [167],
(vii) Coordinate Modal Assurance Criterion (COMAC) [168],
(viii) The Enhanced Coordinate Modal Assurance Criterion(ECOMAC) [169],
(ix) Mutual Correspondence Criterion (MuCC) [170],
(x) Normalized Cross Orthogonality (NCO) [171],
(xi) Modal Correlation Coefficient (MCC) [172],
(xii) Inverse Modal Assurance Criterion (IMAC) [173],
(xiii) Complex Correlation Coefficient (CCF) [174],
(xiv) Frequency Domain Assurance Criterion (FDAC) [175],
(xv) Coordinate Orthogonality Check (CORTHOG) [176],
(xvi) Linear Modal Correlation Coefficient (LNCO) [177],
(xvii) Normalized Modal Difference (NMD) [178].

MAC is expressed by

$$\mathrm{MAC}\left(\mathbf{u}_{e,i}, \mathbf{u}_{c,j}\right) = \frac{|\mathbf{u}_{e,i}^T \mathbf{u}_{c,j}|^2}{\left(\mathbf{u}_{e,i}^T \mathbf{u}_{e,i}\right)\left(\mathbf{u}_{c,j}^T \mathbf{u}_{c,j}\right)} \tag{4.10}$$

where $\mathbf{u}$ denotes an eigenvector; indices e and c indicate experimental and computational results, respectively. The criterion is criticized, since it is nonlinear and does not guarantee the orthogonality condition. These shortcomings and many other problems are attempted to be solved through the procedures offered, where itemized above. Nevertheless, the main problem is the difference in the characteristics of eigenvectors compared. EMA results are based on the complex frequency response functions, where mass, stiffness, and structural damping are characterized through amplitude, frequency, and phase. Note that, eigenvectors derived from polyreference least-squares complex

frequency-domain method are *complex*. On the other hand, computational results yield *real* eigenvectors with no damping information. Yet another approach is the frequency response assurance criterion (FRAC). It is given as

$$\mathrm{FRAC}\left(\mathbf{H}_{c,j}, \mathbf{H}_{e,i}\right) = \frac{|\mathbf{H}_{c,j}\mathbf{H}_{e,i}^{*}|^{2}}{\left(\mathbf{H}_{e,i}\mathbf{H}_{e,i}^{*}\right)\left(\mathbf{H}_{c,j}\mathbf{H}_{c,j}^{*}\right)} \tag{4.11}$$

where $\mathbf{H}$ is the FRF vector; indices e and c indicate experimental and computational results, respectively [179–181]. The FRAC makes sense, when it is evaluated as a function of the forcing frequency. Main difference between MAC and FRAC is that the former correlates individual structural modes, whereas the latter correlates the response, which depends on the modal participation of all modes in the frequency range of interest. Both criterions take values between 0 and 1, where the value 1 means perfect correlation.

4.2. Correlation Analysis

During experimental modal analysis, test data are acquired through uniaxial accelerometers located normal to the plane. Differently, elements of the FE model data take the global axis as a reference. Before any correlation study, reduced FE model, i.e. the wireframe has to be aligned such that all nodes of the model must be compatible with test data. This is achieved by assigning local axes to all nodes of the wireframe, which correspond to output locations of the test model. In Figure 4.13., Euler axes attached at all nodes are shown. Next to the geometrical correlation, a MAC analysis is performed to assess the correlation of measured and computed eigenvectors. Nearly perfect correlation is observed for a number of 18 eigenvectors, i.e. diagonal MAC results are above 0.9 (see Figure 4.14.). Through the commercial code sensitivity and optimization studies are performed [182]. Test model is taken as the reference model in these studies. In total, 37 of 54 test eigenvectors are determined to be used in verification study. Next to the verification study the updated computational model is used in coupled vibro-acoustic analysis.

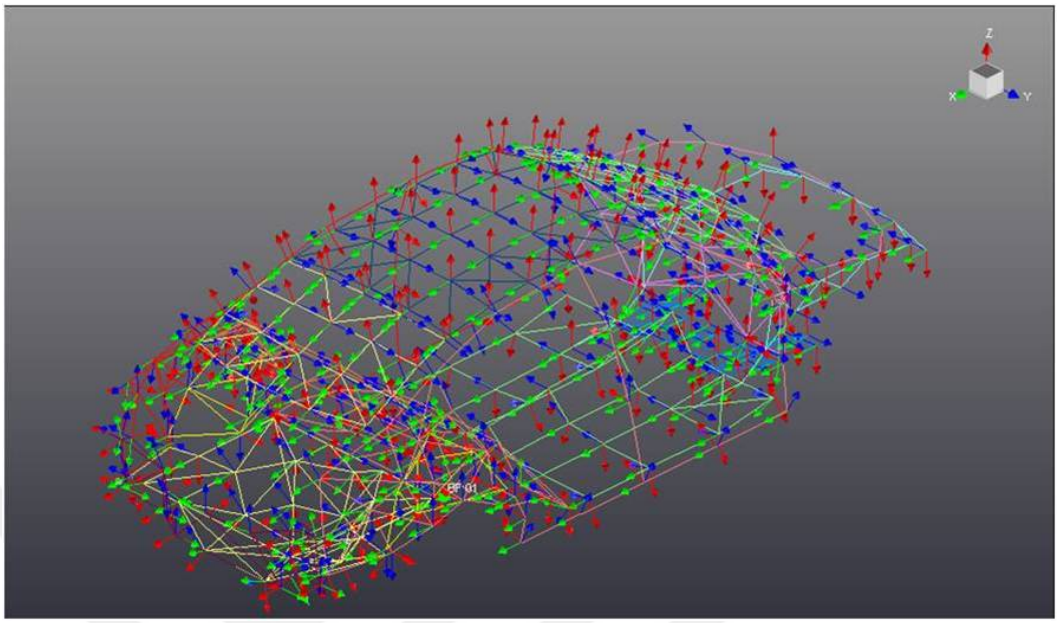


Figure 4.13. Euler axes are attached on every node of the wireframe. There are 380 nodes on the wireframe shown.

4.3. Coupled Vibro-Acoustic Analysis

In a source-path-receiver concept [183], the source is defined as external forces generated by the engine and exhaust systems. Panels of the sedan are the main radiation sources for the structure borne noise inside the cavity. Under the excitation of external forces, the panels which behave as paths, vibrate and excite the air inside the acoustic cavities. In the low frequency range, structure borne sound strictly dominates the acoustic response of the vehicle [184]. The coupled vibro-acoustic problem is computationally solved using Eulerian displacement-pressure formulation, where the structural finite element (FE) model of the body-in-white (BIW) is used to compute nodal displacements, and the acoustic FE models presented in Section 3.2.2 are used to compute the nodal acoustic pressure values of the air inside the two cavities. Among the computed nodal acoustic pressure values, two microphone locations are points of interest: BT:D and BT:K (see Figure 3.21.). They represent the ears of human occupants, i.e. the receivers. For the theoretical background of computational procedure of coupled analysis, the reader is referred to Appendices C to E.

For the three cases defined in Section 3.2.2, the coupled vibro-acoustic analysis is carried out through models that are constructed by employing correlated structural modes, identified force vector, and computed acoustic modes. In Figure 4.15., the force vectors identified using Equation (2.34) are plotted as functions of frequency. In all three cases, same parameters and data are used, except the acoustic modes. The analysis is performed in a 33-193 Hz bandwidth with 0.5 Hz resolution; updated structural modes are used with associated measured damping values. Acoustic modes are included in the analysis with an assigned viscous damping ratio of 8 % to account for acoustic damping elements of the vehicle, which are not explicitly modeled. The interface of acoustic-structure coupling (or, wetted surface) is formed assuming that normal velocities are equal throughout the fluid-structure boundary, as expressed by Equation (E.6).

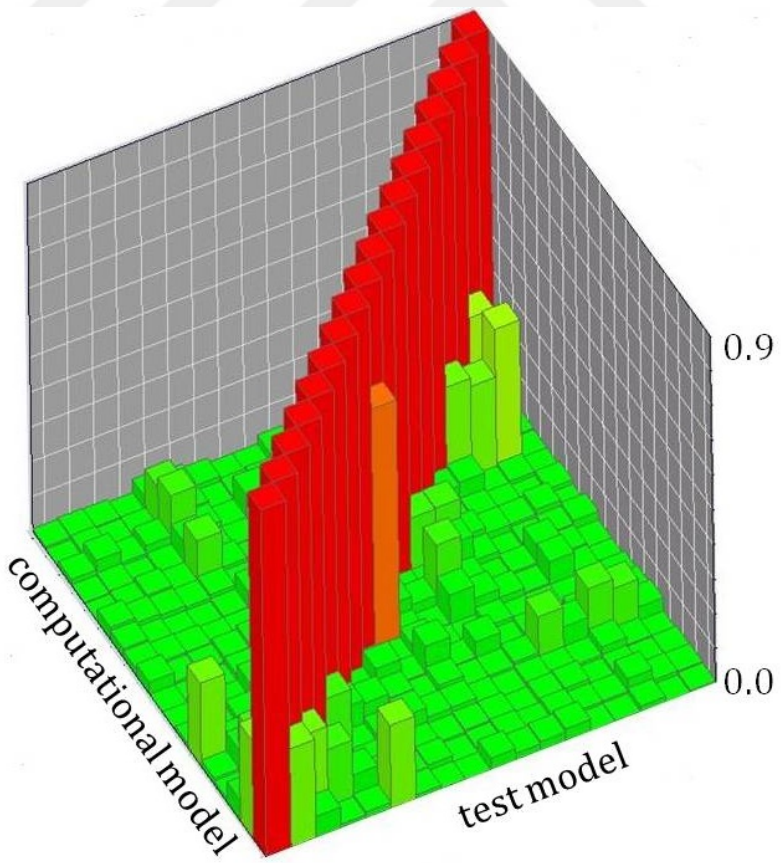


Figure 4.14. MAC plot of test and computational eigenvectors. Nearly perfect correlation (MAC $\geq$ 0.9) is observed in between 18 eigenvectors only.

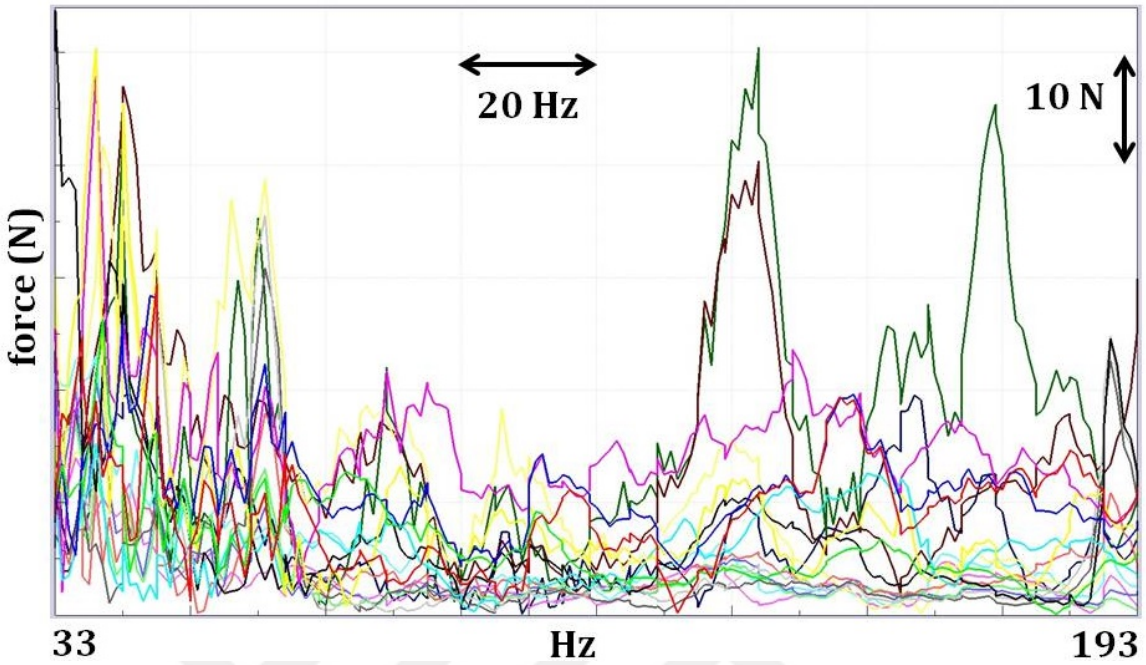


Figure 4.15. Identified operational force vectors, Vehicle L38.

The analysis yields coupled acoustic modes in the vicinity of uncoupled ones, and new complex modes occurred by acoustic-structure coupling phenomenon. Sound pressure levels are predicted through the coupled solution. Measured and predicted second order sound pressure levels at BT:D and BT:K locations are plotted in Figures 4.16. and 4.17.; L_2 norm of differences are tabulated in Table 4.3., in linear weighted decibels. Comparisons show that the results of the model that considers the effect of folding rear seat aperture (Case 1) match well with the measurement results.

Considering the measurement results, all booms are identified in the vicinity of uncoupled acoustic modes, except one. As analytical and computational results agree, instant pressure rises are found around 35, 83, 118, 127 and 166 Hz. Around 62 Hz, one structurally coupled mode is effective, especially at BT:K location, which cannot be identified without performing a coupled analysis. Due to nature of coupling between acoustic and structural modes, it is not straightforward to deduce the contributions of modes directly.

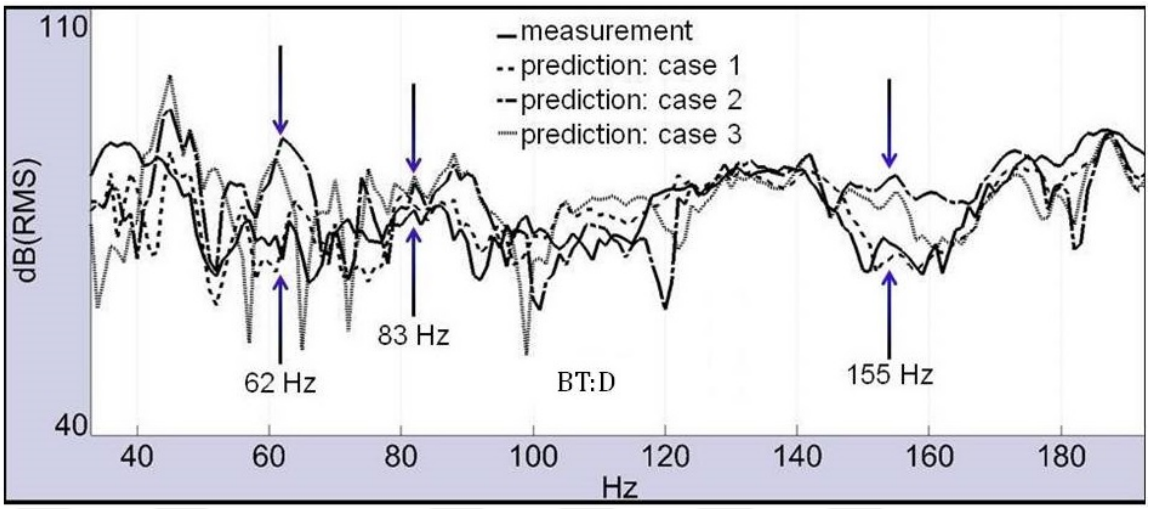


Figure 4.16. Measured vs predicted SPLs at BT:D, Cases 1, 2 and 3.

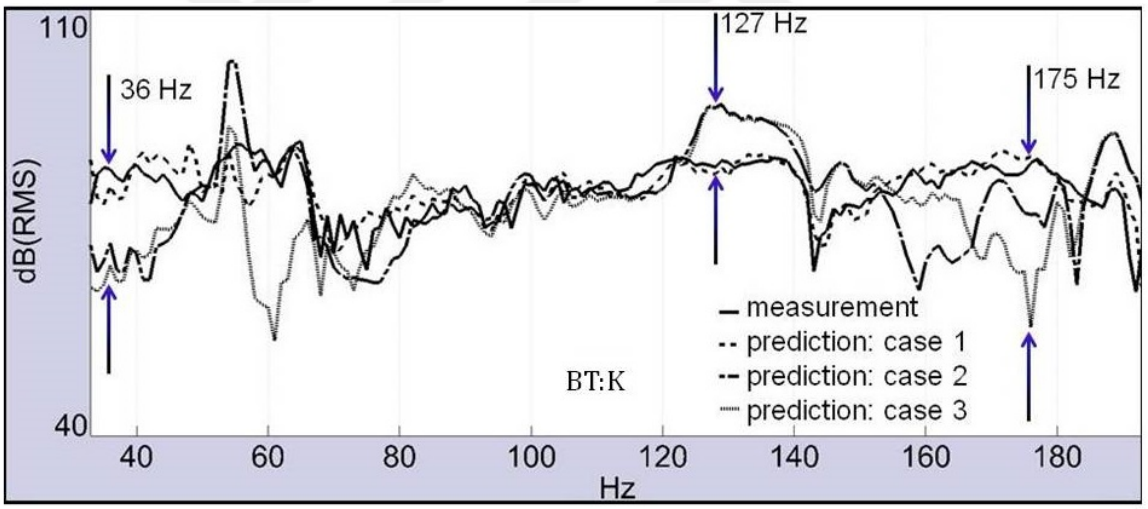


Figure 4.17. Measured vs predicted SPLs at BT:K, Cases 1, 2 and 3.

Table 4.3. L_2 norm of differences between the measured and predicted sound pressure levels.

cases	BT:D (dB,lin)	RSM (dB,lin)
case 1	3.828	4.402
case 2	8.263	6.219
case 3	8.907	7.895

It is shown that a strong coupling between acoustic and structural modes appears in the vicinity of any uncoupled acoustic eigenfrequency, and the coupled solution is actually ruled by these uncoupled acoustic eigenfrequencies [185]. Similarly, in the present study, it is observed that coupled modes appear in the vicinity of uncoupled acoustic eigenfrequencies, where tabulated in Table 3.8. Consequently, in case studies, predicted sound pressure levels differ with respect to the uncoupled acoustic eigenfrequencies. Nevertheless, coupled modes may also occur in the vicinity of global strong structural modes: the coupled mode at 62 Hz, for instance.

In Case 1, the first acoustic eigenfrequency is at 35 Hz; a coupled mode appears in the vicinity of this eigenfrequency, namely at 36 Hz. The effect of the coupled mode on the acoustic response of the system is clear, especially at BT:K microphone (see Figure 4.17.). It is observed that, while the predicted SPL at BT:K location matches with the measured SPL in Case 1, it is not true for Cases 2 and 3.

When the sound pressure level vs. frequency plots in Figures 4.16. and 4.17. are examined, substantial differences are observed, especially around 62, 83, 127, 155 and 175 Hz. In Figures 4.18. to 4.22., sound pressure level distribution inside the acoustic cavity is plotted with regard to these frequency values. Pressure distribution is scaled in a 40-100 dB interval, where the black point indicates the location of microphone. These plots show the acoustic response of the cavity subjected to the operational forces calculated using Equation (2.34). As can be observed from Figure 4.16., the SPL predictions at BT:D are relatively high at 62, 83 and 155 Hz for Cases 2 and 3. The plots given in Figures 4.18. to 4.20. are in accordance with these predictions. The formation of acoustic-structure coupling is different for the three cases as can be observed in Figures 4.16. and 4.19. In Figure 4.16., measurement result indicates a small resonance peak around 83 Hz corresponding to the second longitudinal acoustic mode of the cavity shown in Figure 3.23. This resonance is not as strong as the others, because around that frequency a strong structural mode does not occur. Moreover, in Figure 4.19. the microphone location is quite close to the nodal surface, where SPL values are very low. Therefore, in Figure 4.16. the effect of this acoustic mode is weak. In Figure 4.16., at 155 Hz, the measurement result shows a low SPL value, which is

in accordance with Case 1 prediction. Notice that, in Figure 4.20., the microphone location in Case 1 is close to the nodal surface, where SPL values are low. However, in Cases 2 and 3 a nodal surface does not appear close to the microphone location (see Figure 4.20.). Therefore, in these predictions SPL values are quite high compared to the measurement result.

In Figure 4.17., the SPL predictions at BT:K are observed to be different at 127 and 175 Hz. Figure 4.17. shows that SPL predictions are relatively high around 127 Hz for Cases 2 and 3, which do not agree with the measurement result. The large SPL values around the microphone position in Figure 4.21. match well with the resonances stand out around 127 Hz in Cases 2 and 3 of Figure 4.17. In Figure 4.17., measurement result and Case 1 prediction both show high SPL values at 175 Hz. The other two predictions show lower SPL values (Case 3 prediction even shows an anti-resonance notch at that frequency). Figure 4.22. confirms that the SPL values around the microphone location in Cases 2 and 3 are quite low. Indeed, in Case 3, the microphone location corresponds to a node, which appears as an anti-resonance notch in Figure 4.17. In summary, Case 1 prediction gives closer results to the measurement results over the whole frequency range of interest for both microphone locations. It is obvious that the variances in Figures 4.16. and 4.17. are caused by different modeling of acoustic cavities. The benchmark reveals that modeling of the acoustic cavity plays a vital role in coupled vibro-acoustic simulations.

Recall Equation (3.45), in the upper limit, i.e. when $\xi = 1$, δ becomes zero, and eigenfrequencies can approximately be calculated by Equation (3.30), as suggested by Sanderson [116]. Physically, this case mostly corresponds to station wagon and minivan type vehicles. Yet another possibility is that rear seat may not be a folding one, and/or no plates may exist to support it. Then, rear seat may be assumed to be transparent to noise transmission, as suggested by Lim [121], and which corresponds to Case 2 in the present study. This approach does not ignore the effect of seats, i.e. they can be considered in the model through a heavy air assumption, as suggested by Sung et al [125]. Nevertheless, trunk cavity may still couple with the cabin cavity, through some holes and/or apertures on the parcel shelf, as indicated by Seifzadeh et al [123].

As summarized above, outcomes of the present study agree well with the results available in the literature. Further, the analytical procedure proposed is effective in determination of the uncoupled acoustic eigenfrequencies of typical sedans, and as shown through coupled analysis they rule the acoustic response.

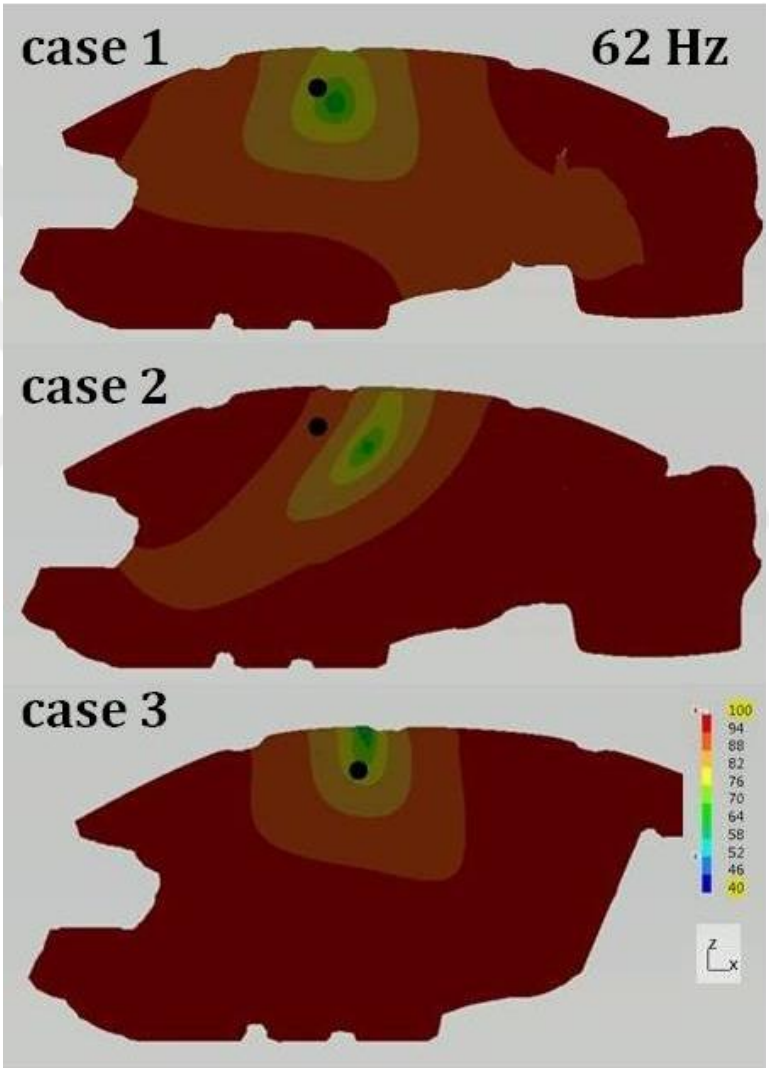


Figure 4.18. Coupled vibro-acoustic response of the system at 62 Hz for three cases, the black point indicates the position of mic. 1 (BT:D).

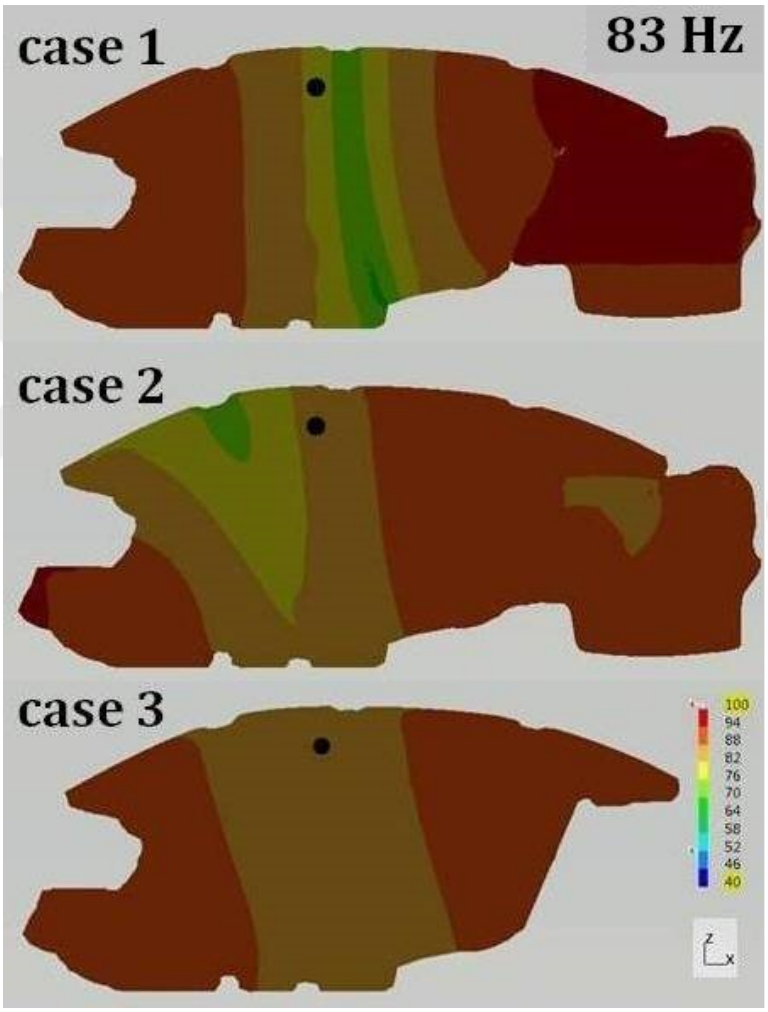


Figure 4.19. Coupled vibro-acoustic response of the system at 83 Hz for three cases, the black point indicates the position of mic. 1 (BT:D).

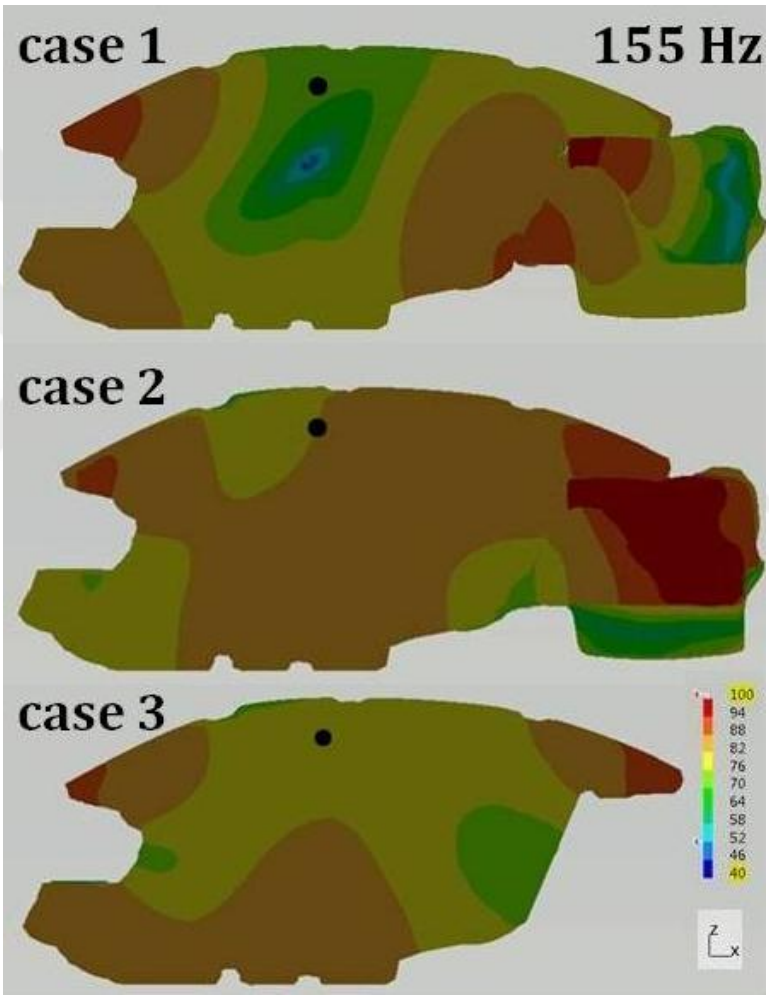


Figure 4.20. Coupled vibro-acoustic response of the system at 155 Hz for three cases, the black point indicates the position of mic. 1 (BT:D).

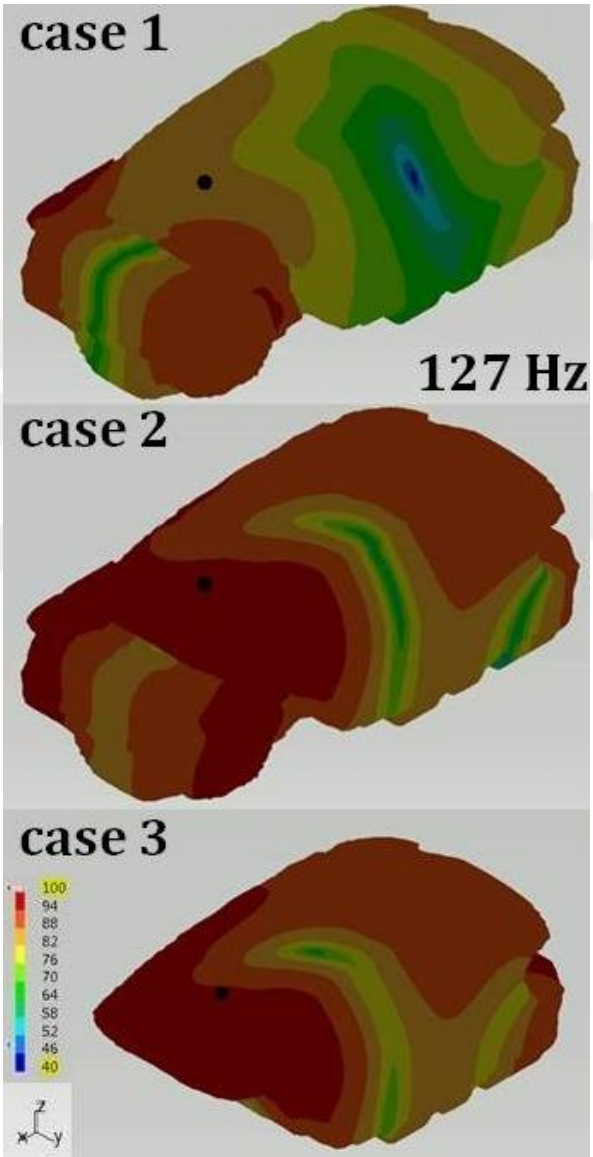


Figure 4.21. Coupled vibro-acoustic response of the system at 127 Hz for three cases, the black point indicates the position of mic. 2 (BT:K).

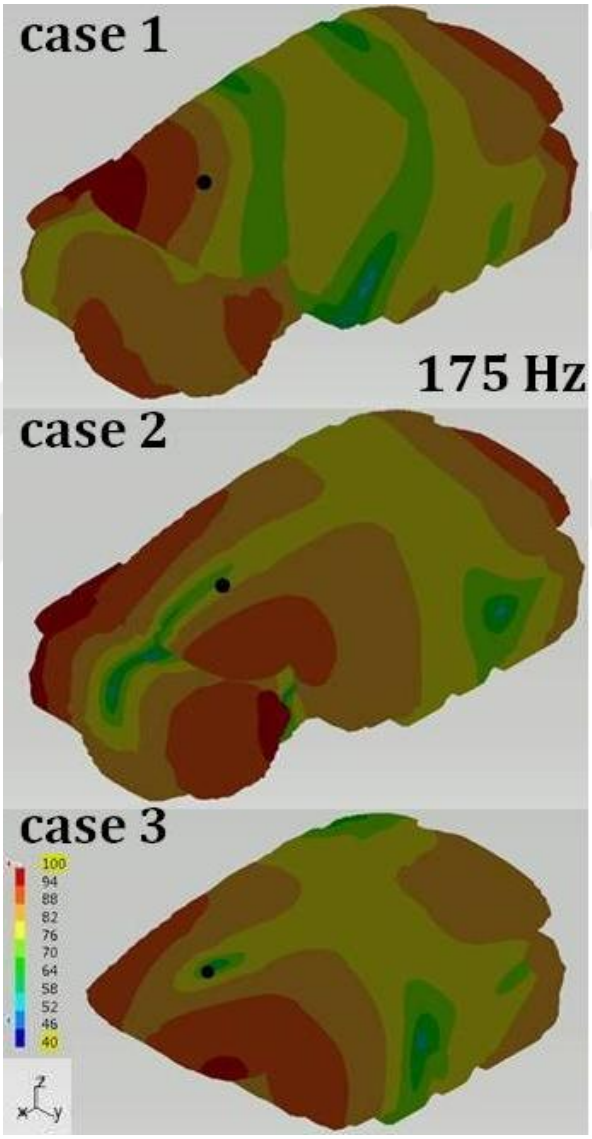


Figure 4.22. Coupled vibro-acoustic response of the system at 175 Hz for three cases, the black point indicates the position of mic. 2 (BT:K).

4.4. Modification Prediction Analysis

The updated computational model is subjected to modification prediction studies to come up with countermeasures to low frequency problems diagnosed. In the literature, many solutions are suggested to refine the interior noise characteristics of passenger vehicles: engine mount optimization, topology optimization, anti-vibration pads, active noise cancelation, refinement of structural members and tuned mass damper are some of them. Current study requires a palliative solution, since the sedan studied is already in the market. Among probable solution techniques, tuned mass damper (TMD) approach is adopted due to the following reasons:

(i) Engine mount optimization affects the handling behavior of the vehicle, as well. This choice is not appropriate after vehicle launch, since all dynamic calculations have to be reconsidered.
(ii) Topology optimization yields effective results in the 100-300 Hz bandwidth, and the cost of the operation is mostly unacceptable after vehicle launch.
(iii) Anti-vibration pads yield worthwhile solutions mostly in the 200-500 Hz bandwidth.
(iv) Active noise cancelation is a sophisticated technique, which is suitable for luxury segment vehicles.
(v) Refinement of structural members is not preferred after vehicle launch, except a few specific cases.

Nevertheless, the choice is up to the designer, and different case studies are obviously beneficial, provided the cost is affordable in terms of time and resources. An updated verified computational model is definitely a common prerequisite for all modification studies. For the sedan studied the following remarks are made on the behalf of studies performed:

(i) It is observed that the anti-vibration pads already attached to the BIW do not yield solutions to the booms identified, although they are effective in some other frequency intervals.

(ii) Three locations are determined on the BIW, after various modification prediction analyses.

(iii) Point masses are added on the locations determined to investigate the feasibility of solutions.

(iv) It is decided to use equivalent tuned mass dampers to deal with the booms identified.

Table 4.4. Refinement achieved on the booms diagnosed.

target	interval (rpm)	improvement (dB)
BT:D	2,350-2,600	6
BT:D	3,500-4,300	10
BT:K	1,600-2,000	7
BT:K	3,500-4,300	3

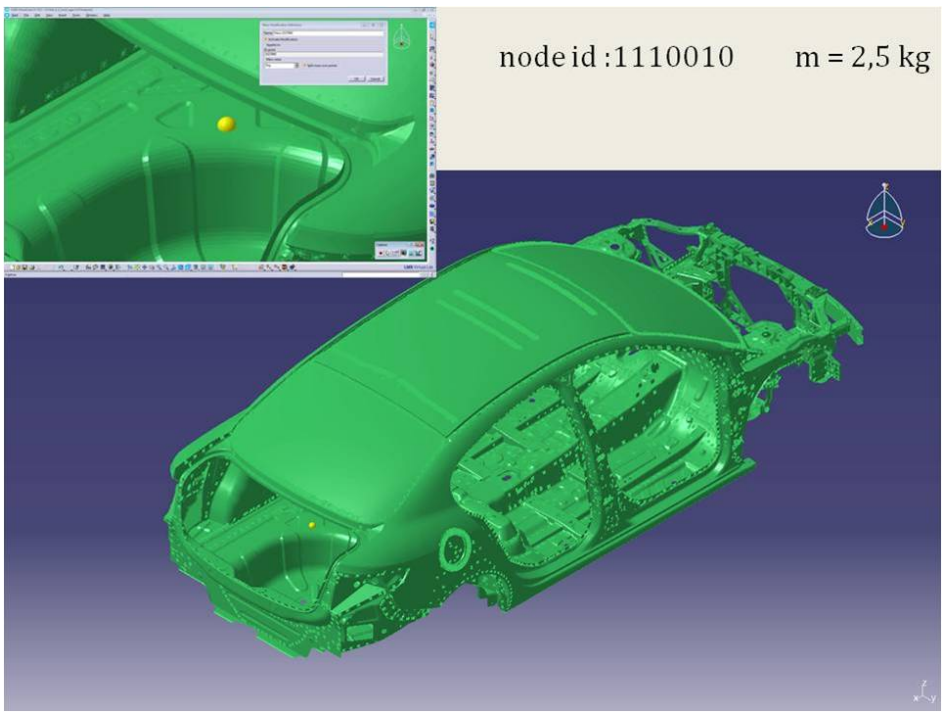


Figure 4.23. An additional 2.5 kg mass is added on the node 1110010 for modification prediction analysis.

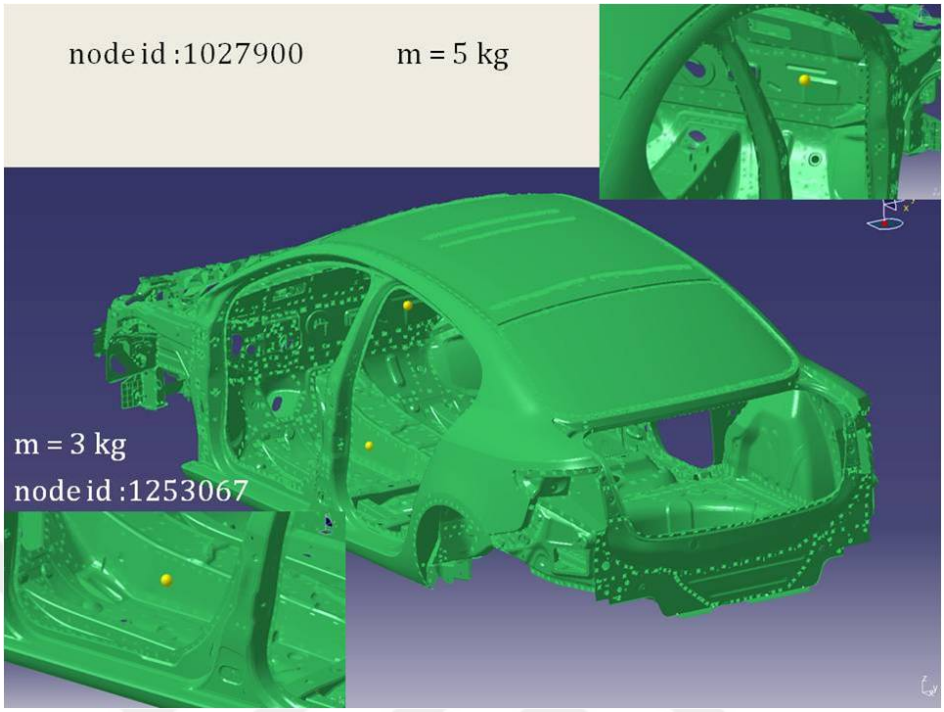


Figure 4.24. Additional 3 and 5 kg masses are added on the nodes 1253067 and 1027900 for modification prediction analysis, respectively.

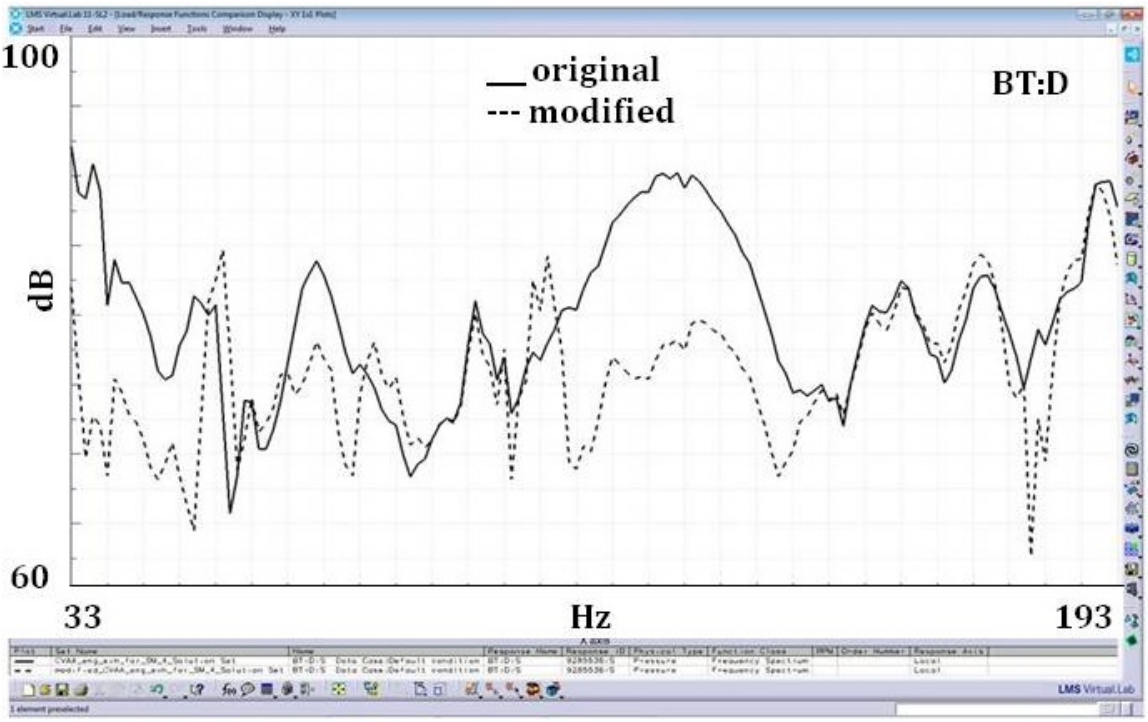


Figure 4.25. Original and modified SPL predictions at BT:D, where modification is achieved through TMDs.

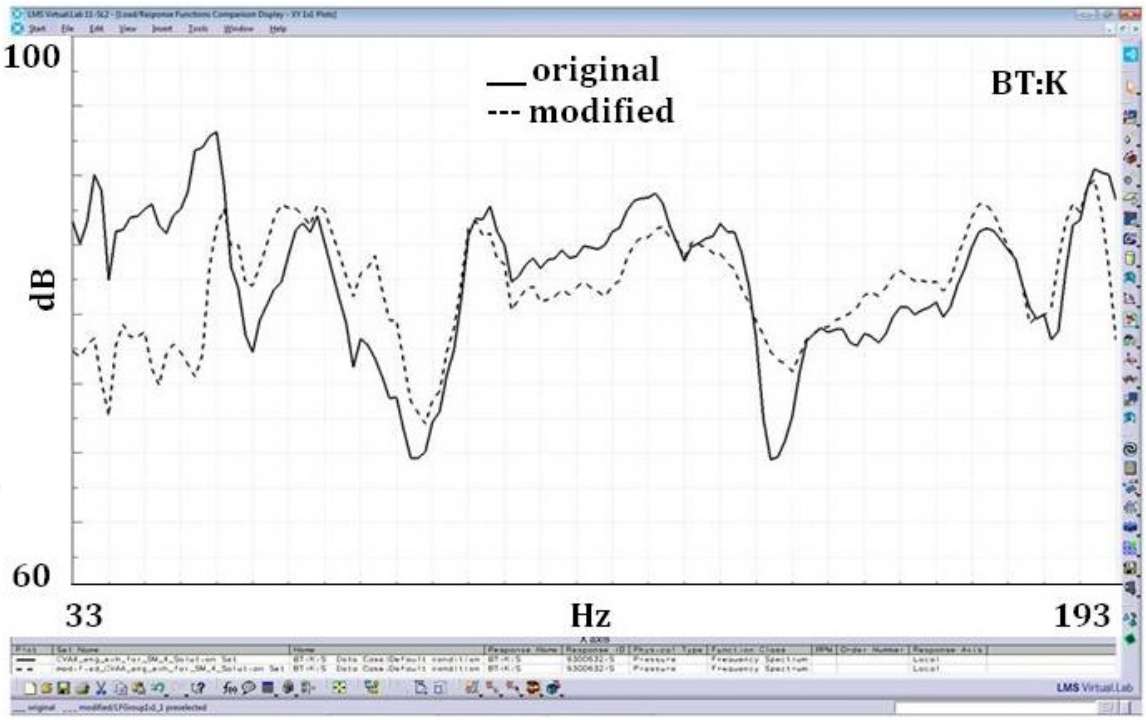


Figure 4.26. Original and modified SPL predictions at BT:K, where modification is achieved through TMDs.

Three locations determined are shown in Figures 4.23. and 4.24. In the updated computational model, these locations correspond to the nodes numbered as 1110010, 1253067 and 1027900. In total, 10.5 kg mass is added to the system at these locations to inspect the feasibility of the problem. Then, it is decided to locate equivalent tuned mass dampers on the same nodes, rather than adding point masses. An optimization study is performed using the commercial code, and the mass added is decreased to 1/10 of the initial trial case. Using three tuned mass dampers, where the total mass of the system is increased only by 1 kg, three booms diagnosed are solved. The modifications achieved in the SPLs are compared to the original ones in Figures 4.25. and 4.26. Refinement in the SPLs predicted at the target microphone locations are tabulated in Table 4.4. Essentially, modifications do not introduce new noise problems in the frequency bandwidth of interest.

5. DISCUSSION AND FUTURE WORK

Another point of interest is that when can holes or apertures be neglected in the model without altering the acoustic response results?

In a computational framework, holes or apertures smaller than the mesh size of an acoustic element can be ignored, which corresponds to Case 3 in the present study (see Sections 3.2.2 and 4.3). Computational analysis suggests that the size of acoustic element depends on the frequency of interest. On the other hand, for an analysis that considers low frequency range only, the acoustic mesh size is not small enough to be continuous through apertures, if present. This does not necessarily mean that those apertures do not alter the acoustic response. Rotes on choosing proper acoustic element size are not all that clear. Some limitations and difficulties of deterministic element based acoustic analysis are discussed in references, e.g. Marburg [186] and Lodygowski and Sumelka [187].

From the theoretical point of view, derivations presented in Section 3.2.2 depend on many assumptions, which are not yet validated for a specific low limit value considering the area of an aperture. Some neglected facts, such as viscosity of the medium and its thermal conductivity may alter results. An experimental investigation is needed to specify an interval for the mentioned lower limit.

The results of modification predictions analysis given in Section 4.4 can be applied through eddy current dampers (ECD). Eddy current damping mechanism can increase the damping ratio by up to 150 times. Although successful applications are available in the literature (see e.g. [188]), to date, an application is not reported yet in the area of vehicle acoustics.

6. CONCLUSION

(i) The inter variability observed among the sound pressure levels of identically produced vehicles is investigated by means of a commonly used experimental tool: transfer path analysis. Five identically produced vehicles are subjected to road test to record sound signals. During test, acceleration data of the active and passive sides of engine and exhaust mounts are acquired, as well. Root causes of diagnosed booms are identified. The booming around 1,800 rpm is important, since this speed is downshifting and stop-and-go rpm in traffic. The booming cantered around 4,000 rpm is certainly critical in the sense of being the cruise speed at top gear.

(ii) Next to identifying booms and observing inter variability; a structural transfer path analysis is followed out for two of the chosen subject vehicles. Several parameters are investigated to find out a reliable prediction result and to observe effects of measurement variability. Benchmark shows that reliable predictions are achieved provided that (a) frequency response function estimations are performed, when the active part, i.e. powertrain is removed; (b) the test vehicle is on ground and (c) the H_v estimator is used. Additionally, it is shown that prediction results can be improved by managing the condition number of the matrix, which is populated by measured accelerance frequency response functions.

(iii) A systematic approach is introduced to find out the cause of inter variability. Eventually, it is shown that predominant paths, which are said to be the main contributors of diagnosed booms, are also causes of variability.

(iv) In matrix inversion method, the complained time cost is actually caused by the following issues: (a) removal of the source; (b) to locate sensors and cables; (c) to measure frequency response functions (FRFs) and noise transfer functions (NTFs) by applying a known force (shaker), or a normalized impact force (hammer). Today, engines of automobiles are installed such that without partially, or in some cases completely removing the engine, even to locate sensors for an operational measurement is hard, if not impossible. Once the source is removed, and sensors are located, to apply an external force is no more a big deal in terms of time cost.

(v) During the population of FRF matrix, unavoidable measurement errors introduce to results. Artificial damping, measurement noise, finite record length, phase, variance and bias errors certainly affect the outcomes of transfer path analysis. Although many of these measurement errors are reported in the literature, damping and its effects are not considered in detail. Present study suggests considering the effects of damping in any TPA framework.

(vi) Dynamic stiffness matrix is the inverse of experimental FRF matrix. During inversion process, measurement errors of FRFs are highly amplified in the dynamic stiffness matrix, since it is dominated by weakest modes. Whether measured directly or reciprocally, all FRFs contain the damping information, and in any method that inverts the FRF matrix, same problem is valid.

(vii) In many studies, predictions of proposed methods are compared with traditional transfer path analysis (TPA) results. In fact traditional TPA has its own assumptions and drawbacks, which motivate new research. In the present study, unlike many reported results in the literature, comparisons are made between calculated and measured sound pressure levels. Current practice is studied on a reference problem, and results are presented. Validity is the greatest for the procedure proposed in Section 2.11.2.

(viii) In computational vehicle acoustics, sound pressure level predictions and measurements do not perfectly match. The reasons for the mismatch are generally thought to be nonlinearities in the vehicle structure, assumptions of the source-path-receiver approach and inadequate modeling of damping. This study shows that proper modeling of acoustic cavity is also critical.

(ix) First longitudinal acoustic eigenfrequency (i.e. 1,0,0) is around 35 Hz for a typical sedan.

(x) Analytical solution proposed in Section 3.2.2 is effective in the prediction of uncoupled planar acoustic eigenfrequencies of sedans. Since coupled modes occur in the vicinity of any uncoupled acoustic mode, it is possible to come up with a prediagnosis on booms, rather performing a detailed computational work.

(xi) Low frequency noise characteristics of the sedan studied are refined. Modifications offered in Section 4.4 do not introduce new noise problems in the frequency bandwidth of interest.

REFERENCES

1. FURORE, *R & D Technology Roadmap: A Contribution to the Identification of Key Technologies for a Sustainable Development of European Road Transport*, Tech. rep., European Automotive Research Partners Association, October 2003.

2. Repik, E. P., "Historical Perspective on Vehicle Interior Noise Development", *SAE Technical Paper, No. 2003-01-1518*, 2003.

3. Jha, S. K. and T. Priede, "Origin of Low Frequency Noise in Motor Cars", *14th Automobile Tech. Congress of Fisita, London*, 1972.

4. Wolf Jr, J. A. and D. J. Nefske, "Nastran Modeling and Analysis of Rigid and Flexible Walled Acoustic Cavities", *Nasa TMX-3278*.

5. Jha, S. K., "Characteristics and Sources of Noise and Vibration and Their Control in Motor Cars", *Journal of Sound and Vibration*, Vol. 47, No. 4, pp. 543–558, 1976.

6. Priede, T. and S. K. Jha, "Low Frequency Noise in Cars: Its Origin and Elimination", *Journal of Automotive Engineering*, Vol. 1, No. 5, pp. 17–21, 1970.

7. Dowell, E. H., G. F. Gorman III and D. A. Smith, "Acoustoelasticity: General Theory, Acoustic Natural Modes and Forced Response to Sinusoidal Excitation, Including Comparisons With Experiment", *Journal of Sound and Vibration*, Vol. 52, No. 4, pp. 519–542, 1977.

8. Petyt, M., G. H. Koopmann and R. J. Pinnington, "The Acoustic Modes of a Rectangular Cavity Containing a Rigid, Incomplete Partition", *Journal of Sound and Vibration*, Vol. 53, No. 1, pp. 71–82, 1977.

9. Au-Yang, M. K., "Pump-Induced Acoustic Pressure Distribution in an Annular

Cavity Bounded by Rigid Walls", *Journal of Sound and Vibration*, Vol. 62, No. 4, pp. 577–591, 1979.

10. Nieter, J. J. and R. Singh, "Acoustic Modal Analysis Experiment", *The Journal of the Acoustical Society of America*, Vol. 72, No. 2, pp. 319–326, 1982.

11. Kung, C.-H. and R. Singh, "Experimental Modal Analysis Technique for Three-Dimensional Acoustic Cavities", *The Journal of the Acoustical Society of America*, Vol. 77, No. 2, pp. 731–738, 1985.

12. Nefske, D. J., J. A. Wolf Jr and L. J. Howell, "Structural-Acoustic Finite Element Analysis of the Automobile Passenger Compartment: A Review of Current Practice", *Journal of Sound and Vibration*, Vol. 80, No. 2, pp. 247–266, 1982.

13. Wood, L. A. and C. A. Joachim, "Variability of Interior Noise Levels in Passenger Cars", *Vehicle Noise and Vibration. Papers read at the International Conference held at the Institution of Mechanical Engineers, London 5-7 June*, 1984.

14. Kompella, M. S. and R. J. Bernhard, "Measurement of the Statistical Variation of Structural-Acoustic Characteristics of Automotive Vehicles", *SAE Technical Paper, No. 931272*, 1993.

15. DeJong, R. G., "A Study of Vehicle Interior Noise Using Statistical Energy Analysis", *SAE Technical Paper, No. 850960*, 1985.

16. Craik, R. J. M., J. A. Steel and D. I. Evans, "Statistical Energy Analysis of Structure-Borne Sound Transmission at Low Frequencies", *Journal of Sound and Vibration*, Vol. 144, No. 1, pp. 95–107, 1991.

17. Suzuki, S., S. Maruyama and H. Ido, "Boundary Element Analysis of Cavity Noise Problems With Complicated Boundary Conditions", *Journal of Sound and Vibration*, Vol. 130, No. 1, pp. 79–96, 1989.

18. Suzuki, S. *et al.*, "Coupling of Boundary Element Method for Vehicle Noise Prob-

lems", *JSME, NCA*, Vol. 9, pp. 17–24, 1990.

19. Koopmann, G. H. and H. Benner, "Method for Computing the Sound Power of Machines Based on the Helmholtz Integral", *The Journal of the Acoustical Society of America*, Vol. 71, No. 1, pp. 78–89, 1982.

20. Cheng, C. Y. R., A. F. Seybert and T. W. Wu, "A Multidomain Boundary Element Solution for Silencer and Muffler Performance Prediction", *Journal of Sound and Vibration*, Vol. 151, No. 1, pp. 119–129, 1991.

21. Soenarko, B., "Recent Developments of the Boundary Element Method to Noise Control Problems in Automotive Engineering", *6th International Pacific Conference on Automotive Engineering, Seoul, Korea*, 1991.

22. Banerjee, P. K., S. Ahmad and H. C. Wang, "A New BEM Formulation for the Acoustic Eigenfrequency Analysis", *International Journal for Numerical Methods in Engineering*, Vol. 26, No. 6, pp. 1299–1309, 1988.

23. Sandberg, G. and P. Göransson, "A Symmetric Finite Element Formulation for Acoustic Fluid-Structure Interaction Analysis", *Journal of Sound and Vibration*, Vol. 123, No. 3, pp. 507–515, 1988.

24. Bendat, J. S. and A. G. Piersol, *Engineering Applications of Correlation and Spectral Analysis*, Wiley-Interscience, New York, 1980.

25. Ewins, D. J., *Modal Testing: Theory and Practice*, Research Studies Press Letchworth, 1984.

26. Verheij, J. W., "Experimental Procedures for Quantifying Sound Paths to the Interior of Road Vehicles", *2nd International Conference on Vehicle Comfort, Part 1*, Vol. 1, pp. 483–491, 1992.

27. De Vis, D. and W. Hendricx, "Development and Integration of an Advanced Unified Approach to Structure Borne Noise Analysis", *INTER-NOISE and NOISE-*

CON Congress and Conference Proceedings, Vol. 1992, pp. 561–564, Institute of Noise Control Engineering, 1992.

28. Mas, P. and K. W. P. Sas, "Indirect Force Identification Based upon Impedance Matrix Inversion: A study on Statistical and Deterministical Accuracy", *19th ISMA Conference, Tools for Noise and Vibration Analysis*, pp. 1049–1065, Leuven, 1994.

29. Wyckaert, K., F. Augusztinovicz and P. Sas, "Vibro-Acoustical Modal Analysis: Reciprocity, Model Symmetry and Model Validity", *The Journal of the Acoustical Society of America*, Vol. 100, No. 5, pp. 3172–3181, 1996.

30. Wyckaert, K. and L. Van Laere, "Operational Analysis, Transfer Path Analysis, Modal Analysis: Tools to Understand Road Noise Problems in Cars", *Journal-SAE of Japan*, Vol. 50, pp. 69–74, 1996.

31. Wyckaert, K., L. Gieien, P. J. van der Linden and H. Van der Auweraer, "An Integrated Approach to Vehicle NVH Optimization", *SAE Technical Paper, No. 962489*, 1996.

32. Kurmaniak, C. V., C. Van Karsen and W. R. Kelley, "Application of Indirect Force Estimation Techniques to the Automotive Transfer Case", *SAE Technical Paper, No. 1999-01-1764*, 1999.

33. *Transfer Path Analysis: The Qualification and Quantification of Vibro-Acoustic Transfer Paths*, Tech. rep., In LMS Technical Notes, 1999.

34. Bitsie, F., *The Structural-Acoustic Energy Finite-Element Method and Energy Boundary-Element Method*, Ph.D. Thesis, Purdue University, Lafayette, IN, 1996.

35. Wang, S. and R. Bernhard, *Energy Finite Element Method (EFEM) and Statistical Energy Analysis (SEA) of a Heavy Equipment Cab*, Tech. rep., 1999.

36. Gur, Y., D. A. Wagner and K. N. Morman, "Energy Finite Element Analysis

Methods for Mid-Frequency NVH Applications", *SAE Technical Paper, No. 1999-01-1801*, 1999.

37. Zhang, W. and S. Raveendra, "Interior Noise Prediction Based on Energy Finite Element Method", *SAE Technical Paper, No. 2005-01-2332*, 2005.

38. Raveendra, S. T., J. Thompson and C. Mollo, "Boundary Element Method for High Frequency Acoustic Analysis", *Proceedings of the ASME Noise Control and Acoustic Division*, pp. 309–313, 1997.

39. Desmet, W., *A Wave Based Prediction Technique for Coupled Vibro-Acoustic Analysis*, Ph.D. Thesis, Katholieke Universiteit Leuven, Leuven, Belgium, 1998.

40. Hepberger, A., H. Priebsch, W. Desmet, B. Van Hal, B. Pluymers and P. Sas, "Application of the Wave Based Method for the Steady-State Acoustic Response Prediction of a Car Cavity in the Mid-Frequency Range", *Proceedings of ISMA*, Vol. 2, pp. 877–884, 2002.

41. Bennighof, J., M. Kaplan, M. Muller and M. Kim, "Meeting the NVH Computational Challenge: Automated Multi-Level Substructuring", *Proceedings of the 18th International Modal Analysis Conference, San Antonio, Texas*, pp. 909–915, Citeseer, 2000.

42. Kropp, A. and D. Heiserer, "Efficient Broadband Vibro-Acoustic Analysis of Passenger Car Bodies Using an FE-Based Component Mode Synthesis Approach", *Journal of Computational Acoustics*, Vol. 11, No. 02, pp. 139–157, 2003.

43. Charpentier, A., P. Sreedhar and K. Fukui, "Validation of Hybrid FE-SEA Model of a Trimmed Full Vehicle for Reduction of Structure Borne Noise in the Mid-Frequency Range", *JSAE Annual Congress (Spring) Pacifico Yokohama, Japan*, Society Of Automotive Engineers Of Japan, 2009.

44. Vlahopoulos, N., S. Li, M. Viktorovitch and D. Caprioli, "Validation of a Hybrid

Finite Element Formulation for Mid-Frequency Analysis of Vehicle Structures", *SAE Technical Paper, No. 2007-01-2303*, 2007.

45. Raveendra, S. and W. Zhang, "Vibro-acoustic Analysis Using a Hybrid Energy Finite Element/Boundary Element Method", *SAE Technical Paper, No. 2007-01-2177*, 2007.

46. Van Genechten, B., B. Pluymers, D. Vandepitte and W. Desmet, "A Hybrid Wave Based-Modally Reduced Finite Element Method for the Efficient Analysis of Low- and Mid-Frequency Car Cavity Acoustics", *SAE International Journal of Passenger Cars-Mechanical Systems*, Vol. 2, No. 1, pp. 1494–1504, 2009.

47. Von Estorff, O., "Numerical Methods in Acoustics: Facts, Fears, Future", *19th International Congress on Acoustics, Madrid, 2-7 September*, 2007.

48. Lyon, R. H., R. G. DeJong and M. Heckl, "Theory and Application of Statistical Energy Analysis", *The Journal of the Acoustical Society of America*, Vol. 98, p. 3021, 1995.

49. Rossing, T. D., *Springer Handbook of Acoustics*, Springer, 2007.

50. Harrison, M., *Vehicle Refinement: Controlling Noise and Vibration in Road Vehicles*, Elsevier, 2004.

51. Hartmann, W. M., "Loudness Perception", *Principles of Musical Acoustics*, pp. 125–136, Springer, 2013.

52. Allemang, R. J., "Analytical and Experimental Modal Analysis", Lecture Notes, UC-SDRL CN-20-263-662, 1999.

53. *The Fundamentals of Modal Testing*, Tech. rep., Agilent Technologies, Note 243 - 3, 2000.

54. "Acoustic Quantities", in LMS TestLab Rev. 9 Help Files, 2009.

55. Ahn, S. J., W. B. Jeong and W. S. Yoo, "An Estimation of Error-Free Frequency Response Function from Impact Hammer Testing", *JSME International Journal, Series C: Mechanical Systems Machine Elements & Manufacturing*, Vol. 47, No. 3, pp. 852–857, 2004.

56. Norton, M. P. and D. G. Karczub, *Fundamentals of Noise and Vibration Analysis for Engineers*, Cambridge University Press, 2003.

57. Hills, E., B. Mace and N. Ferguson, "Acoustic Response Variability in Automotive Vehicles", *Journal of Sound and Vibration*, Vol. 321, No. 1, pp. 286–304, 2009.

58. Evans, T., *Estimation of Uncertainty in the Structure Borne Sound Power Transmission from a Source to a Receiver*, PhD Thesis, University of Salford, 2010.

59. Lionnet, C. and P. Lardeur, "A Hierarchical Approach to the Assessment of the Variability of Interior Noise Levels Measured in Passenger Cars", *Noise Control Engineering Journal*, Vol. 55, No. 1, pp. 29–37, 2007.

60. Scigliano, R., M. Scionti and P. Lardeur, "Verification, Validation and Variability for the Vibration Study of a Car Windscreen Modeled by Finite Elements", *Finite Elements in Analysis and Design*, Vol. 47, No. 1, pp. 17–29, 2011.

61. Oberkampf, W. L. and C. J. Roy, *Verification and Validation in Scientific Computing*, Cambridge University Press, 2010.

62. Roy, C. J. and W. L. Oberkampf, "A Comprehensive Framework for Verification, Validation, and Uncertainty Quantification in Scientific Computing", *Computer Methods in Applied Mechanics and Engineering*, Vol. 200, No. 25, pp. 2131–2144, 2011.

63. ISO, *Acoustics Measurement of Noise Inside Motor Vehicles*, ISO 5128, International Organization for Standardization, Geneva, Switzerland, 1980.

64. Lalor, N. and T. Bharj, "The Application of SEA to the Reduction of Passenger

Car Interior Noise", *Proceedings of the 27th ISATA Conference*, 1994.

65. Shin, S.-H., J.-G. Ih, T. Hashimoto and S. Hatano, "Sound Quality Evaluation of the Booming Sensation for Passenger Cars", *Applied Acoustics*, Vol. 70, No. 2, pp. 309–320, 2009.

66. Wyckaert, K. and H. Van der Auweraer, "Operational Analysis, Transfer Paths Analysis, Modal Analysis: Tools to Understand Road Noise Problems in Cars", *Proc. SAE Noise and Vibration Conference*, pp. 139–143, 1995.

67. Plunt, J., "Finding and Fixing Vehicle NVH Problems with Transfer Path Analysis", *Sound and Vibration*, Vol. 39, No. 11, pp. 12–17, 2005.

68. Otte, D., *Development and Evaluation of Singular Value Analysis Methodologies for Studying Multivariate Noise and Vibration Problems*, PhD Thesis, K.U. Leuven, 1994.

69. Wyckaert, K. and W. Hendricx, "Transmission Path Analysis in View of Active Cancellation of Road Induced Noise in Automotive Vehicles", *Inter-Noise and Noise-Con Congress and Conference Proceedings*, 5, pp. 653–656, Institute of Noise Control Engineering, 1994.

70. Yoo, B. K. and K.-J. Chang, "Road Noise Reduction Using a Source Decomposition and Noise Path Analysis", *SAE Technical Paper, No. 2005-01-2502*, 2005.

71. Padilha, P. E. F. and J. R. de França Arruda, "Comparison of Estimation Techniques for Vibro-Acoustic Transfer Path Analysis", *Shock and Vibration*, Vol. 13, No. 4, pp. 459–467, 2006.

72. Van der Auweraer, H., P. Mas, S. Dom, A. Vecchio, K. Janssens and P. Van de Ponseele, "Transfer Path Analysis in the Critical Path of Vehicle Refinement: The Role of Fast, Hybrid and Operational Path Analysis", *SAE Technical Paper, No. 2007-01-2352*, 2007.

73. Oktav, A., G. Anlaş and C. Yılmaz, "Assessment of Vehicle Noise Variability due to Engine Mounts by Means of Structural Transfer Path Analysis", *7th Automotive Technologies Congress*, OTEKON'14, Bursa, 2014.

74. De Sitter, G., C. Devriendt, P. Guillaume and E. Pruyt, "Operational Transfer Path Analysis", *Mechanical Systems and Signal Processing*, Vol. 24, No. 2, pp. 416–431, 2010.

75. Brandl, S., H.-H. Priebsch, F. Brandl, W. Biermayer, R. Höldrich and A. Sontacchi, "Challenges and New Solutions for Transfer Path Analysis", *ISMA, Leuven, September 15th to 17th*, 2008.

76. Özgen, G. O. and J. H. Kim, "Error Analysis and Feasibility Study of Dynamic Stiffness Matrix-Based Damping Matrix Identification", *Journal of Sound and Vibration*, Vol. 320, No. 1, pp. 60–83, 2009.

77. Fladung, W., "Windows Used for Impact Testing", *Proceedings, SPIE - The International Society for Optical Engineering*, pp. 1662–1666, 1997.

78. Schoukens, J., Y. Rolain and R. Pintelon, "Leakage Reduction in Frequency Response Function Measurements", *IEEE Transactions on Instrumentation and Measurement*, Vol. 55, No. 6, pp. 2282–2287, 2006.

79. Pintelon, R., J. Schoukens, G. Vandersteen and K. Barbé, "Estimation of Nonparametric Noise and FRF Models for Multivariable Systems - Part 1: Theory", *Mechanical Systems and Signal Processing*, Vol. 24, No. 3, pp. 573–595, 2010.

80. Pintelon, R., J. Schoukens, G. Vandersteen and K. Barbé, "Estimation of Nonparametric Noise and FRF Models for Multivariable Systems - Part 2: Extensions, Applications", *Mechanical Systems and Signal Processing*, Vol. 24, No. 3, pp. 596–616, 2010.

81. Ribeiro, A., N. Maia and J. Silva, "Experimental Evaluation of the Transmis-

sibility Matrix", *Proceedings of IMAC, Kissimmee (FL), USA, 1999 February*, 1999.

82. Ribeiro, A., J. Silva and N. Maia, "On the Generalisation of the Transmissibility Concept", *Mechanical Systems and Signal Processing*, Vol. 14, No. 1, pp. 29–35, 2000.

83. Maia, N., J. Silva and A. Ribeiro, "The Transmissibility Concept in Multi-Degree-of-Freedom Systems", *Mechanical Systems and Signal Processing*, Vol. 15, No. 1, pp. 129–137, 2001.

84. Noumura, K. and J. Yoshida, "Method of Transfer Path Analysis for Vehicle Interior Sound with no Excitation Experiment", *Proc. FISITA*, p. F2006D183, 2006.

85. Noumura, K. and J. Yoshida, "Method of Transfer Path Analysis for Interior Vehicle Sound by Actual Measurement Data", *JSAE Paper*, Vol. 55, No. 20065041, pp. 7–12, 2006.

86. Gajdatsy, P., K. Janssens, W. Desmet and H. Van Der Auweraer, "Application of the Transmissibility Concept in Transfer Path Analysis", *Mechanical Systems and Signal Processing*, Vol. 24, No. 7, pp. 1963–1976, 2010.

87. Gajdatsy, P., L. Gielen, K. Janssens, H. Van der Auweraer, P. Mas and W. Desmet, "A Novel TPA Method Using Parametric Load Models: Validation on Experimental and Industrial Cases", *SAE 2009 Noise and Vibration Conference and Exhibition Technical Papers*, 2009.

88. Janssens, K., P. Gajdatsy, L. Gielen, P. Mas, L. Britte, W. Desmet and H. Van der Auweraer, "OPAX: A New Transfer Path Analysis Method Based on Parametric Load Models", *Mechanical Systems and Signal Processing*, Vol. 25, No. 4, pp. 1321–1338, 2011.

89. Janssens, M. and J. Verheij, "A Pseudo-Forces Methodology To Be Used in Characterization of Structure-Borne Sound Sources", *Applied Acoustics*, Vol. 61, No. 3, pp. 285–308, 2000.

90. Janssens, M., J. Verheij and T. Loyau, "Experimental Example of the Pseudo-Forces Method Used in Characterisation of a Structure-Borne Sound Source", *Applied Acoustics*, Vol. 63, No. 1, pp. 9–34, 2002.

91. Moorhouse, A., "On the Characteristic Power of Structure-Borne Sound Sources", *Journal of Sound and Vibration*, Vol. 248, No. 3, pp. 441–459, 2001.

92. Han, X., Y. Guo, Y. Zhao and Z. Lin, "The Application of Power-Based Transfer Path Analysis to Passenger Car Structure-Borne Noise", *Proceedings of the Institution of Mechanical Engineers, Part D: Journal of Automobile Engineering*, Vol. 222, No. 11, pp. 2011–2023, 2008.

93. Fulford, R. and B. Gibbs, "Structure-Borne Sound Power and Source Characterisation in Multi-Point-Connected Systems, Part 1: Case Studies for Assumed Force Distributions", *Journal of Sound and Vibration*, Vol. 204, No. 4, pp. 659–677, 1997.

94. Park, J., P. Gu, M.-R. Lee and A. Ni, "A New Experimental Methodology to Estimate Tire/Wheel Blocked Force for Road NVH Application", *SAE Transactions*, Vol. 114, No. 6, pp. 2596–2602, 2005.

95. Gaudin, A. and L. Gagliardini, "Recent Improvements in Road Noise Control", *SAE Technical Paper, No. 2007-01-2358*, 2007.

96. Guasch, O. and F. Magrans, "The Global Transfer Direct Transfer Method Applied to a Finite Simply Supported Elastic Beam", *Journal of Sound and Vibration*, Vol. 276, No. 1, pp. 335–359, 2004.

97. Guasch, O., "Direct Transfer Functions and Path Blocking in a Discrete Me-

chanical System", *Journal of Sound and Vibration*, Vol. 321, No. 3, pp. 854–874, 2009.

98. Guasch, O., C. García, J. Jové and P. Artís, "Experimental Validation of the Direct Transmissibility Approach to Classical Transfer Path Analysis on a Mechanical Setup", *Mechanical Systems and Signal Processing*, Vol. 37, No. 1, pp. 353–369, 2013.

99. Comesaña, D. F., J. Wind and H.-E. de Bree, "A Scanning Method for Source Visualization and Transfer Path Analysis Using a Single Probe", *SAE Technical Paper, No. 2011-01-1664*, 2011.

100. Comesaña, D. F., K. Holland, J. Wind, H.-E. de Bree *et al.*, "Comparison of Inverse Methods and Particle Velocity Based Techniques for Transfer Path Analysis", *Acoustics 2012 Nantes*, 2012.

101. Inoue, A. and Y. Tanabe, "Development of Particle Velocity Transfer Path Analysis", *ASME 2012 Noise Control and Acoustics Division Conference at InterNoise 2012*, pp. 359–368, American Society of Mechanical Engineers, 2012.

102. Moorhouse, A., A. Elliott and T. Evans, "In Situ Measurement of the Blocked Force of Structure-Borne Sound Sources", *Journal of Sound and Vibration*, Vol. 325, No. 4, pp. 679–685, 2009.

103. Elliott, A., A. Moorhouse, T. Huntley and S. Tate, "In-Situ Source Path Contribution Analysis of Structure Borne Road Noise", *Journal of Sound and Vibration*, Vol. 332, No. 24, pp. 6276–6295, 2013.

104. Sottek, R. and B. Philippen, "An Unusual Way to Improve TPA for Strongly-Coupled Systems", *SAE Technical Paper, No. 2013-01-1970*, 2013.

105. Coster, C., D. Nagahata and P. J. G. Van der Linden, "On the Accuracy Reciprocal and Direct Vibro-Acoustic Transfer-Function Measurements on Vehicles

for Lower and Medium Frequencies", *ISMA 2010-USD 2010 Conference, Leuven; September 20–22*, 2010.

106. Lewis, T. M., "The Effects of Dynamic Strain Amplitude and Static Prestrain on the Properties of Viscoelastic Materials", *SAE Technical Paper, No. 911084*, 1991.

107. Leclère, Q., B. Roozen and C. Sandier, "Experimental Estimation of Transmissibility Matrices", *Proceedings of ISMA-USD Conference, Leuven, Belgium; September 17–19*, 2012.

108. Zafeiropoulos, N., A. Moorhouse, A. Mackay, U. Senapati, P. Lane and C. Crewe, "A Comparison of Two In-Situ Transfer Path Analysis Methods", *RASD 20, 11th International Conference, Pisa; July 1–3*, 2013.

109. Yoshida, J. and K. Noumura, "Noise Reduction Method for Running TPA Using Significance Probability", *Journal of System Design and Dynamics*, Vol. 5, No. 8, pp. 1572–1581, 2011.

110. Yoshida, J., Y. Onishi and Y. Narita, "Consideration and Verification of Accuracy Evaluation Indices for Operational TPA", *Journal of System Design and Dynamics*, Vol. 6, No. 5, pp. 616–625, 2012.

111. Fladung, W. and R. Rost, "Application and Correction of the Exponential Window for Frequency Response Functions", *Mechanical Systems and Signal Processing*, Vol. 11, No. 1, pp. 23–36, 1997.

112. Lee, J.-H. and J. Kim, "Development and Validation of a New Experimental Method to Identify Damping Matrices of a Dynamic System", *Journal of Sound and Vibration*, Vol. 246, No. 3, pp. 505–524, 2001.

113. Chen, S., M. Ju and Y. Tsuei, "Estimation of Mass, Stiffness and Damping Matrices from Frequency Response Functions", *Journal of Vibration and Acoustics*,

Vol. 118, No. 1, pp. 78–82, 1996.

114. Priebsch, H. H., I. Hauer, H. Fellner, G. Polt and F. Brandl, "Numerical Simulation of Vehicle Interior Noise up to 250 Hz", *Integrated Vehicle Acoustics and Comfort, Styrian Noise, Vibration & Harshness Congress, Graz*, 2001.

115. Marburg, S., B. Nolte, R. Bernhard and S. Wang, *Computational Acoustics of Noise Propagation in Fluids: Finite and Boundary Element Methods*, Springer, 2008.

116. Sanderson, M. A. and T. Onsay, "CAE Interior Cavity Model Validation Using Acoustic Modal Analysis", *SAE Technical Paper, No. 2007-01-2167*, 2007.

117. Qatu, M. S., M. K. Abdelhamid, J. Pang and G. Sheng, "Overview of Automotive Noise and Vibration", *International Journal of Vehicle Noise and Vibration*, Vol. 5, No. 1, pp. 1–35, 2009.

118. Sumi, K., K. Yamamoto, L. Gielen and L. Meulewaeter, "Powertrain Noise and Vibration Simulation with Hybrid Models", *International Journal of Vehicle Design*, Vol. 29, No. 1, pp. 149–159, 2002.

119. Onusic, H. and M. Hage, "Parameters Used for Acoustic Qualification/Quantification of Automotive Vehicles", *International Journal Of Vehicle Design*, Vol. 37, No. 1, pp. 81–98, 2005.

120. Kang, S. W., D. C. Park, J. M. Lee and S. H. Kim, "A Study on the Simplified Coupling System of the Cavity and the Structure of a Passenger Vehicle", *In Proceedings of the 14th International Modal Analysis Conference*, pp. 1376–1382, Publisher SEM, 1996.

121. Lim, T. C., "Automotive Panel Noise Contribution Modeling Based on Finite Element and Measured Structural-Acoustic Spectra", *Applied Acoustics*, Vol. 60, No. 4, pp. 505–519, 2000.

122. Pietrzyk, A. and T. Bengtsson, "An Investigation of the Coupling Between the Passenger Compartment and the Trunk in a Sedan", *SAE Technical Paper, No. 2007-01-2356*, 2007.

123. Seifzadeh, A., A. Pietrzyk, P. Göransson and R. Ramakrishnan, "Effect of Coupling Between Passenger Compartment and Trunk of a Car on Coupled System Natural Frequencies Using Acoustic Frequency Response Function", *Applied Acoustics*, Vol. 76, pp. 310–318, 2014.

124. Sheng, G., *Vehicle Noise, Vibration, and Sound Quality*, 2012.

125. Sung, S., S. Chao, H. Lingala and L. Mundy, "Structural-Acoustic Analysis of Vehicle Body Panel Participation to Interior Acoustic Boom Noise", *SAE Technical Paper, No. 2011-01-0496*, 2011.

126. Lee, S., K. Park, S. H. Sung and D. J. Nefske, "Validation of an Acoustic Finite Element Model of an Automobile Passenger Compartment", *ASME 2009 International Mechanical Engineering Congress and Exposition*, pp. 519–525, American Society of Mechanical Engineers, 2009.

127. Lee, S., K. Park, S. H. Sung and D. J. Nefske, "Boundary Condition Effect on the Correlation of an Acoustic Finite Element Passenger Compartment Model", *SAE Technical Paper, No. 2011-01-0506*, 2011.

128. Lee, J., J. Lee and S. Kim, "Acoustical Analysis of Multiple Cavities Connected by Necks in Series with a Consideration of Evanescent Waves", *Journal of Sound and Vibration*, Vol. 273, No. 3, pp. 515–542, 2004.

129. Ahn, C.-G., H. G. Choi and J. M. Lee, "Structural-Acoustic Coupling Analysis of Two Cavities Connected by Boundary Structures and Small Holes", *Journal of Vibration and Acoustics*, Vol. 127, No. 6, pp. 566–574, 2005.

130. Lee, J. W. and J. M. Lee, "Forced Vibro-Acoustical Analysis for a Theoretical

Model of a Passenger Compartment with a TrunkPart II: Experimental Part", *Journal of Sound and Vibration*, Vol. 299, No. 4, pp. 918–932, 2007.

131. Helmholtz, H., "Theorie der Luftschwingungen in Roehren MIT offenen Enden (1859)", *Ostwald's Klassiker der exakten Wissenschaften, Leipzig: Engelmann,—c1896*, Vol. 1, 1896.

132. Rayleigh, J., *The Theory of Sound*, Vol. I and II. Dover Edition, New York, 1945.

133. Nielsen, A. K., "Acoustic Resonators of Circular Cross-Section and with Axial Symmetry", *Trans. Danish Acad. Tech. Sci.*, , No. 10, 1949.

134. Ingard, U., "On the Theory and Design of Acoustic Resonators", *The Journal of the Acoustical Society of America*, Vol. 25, No. 6, pp. 1037–1061, 1953.

135. Panton, R. L. and J. M. Miller, "Resonant Frequencies of Cylindrical Helmholtz Resonators", *The Journal of the Acoustical Society of America*, Vol. 57, No. 6, pp. 1533–1535, 1975.

136. Chanaud, R., "Effects of Geometry on the Resonance Frequency of Helmholtz Resonators", *Journal of Sound and Vibration*, Vol. 178, No. 3, pp. 337–348, 1994.

137. Chanaud, R., "Effects of Geometry on the Resonance Frequency of Helmholtz Resonators, Part II", *Journal of Sound and Vibration*, Vol. 204, No. 5, pp. 829–834, 1997.

138. Selamet, A. and P. Radavich, "The Effect of Length on the Acoustic Attenuation Performance of Concentric Expansion Chambers: An Analytical, Computational and Experimental Investigation", *Journal of Sound and Vibration*, Vol. 201, No. 4, pp. 407–426, 1997.

139. Ingard, U., *Notes on Acoustics*, Laxmi Publications, Ltd., 2010.

140. Cullum, J. K. and R. A. Willoughby, *Lanczos Algorithms for Large Symmetric*

Eigenvalue Computations: Vol. 1: Theory, Vol. 41, SIAM, 2002.

141. Bai, Z., J. Demmel, J. Dongarra, A. Ruhe and H. van der Vorst, *Templates for the Solution of Algebraic Eigenvalue Problems: A Practical Guide*, Vol. 11, SIAM, 2000.

142. Fahy, F. J. and P. Gardonio, *Sound and Structural Vibration: Radiation, Transmission and Response*, Academic Press, 2007.

143. Bennur, M., "Superelement, Component Mode Synthesis, and Automated Multi-Level Substructuring for Rapid Vehicle Development", *SAE Technical Paper, No. 2008-01-0287*, 2008.

144. Bennighof, J. K., M. F. Kaplan, M. Kim, C. Kim and M. Muller, "Implementing Automated Multi-Level Substructuring in Nastran Vibroacoustic Analysis", *SAE Technical Paper, No. 2001-01-1405*, 2001.

145. Van Langenhove, T. and M. Brughmans, "Using MSC/NASTRAN and LMS/Pretest to Find an Optimal Sensor Placement for Modal Identification and Correlation of Aerospace Structures", *LMS International*, 1999.

146. Schwarz, B., M. Richardson and P. Avitabile, "Locating Optimal References for Modal Testing", *Proceedings of the 20th International Modal Analysis Conference, Los Angeles*, 2002.

147. Kammer, D. C. and M. L. Tinker, "Optimal Placement of Triaxial Accelerometers for Modal Vibration Tests", *Mechanical Systems and Signal Processing*, Vol. 18, No. 1, pp. 29–41, 2004.

148. Imamovic, N., *Validation of Large Structural Dynamics Models Using Modal Test Data*, Ph.D. Thesis, London, UK: Imperial College, 1998.

149. Chen, G., *FE Model Validation for Structural Dynamics*, Ph.D. Thesis, University of London, 2001.

150. Davidsson, P., *Structure-Acoustic Analysis; Finite Element Modeling and Reduction Methods*, Ph.D. Thesis, Lund University, 2004.

151. Kientzy, D., M. Richardson and K. Blakely, "Using Finite Element Data to Set Up Modal Tests", *Sound and Vibration Magazine*, Vol. 23, No. 6, pp. 16–23, 1989.

152. Allemang, R. J. and D. L. Brown, "A Correlation Coefficient for Modal Vector Analysis", *Proceedings of the 1st International Modal Analysis Conference*, Vol. 1, pp. 110–116, SEM, Orlando, 1982.

153. Ibrahim, S. R., "Computation of Normal Modes from Identified Complex Modes", *AIAA Journal*, Vol. 21, No. 3, pp. 446–451, 1983.

154. Fuellekrug, U., "Computation of Real Normal Modes from Complex Eigenvectors", *Mechanical Systems and Signal Processing*, Vol. 22, No. 1, pp. 57–65, 2008.

155. Wang, T., L. Zhang and K. F. Tee, "Extraction of Real Modes and Physical Matrices from Modal Testing", *Earthquake Engineering and Engineering Vibration*, Vol. 10, No. 2, pp. 219–227, 2011.

156. Rao, S. S., *Mechanical Vibrations*, Pearson Education, New Jersey, 4 edn., 2004.

157. Inman, D. J., *Engineering Vibrations*, Pearson Education, New Jersey, 3 edn., 2009.

158. Zhang, L., H. Kanda, D. Brown and R. Allemang, "A Polyreference Frequency Domain Method for Modal Parameter Identification", *ASME Design Engineering Technical Conference*, p. 6, 1985.

159. Lembregts, F., J. Leuridan and H. Van Brussel, "Frequency Domain Direct Parameter Identification for Modal Analysis: State Space Formulation", *Mechanical Systems and Signal Processing*, Vol. 4, No. 1, pp. 65–75, 1990.

160. Peeters, B., H. Van der Auweraer, P. Guillaume and J. Leuridan, "The PolyMAX

Frequency-Domain Method: A New Standard for Modal Parameter Estimation?", *Shock and Vibration*, Vol. 11, No. 3-4, pp. 395–409, 2004.

161. Peeters, B. and H. Van der Auweraer, "Polymax: A Revolution in Operational Modal Analysis", *1st International Operational Modal Analysis Conference*, 2005.

162. Allemang, R. J., "The Modal Assurance Criterion–Twenty Years of Use and Abuse", *Sound and Vibration*, Vol. 37, No. 8, pp. 14–23, 2003.

163. Heylen, W. and T. Janter, "Extensions of the Modal Assurance Criterion", *Journal of Vibration and Acoustics*, Vol. 112, No. 4, pp. 468–472, 1990.

164. O'Callahan, J., "Correlation Considerations-Part 4 (Modal Vector Correlation Techniques)", *Proceedings-SPIE The International Society for Optical Engineering*, Vol. 1, pp. 197–206, SPIE, 1998.

165. Brechlin, E., K. Bendel and W. Keiper, "A New Scaled Modal Assurance Criterion for Eigenmodes Containing Rotational Degrees of Freedom", *Proceedings of the International Seminar on Modal Analysis*, Vol. 3, pp. 1175–1182, Katholieke Universiteit Leuven, 1999.

166. Wei, J. J. and R. J. Allemang, "Model Correlation and Orthogonality Criteria Based on Reciprocal Modal Vectors", *9th Conference International Modal Analysis Conference (IMAC)*, Vol. 1, pp. 486–491, 1991.

167. Fotsch, D. and D. Ewins, "Application of MAC in the Frequency Domain", *Rolls Royce Plc-Report-Pnr*, 2000.

168. Lieven, N. and D. Ewins, "Spatial Correlation of Mode Shapes, the Coordinate Modal Assurance Criterion (COMAC)", *Proceedings of the 6th International Modal Analysis Conference*, Vol. 1, pp. 690–695, 1988.

169. Hunt, D. L., "Application of an Enhanced Coordinate Modal Assurance Criterion", *10th International Modal Analysis Conference*, Vol. 1, pp. 66–71, 1992.

170. Milacek, S., "The Use of Modal Assurance Criterion Extended", *Proceedings of the 12th International Modal Analysis*, Vol. 2251, p. 363, 1994.

171. Lieven, N. and T. Waters, "Error Location Using Normalised Orthogonality", *Proceedings-SPIE The International Society for Optical Engineering*, pp. 761–761, SPIE, 1994.

172. Samman, M., "A Modal Correlation Coefficient for Detection of Kinks in Mode Shapes", *Journal of Vibration and Acoustics*, Vol. 118, No. 2, pp. 271–272, 1996.

173. Mitchell, L., "Increasing the Sensitivity of the Modal Assurance Criteria (MAC) to Small Mode Shape Changes: The IMAC", *Proceedings-SPIE The International Society for Optical Engineering*, Vol. 1, pp. 64–69, SPIE, 1998.

174. Van der Auweraer, H., M. Iadevaia, U. Emborg, M. Gustavsson, U. Tengzelius and N. Horlin, "Linking Test and Analysis Results in the Medium Frequency Range Using Principal Field Shapes", *Proceedings of the International Seminar on Modal Analysis*, Vol. 2, pp. 823–830, Katholieke Universiteit Leuven, 1999.

175. Pascual, R., J.-C. Golinval and M. Razeto, "A Frequency Domain Correlation Technique for Model Correlation and Updating", *Proceedings-SPIE The International Society for Optical Engineering*, pp. 587–592, SPIE, 1997.

176. Avitabile, P. and F. Pechinsky, "Coordinate Orthogonality Check (CORTHOG)", *Proceedings-SPIE The International Society for Optical Engineering*, pp. 753–753, SPIE, 1994.

177. Morales, C., "Comments on the MAC and the NCO, and a Linear Modal Correlation Coefficient", *Journal of Sound and Vibration*, Vol. 282, No. 1, pp. 529–537, 2005.

178. Maia, N. M. M. and J. M. M. e Silva, *Theoretical and Experimental Modal Analysis*, Research Studies Press Taunton, 1997.

179. Heylen, W. and S. Lammens, "FRAC: A Consistent Way of Comparing Frequency Response Functions", *Proceedings of the Conference on Identification in Engineering Systems*, pp. 48–57, 1996.

180. Nefske, D. and S. Sung, "Correlation of a Coarse-Mesh Finite Element Model Using Structural System Identification and a Frequency Response Assurance Criterion", *Proceedings-SPIE The International Society for Optical Engineering*, pp. 597–602, SPIE, 1996.

181. Chen, A., "Frequency Response Assurance Criterion and Applications to Model Correlation of Body Structures", *SAE Technical Paper, No. 2003-01-1737*, 2003.

182. "Correlation Analysis", in LMS VirtualLab Rev. 12 Help Files, 2014.

183. Wang, X., *Vehicle Noise and Vibration Refinement*, Elsevier, 2010.

184. Lalor, N. and H. Priebsch, "The Prediction of Low- and Mid-Frequency Internal Road Vehicle Noise: A Literature Survey", *Proceedings of the Institution of Mechanical Engineers, Part D: Journal of Automobile Engineering*, Vol. 221, No. 3, pp. 245–269, 2007.

185. Kruntcheva, M. R., "Acoustic-Structural Resonances of Thin-Walled Structure-Gas Systems", *Journal of Vibration and Acoustics*, Vol. 128, No. 6, pp. 722–731, 2006.

186. Marburg, S., "Six Boundary Elements per Wavelength: Is That Enough?", *Journal of Computational Acoustics*, Vol. 10, No. 01, pp. 25–51, 2002.

187. Łodygowski, T. and W. Sumelka, "Limitations in Application of Finite Element Method in Acoustic Numerical Simulation", *Journal of Theoretical and Applied Mechanics*, Vol. 44, No. 4, pp. 849–865, 2006.

188. Sodano, H. A., J.-S. Bae, D. J. Inman and W. K. Belvin, "Concept and Model of Eddy Current Damper for Vibration Suppression of a Beam", *Journal of Sound*

and Vibration, Vol. 288, No. 4, pp. 1177–1196, 2005.

189. González, A. G., J. Rodrıguez, X. Sagartzazu, A. Schuhmacher and I. Isasa, "Multiple Coherence Method in Time Domain for the Analysis of the Transmission Paths of Noise and Vibrations With Non Stationary Signals", *Proceedings of ISMA including USD2010*, pp. 3927–3942, Leuven, 2010.

190. Kirchhoff, G., "Über das Gleichgewicht und die Bewegung einer Elastischen Scheibe.", *Journal für die Reine und Angewandte Mathematik*, Vol. 40, pp. 51–88, 1850.

191. Leissa, A. W., *Vibration of Plates*, Published for the Acoustical Society of America Through the American Institute of Physics, 1993.

APPENDIX A: Coherence Function

Definitions

$$\text{Auto-correlation function} := R_{xx}(\tau) = \lim_{T\to\infty} \frac{1}{T} \int_0^T x(t)x(t+\tau)dt \tag{A.1}$$

$$\text{Cross-correlation function:}= R_{xy}(\tau) = \lim_{T\to\infty} \frac{1}{T} \int_0^T x(t)y(t+\tau)dt \tag{A.2}$$

$$\text{Autopowers} := S_{xx}(f) = \int_{-\infty}^{\infty} R_{xx}(\tau)e^{-i2\pi ft}d\tau \tag{A.3}$$

$$\text{Crosspowers} := S_{xy}(f) = \int_{-\infty}^{\infty} R_{xy}(\tau)e^{-i2\pi ft}d\tau \tag{A.4}$$

$$\text{Cross-spectrum inequality} := |S_{xy}(f)|^2 \leq S_{xx}(f)S_{yy}(f) \tag{A.5}$$

$$\text{Ordinary coherence function} := \gamma_{xy}^2(f) = \frac{|S_{xy}(f)|^2}{S_{xx}(f)S_{yy}(f)}, \quad 0 \leq \gamma_{xy}^2(f) \leq 1 \tag{A.6}$$

If X is a vector of inputs, then [189]

$$\text{Multiple coherence function} := \gamma_{Xy}^2(f) = \frac{S_{Xy}^H(f)S_{XX}^{-1}(f)S_{Xy}(f)}{S_{yy}(f)}, \quad 0 \leq \gamma_{Xy}^2(f) \leq 1 \tag{A.7}$$

A proof for the ordinary coherence function

Consider two stationary random processes $\{x(t)\}$ and $\{y(t)\}$, where the finite Fourier transforms over the k^{th} record of length T representing each process are given by

$$X_k(f,T) = \int_0^T x_k(t)e^{-i2\pi ft}dt, \quad Y_k(f,T) = \int_0^T y_k(t)e^{-i2\pi ft}dt \tag{A.8}$$

$$S_{xy}(f) := \lim_{T\to\infty} \frac{1}{T} E[X_k^*(f,T)Y_k(f,T)] \tag{A.9}$$

For any real constants, a and b,

$$\frac{1}{T} E\left[|aX_k(f,T) + bY_k(f,T)e^{i\theta_{xy}(f)}|^2\right] \geq 0 \tag{A.10}$$

where $\theta_{xy}(f)$:=cross spectrum phase, and

$$\begin{aligned} &\frac{1}{T}E[a^2|X_k(f,T)|^2 + abX_k^*(f,T)Y_k(f,T)e^{i\theta_{xy}(f)} \\ &+ abX_k(f,T)Y_k^*(f,T)e^{-}i\theta_{xy}(f) + b^2|Y_k(f,T)|^2] \geq 0 \end{aligned} \tag{A.11}$$

Taking the limit $T \to \infty$, we get

$$a^2S_{xx}(f) + ab[S_{xy}(f)e^{i\theta_{xy}(f)} + S_{yx}e^{-i\theta_{xy}(f)}] + b^2S_{yy}(f) \geq 0 \tag{A.12}$$

Since $S_{xy}(-f) = S_{xy}^*(f) = S_{yx}(f)$,

$$S_{xy}(f) = |S_{xy}(f)|e^{-i\theta_{xy}(f)} \quad and \quad S_{yx}(f) = |S_{xy}(f)|e^{i\theta_{xy}(f)} \tag{A.13}$$

$$\Rightarrow a^2S_{xx}(f) + 2ab|S_{xy}(f)| + b^2S_{yy}(f) \geq 0 \tag{A.14}$$

Assuming $b \neq 0$, and dividing Equation (A.13) by b^2 gives

$$\left(\frac{a}{b}\right)^2 S_{xx}(f) + 2\left(\frac{a}{b}\right)|S_{xy}(f)| + S_{yy}(f) \geq 0 \tag{A.15}$$

$$\Rightarrow 4|S_{xy}(f)|^2 - 4S_{xx}(f)S_{yy}(f) \leq 0 \tag{A.16}$$

$$\therefore |S_{xy}(f)|^2 \leq S_{xx}(f)S_{yy}(f) \tag{A.17}$$

□

APPENDIX B: Vibration of Thin Plates

Vehicle structures are composed of assembled thin plates. It is assumed that these thin plates are elastic and made of isotropic, homogeneous materials. Displacements are supposed to be small with respect to the thickness of plate. It is assumed that straight lines normal to the mid-surface remain unstrained after deformation, and no stress is occurred in the mid-surface. These assumptions which are known as Kirchhoff's hypotheses [190], are analogous to those associated with the simple bending theory of beams. In what follows a derivation for the vibration of thin plates is given. This derivation follows the notation used by Leissa [191].

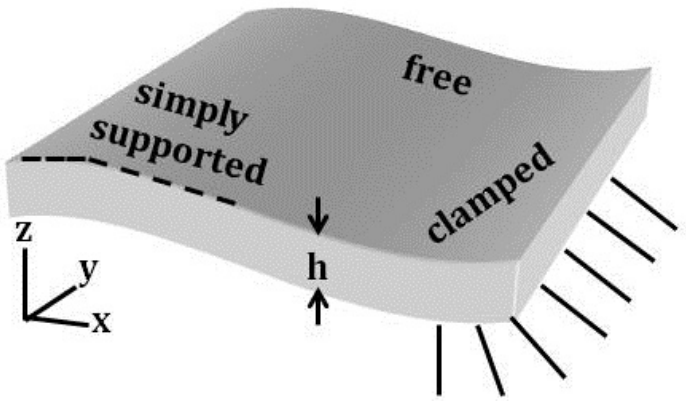


Figure B.1. An arbitrary plate and boundary conditions

An arbitrary plate of thickness h is shown in Figure B.1. Clamped, simply supported and free boundary conditions are used for a general representation. The coordinate system is located at the mid-surface of the plate, and when it is in equilibrium, bottom and top surfaces of the plate are at $z = \pm h/2$, where h is the plate thickness. In Figure B.2., forces and moments acting on the plate element are shown explicitly. Q_x and Q_y are shear forces; q is the distributed pressure, which is applied on surface area; M_x and M_y are bending moments; M_{xy} and M_{yx} are twisting moments; σ_x and σ_y are bending stresses; τ_{xy} and τ_{yx} are shear stresses.

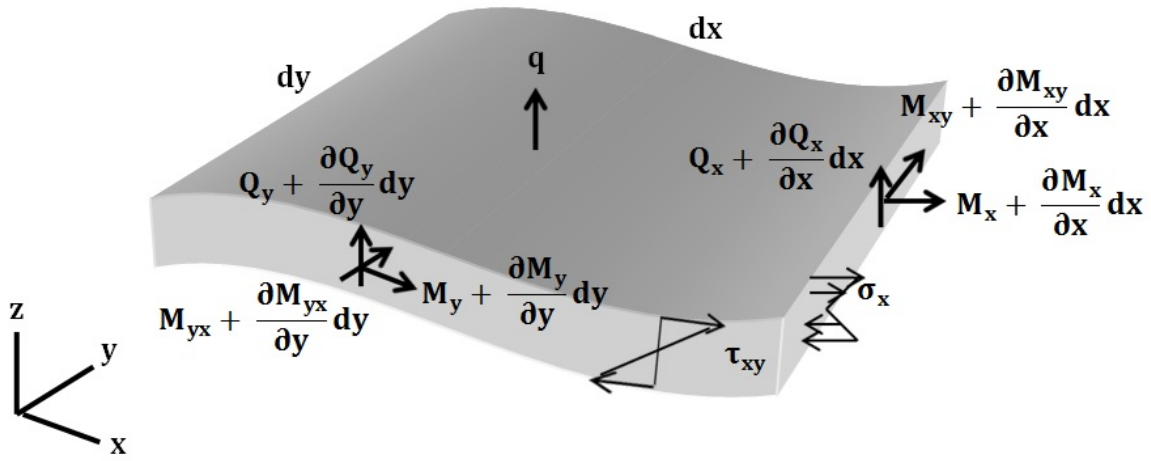


Figure B.2. Forces and moments acting on the deformed plate element

Depending on the aforementioned assumptions, summation of forces in z-direction yields,

$$\begin{aligned} &- Q_x dy + \left(Q_x + \frac{\partial Q_x}{\partial x} dx \right) dy - Q_y dx + \left(Q_y + \frac{\partial Q_y}{\partial y} dx \right) dx + q dx dy \\ &= \rho h dx dy \frac{\partial^2 w}{\partial t^2} \end{aligned} \tag{B.1}$$

where w is the displacement at z-direction and ρ is mass density per unit volume. Rearranging Equation (B.1) and dividing by the area ($dxdy$) yields

$$\frac{\partial Q_x}{\partial x} + \frac{\partial Q_y}{\partial y} + q = \rho h \frac{\partial^2 w}{\partial t^2} \tag{B.2}$$

Summation of moments about x gives

$$Q_y - \frac{\partial M_{xy}}{\partial x} - \frac{\partial M_y}{\partial y} = 0 \tag{B.3}$$

and similarly summation of moments about y gives

$$Q_x - \frac{\partial M_x}{\partial x} - \frac{\partial M_{xy}}{\partial y} = 0 \tag{B.4}$$

Displacements at x- and y-axis are nominated as u and v, respectively. These are related to rotations by

$$u = -z\frac{\partial w}{\partial x}, \quad v = -z\frac{\partial w}{\partial y} \tag{B.5}$$

Normal and shear strains occurred due to these displacements are expressed by

$$\epsilon_x = \frac{\partial u}{\partial x}, \quad \epsilon_y = \frac{\partial v}{\partial y}, \quad \gamma_{xy} = \frac{\partial u}{\partial x} + \frac{\partial v}{\partial y} \tag{B.6}$$

respectively. Substitution of Equation (B.6) into Equation (B.5) yields

$$\epsilon_x = -z\frac{\partial^2 w}{\partial x^2}, \quad \epsilon_y = -z\frac{\partial^2 w}{\partial y^2}, \quad \gamma_{xy} = -2z\frac{\partial^2 w}{\partial x \partial y} \tag{B.7}$$

Depending on aforementioned isotropic material assumption, stresses and strains are related as

$$\epsilon_x = \frac{1}{E}\left(\sigma_x - \nu\sigma_y\right), \quad \epsilon_y = \frac{1}{E}\left(\sigma_y - \nu\sigma_x\right), \quad \gamma_{xy} = \frac{\tau_{xy}}{G} \tag{B.8}$$

where E is Young's modulus, ν is Poisson's ratio and G is shear modulus. They are related as

$$G = \frac{E}{2(1+\nu)} \tag{B.9}$$

Using this relation, Equation (B.8) can be rewritten as

$$\sigma_x = \frac{E}{1-\nu^2}\left(\epsilon_x + \nu\epsilon_y\right), \quad \sigma_y = \frac{E}{1-\nu^2}\left(\epsilon_y + \nu\epsilon_x\right) \quad \tau_{xy} = \frac{E}{2(1+\nu)}\gamma_{xy} \tag{B.10}$$

Once stresses are known moments can be written as

$$M_x = \int_{-h/2}^{h/2} \sigma_x z dz, \quad M_y = \int_{-h/2}^{h/2} \sigma_y z dz, \quad M_{xy} = \int_{-h/2}^{h/2} \tau_{xy} z dz \tag{B.11}$$

and integration yields

$$M_x = -D\left(\frac{\partial^2 w}{\partial x^2} + \nu\frac{\partial^2 w}{\partial y^2}\right), \quad M_y = -D\left(\frac{\partial^2 w}{\partial y^2} + \nu\frac{\partial^2 w}{\partial x^2}\right), \quad M_{xy} = -D\left(1-\nu\right)\frac{\partial^2 w}{\partial x \partial y} \tag{B.12}$$

where D is the flexural rigidity, and given as

$$D = \frac{Eh^3}{12(1-\nu^2)} \tag{B.13}$$

Recalling Equation (B.2) and rearranging, we have

$$D\left(\frac{\partial^4 w}{\partial x^4} + 2\frac{\partial^2 w}{\partial x^2 \partial y^2} + \frac{\partial^4 w}{\partial y^4}\right) + \rho h\frac{\partial^2 w}{\partial t^2} = q \tag{B.14}$$

Equation (B.14) can be expressed in a more compact form, using biharmonic differential operator (∇^4), i.e.

$$D\nabla^4 w + \rho h\frac{\partial^2 w}{\partial t^2} = q \tag{B.15}$$

APPENDIX C: Derivation of Finite Element Equation: Structural Domain

Steady-state dynamic equation for the bending motion of described thin plate is given in Equation (B.15). If we assume free vibrations, the governing equation of motion reduces to

$$D\nabla^4 w + \rho h \frac{\partial^2 w}{\partial t^2} = 0 \tag{C.1}$$

Assuming a sinusoidal form of time response, i.e.

$$w(x, y, t) = W(x, y) \sin(\omega t + \phi) \tag{C.2}$$

Equation (C.1) becomes

$$\left(\nabla^4 w - k_b^4\right) W = 0 \tag{C.3}$$

where $k_b = \sqrt[4]{\rho h \omega^2 / D}$ and referred as bending wavenumber; herein, W is the displacement pattern (mode shape). The weighted residual formulation of Equation (C.3) can be expressed as

$$\begin{aligned} &\int_{\Omega_s} \widetilde{w} \left(q + \rho h \omega^2 w + \frac{\partial Q_x}{\partial x} + \frac{\partial Q_y}{\partial y} \right) d\Omega + \int_{\Omega_s} \frac{\partial \widetilde{w}}{\partial x} \left(Q_x - \frac{\partial M_x}{\partial x} - \frac{\partial M_{xy}}{\partial y} \right) d\Omega \\ &+ \int_{\Omega_s} \frac{\partial \widetilde{w}}{\partial y} \left(Q_y - \frac{\partial M_y}{\partial y} - \frac{\partial M_{xy}}{\partial x} \right) d\Omega = 0 \end{aligned} \tag{C.4}$$

where Ω_s is plate surface. Application of divergence theorem yields

$$\begin{aligned} &\int_{\Omega_s} \left(M_x \frac{\partial^2 \widetilde{w}}{\partial x^2} + M_y \frac{\partial^2 \widetilde{w}}{\partial y^2} + 2 M_{xy} \frac{\partial^2 \widetilde{w}}{\partial x \partial y} \right) d\Omega + \int_{\Omega_s} \rho h \omega^2 \widetilde{w} w d\Omega + \int_{\Omega_s} \widetilde{w} q d\Omega \\ &+ \int_{\Gamma_s} \widetilde{w} Q_n d\Gamma = \int_{\Gamma_s} \frac{\partial \widetilde{w}}{\partial n} M_n d\Gamma \end{aligned} \tag{C.5}$$

where Γ_s is the boundary of Ω_s (plate surface), and n is normal vector. In a finite element framework, Ω_s can be discretized into small surfaces (say Ω_{fe}) through an appropriate number of nodes (say n_t), which can be determined either manually, or through a commercial code. The small surfaces Ω_{fe}, i.e. 'finite elements' have a node at each corner, and beside mid-surface displacement, each node has 2 rotational DOFs with respect to x and y. The mid-surface displacement w can be expanded in terms of shape functions N, i.e.

$$\hat{w} = \sum_{1}^{n_t} \sum_{1}^{3} N\alpha = [N] \cdot \{\hat{w}_i\} \tag{C.6}$$

where $\hat{w}_i$ is the unknown DOFs, and α is the contributions, which can be determined from Equation (C.5). Following the notation used by Desmet [39], the weighting function can be expanded as

$$\widetilde{w} = [N] \cdot \{\widetilde{w}_i\} \tag{C.7}$$

Substitution of these expansions into Equation (C.5) yields

$$\begin{aligned}
&\{\widetilde{w}_i\}^T \cdot \left([K_s] - \omega^2 [M_s]\right) \cdot \{\hat{w}_i\} = \{\widetilde{w}_i\}^T \cdot \left(\int_{\Omega_s} \left([N]^T q\right) d\Omega + \int_{\Gamma_{s2}} \left([N]^T \overline{Q}_n\right) d\Gamma \right) - \\
&\{\widetilde{w}_i\}^T \cdot \left(\int_{\Gamma_{s2+s3}} \left(\left(\{n\}^T [\partial][N]\right)^T \overline{m}_n \right) d\Gamma - \int_{\Gamma_{s1+s3}} \left([N]^T Q_n\right) d\Gamma \right) - \\
&\{\widetilde{w}_i\}^T \cdot \left(\int_{\Gamma_{s1}} \left(\left(\{n\}^T [\partial][N]\right)^T m_n \right) d\Gamma \right)
\end{aligned} \tag{C.8}$$

where bar symbol denotes that variables have prescribed values, through boundary conditions. On the structural boundary Γ_s different type boundary conditions may hold. The integral terms: $s1$, $s2$ and $s3$ are related to Dirichlet, Neumann and Robin type boundary conditions (BCs), respectively. Finally, employing the mentioned BCs, and introducing a structural damping matrix yields

$$\left([K_s] + j\omega[C_s] - \omega^2[M_s]\right) \cdot \{w_i\} = \{F_{si}\} \tag{C.9}$$

APPENDIX D: Derivation of Finite Element Equation: Acoustic Fluid Domain

The principle of conservation of mass states that the increase per unit time of the mass of the fluid volume is equal to the net mass entering to the volume per unit time. If an external acoustic source is present, an additional mass flow is induced in the fluid. Defining q as the volume velocity per unit volume induced by the external acoustic source,

$$q(x,y,z,t) = q_0(x,y,z,t) + q'(x,y,z,t) \tag{D.1}$$

the conservation of mass is expressed by

$$\frac{\partial\left(\rho_0+\rho'\right)}{\partial t} = \left(\rho_0+\rho'\right)q' - \nabla\cdot\left[\left(\rho_0+\rho'\right)\mathbf{v}'\right] \tag{D.2}$$

where ρ and $\mathbf{v}$ are mass density and velocity vector fields, respectively. The primed variables represent the acoustic perturbations into the fields. The conservation of momentum is expressed by

$$\left(\rho_0+\rho'\right)\left(\frac{\partial}{\partial t}+\mathbf{v}'\cdot\nabla\right)\mathbf{v}' = -\nabla\left(\rho_0+\rho'\right) \tag{D.3}$$

In adiabatic conditions, pressure-density relation is expressed by

$$p = C\rho^{\gamma} \tag{D.4}$$

where γ is the specific heat ratio and $C = p_0/\rho_0^{\gamma}$. Provided that the acoustic perturbations are very small, the primed terms in the conservation of mass, the conservation of momentum and the pressure-density relation can be linearized as follows.

$$\frac{\partial p'}{\partial t} = \rho_0 q' - \rho_0\nabla\cdot\mathbf{v}' \tag{D.5}$$

$$\rho_0 \frac{\partial \mathbf{v}'}{\partial t} = -\nabla p' \tag{D.6}$$

$$p' = \gamma \frac{p_0}{\rho_0} \rho' \tag{D.7}$$

Hence, for an inviscid, irrotational fluid that undergoes only small translations, the linear acoustic wave equation is expressed by [142]

$$\frac{\partial^2 p}{\partial t^2} - c^2 \nabla^2 p = c^2 \frac{\partial q}{\partial t} \tag{D.8}$$

where c is the speed of sound. For a time harmonic excitation, Equation (D.8) transforms into the linear Helmholtz equation as

$$\nabla^2 p + k^2 p = -j\rho_0 \omega q \tag{D.9}$$

where $k = \omega/c$ is acoustic wave number. Equivalent integral equation of Equation (D.9) can be expressed in weighted residual concept, which defines an acoustic pressure field in a bounded fluid volume V, i.e.

$$\int_V \tilde{p}(\nabla^2 p + k^2 p + j\rho_0 \omega q) dV = 0 \tag{D.10}$$

Divergence theorem (a.k.a. Gauss's theorem) states that fluid being introduced into a volume is equal to the total fluid flowing outward the boundary of the volume, provided that the fluid quantity is constant. Following the notation used by Desmet [39], for boundary surface Ω, the weak form of the weighted residual formulation of Equation (D.10) can be written as

$$\int_V (\overrightarrow{\nabla} \tilde{p} \overrightarrow{\nabla} p) dV - \omega^2 \int_V (\frac{1}{c^2} \tilde{p} p) dV = \int_V (j\rho_0 \omega \tilde{p} q) dV - \int_\Omega (j\rho_0 \omega \tilde{p} \overrightarrow{v}\, \overrightarrow{n}) d\Omega \tag{D.11}$$

Acoustically, three types of boundary conditions can be imposed;

$$p = \overline{p} \qquad @ \quad \Omega_p \quad \text{(Dirichlet B.C.)} \tag{D.12}$$

$$\overrightarrow{v}\,\overrightarrow{n} = \overline{v}_n \qquad @ \quad \Omega_v \quad \text{(Neumann B.C.)} \tag{D.13}$$

and

$$\overrightarrow{v}\,\overrightarrow{n} = \frac{p}{\overline{Z}} = \overline{A}p \qquad @ \quad \Omega_Z \quad \text{(Robin B.C.)} \tag{D.14}$$

where $\overline{p}$, $\overline{v}_n$ and $\overline{A}$ imposed pressure, imposed normal velocity and imposed normal admittance functions, respectively. In computational acoustics, linear tetrahedral or hexahedral elements are commonly used. Shape function N_i^e is defined, such that it is unity at node i of the considered element, whereas takes zero value at all other nodes. The field variable, say p, is approximated as an expansion $\widehat{p}$,

$$\widehat{p}(x,y,z) = \sum_{i=1}^{n_e} N_i^e(x,y,z)\widehat{p}_i \tag{D.15}$$

A global pressure expansion can be defined as

$$\widehat{p}(x,y,z) = \sum_{i=1}^{n_f} N_i(x,y,z)\widehat{p}_i = [N]\{\widehat{p}_i\} \qquad (x,y,z) \in V \tag{D.16}$$

where n_f is the total number of nodes in the model. Gradient of pressure is approximated as

$$\overrightarrow{\nabla} p \approx \overrightarrow{\nabla}\widehat{p} = \{\partial\}[N]\{\widehat{p}_i\} = [B]\{\widehat{p}_i\} \tag{D.17}$$

where $[B]$ matrix of gradient components of the global shape functions; hence,

$$\widetilde{p}(x,y,z) = \sum_{i=1}^{n_f} N_i(x,y,z)\widetilde{p}_i = [N]\{\widetilde{p}_i\} \qquad (x,y,z) \in V \tag{D.18}$$

and

$$\overrightarrow{\nabla}\widetilde{p} = \{\partial\}[N]\{\widetilde{p}_i\} = [B]\{\widetilde{p}_i\} \tag{D.19}$$

Nodal pressure values ($\widetilde{p}_i$) can be determined by substituting Equations (D.18) and (D.19) into Equation (D.11). For the first term in the left hand side of Equation (D.11), this substitution gives

$$\begin{aligned} \int_V (\overrightarrow{\nabla}\tilde{p}\overrightarrow{\nabla}p)dV &= \int_V \left(([B]\{\widetilde{p}_i\})([B]\{\widehat{p}_i\})^T\right) dV \\ =&\{\widetilde{p}_i\}^T \left(\int_V ([B]^T[B])dV\right)\{\widehat{p}_i\} = \{\widetilde{p}_i\}^T[K]\{\widehat{p}_i\} \end{aligned} \tag{D.20}$$

where $[K]$ is the acoustic stiffness matrix. Similarly, the second term in the left hand side of Equation (D.11) can be expressed as

$$\begin{aligned} -\omega^2 \int_V \left(\frac{1}{c^2}\widetilde{p}\widehat{p}\right) dV &= -\omega^2\{\widetilde{p}_i\}^T \left(\int_V (\frac{1}{c^2}[N]^T[N])dV\right)\{\widetilde{p}_i\} \\ =-\omega^2&\{\widetilde{p}_i\}^T[M]\{\widehat{p}_i\} \end{aligned} \tag{D.21}$$

where $[M]$ is the acoustic mass matrix. The first term in the right hand side of Equation (D.11) can be written as

$$\int_V (j\rho_0\omega\widetilde{p}q)\, dV = \{\widetilde{p}_i\}^T \left(\int_V \left(j\rho_0\omega[N]^T q\right) dV\right) = \{\widetilde{p}_i\}^T\{Q_i\} \tag{D.22}$$

where $\{Q_i\}$ is the acoustic source vector. If acoustic source distribution is assumed to be an acoustic point source of strength $\overline{q}_i$, located at node i, the source vector becomes

$$\{Q_i\} = j\rho_0\omega \left(\int_V (\overline{q}_i[N]^T\delta)dV\right) \tag{D.23}$$

where δ is a Dirac delta function at node i. The second term in the right hand side of Equation (D.11) can be expressed as

$$-\int_{\Omega_v}\left(j\rho_0\omega\widetilde{p}\overline{v}_n\right)d\Omega-\int_{\Omega_Z}\left(j\rho_0\omega\widetilde{p}\overline{A}\widehat{p}\right)d\Omega-\int_{\Omega_p}\left(j\rho_0\omega\widetilde{p}\,\overrightarrow{v}\,\overrightarrow{n}\right)d\Omega \tag{D.24}$$

when boundary conditions given in Equations (D.12) to (D.14) are imposed. The substitution of Equation (D.18) into the first term of Equation (D.24) yields

$$-\int_{\Omega_v}\left(j\rho_0\omega\widetilde{p}\overline{v}_n\right)d\Omega=\{\widetilde{p}_i\}^T\left(\int_{\Omega_v}\left(-j\rho_0\omega[N]^T\overline{v}_n\right)d\Omega\right)=\{\widetilde{p}_i\}^T\{V_m\} \tag{D.25}$$

where $\{V_m\}$ is defined as velocity vector. The second term of Equation (D.24) can be written as

$$\begin{aligned}-\int_{\Omega_Z}\left(j\rho_0\omega\widetilde{p}\overline{A}\widehat{p}\right)d\Omega&=-j\omega\{\widetilde{p}_i\}^T\left(\int_{\Omega_Z}(\rho_0\overline{A}[N]^T[N])d\Omega\right)\{\widehat{p}_i\}\\&=-j\omega\{\widetilde{p}_i\}^T[C]\{\widehat{p}_i\}\end{aligned} \tag{D.26}$$

where $[C]$ is the acoustic damping matrix. The substitution of Equation (D.18) into the third term of Equation (D.24) gives

$$-\int_{\Omega_p}\left(j\rho_0\omega\widetilde{p}\,\overrightarrow{v}\,\overrightarrow{n}\right)d\Omega=\{\widetilde{p}_i\}^T\left(\int_{\Omega_v}(-j\rho_0\omega[N]^T\overrightarrow{v}\,\overrightarrow{n})d\Omega\right)=\{\widetilde{p}_i\}^T\{p_i\} \tag{D.27}$$

By substituting Equations (D.20) and (D.22) to (D.25) into Equation (D.11) and imposing boundary conditions given in Equations (D.13) and (D.14), we have

$$\{\widetilde{p}_i\}^T\left([K]+j\omega[C]-\omega^2[M]\right)\{\widehat{p}_i\}=\{\widetilde{p}_i\}^T\left(\{Q_i\}+\{V_m\}+\{P_i\}\right) \tag{D.28}$$

$$\Rightarrow\left([K]+j\omega[C]-\omega^2[M]\right)\{\widehat{p}_i\}=\{Q_i\}+\{V_m\}+\{P_i\} \tag{D.29}$$

Finally, by imposing Dirichlet type boundary condition of Equation (D.12), the FE model for an uncoupled acoustic problem is written as

$$\left([K_a] + j\omega[C_a] - \omega^2[M_a]\right) \cdot \{p_i\} = \{F_{ai}\} \tag{D.30}$$

where $[K_a]$, $[C_a]$ and $[M_a]$ are acoustic stiffness, damping and mass matrices, respectively. $\{p_i\}$ denotes the unknown nodal pressure approximations and $\{F_{ai}\}$ (i.e. acoustic force vector) represents the stiffness, damping and mass terms in the a priori assigned nodal pressures, and the contributions of the acoustic source vector and the input velocity vector.

APPENDIX E: Eulerian Displacement-Pressure Formulation

In Appendices C and D, structural and acoustic finite element formulations are derived, respectively. These formulations,

$$\big([K_s] + j\omega[C_s] - \omega^2[M_s]\big) \cdot \{w_i\} = \{F_{si}\}, \text{ in } \Omega_s \quad \text{(Structural domain)} \tag{E.1}$$

$$\big([K_a] + j\omega[C_a] - \omega^2[M_a]\big) \cdot \{p_i\} = \{F_{ai}\}, \text{ in } \Omega_a \quad \text{(Acoustic domain)} \tag{E.2}$$

can be used for uncoupled analysis of low frequency vehicle acoustics problems. On the other hand, acoustic pressure forms an additional load on the structural domain for lightweight shells, where mostly used in BIW, where panel thicknesses are in the range of 0.5-0.8 mm. In vehicle structures a strong coupling is observed between acoustical modes of the cavity and structural modes of the body, especially in low frequency range where booming noise frequently occurs. The air, confined inside passenger and trunk cavities, is excited by structural displacements of surrounding panels, causing a volume change and creating high impedance [124]. Consequently, an additional term can be added to the structural FE model, which modifies Equation (E.1) to

$$\big([K_s] + j\omega[C_s] - \omega^2[M_s]\big) \cdot \{w_i\} + [K_c] \cdot \{p_i\} = \{F_{si}\} \tag{E.3}$$

where $[K_c]$ stands for coupling matrix. Likewise, shell velocities occurred in the vicinity of fluid-structure coupling interface may be regarded as an additional load on the acoustic domain. Consequently, an additional term can be added to the acoustic FE model, which modifies Equation (E.2) to

$$\big([K_a] + j\omega[C_a] - \omega^2[M_a]\big) \cdot \{p_i\} - \omega^2[M_c] \cdot \{w_i\} = \{F_{ai}\} \tag{E.4}$$

where $[M_c]$ stands for coupling matrix. The relation between two coupling matrix is given as

$$[M_c] = -\rho_0[K_c] \tag{E.5}$$

This relation means that the additional load on the structure is proportional to the pressure induced by fluid, whereas the additional load on the fluid is proportional to the acceleration of the structure. Hence, combining Equations (E.3) and (E.4), the coupled vibro-acoustic problem is expressed by

$$\begin{bmatrix} K_s & K_c \\ 0 & K_a \end{bmatrix} + j\omega \begin{bmatrix} C_s & 0 \\ 0 & C_a \end{bmatrix} - \omega^2 \begin{bmatrix} M_s & 0 \\ -\rho_0 K_c^T & M_a \end{bmatrix} \begin{Bmatrix} w_i \\ p_i \end{Bmatrix} = \begin{Bmatrix} F_{si} \\ F_{ai} \end{Bmatrix} \tag{E.6}$$

where

M, C, K mass, damping and stiffness matrices,

w nodal displacement vector of the structure at the boundary,

p sound pressure vector of the interior sound field,

F structural or acoustical load vector,

s structure,

a acoustic.